IRE Transactions

on ANTENNAS and PROPAGATION

Volume AP-8 **JANUARY, 1960** **Number 1**

Published Bi-Monthly

TABLE OF CONTENTS

CONTRIBUTIONS

COMMUNICATIONS

PUBLISHED BY THE

Professional Group on Antennas and Propagation

IRE TRANSACTIONS® PGAP IS A PUBLICATION DEVOTED TO EXPERIMENTAL AND THEORETICAL PAPERS ON RADIO ANTENNAS, ON GUIDED OR UNGUIDED PROPAGATION OF RADIO WAVES, AND ON ALLIED FIELDS OF RADIO PHYSICS SUCH AS RADIO ASTRONOMY

MANUSCRIPTS should be submitted to S. A. Bowhill, 222 Electrical Engineering, Pennsylvania State University, University Park, Pa. Manuscripts should be original typewritten copy, double spaced, plus one carbon copy. References should appear as footnotes and include author's name, title, journal, volume, initial and final page numbers, and date. Each paper must have a summary of not more than 200 words. News items concerning PGAP members and group activities should be sent to the News Editor, R. C. Hansen, Space Technology Laboratories, P.O. Box 95001, Los Angeles 45, Calif.

ILLUSTRATIONS should be submitted as follows: All line drawings (graphs, charts, block diagrams, cutaways, etc.) should be inked uniformly and ready for reproduction. If commercially printed grids are used in graph drawings, author should be sure printer's ink is of a color that will reproduce. All half-tone illustrations (photographs, wash, airbrush, or pencil renderings, etc.) should be clean and ready to reproduce. Photographs should be glossy prints. Call-outs or labels should be marked on a registered tissue overlay, not on the illustration itself. No illustration should be larger than 8 x 10 inches.

Copies can be purchased from **THE INSTITUTE OF RADIO ENGINEERS, 1 East 79 St., New York 21, N.Y. PRICE PER COPY:** members of the Professional Group on Antennas and Propagation, $2.40; members of the IRE $3.60; nonmembers, $7.20. **ANNUAL SUBSCRIPTION PRICE:** PGAP members, included in PGAP fee of $4.00; IRE members, $8.50; Colleges and public libraries, $10.00; nonmembers, $17.00. IRE TRANSACTIONS ON ANTENNAS AND PROPAGATION.

Entered as second-class matter, at the post office at Menasha, Wisconsin, under the act of August 24, 1912. Acceptance for mailing at a special rate of postage is provided for in the act of February 28, 1925, embodied in Paragraph 4, Section 412, P. L. & R., authorized October 26, 1927.

contributions

Back Scattering Cross Sections of Cylindrical Wires of Finite Conductivity*

E. S. CASSEDY† AND J. FAINBERG†

Summary—**The back scattering cross sections of fine wires, taking the effect of finite conductivity into account, have been found. The variational procedure is used to find theoretical expressions for the cross section and it is concluded that the zeroth and the first-order solutions of Tai converge to one another with the addition of loss, in the region of first resonance. For fine copper, platinum and bismuth wires, experimentally determined cross sections agree with the theoretical results calculated from the zero-order solution to within 4 per cent in peak resonant values and 1.5 per cent in bandwidth.**

Introduction

In recent years the back scattering cross sections of thin metallic cylinders have been computed by means of formulas based on the assumption of perfect conductivity.[1–6] These formulas have been derived through the use of EMF principles[1] or the variational technique.[2–6] The agreement of computed cross sections with experimentally obtained values is good in the range of physical parameters where the absorption losses are small.[2–6]

The effects of loss in the cylindrical conductor can be computed by extending the variational analysis of Tai[2] and Sevick.[3,6] This can be done by using the skin impedance per unit length[7] in the equation for the boundary condition at the surface of the cylinder. The expression for the back scattering cross section will then include an impedance term dependent on losses in the cylinder. Kouyoumjian[4] has given the results of this procedure using the zero-order solution trial function of Tai[2] but has not indicated further investigation of the validity of the results.

In the present work, both the zero- and the first-order trial functions of Tai[2] are used to obtain the loss-dependent back scattering cross sections of thin cylinders. The zero-order expression agrees with that given by Kouyoumjian.[4] These results are then compared with experimentally obtained values for cases where the cross sections are significantly affected by losses in the cylinder.

From the computed expressions for lossy cylinders less than one wavelength long, it is found that there is a negligible difference in numerical results in using the two trial functions. This is true for the lossless case also.[2] Furthermore, an investigation of the adjusted

* Manuscript received by the PGAP, January 12, 1959; revised manuscript received, August 10, 1959. This research was supported by the U. S. Air Force through the Wright Air Dev. Center of the Air Res. and Dev. Command.

† Radiation Lab., The Johns Hopkins University, Baltimore, Md.

[1] J. H. Van Vleck, F. Bloch, and M. Hamermesh, "Theory of radar reflection from wires or thin metallic strips," *J. Appl. Phys.*, vol. 18, pp. 274–294; March, 1947.

[2] C. T. Tai, "Electromagnetic back scattering from cylindrical wires," *J. Appl. Phys.*, vol. 23, pp. 909–916; August, 1952.

[3] J. E. Storer and J. Sevick, "General theory of plane-wave scattering from finite, conducting obstacles with application to the two antenna problems," *J. Appl. Phys.*, vol. 25, pp. 369–376; March, 1954.

[4] R. C. Kouyoumjian, "The Calculation of the Echo Areas of Perfectly Conducting Objects by the Variational Method," Antenna Lab., The Ohio State University, Columbus, Ohio, Tech. Rept. No. 44-13; 1953.

[5] J. M. Minkowski and E. S. Cassedy, "Cross section of collinear arrays at normal incidence," *J. Appl. Phys.*, vol. 27, pp. 313–317; March, 1956.

[6] J. Sevick, "Experimental and Theoretical Results on the Back Scattering Cross Section of Coupled Antennas," Cruft Lab., Harvard University, Cambridge, Mass., Tech. Rept. No. 150; May, 1952.

[7] S. Ramo and J. R. Whinnery, "Fields and Waves in Modern Radio," John Wiley and Sons, Inc., New York, N. Y.; 1949.

first-order constant in the trial function shows that the first-order trial function converges to the zero-order trial function with the addition of loss.

The general effect of loss is to reduce the scattering cross section and to widen the bandwidth. The resonant length is virtually unaffected. Experimental measurements of scattering cross sections of fine copper, platinum, and bismuth wires were made, and a comparison with computed results yields agreement to within 4 per cent in peak values and to within 1.5 per cent in bandwidth, wherever good experimental control was obtained on alignment of the wires.

Variational Method Applied to a Cylindrical Wire of Finite Conductivity at Broad Aspect

Consider a plane electromagnetic wave incident upon a cylindrical wire of finite conductivity, known permeability and a diameter small in comparison with wavelength, as shown in Fig. 1. The electric vector of the incident wave is parallel to the axis of the cylinder and the incident direction is normal to the cylinder axis. Using Hallén's equation,[8] and rationalized mks units, we are able to write the following scalar approximation for the electric field at the surface of the cylinder due to currents induced in the wire:

$$E_z(z) \approx \frac{-j\omega\mu}{4\pi}\int_{-l}^{l} I(z')\left[1-\frac{1}{k^2}\frac{\partial^2}{\partial z\partial z'}\right]\frac{\exp(-ikR)}{R}\,dz' \quad (1)$$

where:

$$I(z') = \text{"total current"}$$
$$R = \sqrt{(z-z')^2+a^2}$$
$$k = 2\pi/\lambda$$
$$\text{time dependence} = \exp(j\omega t)$$
$$E_z = E_y = 0.$$

For this approximation, it is assumed that the wire is sufficiently thin for the current at a given position along the wire to be uniform around the axis of the wire and so that it may be considered as a current filament $[I(z)]$ on the axis. In the lossless case, the integral in (1) is reduced from a surface integral[3] over both z and ϕ involving the exact expression for the distance:

$$R = \sqrt{(z-z')^2 + 4a^2\sin^2\left(\frac{\phi-\phi'}{2}\right)}.$$

It is possible to include a small correction term due to the angular dependence[3] of R, and results of such computations compared with experimentally determined results on wires having negligible losses are very good.[6] Both analyses, of course, neglect the effect of the end faces of the cylinder. The only attempt to consider this

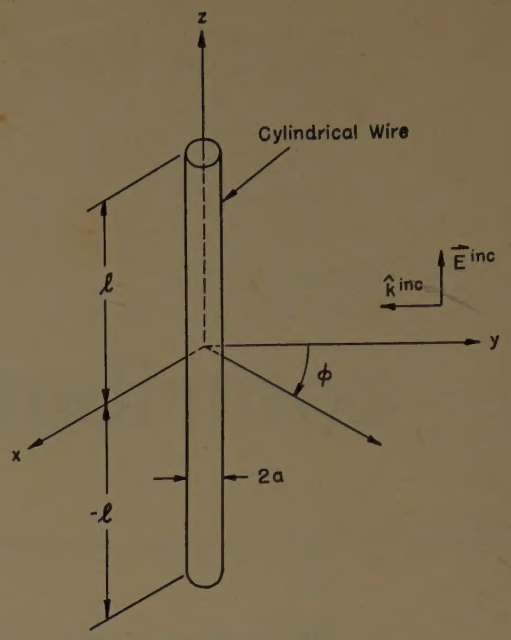

Fig. 1—Cylindrical wire scatterer at broadside incidence.

effect is in the choice of a trial function in the variational procedure.[2]

In the following we use the approximation shown in (1) for the case of a cylinder of finite conductivity. For this case, the currents actually penetrate into the volume of the cylinder, and the assumption of the "total current" filament used in the near field integral (1) is at least as good as for the lossless case.

With this approximation for the near field and with the approximation of the filamentary current with the skin impedance per unit length, the boundary condition at the surface of a cylinder of finite conductivity becomes

$$I(z)Z_i = E^{inc}(z) - \frac{j\omega\mu}{4\pi}\int_{-l}^{l} I(z')\left[1-\frac{1}{k^2}\frac{\partial^2}{\partial z\partial z'}\right]\frac{\exp(-ikR)}{R}\,dz' \quad (2)$$

where[7]

$$Z_i = R_i + j\omega L_i = \frac{j}{a}\sqrt{\frac{f\mu}{2\pi\sigma}}\left[\frac{\text{Ber}(q)+j\,\text{Bei}(q)}{\text{Ber}'(q)+j\,\text{Bei}'(q)}\right]$$

where

$$q = (\omega\mu\sigma)^{1/2}a$$
$$\text{Ber}(q) = \text{Re}\,J_0(j^{-1/2}q)$$
$$\text{Bei}(q) = \text{Im}\,J_0(j^{-1/2}q).$$

This reduces to the case of a vanishing tangential field at the cylinder surface for the lossless case ($Z_i = 0$).

The procedure from this point on is the usual variational method[2] of constructing a homogeneous functional for the "far scattered amplitude." The result of this procedure applied to (2) is as follows:

[8] E. Hallén, "Theoretical investigation into the transmitting and receiving qualities of antennas," *Nova Octa (Upsala)*, vol. 11, p. 1; January, 1938.

$$\frac{1}{S}=\frac{k\int_{-l}^{l}\int_{-l}^{l}I(z')\left[1-\frac{1}{k^2}\frac{\partial^2}{\partial z\partial z'}\right]\frac{\exp(-ikR)}{R}I(z)dz'dz-j\frac{4\pi Z_i}{\eta}\int_{-l}^{l}I^2(z)dz}{\left[k\int_{-l}^{l}I(z)dz\right]^2} \tag{3}$$

where S is the usual far field functional[2] such that

$$\frac{E_z^{sc}(r)}{E^{inc}}=\frac{\exp(-ikr)}{kr}S$$

with

r = distance to observer in the direction back toward the transmitter, and
$\eta=\sqrt{\mu/\epsilon}$.

This also reduces to the lossless case[2] when $Z_i=0$. The condition for stationarity is the boundary condition (2), as in the usual variational treatment of electromagnetic problems.

Solutions

The variational treatment is completed by the substitution of a proper trial function in (3). The simplest trial function, used in the treatment of the lossless case at broadside incidence,[2] is the shifted cosine distribution

$$I(z)=I_0(\cos kz-\cos kl). \tag{4}$$

The use of this trial function in (3) yields a solution which corresponds to the zeroth order solution of Tai.[2] The solution is obtained directly, since (3) is homogeneous, and the trial function involves just the single constant multiplier. The first integral of the numerator of (3) is evaluated for the shifted cosine $I(z)$[3,9] and will be signified as g. The second integral of the numerator and the integral in the denominator of (3) are elementary and are denoted as g' and f respectively. The zeroth order solution, for the case including losses, is then

$$\frac{1}{S}=\frac{g+g'}{f^2}, \tag{5}$$

where:

$$\begin{aligned}g^{3,9}&=Si(4kl)+jCi(4kl)-jln(\gamma 4kl)\\&\quad+4[\cos kl][kl\cos kl-\sin kl]\\&\quad\times\left[Ci(2kl)-jSi(2kl)-ln(\gamma 2kl)+ln\frac{4l}{a}\right]\\&\quad-j2[\cos^2 kl][\exp(-j2kl)-1]\\&\quad-\frac{4ka}{\pi}\sin^2 kl\end{aligned}$$

$$g'=-j\frac{4\pi}{k\eta}Z_i[kl(2+\cos 2kl)-3/2\sin 2kl]$$

$$f=2(\sin kl-kl\cos kl)$$

[9] C. T. Tai, "Radar Response from Thin Wires," Stanford Res. Inst., Stanford University, Stanford, Calif., Tech. Rept. No. 18; March, 1951.

where

$$\gamma=1.781072.$$

The zero order solution shown in (5) is subject to the restriction that the current vanishes at both ends $[I(\pm l)=0]$. In order to obtain some data on the effect of losses on the current wave shape, the trial function with "relaxed" end conditions was used next to obtain a "first order solution" as defined by Tai.[2] That is, the trial function

$$I_1(z)=I_0(\cos kz-K) \tag{6}$$

is substituted into (3) and the functional S is evaluated. In this case the constant K is evaluated from the condition

$$\frac{\partial S}{\partial K}=0.$$

The procedure followed is well known[2,3,5] and has the following result in this case:

$$\frac{1}{S_1}=\frac{\mu_{11}-2K\mu_{12}+K^2\mu_{22}-j\frac{4\pi Z_i}{k\eta}[h_1-2Kg_1+K^2g_2]}{[g_1-Kg_2]^2} \tag{7}$$

where

$$K=\frac{g_1\mu_{12}-g_2\mu_{11}-j\frac{4\pi Z_i}{k\eta}(g_1^2-h_1g_2)}{g_1\mu_{22}-g_2\mu_{12}}$$

and[9]

$$\begin{aligned}\mu_{11}&=-\Lambda\cos^2 kl-jL(4kl)\\\mu_{12}&=-\Lambda\cos kl+[ln4+\Omega-2L(2kl)]\sin kl\\\mu_{22}&=-\Lambda+j2[1-\cos 2kl+j\sin 2kl]\\&\quad+2kl[ln4+\Omega-2L(2kl)]\end{aligned}$$

$$g_1=2\sin kl$$

$$g_2=2kl$$

$$h_1=kl+\tfrac{1}{2}\sin 2kl$$

where

$$\Lambda=\frac{1}{kl}[\exp(\Omega/2)-\exp(-j2kl)]$$

$$L(x)=\overline{Ci}(x)+jSi(x)$$

$$\Omega=2ln\frac{2l}{a}$$

$$\overline{Ci}(x)=ln(\gamma x)-Ci(x).$$

This reduces to the first order solution of Tai[9] for the case $Z_i = 0$.

The normalized back scattering cross section is found by use of the following well known relation:[4-6]

$$\sigma/\lambda^2 = \frac{1}{\pi}|S|^2. \tag{8}$$

Computations of back scattering cross section have been made using the zero-order solution and the results thus obtained have been compared with first-order solution results in the region of first resonance. The results are nearly identical (for $kl < \pi$) over a wide range of conductor losses. Computations have been made for various amounts of loss up to the case where the resonant cross section is reduced to 4 per cent of the no loss value and the zero- and first-order results differ by less than 0.25 per cent. This coincidence of results is further verified by inspection of the curves of the first-order parameter K and cos kl as functions of kl, as shown in Fig. 2. It is seen that the small difference between K and cos kl, for the case of no loss, is further diminished by losses. (All losses less than 96 per cent give curves of Re (K) that lie between the two shown.) Tai[2] has shown that K is nearly identical with cos kl over the range $kl \leq \pi$. The present results show that in the region of first resonance this correspondence increases with the addition of loss.

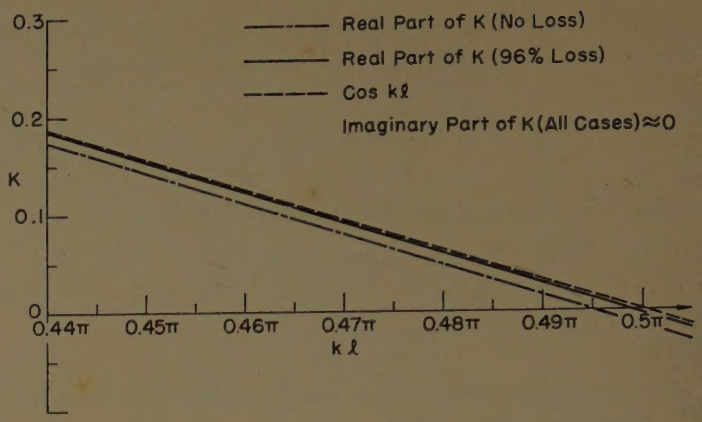

Fig. 2—Parameter K as a function of kl.

Comparison of Theoretical Results with Experimental Results

Computations were made using the formulas developed from the variational method. These were compared with experimental results measured on thin copper, platinum and bismuth wires in the region of the first resonant length. Due to the close correspondence of the results from the zeroth and first-order solutions, the simpler of the two, (5), was naturally chosen to make the computations.

The apparatus and the experimental method used in determining the radar cross sections of the thin wires have been fully described elsewhere.[10] The method rests on the Doppler modulation of the signal by the motion of the scatterer. In the particular arrangement used, the sample and the standard of known radar cross section are alternately presented to the incident field. The styrofoam bar of six-foot length, which supports the sample and the standard, rotates with an angular velocity of 1 rps. The synchronously detected Doppler modulation is commutated to twin feedback rectifier systems, providing a comparison of voltages which are linearly dependent on back scattered fields of the standard and of the sample.

In order to support the fine wires (diameters 0.001 to 0.005 inch) adequately, it was necessary to have the dipoles mounted completely in styrofoam holders. Although styrofoam has a dielectric constant of 1.03 at the 3000-mc measurement frequency, small end loading effects are observed on a dipole completely immersed in it. These loading effects of styrofoam have been measured on thick rigid dipoles. The back scattering cross section was measured with the dipole completely immersed in styrofoam and also with only the middle of the dipole supported, leaving the ends in air. In Fig. 3, experimental results are compared with zero-order variational results. The experimental resonant length of the dipole completely immersed in styrofoam is shifted from the theoretical value by 0.01 λ more than the experimental resonant length of the dipole supported in the middle. In addition, the experimental resonant length of the dipole supported in the middle is shifted by 0.01 λ from the theoretical result which does not include end effects.[4,5]

The "end loading" effects just described are also evident in the results shown for the fine wires in Figs. 4–10. The total discrepancy between the theoretical and the experimental resonant lengths is only 0.010 λ in all cases, except in the case of the 0.005-inch diameter platinum wire where it is 0.012 λ.

Inspection of the curves of back scattering cross section vs lengths of fine wire in Figs. 4–10 shows, after accounting for the end loading effects, that the assumptions of the theory are fairly well supported by the experimental results. The experimental curves are consistently lower (about 4 per cent on the average) than the theoretical curves, indicating that the theory has not accounted for all of the loss. A tabulation of results for each case is shown in Table I. It should be noted that the discrepancy between theory and experiment does not appear to diverge with increasing losses.

A further comparison of experiments with theory of practical interest is that of bandwidth. The half-power (cross section) bandwidths of the experimental and theoretical curves from Figs. 4–10 are listed in Table I. The maximum discrepancy of the theory and the measurements is 1.5 per cent.

The limit of statistical error in the experimental

[10] H. Scharfman and D. D. King, "Antenna measurements by modulation of the scatterer," Proc. IRE, vol. 42, pp. 854–858; May, 1954.

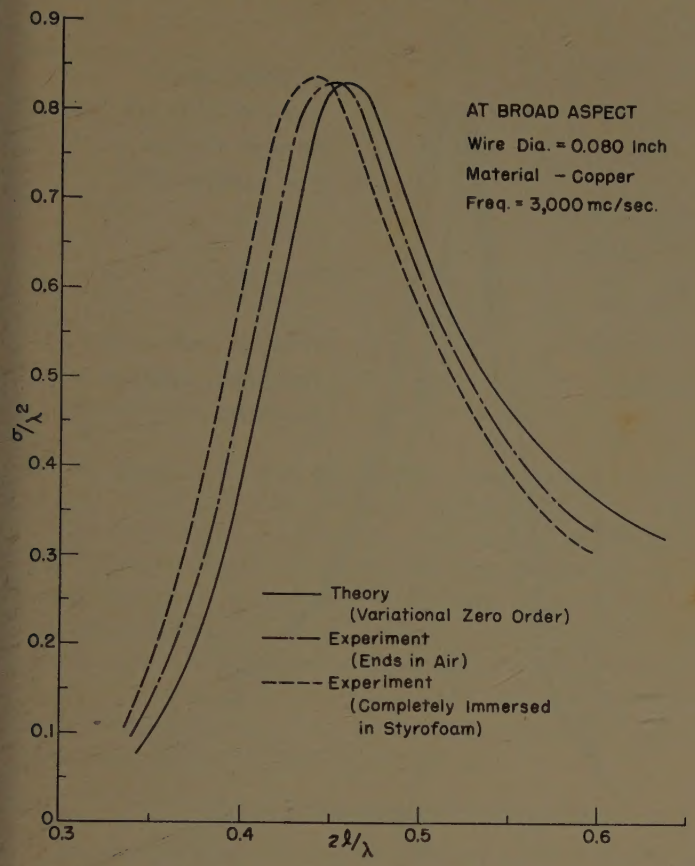

Fig. 3—Back scattering cross section vs length of thick wire.

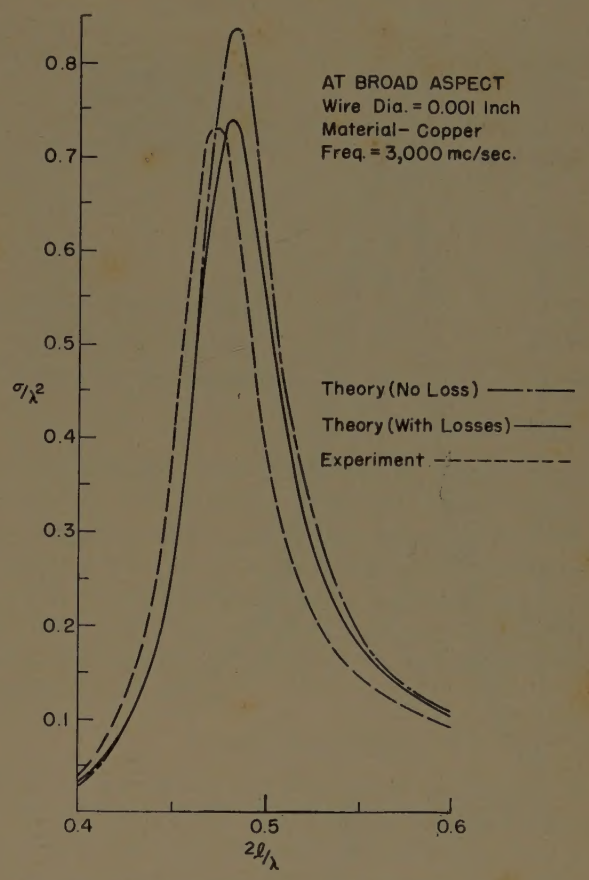

Fig. 4—Back scattering cross section vs length of fine wire.

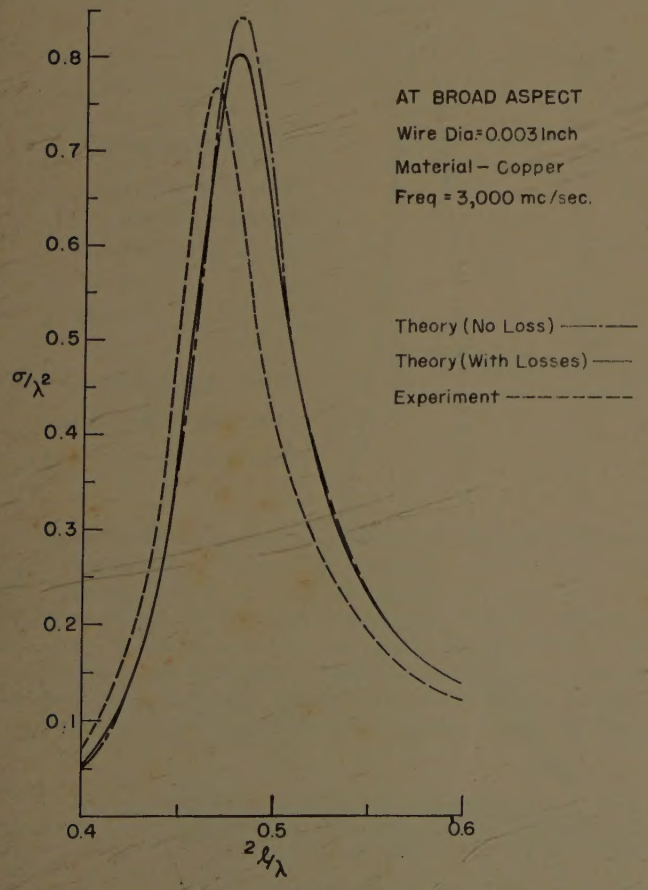

Fig. 5—Back scattering cross section vs length of fine wire.

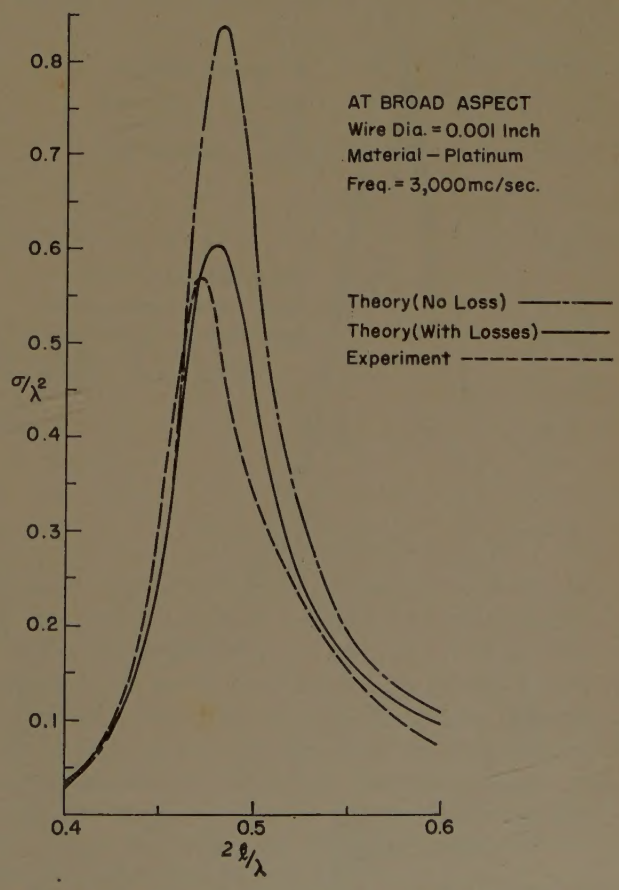

Fig. 6—Back scattering cross section vs length of fine wire.

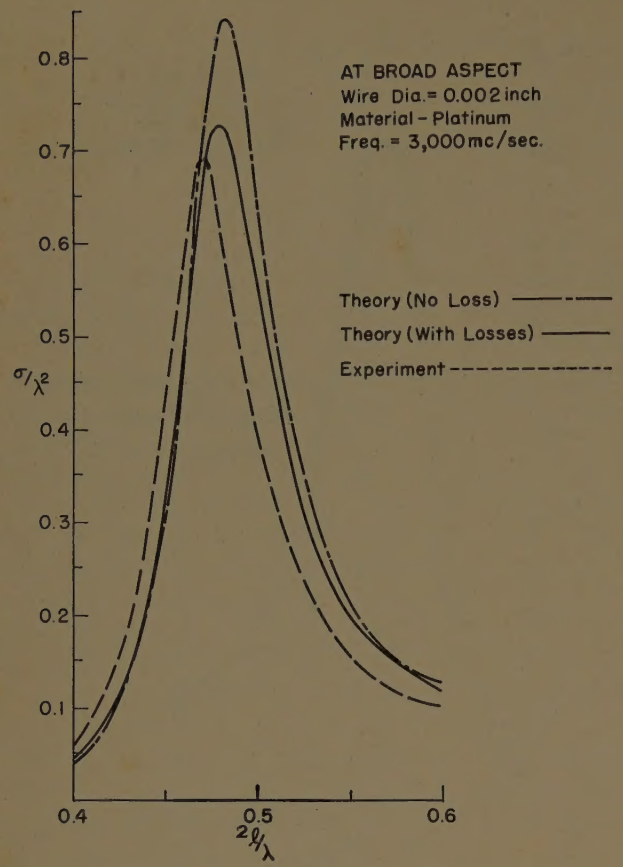

Fig. 7—Back scattering cross section vs length of fine wire.

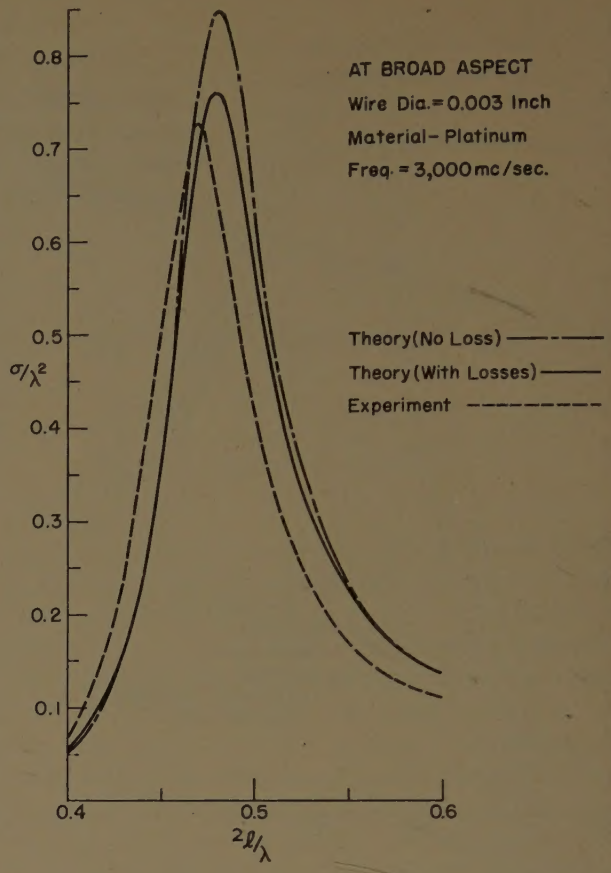

Fig. 8—Back scattering cross section vs length of fine wire.

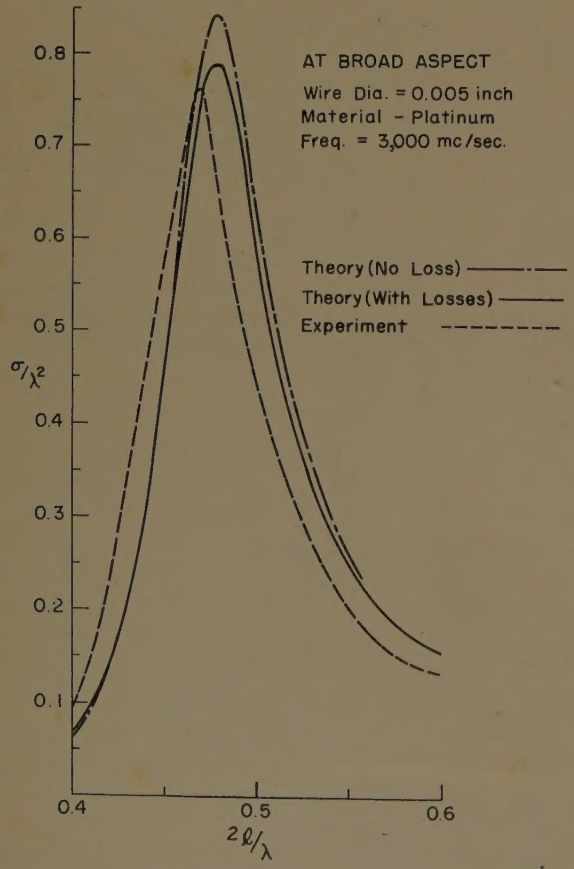

Fig. 9—Back scattering cross section vs length of fine wire.

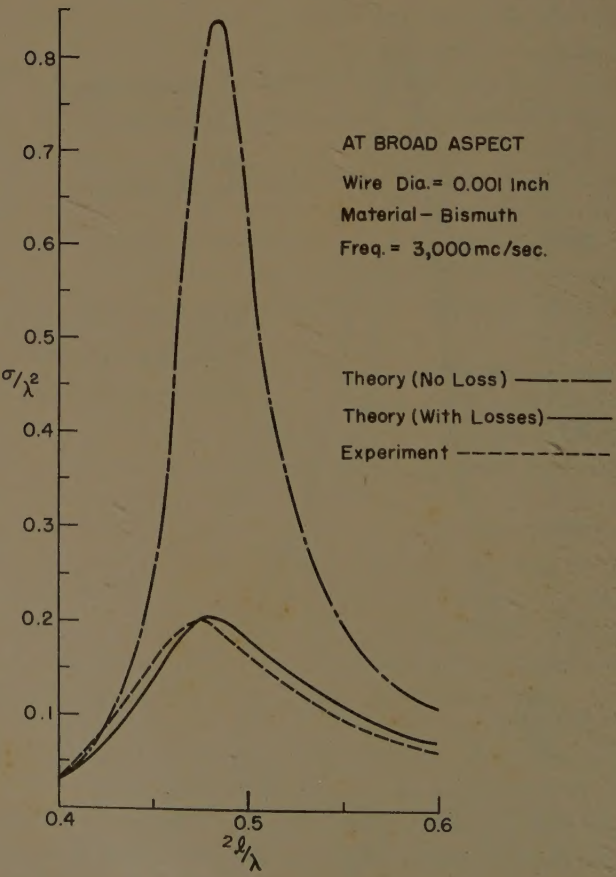

Fig. 10—Back scattering cross section vs length of fine wire.

TABLE I

Dipole		Measured	Computed	Peak Values		Per Cent Bandwidth	
Diameter (Nominal) in Inches	Material	R_0 in Ω/m	Z_i in Ω/m	Theory σ/λ^2	Experiment σ/λ^2	Theory in Per Cent	Experiment in Per Cent
0.001	Copper	34.0	$189+j180$	0.742	0.733	12.1	11.2
0.003	Copper	3.79	$62.5+j59.7$	0.805	0.768	14.0	13.5
0.001	Platinum	229.	$527+j458$	0.603	0.572	13.1	14.0
0.002	Platinum	53.5	$227+j221$	0.725	0.690	13.5	14.4
0.003	Platinum	23.7	$115+j147$	0.760	0.727	13.8	15.3
0.005	Platinum	8.56	$93.0+j88.6$	0.788	0.763	15.6	16.4
0.001	Bismuth	2800.	$2940+j700$	0.202	0.195	25.3	24.7

measurement of back scattering cross section is estimated at ±4 per cent and the lengths of the wires used in the experiment were determined to within $\pm 0.002\,\lambda$. The limit of error in cross section due to the values of resistivity used for the skin impedance in the computations is estimated to be an additional ± 2 per cent. The resistances of the wires were measured on a General Radio Resistance Limit Bridge, and the permeabilities were all taken as $\mu_0 = 4\pi \times 10^{-7}$ henrys per meter. From these the values of Z_i were computed.[7]

Conclusion

Resistance losses in a thin cylinder modify the back scattering results in the region of first resonance by reducing the cross section and increasing the bandwidth. The first resonant peak occurs virtually at the same cylinder length. The experimental results reported above show that the zero-order variational expressions for back scattering describe fairly accurately the behavior when losses cause as much as a 75 per cent reduction in the peak cross section. Furthermore, for computations in the region of first resonance, no additional accuracy is gained by the use of the next higher order of approximation of Tai.

Acknowledgment

The work described in this paper was supported by the Wright Air Development Center under Contract No. AF 33(616)-68. The authors are indebted to J. M. Minkowski for his many helpful suggestions and to Dr. J. M. Kopper for review of the manuscript. F. G. Trageser performed the experiments.

A Multipurpose Radar Target*

J. W. CARR†

Summary—**Consideration of methods of simulating a moving target by making a mechanically stationary target appear [to an MTI (Moving Target Indicator)-equipped radar] to be moving resulted in the use of crystals as switching elements in a low-voltage low-energy battery-powered device. Extending the use of these switching elements results in a target that is visible to any polarization. By applying these concepts to composite waveguide structures, a dual-band simulated target head was developed and field tested.**

* Manuscript received by the PGAP, October 9, 1958; revised manuscript received, August 19, 1959. The work presented here was done at Gilfillan Bros., Inc., Los Angeles, Calif., where it was officially disclosed on June 6, 1955.

† Missile System Div., Lockheed Aircraft Corp., Sunnyvale, Calif.

Introduction

In several radar systems, especially in some particular aircraft landing systems, two of the most valuable adjuncts are 1) an MTI for detecting moving targets in the presence of stationary ground clutter and 2) circularly polarized antennas for better target detection in the presence of rain. Standard geographically-located stationary reference targets provide definite range and angle markers for normal radar use when 1) and 2) are not employed. However, when the MTI is placed in operation, a standard passive target reflector is cancelled out along with the rest of the stationary

clutter; this leaves only synthetic geographical reference points, if such are provided, on the indicator. When circular polarization is employed in the radar antennas, the plane reflector-type target is masked, since the reflected wave is polarized in the opposite sense to the radar antenna. An active device is required in order to provide a visible target when MTI is used, whereas the requirements for circular polarization alone can be achieved by a passive scheme.

After considering several schemes to simulate a moving target, the nonlinear impedance characteristic of a crystal looked the most promising from the standpoint of low power requirement. Also, there was a large range of commercially available silicon and germanium crystal diodes to choose from.

Principles of Operation

Fig. 1 shows qualitatively the dc forward resistance characteristic of a crystal diode. For little or no applied forward voltage V_1, the resistance is high in the vicinity of A. For some value V_2 of applied potential difference, the resistance is some low value in the vicinity of C. If the RF resistance has a similar characteristic, one sees the possibility of controlling the RF impedance by externally applied biasing voltages. Suppose a crystal and a transmission line are so chosen that the characteristic impedance Z_0 of the transmission line lies in the vicinity of B. Further, assume that the combined crystal and mount can be designed such that the impedance presented to the line is mainly the crystal resistance. Let Z_t be the predominantly real terminal impedance presented to the line by the crystal and its mount. Let $ke^{j\theta}$ be the reflection coefficient.

For $V=V_1$, $Z_{t1}>Z_0$, and $k_1e^{j\theta_1}\simeq k_1$.
For $V=V_2$, $Z_{t2}<Z_0$, and $k_2e^{j\theta_2}\simeq -k_2$.

Thus, if the applied bias is V_1 on the nth incident radar pulse and V_2 on the $(n\pm1)$ radar pulse, it is noted that the phase of the reflected RF signal has been changed on the order of 180° from pulse to pulse. On a voltage basis the efficiency of the target head (transmission line-crystal network) may be expressed as

$$\text{per cent voltage efficiency} = 100\left|\frac{k_1e^{j\theta_1}-k_2e^{j\theta_2}}{2}\right|$$

$$= 50\left|k_1-k_2e^{j(\theta_2-\theta_1)}\right|.$$

When $k_1=k_2=1$ and $\theta_2-\theta_1=\pi$, the efficiency is 100 per cent.

A voltage efficiency is defined since the most common MTI systems linearly detect the echo pattern from one pulse, delay it and compare it with the return from the next pulse, etc.

Fig. 2 shows some measured efficiencies at S band. X-band efficiencies were approximately the same. These 4 per cent bandwidth data do not represent bandwidth limitations. Tests were made only on commercially available crystals. With switching characteristics considered as the main design parameter it may be possible to develop and package a crystal, or family of crystals, which has much more efficient switching characteristics. In an attempt to apply the technique to an externally pulsed low-power TR device only about 10-db rejection was realized. No further investigation was made.

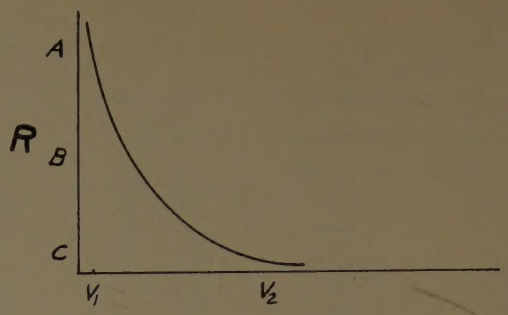

Fig. 1—Forward bias.

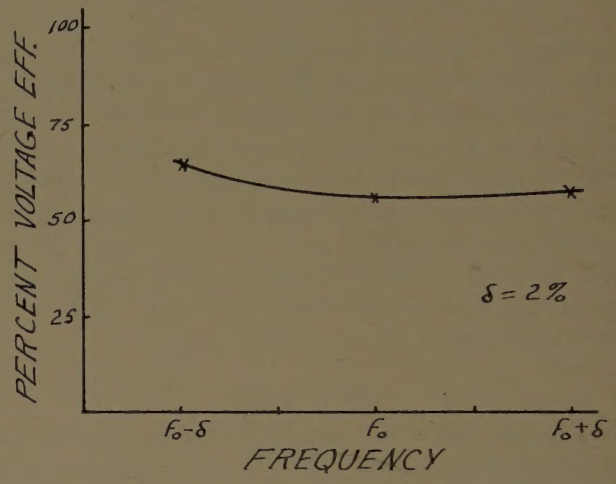

Fig. 2.

Fig. 3 shows schematically a primary feed horn with a crystal-terminated transmission line.

Fig. 4(a) shows an RF pulse chain and Fig. 4(b) shows an enveloping symmetrical waveform from a multivibrator with a frequency half of that of the radar PRF.

The multivibrator waveform is the bias waveform externally applied to the crystal. It may be assumed, for the sake of presentation, that the multivibrator is synchronized with the radar PRF. However, this is not necessary in systems where the pulse-to-pulse signal differences due to a phase differential at the target are integrated over many pulses, *i.e.*, over the number of pulses per sweeping antenna beamwidth.

The above discussion has demonstrated how such a device can return a detectable signal to a linearly polarized radar set equipped with a pulse-to-pulse phase comparison MTI. If only an amplitude-sensitive radar detection system is used, it may be desirable to design

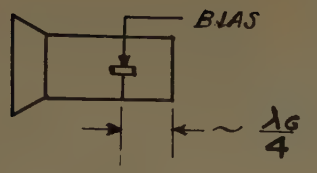

Fig. 3.

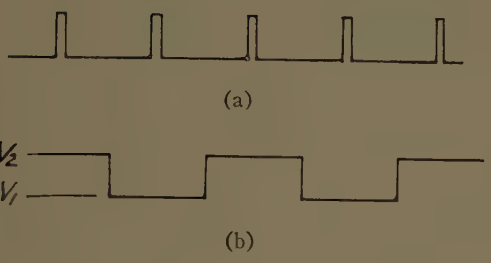

Fig. 4—(a) Pulsed *RF* envelope. (b) Pulsed bias.

a high reflection coefficient for the nth pulse and a matched termination for the $(n+1)$th pulse. This mode of operation was accomplished.

Design of the Target for Circularly Polarized Radars

Consider Fig. 3 again, but now use a waveguide with orthogonal symmetry such that it can support two orthogonal modes with the same phase and impedance characteristics. Add a second crystal half-a-guide-wavelength towards the horn from the first one and at right angles to it. Apply V_1 to one crystal and V_2 to the other. The arrangement is shown in Fig. 5.

For any RF pulse, if the polarization is circular or elliptical, the vertical component will be biased for a positive reflection coefficient, while the horizontal component will be biased for a negative reflection coefficient. The $\lambda g/2$ spacing is necessary in the above scheme in hollow waveguide to provide a round-trip 360° phase lag of k_2 with respect to k_1, so that the phase difference between orthogonal components is $2n\pi+(\theta_2-\theta_1)$. $(\theta_2-\theta_1)$ is the phase difference due to the difference of bias levels. This results in a target which is now detectable on a radar equipped with both MTI and circularly polarized antennas. If $k_1=k_2$ and $\theta_2-\theta_1=\pi$, the sense of polarization of a reflected circularly polarized wave is of the proper sense to be received most effectively by the circularly polarized radar antenna.

A Dual Band Target

Some radar systems are equipped with a higher frequency microwave radar for short-range precision data, and a lower frequency microwave radar for longer range search purposes. Fig. 6 shows a diagram of a combination *XS*-band target head, which, when used by itself or with an axially symmetrical reflector such as a paraboloid, will provide a target return for the following types of operation on both *S* and *X* band (pulse-to-pulse phase comparison MTI):

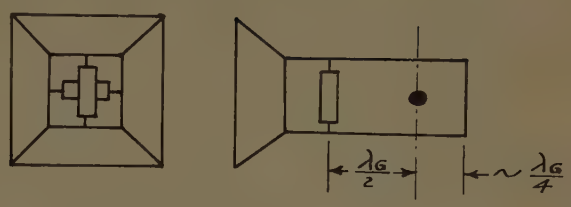

Fig. 5.

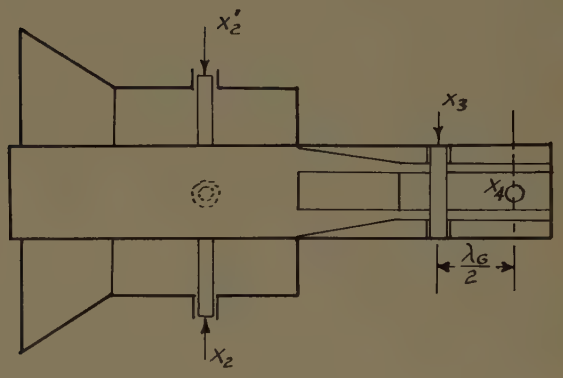

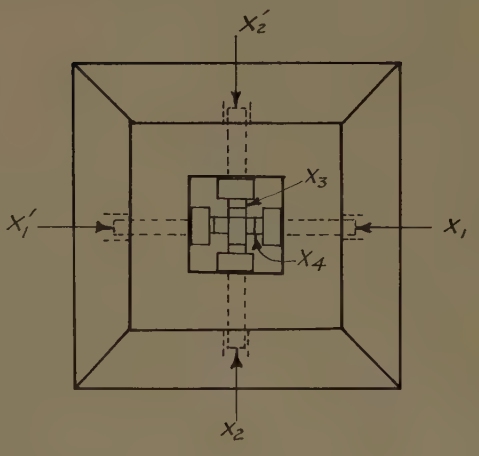

Fig. 6—(a) Side half-section. (b) Front view.

1) circular polarization,
2) horizontal polarization,
3) vertical polarization,
4) circular polarization with the MTI in operation,
5) horizontal polarization with the MTI in operation,
6) vertical polarization with the MTI in operation.

Voltage efficiencies of the device on the order of 50 per cent were achieved over 10 per cent bandwidths for total battery current drain on the order of 20 ma. This is for the combined feed shown in Fig. 6, where 6 crystals are driven by a transistorized free-running multivibrator powered by a 6-volt dry cell (see Fig. 7).

Neither the frequency of the multivibrator nor the battery voltage (limiting the driving current for the crystals) is critical. Dropping the battery voltage from 6 to 3 volts resulted in only a small reduction in efficiency. This is due to the fact that the crystal current

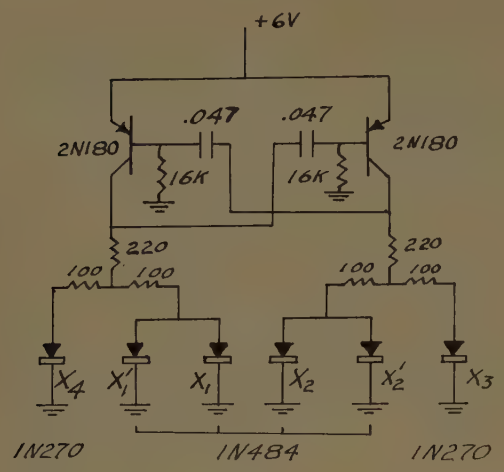

Fig. 7.

is still near its saturation value for the lower applied voltages.

As suspected, it was found that the efficiency of the crystal as a control element depends greatly not only on the type of crystal but on the crystal "package" and mount as well.

The *S*-band target head is a square coaxial arrangement in which 2 TE_{11} orthogonal modes are excited. The terminal impedance for each of these modes is controlled by 2 crystals, one on each of opposite sides of the square center conductor. The cross talk between the modes is not great enough to cause any difficulty. Values of cross talk obtained were estimated as being about −20 db.

The *X*-band target head is a square quadruple ridge waveguide with a gradual transition into a square waveguide, the open end of which serves as the horn aperture. It supports two orthogonal ridge waveguide TE_{10} modes each terminated by one crystal. This choice of waveguide was made to obtain a working combination of waveguide impedance relative to the crystal characteristic (for orthogonal mode operation) and to minimize crystal lead inductance.

Because of the following factors, microwave crystals were not used in a working model. Microwave crystals have low burnout levels, a weakness which was enhanced by the forward biasing. Also, the microwave crystals did not exhibit as large a change in impedance between low- and high-level biasing states for higher incident RF power levels. The amount of change varied much more with change of incident RF power level than was the case for the low-frequency point-contact or junction-type diodes. On a sample germanium point-contact crystal the efficiency remained practically constant (dropping off a little at higher power levels) for incident 0.5-μsec pulses of peak incident RF power level variations over a 40-db range from one milliwatt to ten watts.

A compromise multivibrator frequency of about 0.7 of the *S*-band radar PRF and about 0.2 of the *X*-band radar PRF was used. It was estimated that this gives pulse-to-pulse bias state changes to about one-third of the pulses per beamwidth on the higher PRF *X*-band radar and about one-half of the pulses per beamwidth on the *S*-band radar. Field tests disclosed that the multivibrator frequency was not critical. The optimum bias frequency for a single fixed PRF radar would be in the vicinity of one-half the radar PRF so that practically 100 per cent of contiguous incident radar pulses are alternately biased and unbiased. Fig. 7 shows the transistor multivibrator circuit and shows how the crystals are driven. This particular circuit had very good frequency stability up to ambient temperatures of 140°F and for large changes in power supply voltage. As previously noted, the voltage level or frequency is not critical. The main concern is to sustain oscillations under large changes in ambient temperature levels.

Conclusion

This type of target [meeting the requirements of 1) and 2) in the Introduction] appears to offer the most versatility and most economical fabrication and maintenance of the various types considered. For fewer functional requirements fewer crystals are required and therefore longer battery life is obtained. The low power requirements make its use more widely applicable than some device requiring a line power source. The ability to produce pulse-to-pulse amplitude changes as well as phase changes may make it applicable for monitoring radar systems equipped with pulse-to-pulse amplitude-sensitive MTI.

Acknowledgment

The author wishes to express his appreciation to those who contributed to the development of this work. H. Schauwecker designed the transistor circuit and conducted environmental tests and H. Kusunoki did much of the developmental fabrication, most of the laboratory testing, and made several valuable contributory observations.

On Uniform and Linearly Tapered Long Yagi Antennas*

DIPAK L. SENGUPTA†

Summary—Traveling-wave analysis of long Yagi antennas is reviewed briefly. The method of designing a Yagi antenna from this viewpoint is discussed and some experimental results are given in order to verify the analysis. A long Yagi antenna, when designed according to the Hansen and Woodyard condition, has a sidelobe ratio of 9.32 db in its radiation pattern, irrespective of the length of the antenna. It is shown that by varying the propagation constant linearly along the length of the antenna, the sidelobe ratio can be improved considerably without sacrificing much of the antenna gain. This linear variation of the propagation constant may be obtained by slowly tapering the element lengths and/or element spacings along the length of the antenna. An approximate theory is developed for the linearly tapered long Yagi antenna and it is verified by actual measurements. A comparison between the radiation patterns of the uniform and the tapered long Yagi antennas clearly shows the advantage of tapering.

Introduction

THE Yagi antenna is one of the cheapest and simplest of the antennas which are commonly used for directional reception of linearly polarized electromagnetic waves in the VHF and UHF ranges. The conventional analysis which considers the Yagi strictly as a resonant antenna is adequate for the practical design of short Yagi antennas consisting of three or four director elements. In the case of long Yagi antennas, where the number of elements may be very large, the design of the antenna according to this method becomes very complicated, if not impossible. However, the uniform long Yagi antenna may be designed[1] in a simpler way by considering it as a traveling-wave antenna. It can be shown that when the antenna is designed to have maximum gain, the sidelobe level in its radiation pattern is 9.32 db down, irrespective of the length of the antenna. This ratio may be improved up to a theoretical limit of 13.2 db down, but at a considerable sacrifice of the antenna gain. In the present paper, it is shown that by varying the phase velocity of wave propagation according to a predetermined fashion along the length of the antenna, the sidelobe level can be improved considerably without deteriorating the gain appreciably. A Yagi antenna having such propagating characteristics will be called a tapered Yagi antenna in contrast to the uniform case where the phase velocity is maintained constant along the length of the antenna. This idea of tapering the phase velocity is similar to the idea used in the case of modulated surface wave antennas.[2] However, in the present case, the phase velocity is allowed to vary monotonically with length rather than periodically along the length, as is done in the latter case.

In the following sections, the traveling-wave analysis of the uniform long Yagi antenna is reviewed first, and the method of design is discussed briefly. The experimentally determined radiation patterns of such an antenna of length $L=6\lambda$ at 3000 mc are given and compared with the theoretical results. Secondly, the radiation properties of a tapered long Yagi antenna are investigated. An approximate theory is developed to explain the action of tapering. The theory is verified by actual measurements. A comparison between the results of the uniform and tapered cases clearly points out the advantages of tapering.

Uniform Long Yagi Antennas

As mentioned in the Introduction, the analysis of long Yagi antennas becomes very complicated if one follows the conventional analysis.[3] This is because one has to adjust too many parameters in order to obtain the desired performance from the antenna. However, the analysis becomes much simpler if one considers the Yagi as a traveling-wave antenna. It can be shown that the radiation properties of a long Yagi antenna may be determined once the phase velocity of the traveling wave along it is known. The phase velocity itself being a function of the different physical parameters of the antenna, the complete design of the antenna can be carried out once the phase velocity along it is known.

The application of traveling-wave ideas to the Yagi antenna is a relatively new concept. Smith[4] suggested that the physical action of the director elements in the Yagi is to reduce the phase velocity of the wave traveling along the length of the antenna. In other words, it may be said that the driven element of the Yagi launches a traveling wave which moves through a region of refractive index greater than unity. Ehrenspeck and Poehler,[5] Spector,[6] and Reynolds[7] have made extensive

* Manuscript received by the PGAP, February 16, 1959; revised manuscript received, August 10, 1959. The research reported herein was made possible through support to the Dept. of Elec. Engrg., University of Toronto, Canada, by the Natl. Res. Council of Canada, under Radio-Astronomy Project, Grant No. G587.

† Gordon McKay Lab. of Applied Science, Harvard University, Cambridge, Mass.; formerly with the Dept. of Elec. Engrg., University of Toronto, Canada.

[1] D. L. Sengupta, "Traveling Wave Analysis of Certain End-Fire Antennas," Ph.D. dissertation, University of Toronto, Canada, pp. 81–86; 1958.

[2] F. J. Zucker and A. S. Thomas, "Radiation from modulated surface wave structures I," 1957 IRE National Convention Record, pt. 1, pp. 153–160.

[3] U. Shintaro and Y. Mushiake, "Yagi-Uda Antenna," The Res. Inst. of Electrical Communication, Tohoko University, Sendai, Japan, ch. 9; 1954.

[4] R. A. Smith, "Aerials for Metre and Decimetre Wavelengths," Cambridge University Press, Cambridge, England, pp. 150–151; 1950.

[5] H. W. Ehrenspeck and H. Poehler, "A New Method for Obtaining Maximum Gain from Yagi Antennas," Antenna Lab., AF Cambridge Res. Center, Bedford, Mass.; July, 1956. Also, IRE Trans. on Antennas and Propagation, vol. AP-7, pp. 379–386; October, 1959.

[6] J. O. Spector, "An investigation of periodic rod structures for Yagi aerials," *J. IEE*, pt. B, vol. 105, pp. 38–43; January, 1958.

[7] D. K. Reynolds, "Broad-band travelling-wave antennas," 1957 IRE National Convention Record, pt. 1, pp. 99–107.

experimental investigations on the properties of the uniform long Yagi antenna considered as a traveling-wave antenna. In the following sections, the design of the long Yagi antenna and its radiation properties are discussed briefly.

In order to obtain an expression for the radiation pattern, the uniform long Yagi antenna of length L is replaced[8] by an equivalent line source of longth L which is assumed to be excited by a traveling wave whose velocity of propagation is equal to the phase velocity of propagation along the antenna. The radiation pattern of the uniform long Yagi antenna is then obtained from the following expression:

$$S(\theta) = \int_{-L/2}^{L/2} \exp - i(\beta - k\cos\theta)dz$$

$$= L\left[\frac{\sin\left[\frac{\pi L}{\lambda}\left(\frac{\beta}{k} - \cos\theta\right)\right]}{\left[\frac{\pi L}{\lambda}\left(\frac{\beta}{k} - \cos\theta\right)\right]}\right] \qquad (1)$$

where

k is the propagation constant in free space,
β is the propagation constant in the antenna,
θ is the angle measured from the axis of the antenna which is aligned along the z-axis,
ω is the angular frequency and the assumed time dependence is of the form $e^{i\omega t}$.

Eq. (1) may be recognized as the usual expression for endfire radiation pattern if $\beta > k$. It should be mentioned at this stage that (1) is approximate; it can explain the main beam and the first sidelobe characteristics of the antenna with an amount of accuracy sufficient for practical purposes. A better theory is required to explain the minor lobe details of the pattern. In a recent paper,[9] Zucker and Kay theoretically discussed the problem of radiation from this kind of antenna by applying the concept of surface wave. Although from the surface wave point of view, the approximations made in deriving (1) are questionable, this expression is found to be extremely useful for the practical design of the antenna. It can be shown [10] that for obtaining maximum gain from an antenna having a radiation pattern given by (1), the following relation must be satisfied,

$$\left.\begin{aligned} &(\beta - k)L = \pi \\ &\text{or,} \quad \frac{v}{c} = \frac{L/\lambda}{0.5 + L/\lambda} \end{aligned}\right\} \qquad (2)$$

where

c is the phase velocity in free space,
v is the phase velocity in the antenna.

Eq. (2) is the well-known Hansen and Woodyard condition which predicts that the phase velocity in the antenna should be less than free-space velocity in order that the condition may be satisfied. Fig. 1 shows the required value of the phase velocity (v/c) in the antenna as a function of the antenna length. Once the necessary phase velocity is chosen, the radiation pattern of the antenna may be analyzed by using (1).

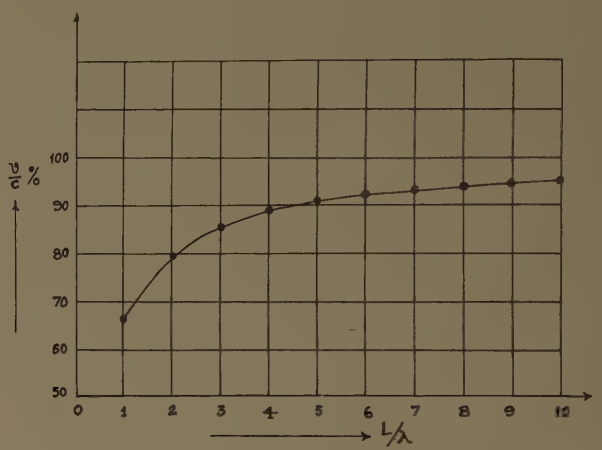

Fig. 1—The optimum phase velocity as a function of the antenna length.

The propagation constant β (from which the phase velocity may be obtained by using the relation $v = \omega/\beta$) in the antenna is a function of the different physical parameters of the antenna and can be obtained from the following approximate expression,[11]

$$\cos\beta d = \cos kd - \tfrac{1}{2}\exp kdf(a, R) \qquad (3)$$

where

$$f(a, R) = \frac{(\cos ka)\left(\frac{\sin ka}{ka}\right) - ka(\cos ka)\left(\frac{\cos kR}{kR}\right)}{\sin ka - ka\cos ka} \qquad (4)$$

and

$2a$ is the length of each director element,
d is the spacing between two adjacent elements,
R is the radius of each element.

The approximations involved in (3) are $d \gg R$, $a \gg R$, $d \gg a/2$.

Perhaps it will not be inappropriate at this stage to make the following comments about (3).

1) The expression is obtained for an infinite structure

[8] Sengupta, *op. cit.*, p. 12.
[9] The author is indebted to one of the reviewers for pointing out the paper of F. J. Zucker and A. F. Kay, "A surface wave antenna paradox," presented at the Fall URSI meeting, Pennsylvania State University, University Park; October 20–22, 1958.
[10] W. W. Hansen and J. R. Woodyard, "A new principle in directional antenna design," Proc. IRE, vol. 26, pp. 333–345; March, 1938.
[11] D. L. Sengupta, *op. cit.*, p. 45. Also, "On the phase velocity of wave propagation along an infinite Yagi structure," IRE Trans. on Antennas and Propagation, vol. AP-7, pp. 234–239; July, 1959.

which extends to infinity in both the positive and negative directions along the axis of the structure. However, since the phase velocity is independent of the length of the structure, this expression can be used for calculating the phase velocity in a long but finite Yagi antenna.

2) The phase velocity is less than the free-space velocity as long as $a < \lambda/4$. This is the range of practical interest, since the antenna utilizes the slow-wave nature of the propagation.

3) The phase velocity decreases continuously with increase of a and decrease of d. Its value is very close to c for small values of a and large values of d. The phase velocity increases with decrease of R, and its value approaches the free-space value in the ideal case of $R=0$.

4) The phase velocity decreases continuously with increase of frequency.

Thus it is seen that by using (3) and (4), the different parameters of the uniform long Yagi antennas can be chosen for any desired value of β. These can also be determined by consulting the published experimental and theoretical curves.[5,6,11]

By following the above technique, a uniform Yagi antenna of length $L=6\lambda$ at 3000 mc has been designed. The design values of the different parameters are given below:

operating frequency $f_0=3000$ mc,
relative phase velocity $v/c=0.923$,
radius of the director element $R=0.008\lambda$,
spacing between the two adjacent directors $d=0.15\lambda$,
length of each director element $2a=0.352\lambda$.

It should be noted that for a given length L of the antenna, the optimum phase velocity may be achieved for different combinations of the three parameters d, a, and R. In this sense, the design method outlined above is not unique. However, from a critical study[11] of the variation of phase velocity with the different parameters, suitable ranges of values for these parameters may be given. The value of R should be chosen between $kR=0.05$ and $kR=0.15$. For this choice of R the desired phase velocity may be obtained for suitable values of the parameters a and d. The directivity of the antenna becomes less frequency sensitive for values of $d<\lambda/4$. The proper choice of d should be governed by this consideration; for cases of practical interest, a possible range for d may be given as between 0.1λ and 0.25λ. Once R and d are chosen, the parameter a is automatically fixed.

The principal plane radiation patterns of the above antenna have been measured experimentally and compared with the theoretical patterns. The results are reproduced in Figs. 2 and 3. It can be seen from the two figures that the sidelobe ratio in the pattern is about 9.32 db down, as expected from the theory. A better sidelobe ratio may be achieved from the antenna by operating it at a frequency lower than the design frequency f_0. This, however, reduces the antenna gain because of the

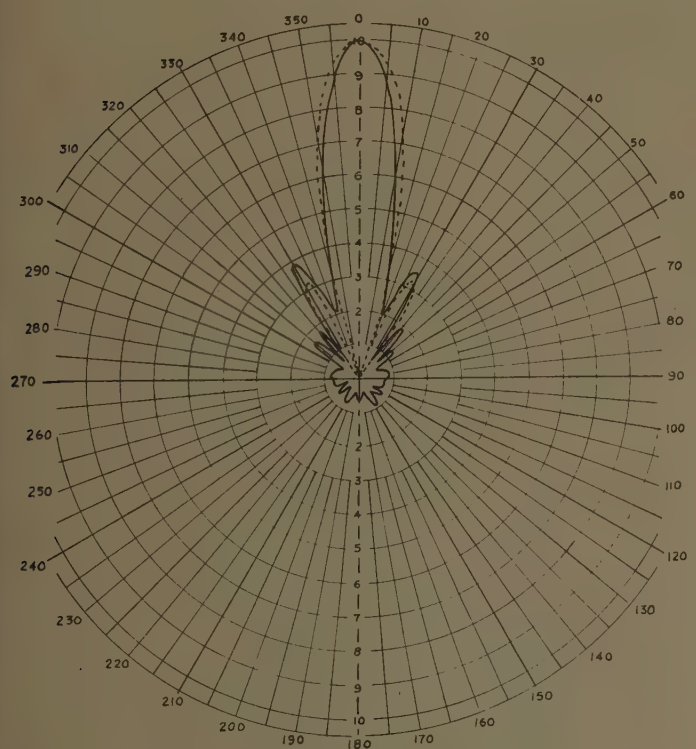

Fig. 2—The E-plane radiation pattern of a uniform long Yagi antenna of length L at 3000 mc. Dashed line: theoretical; solid line: experimental.

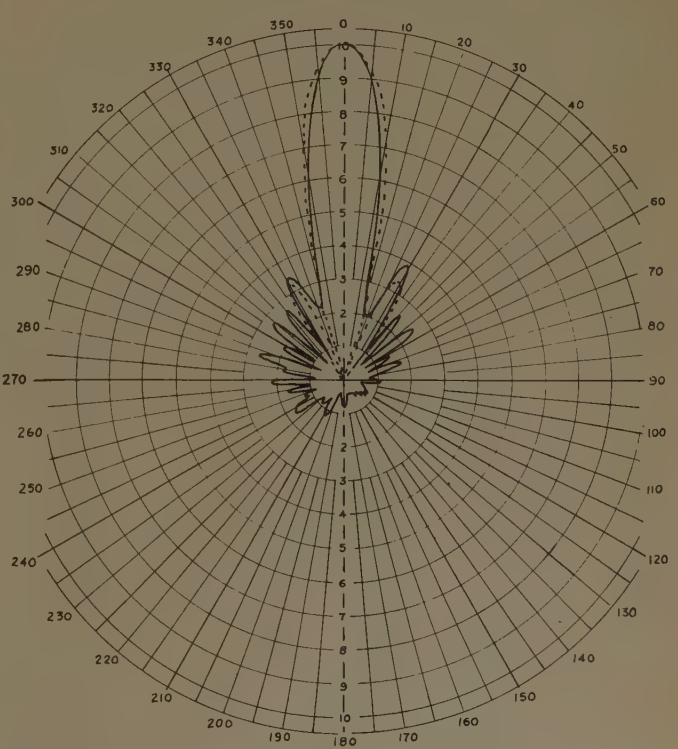

Fig. 3—The H-plane radiation field pattern of a uniform long Yagi antenna of length $L=6\lambda$ at 3000 mc. Dashed line: theoretical; solid line: experimental.

excessive broadening of the main beam. This can be seen from Fig. 4, which shows the variation of the relative directivity and the sidelobe ratio of the antenna as functions of the frequency deviation from the design frequency f_0. The directivity of the antenna at $f=f_0$, as computed graphically from the experimental pattern, is found to be 16.6 db compared to an isotropic radiator.

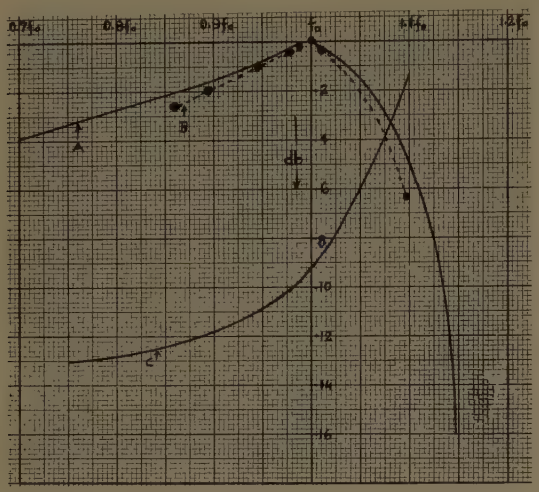

Fig. 4—The variation of the directivity and the sidelobe ratio of a uniform long Yagi antenna with frequency. (Length of the antenna $L=6\ \lambda$ at the optimum frequency $f_0=3000$ mc.) A = theoretical curve for relative directivity; B = curve for relative directivity as calculated graphically from the experimental patterns; and C = theoretical curve for the sidelobe ratio.

Tapered Long Yagi Antenna

It is shown in the following sections that by using a linear variation of the propagation constant along the length of the antenna, the sidelobe level in its radiation pattern can be improved considerably without sacrificing much of the directivity. This type of variation of propagation constant should be distinguished from the arbitrary periodic variation used by Zucker[2] in the case of modulated surface wave antennas, of which the tapered long Yagi antenna may be thought of as a special case. Zucker showed that the periodic variation of β gives rise to several constant velocity and constant amplitude space harmonic wave components. The over-all pattern of the antenna is assumed to be the superposition of the patterns of these individual components. In a recent report, Malech and Blank[12] considered the effect of tapering on a printed circuit equivalent of the long Yagi antenna. To explain the improved sidelobe ratio in the tapered case, they used Zucker's method of space harmonic analysis. In the following analysis, a different approach is used; the radiation pattern is calculated from field theory considerations instead of the harmonic analysis. In the present analysis, it will be found that the amplitude distribution of the field along the length of the antenna can no longer be assumed to be constant if the propagation constant is varied. The theory given below explains the effect of tapering with an accuracy better than the first approximation to Zucker's method as given by Malech and Blank.

[12] R. G. Malech and S. J. Blank, "Final Report on Propagation of Electromagnetic Waves," Airborne Instruments Lab., Mineola, N. Y., Contract AF 19(604)-2446, Rept. No. 4571-1, pp. 15–22; June, 1958.

Physical Explanation of the Action of Tapering

In this section the action of tapering the propagation constant β along the length of the antenna is discussed purely from physical considerations. In the case of constant β, the field distribution along the length of the antenna is uniform. The effect of varying β is to produce a nonuniform field distribution in the antenna. It is a well-known fact in antenna theory that a proper nonuniform source distribution produces better sidelobe ratio in the radiation pattern than that produced by a uniform distribution. Moreover, if the propagation constant is decreased slowly towards the open end of the antenna, then the effect of any possible reflection at that end will be reduced. It is thus reasonable to expect that the sidelobe level in the radiation pattern of a long Yagi antenna may be improved by judiciously tapering the propagation constant along its length. It should, however, be noticed that the amount of tapering should be kept very small so that the average value of β in the antenna may not be too different from that required by the Hansen and Woodyard condition. Otherwise, the advantage of tapering will be lost due to too much broadening of the main beam of the radiation pattern [see (1)].

Method of Tapering

As mentioned before, the phase velocity along the long Yagi antenna increases continuously with increase of the spacing between the director elements d or with decrease of the element length $2a$. Therefore, the required variation of the propagation constant along the length of the antenna may be obtained by varying either of the above two parameters, or by a combination of both. In the present case, for experimental verification of the approximate theory given below, the variation of a is used at first because of its simplicity. Later, the effects of the combined tapering of both the parameters are investigated and the results are then compared with the previous case. It should be remembered that this variation of the element length and/or spacing should be a very slowly-varying function of antenna length so that the propagation constant at any point along the structure may be assumed to have the value equal to what it would be on an infinite homogeneous structure characterized by the parameters at that point. The approximate theory given below is valid under this assumption only.

An Approximate Theory of Tapering

Let it be assumed that the propagation constant along the length of the antenna varies linearly from β_1 at the feed end of the antenna to a value β_2 at the open end. The propagation constant at any point z along the antenna may be represented by the following relation

$$\beta(z) = \beta_{av} - \alpha z \tag{5}$$

where

$\beta_{av} = (\beta_1 + \beta_2)/2$ is the average value of the propagation constant;

$\alpha = (\beta_1 - \beta_2)/L$ is the average variation of β per unit length along the antenna; for the present case, α is a positive constant.

The fields existing above such a structure must satisfy the following wave equation:

$$\frac{d^2\psi}{dz^2} + \beta^2(z)\psi = 0, \tag{6}$$

the assumed time dependence being of the form $e^{i\omega t}$.

Eq. (6) is extremely difficult to solve exactly, but it may be solved approximately by the WKB Approximation Method,[13] provided β varies slowly in one wavelength along the structure. If α is small compared to unity, the above condition is true and the following solution of (6) is obtained by WKB approximation:

$$\psi(z) \approx \frac{1}{\sqrt{\beta(z)}} \cdot \exp - i \int \beta(z) dz. \tag{7}$$

From (7), it is evident that by varying the propagation constant, a tapered amplitude distribution of field is obtained along the length of the antenna. Assuming $\alpha/2\beta_{av} \ll 1$ and performing the phase integration, (7) may be written in the following form:

$$\psi(z) \approx \frac{1}{\sqrt{\beta_{av}}} \left(1 + \frac{\alpha z}{2\beta_{av}}\right) \exp - i\left(\beta_{av} z - \frac{\alpha z^2}{2}\right). \tag{8}$$

Eq. (8) gives the proper traveling wave which should be used to calculate the radiation field of the tapered long Yagi antenna by the equivalent line source approach. After introducing this in (1), the following is obtained for the radiation pattern of the tapered Yagi:

$$S(\theta) = \int_{L/2}^{L/2} \psi(z) \exp ikz \cos\theta \cdot dz. \tag{9}$$

After omitting the term $1/\sqrt{\beta_{av}}$ in (8) and substituting the value of $\psi(z)$ in (9), the following result is obtained:

$$S(\theta) = \int_{-L/2}^{L/2} \left(1 + \frac{\alpha z}{2\beta_{av}}\right) \cdot \exp i\left(\frac{\alpha z^2}{2} - bz\right) \cdot dz \tag{10}$$

where

$$b = (\beta_{av} - k \cos\theta). \tag{11}$$

The integration involved in (10) can be carried out in terms of Fresnel integrals. The final expression for $S(\theta)$ may be written in the following form:

$$S(\theta) = \left[1 + \frac{b}{2\beta_{av}}\right] \sqrt{\frac{\pi}{\alpha}} \cdot e^{-ib^2/2\alpha} [F(v_2) - F(v_1)] - \frac{e^{i\alpha L^2/8}}{\beta_{av}} \cdot \sin\frac{bL}{2} \tag{12}$$

where $F(v)$ is the complex form of Fresnel integral[14] defined as follows:

$$F(v) = \int_0^v e^{i(\pi/2)\tau^2} \cdot d\tau \tag{13}$$

and

$$\left.\begin{aligned} v_1 &= \sqrt{\frac{2}{\pi}} \left(-\sqrt{\frac{\alpha}{2}} \cdot \frac{L}{2} - \frac{b}{2\sqrt{\alpha/2}}\right) \\ v_2 &= \sqrt{\frac{2}{\pi}} \left(\sqrt{\frac{\alpha}{2}} \cdot \frac{L}{2} - \frac{b}{2\sqrt{\alpha/2}}\right) \end{aligned}\right\}. \tag{14}$$

It can be shown[15] that for small values of α, (12) reduces to the following form:

$$S(\theta) = L e^{i\alpha L^2/8} \cdot \left[\frac{\sin\frac{bL}{2}}{\frac{bL}{2}} + i\frac{\alpha L}{2b}\left(1 + \frac{b}{2\beta_{av}}\right) \cdot \frac{\cos\frac{bL}{2}}{\frac{bL}{2}}\right]. \tag{15}$$

It may be seen that for $\alpha = 0$, (15) reduces to the radiation pattern for the uniform case given by (1). After taking the magnitude of (15) and omitting the terms independent of θ, the following expression is obtained for the radiation pattern of a tapered long Yagi antenna:

$$S(\theta) = \left[\left\{\frac{\sin\frac{bL}{2}}{bL/2}\right\}^2 + \left\{\frac{\alpha L}{2b}\left(1 + \frac{b}{2\beta_{av}}\right) \frac{\cos\frac{bL}{2}}{\frac{bL}{2}}\right\}^2\right]^{1/2} \tag{16}$$

where b is given by (11).

[13] P. M. Morse and H. Feshbach, "Methods of Theoretical Physics, Part II," McGraw-Hill Book Co., Inc., New York, N. Y., pp. 1092–1094; 1953.

[14] A. Summerfeld, "Optics," Academic Press, Inc., New York, N. Y., pp. 239–249; 1954.

[15] Sengupta, *op. cit.*, footnote 1, pp. 138–141.

Experimental Results and Discussions

In the specific case of a long Yagi antenna of length $L=6\ \lambda$ at 3000 mc (the design of this uniform case is given already), the elements are tapered so as to obtain the desired variation of β along the length of the antenna. This is done in the following manner. First, a convenient value of α is chosen; from this, the desired β is calculated by using (5) at some discrete points along the antenna length. Then the corresponding director lengths at these points are calculated by using (3) and (4). The intermediate directors are then slowly tapered in length while the director spacing and director radii are kept the same throughout.

The radiation patterns of the tapered long Yagi antenna are measured at 3000 mc in both E and H planes for various tapering ratios. The tapering ratio is defined as the ratio $a_{\max}/a_{\min}$, where $2a_{\max}$ is the element length at the feed end of the antenna and $2a_{\min}$ is the element length at the open end of the antenna. The results are reproduced in Figs. 5 and 6. The theoretical pattern of the tapered antenna is calculated by using (16) for the case with tapering ratio $a_{\max}/a_{\min}=1.176$ ($\alpha=0.013$) and is superposed on the corresponding experimental patterns in Figs. 5 and 6. [For the case with $a_{\max}/a_{\min}=1.176$, $\alpha=0.013$, $\beta_1/k=1.136$, $\beta_2/k=1.030$, and $\beta_{av}/k=1.083$, as required by (2).] The theoretical sidelobe ratio for this case is 15.37 db down, whereas the measured sidelobe ratios are 16.6 and 13.6 db down in the E and H planes respectively. The marked improvement in the sidelobe level for this tapered case as compared to the uniform case may be seen from Figs. 2, 3, 5, and 6. It can also be seen that the beamwidths of the radiation patterns for the uniform and tapered ($a_{\max}/a_{\min}=1.176$) cases are approximately the same. This means that for this particular value of the tapering ratio, the directivity of the antenna is not reduced appreciably as compared with the uniform case. For tapering ratios beyond 1.176, the main beam in the radiation pattern broadens considerably, thereby reducing the directivity of the antenna. This broadening of the main beam for larger values of tapering ratios may be explained if one considers that for large tapering ratios, the element lengths near the open end of the antenna become too short, thereby reducing the effective radiating length of the antenna. From this consideration, one might expect a better result by using a combination of tapering in length and spacing, because this will enable one to achieve the desired tapering of β without making the element lengths near the open end of the antenna too short. This has actually been found experimentally, as discussed below.

Let it be assumed that β varies linearly from β_1 at the feed end to β_2 at the open end of the antenna, the average value $\beta_{av}=(\beta_1+\beta_2)/2$ being the value required by (2). The tapering is obtained in two steps. First, β is varied linearly from β_1 to $[\beta_1-(\beta_1-\beta_2)/2]$ by gradually

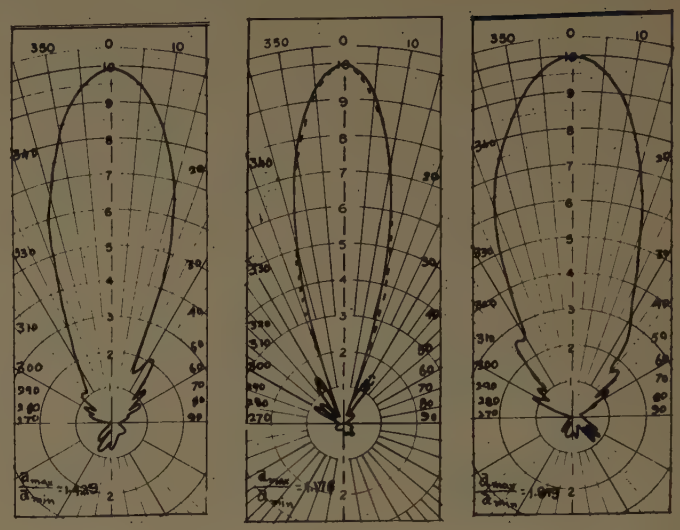

Fig. 5—The E-plane radiation patterns of a tapered long Yagi antenna for different tapering ratios. Frequency of measurement $=3000$ mc; antenna length $L=6$ at 3000 mc. Dashed line: theoretical; solid line: experimental.

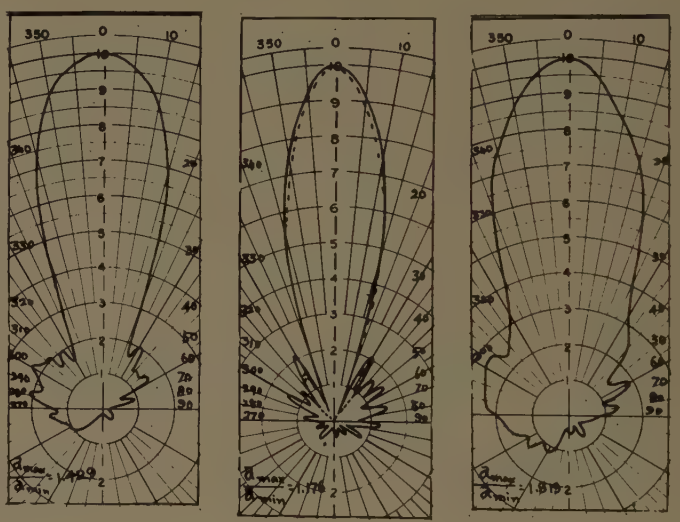

Fig. 6—The H-plane radiation patterns of a tapered long Yagi antenna for different tapering ratios. Antenna length $L=6\ \lambda$ at the frequency of measurement 3000 mc. Dashed line: theoretical; solid line: experimental.

increasing the spacing d toward the open end of the antenna, while keeping a constant all through. In the next step, a is tapered to obtain the rest of the variation of β, thereby obtaining β_1 at one end and β_2 at the other end of the antenna. This technique has been applied to a tapered long Yagi antenna of length $L=10\ \lambda$ at 3000 mc. For this case, $\beta_1/k=1.082$, $\beta_{av}/k=1.050$, $\beta_2/k=1.008$, and $\alpha=0.0074$. With this arrangement, a sidelobe ratio of 19.9 db down has been obtained without appreciably broadening the main beam in the radiation pattern. By using only length tapering in the same antenna, a maximum sidelobe improvement of about 16.9 db may be obtained without too much broadening of the main beam of the radiation pattern.

Conclusions

From the above investigation, it may be said that by using a linear variation of the propagation constant along the length of a long Yagi antenna, the sidelobe level in the radiation pattern may be improved considerably without reducing appreciably the gain obtainable from the antenna. This increases the possibility of using such an antenna for directional reception, particularly in radar and radio-astronomical applications. The approximate theory as given above is able to explain the action of tapering with an amount of accuracy sufficient for practical purposes. Since the tapering function is required to be a very slowly-varying function of the antenna length, the method can be applied advantageously only to long Yagi antennas. The effect of tapering in the case of short Yagi antennas has not been investigated, but it is probable that the sidelobe level in the radiation pattern of a short Yagi antenna may be improved by this method; the improvement may not be as good as in the case of long Yagi antennas. This method of tapering, although applied here to the particular case of long Yagi antennas, may be utilized in the case of other long end-fire antennas of traveling-wave type.

Acknowledgment

The author wishes to express his thanks to Prof. G. Sinclair for the encouragement received from him at all times, and to Prof. J. L. Yen for many discussions and suggestions during the course of this research. Thanks are also acknowledged to the Sinclair Radio Laboratories for allowing the author to use their antenna pattern recorder.

Design of Circular Apertures for Narrow Beamwidth and Low Sidelobes*

T. T. TAYLOR†

***Summary*—This article extends a method of antenna design described in an earlier article[1] by the same author. A family of continuous circular aperture distributions is developed in such a way as to involve only two independent parameters, A, a quantity uniquely related to the design sidelobe level and $\bar{n}$ a number controlling the degree of uniformity of the sidelobes. An asymptotic approach to the condition of uniform sidelobes thus becomes possible. A companion article by Robert Hansen contains aperture distribution tables and examples.**

Introduction

THE advent of maser and parametric low-noise amplifiers has, for many radio astronomy, scatter communications, and radar applications, made the antenna a major noise source with a typical noise temperature several times that of the amplifier. This troublesome situation, together with the long-standing clutter return problem, makes urgent the consideration of sidelobe reduction in circular aperture antennas. A recent commentary[2] by Jacquinot reveals that the corresponding problem in the diffraction of light, known as "apodization," has also become important to optical astronomers and spectroscopists and that a considerable volume of research on this problem has been undertaken. Of particular interest are the works of Osterberg and Wilkins[3] and Dossier,[4] a student of Jacquinot. For distribution functions, these authors propose superpositions of certain component functions whose individual diffraction patterns are well known and the problem becomes one of ascertaining what requirements to impose upon the total diffraction patterns, given that they must be compounded of partial patterns of a certain type. This point of view is probably better known in the antenna field because of the work of Woodward.[5] In any event, some very good examples of apodization have been reported. The method of the present article is somewhat different in that a certain arrangement of

* Manuscript received by the PGAP, March 16, 1959; revised manuscript received, July 8, 1959. The work reported in this article was performed at the Hughes Aircraft Co. and has been described in somewhat greater detail in Hughes Aircraft Co. Tech. Memo. No. 372 dated August 30, 1954. The work was partially supported by the AF Cambridge Res. C. under Contract AF 19(604)-262.

† University of California, Riverside; formerly with Hughes Aircraft Co., Culver City, Calif.

[1] T. T. Taylor, "Design of line-source antennas for narrow beamwidth and low sidelobes," IRE Trans. on Antennas and Propagation, vol. AP-3, pp. 16–28; January, 1955.

[2] J. Strong, "Concepts of Classical Optics," W. H. Freeman and Co., pp. 410–418; 1958.

[3] H. Osterberg and J. E. Wilkins, Jr., "The resolving power of a coated objective," *J. Opt. Soc. Amer.*, vol. 39, pp. 553–557; July, 1949.

[4] B. Dossier, "Récherches sur l'apodization des images optiques," *Rev. Opt.*, vol. 33, pp. 57–111, 147–178, 267–296, and 552; 1954.

[5] P. M. Woodward, "A method of calculating the field over a plane aperture required to produce a given polar diagram," *J. IEE*, vol. 93, pp. 1554–1558; 1946.

zeros in the total pattern, chosen with due regard for the general properties which the arrangement must possess, is first proposed and then a method, employed by Dossier and similar to that of Woodward, is invoked for the calculation of the distribution function. It may be remarked that the practical realization of optical apodization in the general case is contingent upon the successful construction of absorbing screens which are free from phase errors.

The concept of a "circular aperture" as a source of radiation is, in the field of antenna theory, an outgrowth of the analysis of that very common configuration which consists of a paraboloidal reflector and feed. If such a device is completely enclosed by an imaginary surface, then, in principle, it is merely necessary to know tangential E and H upon this surface in order to calculate the radiated fields. It is customary to draw the surface in such a way that it has a large plane expanse just in front of the antenna configuration and to suppose that the tangential fields are zero except within the circular area which is directly "illuminated." This circular area is regarded as the aperture.

In this article it will be assumed that, upon any small element of the aperture, the fields are identical in character with those which would be found in an emerging plane electromagnetic wave. It is further assumed that the direction of polarization is the same for all elements but that the field strength varies from place to place, perhaps in both amplitude and phase, and is proportional to a distribution function $g(\rho, \zeta)$. It is not necessary, of course, that the device producing the fields actually be a reflector and feed; any device which generates fields of the type assumed over a circular area would come under the scope of this article.

Let the geometry of the aperture, which has radius a, be as illustrated in Fig. 1. The radiation pattern in power per unit solid angle is

$$\psi = \psi_0 \left| k^2 \int_0^{2\pi} \int_0^a g(\rho, \zeta) e^{ik\rho \cos\gamma} \rho d\rho d\zeta \right|^2. \qquad (1)$$

Here ψ_0 which is proportional to $(1+\cos\theta)^2$ is the "obliquity factor" of a Huygens source[6] and is what would normally be called the element factor. The integral is called the space factor and, because of the broadness of the obliquity factor, the relationship between the beamwidth and sidelobe level of the space factor alone will be adopted as the subject for discussion.

In (1), k is the free space wave number, $2\pi/\lambda$, and γ is the angle measured between the observer's direction and the radius vector to the element $\rho d\rho d\zeta$. Since the scope of this article will be restricted to those cases in which the space factor has rotational symmetry about the w axis [an extension to certain other cases involving a linear phase shift in $g(\rho, \zeta)$ is obvious], the same type

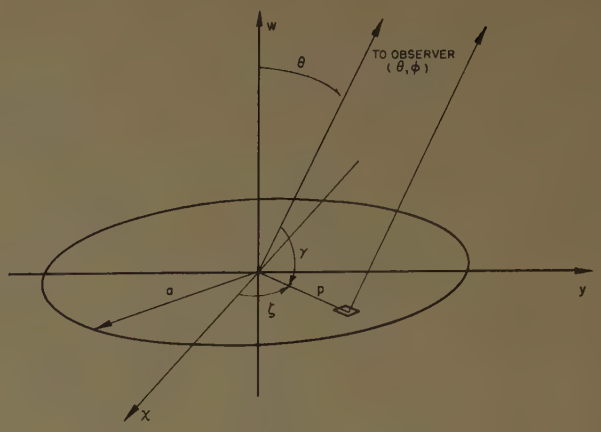

Fig. 1—Geometry of circular aperture.

of symmetry devolves upon the distribution function and the latter becomes a function of ρ only. A well-known Fourier expansion[7] makes it possible to write the space factor as a Hankel transform:

$$S(\theta) = 2\pi k^2 \int_0^a \rho g(\rho) J_0(k\rho \sin\theta) d\rho. \qquad (2)$$

It will be advantageous to introduce new variables as follows:

$$p = \frac{\pi}{a}\rho; \qquad (3)$$

$$u = \frac{2a \sin\theta}{\lambda}. \qquad (4)$$

The quantity $\lambda/2a$ will be known as a standard beamwidth; the beamwidth (in radians) between half-power points for a uniformly illuminated circular aperture is 1.029 standard beamwidths. It is interesting to recall the corresponding figure for a uniformly illuminated line source, 0.8859 standard beamwidth.

With the substitution of (3) and (4), (2) becomes

$$S(u) = 2\pi \left(\frac{2a}{\lambda}\right)^2 \int_0^\pi p g(p) J_0(pu) dp. \qquad (5)$$

The constant factors will be dropped and the integral denoted $F(u)$:

$$F(u) = \int_0^\pi p g(p) J_0(pu) dp. \qquad (6)$$

Eq. (6) expresses the basic relationship which will be studied here.

Properties of the Distribution Function

As in the corresponding article[1] on line sources, the variables p and u are imbedded in the complex domains ξ and z, respectively, such that $\xi = p + iq$ and $z = u + iv$. The "visible range" of the z plane is the real segment

[6] S. A. Schelkunoff, "Electromagnetic Waves," D. Van Nostrand Co., Inc., New York, N. Y., p. 354; 1943.

[7] J. A. Stratton, "Electromagnetic Theory," McGraw-Hill Book Co., Inc., New York, N. Y., p. 372; 1941.

$0 \leq u \leq 2a/\lambda$ and a unit distance in the z plane corresponds to one standard beamwidth. An observer who travels around the aperture to examine its radiation pattern will cover all real angles in the range $0 \leq \theta \leq \pi$. This coverage is translated twice into the point set $0 \leq u \leq 2a/\lambda$, $v=0$, in the z plane by the relationship $u=2a(\sin\theta)/\lambda$ as shown graphically in Fig. 2. The profile of $F(z)$ on the visible range is the only part of $F(z)$ which enters into the formation of the radiation pattern. It is evident from Fig. 2 that the space factor attains the same value at $\pi-\theta$ as it does at θ; the total radiation pattern is not "double-ended," however, for the obliquity factor nullifies the rearward beam.

Consider, now, the ξ plane. The integral in (6) becomes the limit as τ tends to zero of the integral along the path C of Fig. 3, beginning at zero and following the axis of reals to $\pi-\tau$. The reason for the limiting process will be made evident later. Eq. (6) becomes

$$F(z) = \lim_{\tau \to 0} \int_C \xi g(\xi) J_0(\xi z) d\xi. \qquad (7)$$

It is assumed at the outset that $g(\xi)$ can be written as the product,

$$g(\xi) = h(\xi)(\pi^2 - \xi^2)^\alpha; \qquad \alpha \text{ real and } > -1. \qquad (8)$$

The quantity $(\pi^2-\xi^2)^\alpha$ is regarded as having its principal value in that region of the ξ plane which remains after the latter is cut from $-\infty$ to $-\pi$ and from π to ∞ along the axis of reals. The function $h(\xi)$ is supposed to be even, nonvanishing at $\xi = \pm\pi$, and regular in the racetrack shaped region R of Fig. 3, the ends of which have a radius $\delta > 0$. Singularities of $h(\xi)$, therefore, may be arbitrarily close to the real line segment $-\pi \leq p \leq \pi$ but may not fall exactly upon it; the only singularity actually permitted in the distribution function is the one which must necessarily occur when this function ceases to exist physically for values of $p > \pi$ and which corresponds to the branch point at $\xi = \pi$ in (8). It is considered necessary that α be greater than or equal to zero for physically realizable distributions; nevertheless, values of α between -1 and zero will be included for completeness since $F(z)$ exists even for these values.

Care should be taken not to confuse the ξ plane of Fig. 3 with the xy plane of Fig. 1. The function $g(\rho, \zeta)$ which is defined on the real xy (or $\rho\zeta$) plane is a surface of revolution formed by rotating $g(\rho)$ about the w axis. The function $g(\rho)$ or $g(p)$, however, is obtained by taking the profile of $h(\xi)$ $(\pi^2-\xi^2)^\alpha$ on the real axis of the complex ξ plane. Thus the ξ plane is a mathematical construct from which the function $g(p)$ is derived; this function is then rotated in the real xy plane to give the actual distribution function.

The fact that the singularities of $h(\xi)$ are not limited as to number and can be arbitrarily close to the real line segment just mentioned gives the function $g(\xi)$ enough flexibility, in the author's opinion, to make it representative of any aperture distribution likely to be encountered in practice. The postulate of the evenness of $h(\xi)$ is no essential handicap here since the radius of curvature at the origin can be made arbitrarily small; the fact that such a radius does exist, however, precludes the possibility of a singularity being generated as $g(p)$ is rotated about the w axis in the xy plane.

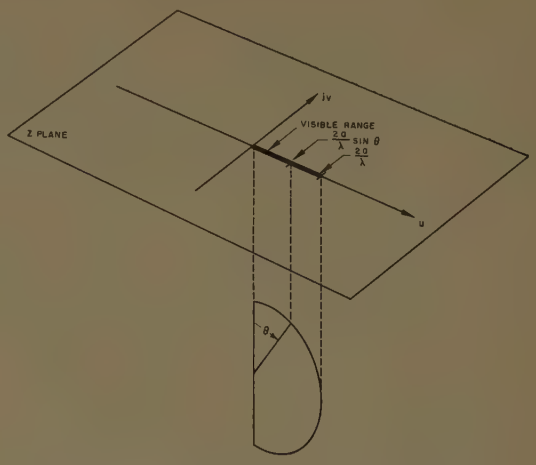

Fig. 2—Relationship between real space and complex z plane.

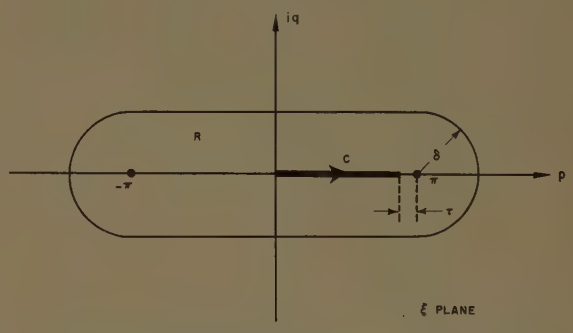

Fig. 3—Contour of integration in complex ξ plane.

Properties of the Space Factor

Given that the distribution function is in accord with the mathematical model just described and following a procedure analogous to that employed earlier,[1] it is easy to prove that $F(z)$ is an even entire function of z with the following asymptotic forms for large z:

$$F(z) \sim \frac{h(\pi)(2\pi)^{1+\alpha}\Gamma(1+\alpha)}{\sqrt{2}} \cdot \frac{\cos\pi\left(z - \dfrac{1.5+\alpha}{2}\right)}{\pi z^{(1.5+\alpha)}}$$

$$\text{for Re } z > 0; \qquad (9)$$

$$F(z) \sim \frac{h(\pi)(2\pi)^{1+\alpha}\Gamma(1+\alpha)}{\sqrt{2}} \cdot \frac{\cos\pi\left(-z - \dfrac{1.5+\alpha}{2}\right)}{\pi(-z)^{(1.5+\alpha)}}$$

$$\text{for Re } z < 0; \qquad (10)$$

$$F(z) \sim \frac{h(\pi)(2\pi)^{1+\alpha}\Gamma(1+\alpha)}{\sqrt{2}} \cdot \frac{e^{\pi|z|}}{2\pi|z|^{(1.5+\alpha)}}$$

$$\text{for Re } z = 0. \qquad (11)$$

It is interesting to compare the asymptotic forms of $F(z)$ for the line source and for the circular aperture. Table I makes this comparison for integral values of α and for z in the right-half plane. From Fig. 2, the right-half plane forms are obviously sufficient for making predictions concerning the radiation pattern.

TABLE I
COMPARISON OF ASYMPTOTIC FORMS OF $F(z)$ FOR LINE SOURCE AND CIRCULAR APERTURE

α	Asymptotic Form of $F(z)$, Re $z > 0$	
	Line Source	Circular Aperture
0	$h(\pi)(2\pi)\dfrac{\sin \pi z}{\pi z}$	$\dfrac{h(\pi)(2\pi)}{\sqrt{2}}\cdot\dfrac{\sin \pi(z-1/4)}{\pi z^{1.5}}$
1	$h(\pi)(2\pi)^2\dfrac{\cos \pi z}{\pi z^2}$	$\dfrac{h(\pi)(2\pi)^2}{\sqrt{2}}\cdot\dfrac{-\cos \pi(z-1/4)}{\pi z^{2.5}}$
2	$h(\pi)(2\pi)^3(2)\dfrac{\sin \pi z}{\pi z^3}$	$\dfrac{h(\pi)(2\pi)^3(2)}{\sqrt{2}}\cdot\dfrac{-\sin \pi(z-1/4)}{\pi z^{3.5}}$
3	$h(\pi)(2\pi)^4(6)\dfrac{\cos \pi z}{\pi z^4}$	$\dfrac{h(\pi)(2\pi)^4(6)}{\sqrt{2}}\cdot\dfrac{\cos \pi(z-1/4)}{\pi z^{4.5}}$

When α is an integer, as in Table I, the results agree with those of Dossier who predicts the relationship between the asymptotic form of $F(z)$ and the value of the first nonvanishing derivative of $g(\xi)$ at the edge of the aperture.

As with line sources, the decay rate of the remote sidelobes is dependent only on the behavior of the distribution function at the edge of the aperture. It is always greater for the circular aperture, however, by a factor of $z^{-1/2}$ if the α values are the same.

Finally, it is possible to prove that if the zeros of $F(z)$ are grouped in pairs, $\pm z_1$, $\pm z_2$, etc., and numbered in such a way that the moduli of successive pairs do not decrease, then the members of the nth zero pair tend to the positions $\pm(n+\alpha/2+1/4)$ as n tends to infinity. This statement should be compared with the corresponding one for line sources in which the members of the nth zero pair tend to the positions $\pm(n+\alpha/2)$.

Design of a Practical Circular Aperture Distribution Function

As was pointed out in the earlier article on line sources,[1] essentially two areas of flexibility are available in regard to the form of $F(z)$. These are 1) the value of α and 2) the placement of the central zeros, that is, the zeros near the origin in the z plane. It is possible to draw the same conclusions as before, namely, that for highly directive patterns, α should equal zero (this gives the distribution a "pedestal"), and that the central zeros as well as the remote zeros of $F(z)$ should be simple zeros on the axis of reals. For choosing the positions of the central zeros, the scheme used for line sources will be employed again. This scheme permits the space factor function $F(z)$ to approach the ideal function $\cos \pi\sqrt{z^2-A^2}$ as a certain parameter is increased; it involves setting a finite number of the central zeros of $F(z)$ equal to the corresponding zeros of the function,

$$F_1(z, A) = \cos \pi \sqrt{\left(\frac{z}{\sigma}\right)^2 - A^2}, \tag{12}$$

which, for σ slightly greater than unity, is an ideal function with slight horizontal dilation.

A set of points on the axis of reals, hereafter designated as the "μ points," will now be defined. The definition of μ_n, the nth such point, is simply

$$J_1(\pi\mu_n) = 0. \tag{13}$$

The points are counted in the order of increasing value and are shown in Table II. Evidently $\mu_n \to n+\frac{1}{4}$ as $n \to \infty$, from the well-known asymptotic formula for

TABLE II
SOLUTIONS OF $J_1(\pi\mu_n)=0$

n	μ_n
0	0
1	1.2196699
2	2.2331306
3	3.2383154
4	4.2410628
5	5.2427643
6	6.2439216
7	7.2447598
8	8.2453948
9	9.2458927
10	10.2462933

$J_1(\pi z)$. It is also evident that if an even entire function has its zeros positioned in such a way that the nth zero pair approaches $\pm\mu_n$ as $n \to \infty$, it will be an acceptable space factor functioning with an α value of zero. The reason for introducing the μ points is not obvious now but will become so later.

The zeros of (12) lie at the points,

$$z_n = \pm \sigma\sqrt{A^2 + (n - 1/2)^2}. \tag{14}$$

Let the dilation factor σ be chosen so that eventually one of these zeros falls on a specifically chosen μ point, $\mu_{\bar{n}}$. Then

$$\sigma = \frac{\mu_{\bar{n}}}{\sqrt{A^2 + (\bar{n} - 1/2)^2}}. \tag{15}$$

The plan is now to construct an entire function with the following zeros:

$$\left.\begin{aligned} z_n &= \pm \sigma\sqrt{A^2 + (n - 1/2)^2} && \text{for } 1 \le n < \bar{n} \\ z_n &= \pm \mu_n && \text{for } \bar{n} \le n < \infty \end{aligned}\right\}. \tag{16}$$

This function, normalized so as to have unit value at the origin, is as follows:

$$F(z, A, \bar{n}) = \frac{2J_1(\pi z)}{\pi z} \prod_{n=1}^{\bar{n}-1} \frac{1 - \dfrac{z^2}{\sigma^2[A^2 + (n - 1/2)^2]}}{1 - \dfrac{z^2}{\mu_n^2}}. \quad (17)$$

This expression defines a two-parameter family of entire functions whose members approach the (normalized) ideal space factor, $\cos \pi\sqrt{z^2 - A^2}/\cosh \pi A$, *arbitrarily exactly as* $\bar{n}$ *is increased.* The value of $\bar{n}$, which is finite in any practical case, is of considerable significance. In relationship to the pattern, the points $\pm\mu_{\bar{n}}$ divide the region of uniform sidelobes ($|u| < \mu_{\bar{n}}$) from the region of decaying sidelobes ($|u| > \mu_{\bar{n}}$) where here, as before; $z = u + iv$. As $\bar{n}$ is increased, the region of uniform sidelobes extends farther out from the main beam. In the region of uniform sidelobes the lobes actually decrease slightly as $|u|$ increases and their initial level is very slightly lower (that is, better) than the design level η. This design sidelobe ratio is related to A as follows:

$$\eta = \cosh \pi A, \quad (18)$$

which is the same as in the case of line sources since the same ideal space factor is approached in either case.

The chief disparity between the practical pattern and the ideal is in the beamwidth which is greater than the ideal by a factor almost exactly equal to σ. However, $\bar{n}$ does not have to be very large to make σ only a few per cent greater than unity.

To summarize, the members of the pattern family $F(z, A, \bar{n})$ have two independent characteristics:

1) The design sidelobe ratio, η.
2) The boundary of the region of approximately uniform sidelobes, $\mu_{\bar{n}}$, which depends directly upon $\bar{n}$, an integer.

Once these two parameters have been chosen, the pattern, the distribution function, and all other relevant data may be calculated. In selecting $\bar{n}$, it is essential to avoid values that are too small; the change from $F_1(z, A)$ to $F(z, A, \bar{n})$, in which the trans-$\mu_{\bar{n}}$ zeros migrate to the μ-points, must be such that the spacing never increases between any of these zeros. In order that this condition be fulfilled, $\bar{n}$ must be chosen such that a unit increases in $\bar{n}$ does not increase σ. Practically, this selection means for a space factor with a design sidelobe ratio of 30 db, $\bar{n}$ must be at least 3 and that for a design sidelobe ratio of 40 db, it must be at least 4. Apart from this limitation, one has considerable liberty in the choice of $\bar{n}$; large values make σ more nearly equal to unity, thereby sharpening the beam; however, the additional benefit obtained in this way soon becomes negligible as $\bar{n}$ increases. If $\bar{n}$ is increased so as to place $\mu_{\bar{n}}$ well beyond the endpoint of the visible range ($2a/\lambda$), the effect is to make all the visible sidelobes uniform. Further increase of $\bar{n}$ has little influence upon the visible pattern but has the effect of increasing the invisible sidelobe energy and "super-gaining" the aperture.

The beamwidth of the ideal space factor (in terms of standard beamwidths) is a function of the sidelobe ratio η only. It is given rigorously as follows:

$$\beta_0 = \frac{2}{\pi} \sqrt{(\operatorname{arc\,cosh} \eta)^2 - \left(\operatorname{arc\,cosh} \frac{\eta}{\sqrt{2}}\right)^2}. \quad (19)$$

This relationship is illustrated graphically in Fig. 7 in Taylor.[1] From what has been said before, it is evident that this beamwidth cannot be equalled without either 1) allowing $\bar{n}$ to become infinite or 2) making the visible zeros of the given space factor coincide with, or perhaps fall within, those of the ideal space factor and accepting high invisible lobes at the inevitable transition regions which will separate the visible zeros from the remote zeros. Both of these alternatives result in super-gain apertures. For $\bar{n}$ finite, the beamwidth of an $F(z, A, \bar{n})$ space factor is given by the following extremely good approximation:

$$\beta \doteq \sigma\beta_0 = \frac{\mu_{\bar{n}}\beta_0}{\sqrt{A^2 + (\bar{n} - 1/2)^2}}. \quad (20)$$

The Inverse Transform

In calculating the distribution function $g(p)$ to give the space factor $F(z, A, \bar{n})$, the method of Dossier will be used. Let the distribution function $g(p)$ be built out of functions of the form $J_0(\mu_m p)$. In other words,

$$g(p) = \sum_{m=0}^{\infty} D_m J_0(\mu_m p). \quad (21)$$

Applying the Hankel transformation (6) to this expression term by term yields the following results:

$$F(u) = \sum_{m=0}^{\infty} D_m \int_0^{\pi} pJ_0(p\mu_m)J_0(pu)dp. \quad (22)$$

The integral in (22) is well known[8] and given by

$$\int_0^{\pi} pJ_0(p\mu_m)J_0(pu)dp$$

$$= \left[\frac{p\mu_m J_1(p\mu_m)J_0(pu) - puJ_0(p\mu_m)J_1(pu)}{\mu_m^2 - u^2}\right]_0^{\pi} \quad (23)$$

$$= \frac{\pi u J_0(\pi\mu_m)J_1(\pi u)}{u^2 - \mu_m^2}. \quad (24)$$

The above expression is an even function of u with a zero at every μ point except at $\pm\mu_m$, at which points it attains the value,

[8] E. Jahnke and F. Emde, "Tables of Functions," Dover Publications, New York, N. Y., p. 146; 1943.

$$\lim_{u\to\mu_m} \frac{\pi u J_0(\pi\mu_m)J_1(\pi u)}{u^2-\mu_m{}^2} = \frac{\pi^2}{2}\,[J_0(\pi\mu_m)]^2. \qquad (25)$$

Just as in the Woodward method, then, the pattern is a superposition of functions

$$F(u) = \sum_{m=0}^{\infty} D_m J_0(\pi\mu_m)\,\frac{\pi u J_1(\pi u)}{u^2-\mu_m{}^2}. \qquad (26)$$

Each of these functions has its principal maxima (or maximum, in the case of $m=0$) at the points $\pm\mu_m$, points which are zeros for all the other functions. It follows then, that

$$F(\mu_m) = \frac{D_m\pi^2}{2}\,[J_0(\pi\mu_m)]^2 \qquad (27)$$

or

$$D_m = \frac{2F(\mu_m)}{[J_0(\pi\mu_m)]^2\pi^2}. \qquad (28)$$

In the present situation, $F(\mu_m)$ means $F(\mu_m, A, \bar{n})$ as given by (17). The process of setting z equal to μ_m in this equation, however, is complicated by the presence of removable singularities at all the μ points for which $m<\bar{n}$. At $m=0$, the singular factor is $J_1(\pi z)/\pi z$ and for $0<m<\bar{n}$, it is $J_1(\pi z)/(1-z^2/\mu_m{}^2)$. These can be evaluated by well-known methods and the results are

$$F(\mu_m, A, \bar{n}) = \left\{ \begin{array}{ll} 1 & m=0 \\ -J_0(\pi\mu_m)\,\dfrac{\displaystyle\prod_{n=1}^{\bar{n}-1}\left[1-\dfrac{\mu_m{}^2}{\sigma^2[A^2+(n-\frac{1}{2})^2]}\right]}{\displaystyle\prod_{\substack{n=1\\ n\neq m}}^{\bar{n}-1}\left[1-\dfrac{\mu_m{}^2}{\mu_n{}^2}\right]} & 0<m<\bar{n} \\ 0 & m\geq\bar{n} \end{array} \right\}. \qquad (29)$$

Since these numbers (and hence the D_m) vanish for $m\geq\bar{n}$, it is clear that $g(p)$ will actually be given by a finite sum. In other words, no Bessel component of the form $J_0(\mu_m p)$ with $m\geq\bar{n}$ can appear in the distribution function; such components would generate partial patterns having principal maxima at points for which the total pattern, according to (16), is supposed to be zero. Thus $g(p)$ is

$$g(p) = \sum_{m=0}^{\bar{n}-1} \frac{2F(\mu_m, A, \bar{n})}{[J_0(\pi\mu_m)]^2\pi^2}\,J_0(\mu_m p). \qquad (30)$$

The article by Hansen which follows[9] contains tables of this function for a variety of parameter values together with illustrated examples.

Acknowledgment

The writer is happy to acknowledge the cooperation, both past and present, which he has received from members of the technical staff of the Hughes Aircraft Company. He is especially indebted to Dr. Robert S. Elliott who checked the manuscript of Technical Memorandum No. 372 very carefully and thereby contributed materially to the accuracy of that presentation and, indirectly, to that of the present article.

[9] R. C. Hansen, "Tables of Taylor distributions for circular aperture antennas," this issue, p. 23.

Tables of Taylor Distributions for Circular Aperture Antennas*

R. C. HANSEN†

Summary—**Tables of the circular aperture distributions described in the preceding paper by Taylor[1] are given. Steps in the design process are illustrated by examples.**

THE appropriate formulas from Taylor's paper[1] have been collected here for easy reference. The ideal beamwidth of a one-wavelength source in z is

$$\beta_0 = \frac{2}{\pi}\sqrt{(\operatorname{arc\,cosh}\eta)^2 - (\operatorname{arc\,cosh}\eta/\sqrt{2})^2} \qquad (1)$$

where η is the sidelobe voltage ratio. The actual beamwidth is

$$\beta = \beta_0\sigma\frac{\lambda}{2a} \quad \text{or} \quad \theta = 2\arcsin\frac{\lambda\sigma\beta_0}{4a} \qquad (2)$$

where a is the aperture radius, and σ is the beam broadening factor due to the $\bar{n}$ approximation to the ideal space factor, so that

$$\sigma = \frac{\mu_{\bar{n}}}{\sqrt{A^2 + (\bar{n} - 1/2)^2}} \qquad (3)$$

in which $\eta = \cosh A$ and $\mu_{\bar{n}}$ is given in Table II of Taylor's paper. The values of σ and β_0 have been summarized here in Table I. For ease in using (2) with arc sine approximated by argument, β_0 is given in degrees. Where σ values are omitted from Table I, the choices of $\bar{n}$ are sufficiently small to produce shifting of trans-$\bar{n}$ zeros and are thus unallowable. In general, higher values of $\bar{n}$ produce peaked distributions (peaked at the center and edge of the aperture), while low values produce tapered distributions (tapered from a maximum value at the aperture center to a minimum at the edge). The distribution shapes produced by different $\bar{n}$ values are shown in Table II.

The aperture distribution $g(p)$, where $p = \pi\rho/a$ is the normalized radius, is

$$g(p) = \frac{2}{\pi^2}\sum_{m=0}^{\bar{n}-1}\frac{J_0(\mu_m p)F(\mu_m, A, \bar{n})}{[J_0(\pi\mu_m)]^2} \qquad (4)$$

where

$$F(\mu_0, A, \bar{n}) = 1 \quad \text{for} \quad m = 0 \qquad (5)$$

and

$$F(\mu_m, A, \bar{n}) = -J_0(\pi\mu_m)\frac{\prod_{n=1}^{\bar{n}-1}\left(1 - \dfrac{\mu_m^2}{\sigma^2[A^2 + (n - 1/2)^2]}\right)}{\prod_{\substack{n=1 \\ n\neq m}}^{\bar{n}-1}\left(1 - \dfrac{\mu_m^2}{\mu_n^2}\right)} \qquad (6)$$

for $m > 0$.

With the radius divided into 20 divisions where $p = k\pi/20$, $g(p)$ is tabulated for sidelobe ratios of 25, 30 and 35 db with $\bar{n} = 3(1)10$, in Table III. Only rotationally symmetric distribtuions have been considered; thus the figures and tables give values only along a radius of the aperture. Typical curves are shown for sidelobe levels of 25, 30, and 35 db in Figs. 1–3. [More extensive tables have also been published[2] for sidelobe ratios 15(1)40 db, and $\bar{n} = 3(1)10$.]

The antenna pattern is given by

$$F(z, A, \bar{n}) = +\frac{J_1(\pi z)}{\pi z}\prod_{n=1}^{\bar{n}-1}\left\{\frac{1 - \dfrac{z^2}{\sigma^2[A^2 + (n - 1/2)^2]}}{1 - \dfrac{z^2}{\mu_n^2}}\right\} \qquad (7)$$

with $(z = 2a/\lambda)\sin\theta$.

In the design of a circular aperture, (2) and Table I are the starting point. If the diameter and sidelobe level are specified, β_0 is found from Table I, and beamwidth vs σ from (2). Large values of $\bar{n}$ give slight improvement in beamwidth at a cost of a peaked (at center and edge of aperture) distribution. Small $\bar{n}$ produce tapered distributions. The compromise σ is chosen by a balance of beamwidth against the distribution shape, found from Table I. Tables of the pattern function are not given since the sidelobes are nearly constant out to $\bar{n}$, then taper off.

As an example, suppose a beamwidth of 3° with 30-db sidelobes is desired. From (2)

$$\frac{2a}{\lambda\sigma} = \frac{60.55}{3} = 20.18.$$

* Manuscript received by the PGAP, May 12, 1959.

† Space Technology Labs., Los Angeles, Calif. Formerly at Microwave Lab., Hughes Aircraft Co., Culver City, Calif.

[1] T. T. Taylor, "Design of circular apertures for narrow beamwidth and low sidelobes," this issue, p. 17.

[2] R. C. Hansen, "Tables of Taylor Distributions for Circular Aperture Antennas," Hughes Aircraft Co., Culver City, Calif., Tech. Memo. No. 587; February, 1959.

TABLE I

IDEAL BEAMWIDTH AND BEAM BROADENING FACTOR

Design Sidelobe Level, Decibels	η (Sidelobe Voltage Ratio)	Ideal Beamwidth, β_0, Degrees	A^2	Beam Broadening Factor σ							
				$\bar{n}=3$	$\bar{n}=4$	$\bar{n}=5$	$\bar{n}=6$	$\bar{n}=7$	$\bar{n}=8$	$\bar{n}=9$	$\bar{n}=10$
15	5.62341	45.93	0.58950	1.2382	1.1836	1.1485	1.1244	1.1069	1.0937	1.0833	1.0751
16	6.30957	47.01	0.64798	1.2330	1.1809	1.1469	1.1233	1.1061	1.0931	1.0829	1.0747
17	7.07946	48.07	0.70901	1.2276	1.1781	1.1452	1.1222	1.1053	1.0925	1.0825	1.0743
18	7.94328	49.12	0.77266	1.2220	1.1752	1.1434	1.1210	1.1045	1.0919	1.0820	1.0740
19	8.91251	50.15	0.83891	1.2163	1.1723	1.1416	1.1198	1.1037	1.0913	1.0815	1.0736
20	10.00000	51.17	0.90777	1.2104	1.1692	1.1398	1.1186	1.1028	1.0906	1.0810	1.0732
21	11.2202	52.17	0.97927	1.2044	1.1660	1.1379	1.1173	1.1019	1.0899	1.0805	1.0728
22	12.5893	53.16	1.05341	1.1983	1.1628	1.1359	1.1160	1.1009	1.0892	1.0799	1.0723
23	14.1254	54.13	1.13020	1.1920	1.1594	1.1338	1.1146	1.1000	1.0885	1.0793	1.0719
24	15.8489	55.09	1.20965	1.1857	1.1560	1.1317	1.1132	1.0990	1.0878	1.0788	1.0714
25	17.7828	56.04	1.29177	1.1792	1.1525	1.1296	1.1118	1.0979	1.0870	1.0782	1.0708
26	19.9526	56.97	1.37654	1.1726	1.1489	1.1274	1.1103	1.0969	1.0862	1.0775	1.0704
27	22.3872	57.88	1.46395	1.1660	1.1452	1.1251	1.1087	1.0958	1.0854	1.0769	1.0699
28	25.1189	58.78	1.55406	1.1592	1.1415	1.1228	1.1072	1.0946	1.0845	1.0762	1.0694
29	28.1838	59.67	1.64683	1.1524	1.1377	1.1204	1.1056	1.0935	1.0836	1.0756	1.0688
30	31.6228	60.55	1.74229	1.1455	1.1338	1.1180	1.1039	1.0923	1.0827	1.0749	1.0683
31	35.4813	61.42	1.84044	1.1385	1.1298	1.1155	1.1022	1.0911	1.0818	1.0742	1.0677
32	39.8107	62.28	1.94126	1.1315	1.1258	1.1129	1.1005	1.0898	1.0809	1.0734	1.0671
33	44.6684	63.12	2.04473	1.1244	1.1217	1.1103	1.0987	1.0885	1.0799	1.0727	1.0665
34	50.1187	63.96	2.15092		1.1176	1.1077	1.0969	1.0872	1.0790	1.0719	1.0659
35	56.2341	64.78	2.25976		1.1134	1.1050	1.0951	1.0859	1.0779	1.0711	1.0653
36	63.0957	65.60	2.37129		1.1091	1.1023	1.0932	1.0846	1.0769	1.0703	1.0647
37	70.7946	66.40	2.48551		1.1048	1.0995	1.0913	1.0832	1.0759	1.0695	1.0640
38	79.4328	67.19	2.60241		1.1005	1.0967	1.0894	1.0818	1.0748	1.0687	1.0633
39	89.1251	67.98	2.72201		1.0961	1.0938	1.0874	1.0803	1.0737	1.0678	1.0627
40	100.0000	68.76	2.84428		1.0916	1.0910	1.0854	1.0789	1.0726	1.0670	1.0620

TABLE II

DISTRIBUTION SHAPES

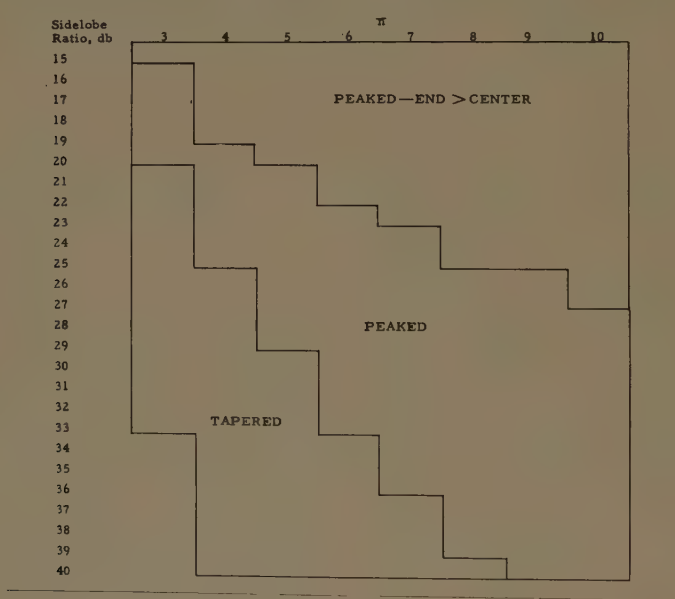

Now from Tables I and II, a good choice of $\bar{n}$ is 4. So

$$\frac{2a}{\lambda} = 20.18 \times 1.134 = 22.9$$

and an aperture diameter of 23 wavelengths is required. Plots of the aperture distribution and of the far field pattern, plotted in z, are given in Fig. 4.

The Taylor distributions may be compared with commonly used $(1-\rho^2)^N$ distributions[3] (see Table IV). Here the beamwidths given are standard beamwidths (for a one-wavelength source) in radians. It is apparent that the Taylor distributions offer a significant beamwidth reduction for a given sidelobe level or, conversely, a significant sidelobe reduction for a given beamwidth.

[3] S. Silver, "Microwave Antenna Theory and Design," M.I.T. Rad. Lab. Ser., McGraw-Hill Book Co., Inc., New York, N. Y., vol. 12, p. 195; 1949.

TABLE III

APERTURE DISTRIBUTIONS

$g(p, A, \bar{n})$ for 25 db sidelobe level

k	$\bar{n}=3$	$\bar{n}=4$	$\bar{n}=5$	$\bar{n}=6$	k	$\bar{n}=7$	$\bar{n}=8$	$\bar{n}=9$	$\bar{n}=10$
0	0.36063	0.33057	0.33889	0.30780	0	0.32293	0.29429	0.31251	0.28546
1	0.35908	0.33046	0.33615	0.30936	1	0.31857	0.29778	0.30630	0.29114
2	0.35448	0.32990	0.32868	0.31243	2	0.30844	0.30347	0.29483	0.29786
3	0.34699	0.32819	0.31847	0.31329	3	0.29874	0.30270	0.28924	0.29244
4	0.33686	0.32441	0.30786	0.30862	4	0.29329	0.29297	0.28900	0.28061
5	0.32441	0.31761	0.29845	0.29777	5	0.29021	0.28045	0.28399	0.27480
6	0.31004	0.30716	0.29043	0.28328	6	0.28401	0.27201	0.27059	0.27154
7	0.29420	0.29287	0.28245	0.26914	7	0.27113	0.26663	0.25695	0.25973
8	0.27735	0.27519	0.27223	0.25796	8	0.25370	0.25698	0.24939	0.24310
9	0.25998	0.25514	0.25766	0.24895	9	0.23775	0.23950	0.24153	0.23334
10	0.24258	0.23419	0.23796	0.23816	10	0.22708	0.22022	0.22447	0.22620
11	0.22559	0.21398	0.21432	0.22111	11	0.21856	0.20772	0.20305	0.20819
12	0.20943	0.19607	0.18984	0.19633	12	0.20383	0.20070	0.19047	0.18528
13	0.19448	0.18162	0.16871	0.16752	13	0.17714	0.18611	0.18518	0.17583
14	0.18104	0.17124	0.15478	0.14286	14	0.14308	0.15375	0.16591	0.17068
15	0.16938	0.16488	0.15027	0.13135	15	0.11694	0.11358	0.12166	0.13628
16	0.15968	0.16195	0.15485	0.13805	16	0.11588	0.09509	0.08151	0.07862
17	0.15209	0.16141	0.16570	0.16088	17	0.14629	0.12389	0.09701	0.06963
18	0.14666	0.16210	0.17835	0.19077	18	0.19682	0.19498	0.18478	0.16623
19	0.14344	0.16298	0.18816	0.21541	19	0.24302	0.26935	0.29361	0.31510
20	0.14238	0.16335	0.19180	0.22481	20	0.26143	0.30063	0.34238	0.38688

$g(p, A, \bar{n})$ for 30 db sidelobe level

k	$\bar{n}=3$	$\bar{n}=4$	$\bar{n}=5$	$\bar{n}=6$	k	$\bar{n}=7$	$\bar{n}=8$	$\bar{n}=9$	$\bar{n}=10$
0	0.41139	0.39967	0.39892	0.37942	0	0.38363	0.36543	0.37280	0.35611
1	0.40974	0.39847	0.39661	0.37926	1	0.38048	0.36644	0.36862	0.35833
2	0.40483	0.39480	0.39006	0.37798	2	0.37254	0.36695	0.35995	0.35949
3	0.39672	0.38849	0.38025	0.37378	3	0.36307	0.36235	0.35280	0.35256
4	0.38552	0.37932	0.36834	0.36508	4	0.35412	0.35135	0.34701	0.34066
5	0.37139	0.36707	0.35524	0.35165	5	0.34489	0.33734	0.33726	0.33059
6	0.35458	0.35169	0.34123	0.33489	6	0.33269	0.32416	0.32170	0.32064
7	0.33538	0.33328	0.32595	0.31697	7	0.31584	0.31151	0.30482	0.30499
8	0.31419	0.31221	0.30856	0.29946	8	0.29557	0.29568	0.29024	0.28576
9	0.29146	0.28909	0.28833	0.28226	9	0.27519	0.27488	0.27480	0.26945
10	0.26773	0.26471	0.26507	0.26369	10	0.25691	0.25241	0.25389	0.25402
11	0.24361	0.24001	0.23947	0.24175	11	0.23949	0.23310	0.23018	0.23244
12	0.21974	0.21595	0.21315	0.21581	12	0.21892	0.21671	0.21095	0.20796
13	0.19680	0.19342	0.18824	0.18777	13	0.19238	0.19669	0.19583	0.19067
14	0.17546	0.17316	0.16688	0.16176	14	0.16218	0.16773	0.17390	0.17621
15	0.15633	0.15572	0.15056	0.14251	15	0.13611	0.13481	0.13925	0.14695
16	0.13999	0.14143	0.13973	0.13304	16	0.12316	0.11326	0.10685	0.10573
17	0.12689	0.13044	0.13378	0.13307	17	0.12726	0.11690	0.10397	0.09040
18	0.11738	0.12273	0.13130	0.13899	18	0.14366	0.14426	0.14032	0.13180
19	0.11166	0.11821	0.13066	0.14554	19	0.16106	0.17646	0.19066	0.20350
20	0.10977	0.11674	0.13061	0.14827	20	0.16831	0.19045	0.21382	0.23888

$g(p, A, \bar{n})$ for 35 db sidelobe level

k	$\bar{n}=4$	$\bar{n}=5$	$\bar{n}=6$	$\bar{n}=7$	k	$\bar{n}=8$	$\bar{n}=9$	$\bar{n}=10$
0	0.46024	0.45750	0.44562	0.44456	0	0.43248	0.43396	0.42295
1	0.45821	0.45511	0.44421	0.44174	1	0.43181	0.43058	0.42301
2	0.45212	0.44813	0.43968	0.43406	2	0.42852	0.42253	0.42029
3	0.44211	0.43704	0.43127	0.42323	3	0.42034	0.41310	0.41111
4	0.42832	0.42249	0.41840	0.41043	4	0.40671	0.40237	0.39726
5	0.41100	0.40508	0.40116	0.39548	5	0.38956	0.38768	0.38251
6	0.39046	0.38524	0.38043	0.37728	6	0.37109	0.36821	0.36622
7	0.36706	0.36316	0.35751	0.35525	7	0.35145	0.34658	0.34551
8	0.34124	0.33888	0.33348	0.33026	8	0.32904	0.32504	0.32175
9	0.31353	0.31245	0.30869	0.30426	9	0.30319	0.30227	0.29867
10	0.28452	0.28413	0.28275	0.27874	10	0.27588	0.27609	0.27558
11	0.25488	0.25450	0.25507	0.25350	11	0.24991	0.24810	0.24900
12	0.22537	0.22451	0.22562	0.22691	12	0.22559	0.22246	0.22085
13	0.19679	0.19536	0.19547	0.19780	13	0.19995	0.19946	0.19679
14	0.16998	0.16836	0.16674	0.16739	14	0.17043	0.17375	0.17500
15	0.14576	0.14463	0.14195	0.13963	15	0.13956	0.14223	0.14645
16	0.12491	0.12501	0.12304	0.11924	16	0.11515	0.11251	0.11243
17	0.10808	0.10991	0.11057	0.10883	17	0.10466	0.09886	0.09260
18	0.09580	0.09938	0.10369	0.10699	18	0.10833	0.10728	0.10378
19	0.08837	0.09326	0.10067	0.10915	19	0.11786	0.12620	0.13380
20	0.08592	0.09128	0.09988	0.11052	20	0.12258	0.13565	0.14959

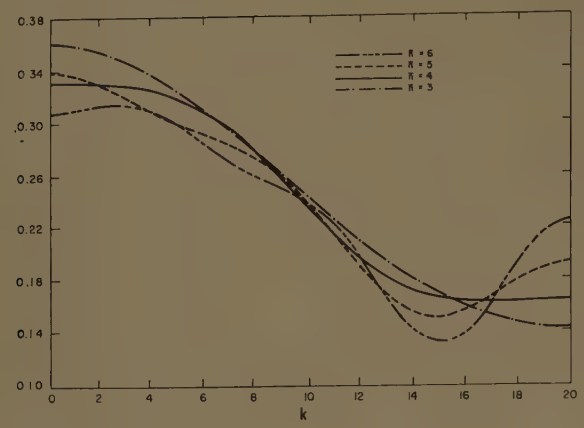

Fig. 1—Aperture distribution for 25-db sidelobes.

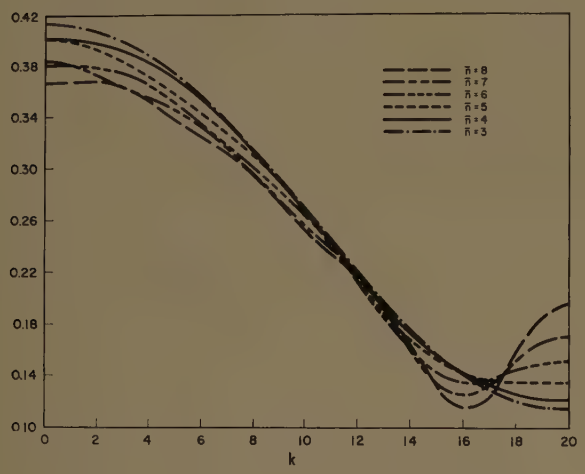

Fig. 2—Aperture distribution for 30-db sidelobes.

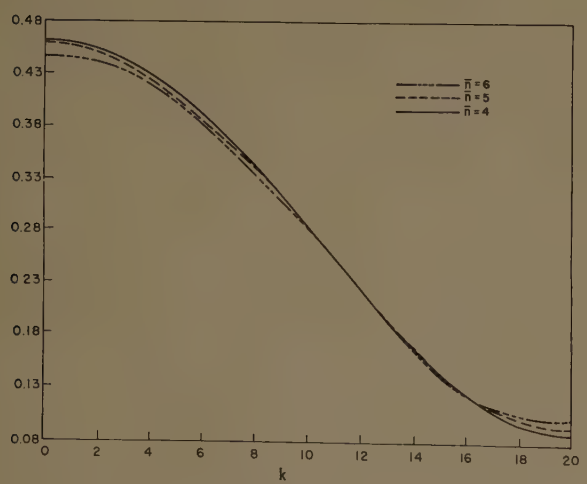

Fig. 3—Aperture distribution for 35-db sidelobes.

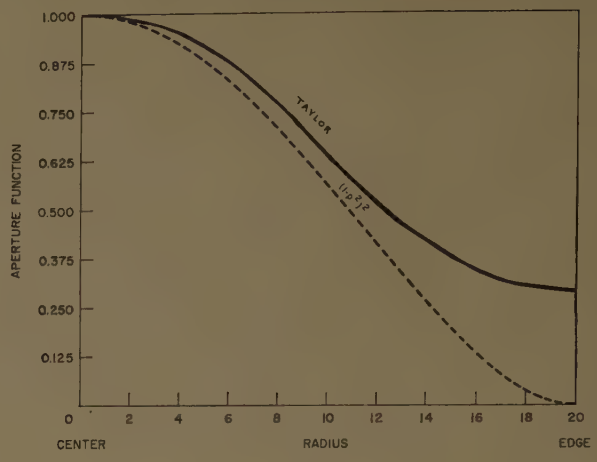

(a)

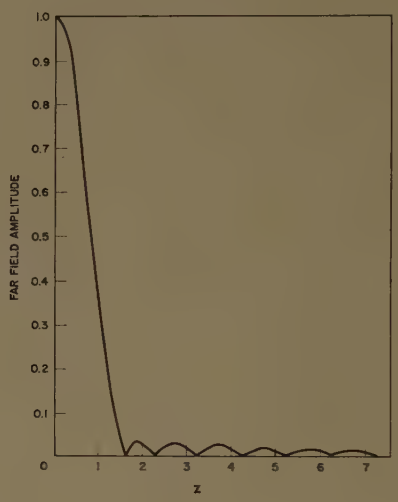

(b)

Fig. 4—Aperture and pattern plots for 30-db case.

TABLE IV

COMPARATIVE BEAMWIDTHS

Taylor			$(1-\rho^2)^N$		
Sidelobe level, db	$\bar{n}$	$\beta\sigma$	Sidelobe level, db	N	Beamwidth
25	4	$1.13\ \lambda/2a$	24.6	1	$1.27\ \lambda/2a$
30	4	$1.20\ \lambda/2a$	30.6	2	$1.47\ \lambda/2a$
35	5	$1.25\ \lambda/2a$	36.0	3	$1.65\ \lambda/2a$
40	5	$1.31\ \lambda/2a$	40.9	4	$1.81\ \lambda/2a$

ACKNOWLEDGMENT

Examples were computed by Mrs. Elaine Walden. IBM programming was performed by Miss Letha Franse.

High-Frequency Diffraction of Electromagnetic Waves by a Circular Aperture in an Infinite Plane Conducting Screen*

S. R. SESHADRI† AND T. T. WU†

Summary—**The scattering of plane electromagnetic wave of wave number k by a circular aperture of radius a in an infinitely conducting plane screen of zero thickness and infinite extent is considered. In the limit of large ka and at normal incidence, the ratio of the transmission cross section to the geometrical optical value πa^2, is found up to the order $(ka)^{-5/2}$.**

Introduction

An exact solution of the problem of diffraction of electromagnetic waves by a circular aperture in an infinite perfectly conducting plane screen was obtained by Meixner and Andrejewski.[1] Although their method is valid for all frequencies, their solution in the form of a series expression converges slowly. This makes numerical computation laborious. Frahn[2] used, in the study of this problem, Braunbek's idea that in the high-frequency region the current on the shadow side of the screen vanishes everywhere except in a very small zone near the rim, and that the tangential electric field in the aperture is identical to the incident electric field except in a very small region near the rim. Levine and Schwinger[3] used a variational method in the study of the aperture diffraction problem and have obtained an approximate formula for the transmission coefficient of a circular aperture for normally incident plane waves. Using the variational principles of Levine and Schwinger, Chang[4] has obtained two different expressions for the transmission coefficient of a large circular aperture for normally incident plane waves. Recently Millar[5] has treated the aperture problem by assuming the aperture to be the envelope of a system of perfectly conducting half-planes lying in the plane of the screen. He obtained an expression for the transmission coefficient which is identical to one of Chang's approximations to the order of $(ka)^{-3/2}$. Furthermore he assumed that the next correction term is of the form $(ka)^{-2}$ in the normal incidence transmission coefficient of a circular aperture, and estimated by numerical means the coefficient of the $(ka)^{-2}$ term by comparing the results of the semi-empirical transmission coefficient with the results of the exact theory. Millar's result is in closer agreement with the results of the exact theory than those of Frahn, Levine and Schwinger, and Chang. In this report, employing the general technique used by Levine and Wu,[6] for the high-frequency diffraction of scalar waves by a circular aperture, the first few terms in the asymptotic expansion of the transmission coefficient of a circular aperture in a plane conducting screen are calculated directly from the integral equation without employing any numerical procedure.

The formulation is based on the integral equation for the current induced on the shadow side of the screen. In this formulation the geometrical optics part separates out in a natural way in the expression for the transmission coefficient. Two simultaneous integral equations are obtained for the two components of the current on the shadow side of the screen. The radial and the angular components of the current have simple dependencies on the angle variable and the integrals occurring in the kernels of the integral equations are approximated by an asymptotic evaluation with respect to the angle variable. The resulting simultaneous integral equations for the components of the current involve only the radial coordinate and are solved by an iterative procedure.

Integral Equation Formulation of the Problem

Consider an infinitesimally thin, perfectly conducting plane screen S, of infinite extent, which is perforated by a circular aperture A of radius a. A rectangular coordinate system is chosen whose origin is at the center of the aperture and which is oriented so that the screen lies in the xy plane (Fig. 1). The position vector of a point $P(x, y, z)$ in space will be denoted by $\boldsymbol{r}$ while the position vector of a point $P(x, y, 0)$ in the xy plane will be denoted by $\boldsymbol{\rho}$.

A plane electromagnetic wave is incident normally on the aperture in the half-space $z<0$. The coordinate system is chosen such that

$$E^{\text{inc}}(\boldsymbol{r}) = \hat{x}e^{ikz}$$

$$H^{\text{inc}}(\boldsymbol{r}) = \hat{y}\left(\frac{\epsilon}{\mu}\right)^{1/2} e^{ikz} \tag{1}$$

* Manuscript received by the PGAP, November 1, 1958. This research was supported in part by the U. S. Air Force under contract with Harvard University. This work was carried out while Dr. Wu was Junior Fellow of the Society of Fellows, Harvard University.

† Gordon McKay Lab. of Applied Science, Harvard University, Cambridge, Mass.

[1] J. Meixner and W. Andrejewski, "Strenge Theorie der Beugung ebener elektromagnetischer Wellen an der vollkommen leitenden Kreisscheibe und an der kreisformigen Offnung im vollkommen leitenden ebenen Schirm," *Ann. Phys.*, vol. 7, pp. 157–168; April, 1950.

[2] W. Frahn, "Die Anwendung des Braundek' schen Naherungsverfahrens auf die Beugung electromagnetischer wellen an der Dreisformigen Offnung im wollkemmen leitenden ebenen schrim und an der vollkimmen leitenden Kreisscheibe," Diplomarbeit, Rheinisch-Westfalische Technische Hochschule, Aachen, Germany, 1951. Unpublished.

[3] H. Levine and J. Schwinger, "On the theory of electromagnetic wave diffraction by an aperture in an infinite plane conducting screen," *Commun. Pure Appl. Math.*, vol. 3, pp. 355–391; December, 1950.

[4] H. H. C. Chang, "On the Diffraction of Electromagnetic Waves by a Circular Aperture," Cruft Lab., Harvard University, Cambridge, Mass., Sci. Rept. No. 2; 1955 (unpublished).

[5] R. F. Millar, "The diffraction of an electromagnetic wave by a circular aperture," *Proc. IEE (London)*, Monograph No. 196R; 1956.

[6] H. Levine and T. T. Wu, "Diffraction by an Aperture at High Frequencies," Appl. Math. and Statistics Lab., Stanford University, Stanford, Calif., Tech. Rept. No. 71; 1957 (unpublished).

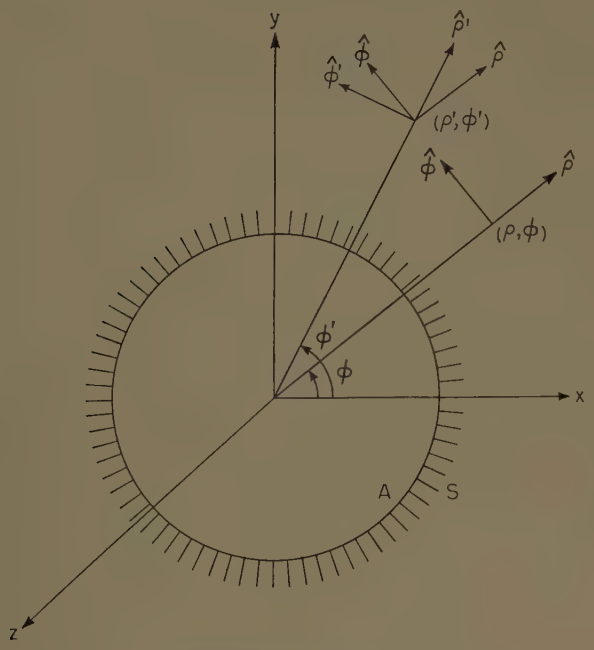

Fig. 1—Coordinate system for the diffraction by a circular aperture.

where k is the wave number and the harmonic time dependence $e^{-i\omega t}$ is omitted throughout. In polar coordinates the incident wave is described by

$$E_\rho^{\text{inc}}(\rho, \phi, z) = E_{\rho 0} \cos\phi \qquad H_\rho^{\text{inc}}(\rho, \phi, z) = H_{\rho 0} \sin\phi$$
$$E_\phi^{\text{inc}}(\rho, \phi, z) = E_{\phi 0} \sin\phi \qquad H_\phi^{\text{inc}}(\rho, \phi, z) = H_{\phi 0} \cos\phi \tag{2}$$

where

$$E_{\rho 0} = -E_{\phi 0} = e^{ikz} \qquad H_{\rho 0} = H_{\phi 0} = \left(\frac{\epsilon}{\mu}\right)^{1/2} e^{ikz}. \tag{3}$$

The total electric and magnetic fields satisfy the free space Maxwell's equations subject to the boundary condition

$$E_\phi(\varrho) = E_\rho(\varrho) = 0 \qquad \varrho \text{ on the screen.} \tag{4}$$

The electric and magnetic fields vary continuously through the aperture.

From the Maxwell's equations (3) it follows that the total electric and magnetic fields are of the form

$$E_\rho(\rho, \phi, z) = E_{\rho 0} \cos\phi \qquad H_\rho(\rho, \phi, z) = H_{\rho 0} \sin\phi$$
$$E_\phi(\rho, \phi, z) = E_{\phi 0} \sin\phi \qquad H_\phi(\rho, \phi, z) = H_{\phi 0} \cos\phi$$
$$E_z(\rho, \phi, z) = E_{z 0} \cos\phi \qquad H_z(\rho, \phi, z) = H_{z 0} \sin\phi,$$

and the components of the total surface current density $J = \hat{n} \times H$ are therefore of the form

$$J_\rho(\rho, \phi) = J_{\rho 0} \cos\phi$$
$$J_\phi(\rho, \phi) = J_{\phi 0} \sin\phi \tag{6}$$

where $E_{\rho 0}$, $E_{\phi 0}$, $E_{z 0}$, $H_{\rho 0}$, $H_{\phi 0}$, $H_{z 0}$, $J_{\rho 0}$ and $J_{\phi 0}$ are functions independent of ϕ.

Define the surface current on the illuminated side of the screen $z = 0^-$ as J^-, and that on the shadow side of the screen $z = 0^+$ an J^+. Denote their sum as

$$J = J^+ + J^-. \tag{7}$$

In the absence of the aperture, it is obvious that

$$J^+ = 0$$
$$J^- = 2\left(\frac{\epsilon}{\mu}\right)^{1/2} x = J^0 \tag{8}$$

and thus, by (6),

$$J_{\rho 0}{}^0 = 2\left(\frac{\epsilon}{\mu}\right)^{1/2}$$
$$J_{\phi 0}{}^0 = -2\left(\frac{\epsilon}{\mu}\right)^{1/2}. \tag{9}$$

In the presence of the aperture, J^+ and J^- have different values from that given in (8). It is convenient to introduce

$$J^{-\prime} = J^- - J^0$$
$$J' = J^+ + J^{-\prime}. \tag{10}$$

Since $J = 0$ in the aperture, it follows that

$$J' = -J^0 \tag{11}$$

for $\rho < a$.

The total electromagnetic field is decomposed into the incident fields, $\boldsymbol{E}^{\text{inc}}(r)$ and $\boldsymbol{H}^{\text{inc}}(r)$; the specularly reflected fields, $\boldsymbol{E}^{\text{ref}}(r)$ and $\boldsymbol{H}^{\text{ref}}(r)$, due to the reflected wave which would result if the screen were complete; and the diffracted fields, $\boldsymbol{E}^{\text{dif}}(r)$ and $\boldsymbol{H}^{\text{dif}}(r)$, due to the presence of the aperture

$$\begin{aligned} \boldsymbol{E}(r) &= \boldsymbol{E}^{\text{inc}}(r) + \boldsymbol{E}^{\text{ref}}(r) + \boldsymbol{E}^{\text{dif}}(r) \\ \boldsymbol{H}(r) &= \boldsymbol{H}^{\text{inc}}(r) + \boldsymbol{H}^{\text{ref}}(r) + \boldsymbol{H}^{\text{dif}}(r) \qquad z < 0 \\ \boldsymbol{E}(r) &= \boldsymbol{E}^{\text{dif}}(r) \\ \boldsymbol{H}(r) &= \boldsymbol{H}^{\text{dif}}(r) \qquad z > 0. \end{aligned} \tag{12}$$

The entire diffracted field is due to J' and can be derived from the vector potential

$$\boldsymbol{A}^{\text{dif}}(r) = \frac{\mu}{4\pi} \int_{S+A} J'(\varrho') \frac{\exp\left[ik \left| r - \varrho' \right|\right]}{\left| r - \varrho' \right|} dS'. \tag{13}$$

$\boldsymbol{A}^{\text{dif}}(r)$ satisfies the equation

$$(\nabla^2 + k^2)\boldsymbol{A}^{\text{dif}}(r) = 0 \tag{14}$$

everywhere except at $z = 0$. The diffracted fields are obtained through the use of the formulas

$$\boldsymbol{H}^{\text{dif}}(r) = \frac{1}{\mu} \nabla \times \boldsymbol{A}^{\text{dif}} \tag{15a}$$

$$\boldsymbol{E}^{\text{dif}}(r) = \frac{i}{\omega\mu\epsilon} \nabla \times \nabla \times \boldsymbol{A}^{\text{dif}}. \tag{15b}$$

Because of symmetry, the vector potentials $\boldsymbol{A}^{\text{dif}}$ are identical at the corresponding points in the half-spaces

$z<0$ and $z>0$. It follows from (15a) that the perpendicular components of H^{dif} are equal and in the same direction whereas the tangential components are equal and in opposite directions. On the planes $z=0^{\pm}$, the unit vectors $\hat{n}$ are oppositely directed and hence the currents are identical:

$$J^{+} = J^{-\prime} \tag{16}$$

so that

$$J' = 2J^{+} = 2J^{-\prime}. \tag{17}$$

The electric field at any point (ρ, ϕ) on the screen is obtained from (15b) using (13). With (14) it is given by

$$\begin{aligned} \boldsymbol{E}^{\text{dif}}(\rho, \phi) &= \frac{i}{4\pi\omega\epsilon}\int_{S+A} [\nabla\nabla\cdot + k^2] \\ &\quad J'(\rho', \phi') \frac{\exp\,[ik\,|\,\varrho - \varrho'\,|\,]}{|\,\varrho - \varrho'\,|}\cdot dS' \\ &= \frac{i}{4\pi\omega\epsilon}\int_{S+A} [J'(\rho', \phi')\cdot\nabla \\ &\quad + k^2 J'(\rho', \phi')] \frac{\exp\,[ik\,|\,\varrho - \varrho'\,|\,]}{|\,\varrho - \varrho'\,|}\cdot dS' \end{aligned} \tag{18}$$

Here it is to be understood that the differentiations with respect to ρ and ϕ, should be carried out after the integration with respect to ρ' and ϕ', even though ∇ is written under the integral sign. It follows that the ρ and ϕ components of the electric field at (ρ, ϕ) are

$$\begin{aligned} \boldsymbol{E}_{\rho}^{\text{dif}}(\rho, \phi) &= \frac{i}{2\pi\omega\epsilon}\int_0^{\infty} \rho' d\rho' \int_{-\pi}^{\pi} d\phi' \\ &\quad \cdot\Big[J_{\rho'0}^{+} \cos(\phi' - \phi) \cos\phi' \frac{\partial^2}{\partial_{\rho}^{\,2}} \\ &\quad + \frac{J_{\rho'0}^{+}}{\rho} \sin(\phi' - \phi) \cos\phi' \frac{\partial^2}{\partial\phi\partial\rho} \\ &\quad - \frac{J_{\rho'0}^{+}}{\rho^2} \sin(\phi' - \phi) \cos\phi' \frac{\partial}{\partial\phi} \\ &\quad + k^2 J_{\rho'0}^{+} \cos(\phi' - \phi) \cos\phi' \\ &\quad - J_{\phi'0}^{+} \sin(\phi' - \phi) \sin\phi' \frac{\partial^2}{\partial\rho^2} \\ &\quad + \frac{J_{\phi'0}^{+}}{\rho} \cos(\phi' - \phi) \sin\phi' \frac{\partial^2}{\partial\rho\partial\phi} \\ &\quad - \frac{J_{\phi'0}^{+}}{\rho^2} \cos(\phi' - \phi) \sin\phi' \frac{\partial}{\partial\phi} \\ &\quad - k^2 J_{\phi'0}^{+} \sin(\phi' - \phi) \sin\phi' \Big] \\ &\quad \frac{\exp\,[ik\,|\,\varrho - \varrho'\,|\,]}{|\,\varrho - \varrho'\,|} \end{aligned} \tag{19}$$

and

$$\begin{aligned} \boldsymbol{E}_{\phi}^{\text{dif}}(\rho, \phi) &= \frac{i}{2\pi\omega\epsilon}\int_0^{\infty} \rho' d\rho' \int_{-\pi}^{\pi} d\phi' \\ &\quad \cdot\Big[J_{\rho'0}^{+} \cos(\phi' - \phi) \cos\phi' \frac{\partial}{\partial\rho} \frac{1}{\rho} \frac{\partial}{\partial\phi} \\ &\quad + \frac{J_{\rho'0}^{+}}{\rho} \sin(\phi' - \phi) \cos\phi' \frac{\partial}{\partial\rho} \\ &\quad + \frac{J_{\rho'0}^{+}}{\rho^2} \sin(\phi' - \phi) \cos\phi' \frac{\partial^2}{\partial\phi^2} \\ &\quad + k^2 J_{\rho'0}^{+} \sin(\phi' - \phi) \cos\phi' \\ &\quad - J_{\phi'0}^{+} \sin(\phi' - \phi) \sin\phi' \frac{\partial}{\partial\rho} \frac{1}{\rho} \frac{\partial}{\partial\phi} \\ &\quad + \frac{J_{\phi'0}^{+}}{\rho} \cos(\phi' - \phi) \sin\phi' \frac{\partial}{\partial\rho} \\ &\quad + \frac{J_{\phi'0}^{+}}{\rho^2} \cos(\phi' - \phi) \sin\phi' \frac{\partial^2}{\partial\phi^2} \\ &\quad + k^2 J_{\phi'0}^{+} \cos(\phi' - \phi) \sin\phi' \Big] \\ &\quad \cdot\frac{\exp\,[ik\,|\,\varrho - \varrho'\,|\,]}{|\,\varrho - \varrho'\,|}\cdot \end{aligned} \tag{20}$$

It is useful to define

$$A(\rho, \rho') = \int_{-\pi}^{\pi} d\phi' \cos^2\phi' \frac{\exp\,[ik(\rho^2 + \rho'^2 - 2\rho\rho'\cos\phi')^{1/2}]}{(\rho^2 + \rho'^2 - 2\rho\rho'\cos\phi')^{1/2}}$$

and

$$B(\rho, \rho') = \int_{-\pi}^{\pi} d\phi' \sin^2\phi' \frac{\exp\,[ik(\rho^2 + \rho'^2 - 2\rho\rho'\cos\phi')^{1/2}]}{(\rho^2 + \rho'^2 - 2\rho\rho'\cos\phi')^{1/2}}\cdot \tag{21}$$

Then

$$\begin{aligned} E_{\rho}^{\text{dif}}(\rho, \phi) &= \frac{i\cos\phi}{2\pi\omega\epsilon}\int_0^{\infty} \rho' d\rho' \\ &\quad \cdot\Big[\Big\{ J_{\rho'0}^{+}\Big(\frac{\partial^2}{\partial_{\rho}^{\,2}} + \frac{1}{\rho}\frac{\partial}{\partial\rho} - \frac{1}{\rho^2} + k^2\Big) \\ &\quad + J_{\phi'0}^{+}\Big(\frac{1}{\rho}\frac{\partial}{\partial\rho} - \frac{1}{\rho^2}\Big)\Big\} A(\rho, \rho') \\ &\quad - \Big\{ J_{\rho'0}^{+}\Big(\frac{1}{\rho}\frac{\partial}{\partial\rho} - \frac{1}{\rho^2}\Big) \\ &\quad + J_{\phi'0}^{+}\Big(\frac{\partial^2}{\partial_{\rho}^{\,2}} + \frac{1}{\rho}\frac{\partial}{\partial\rho} \\ &\quad - \frac{1}{\rho^2} + k^2\Big)\Big\} B(\rho, \rho')\Big] \end{aligned} \tag{22}$$

and

$$E_\phi^{\text{dif}}(\rho,\phi)=\frac{i\sin\phi}{2\pi\omega\epsilon}\int_0^\infty \rho' d\rho'\Big[-\Big\{J_{\rho'0}^{+}\Big(\frac{1}{\rho}\frac{\partial}{\partial\rho}+\frac{1}{\rho^2}\Big)\Big\}+J_{\phi 0}^{+}\Big(\frac{1}{\rho^2}-k^2\Big)\Big\}A(\rho,\rho')+\Big\{J_{\rho'0}^{+}\Big(\frac{1}{\rho^2}-k^2\Big)+J_{\phi'0}^{+}\cdot\Big(\frac{1}{\rho}\frac{\partial}{\partial\rho}+\frac{1}{\rho^2}\Big)\Big\}B(\rho,\rho')\Big]. \quad (23)$$

The use of the boundary condition that the tangential electric field vanish on the screen, *i.e.*, $E_\rho^{\text{dif}}(\rho,\phi)=E_\phi^{\text{dif}}(\rho,\phi)=0$ for $\rho>a$, in (22) and (23) results in the following simultaneous integral equations for the two components of the current on the shadow side of the screen. They are valid for $\rho>a$.

$$\int_0^\infty \rho' d\rho'\Big[\Big\{J_{\rho'0}^{+}\Big(\frac{\partial^2}{\partial\rho^2}+\frac{1}{\rho}\frac{\partial}{\partial\rho}-\frac{1}{\rho^2}+k^2\Big)+J_{\phi'0}^{+}\Big(\frac{1}{\rho}\frac{\partial}{\partial\rho}-\frac{1}{\rho^2}\Big)\Big\}A(\rho,\rho')-\Big\{J_{\rho'0}^{+}\Big(\frac{1}{\rho}\frac{\partial}{\partial\rho}-\frac{1}{\rho^2}\Big)+J_{\phi 0}^{+}\Big(\frac{\partial^2}{\partial\rho^2}+\frac{1}{\rho}\frac{\partial}{\partial\rho}-\frac{1}{\rho^2}+k^2\Big)\Big\}B(\rho,\rho')\Big]=0 \quad (24)$$

and

$$\int_0^\infty \rho' d\rho'\Big[-\Big\{J_{\rho'0}^{+}\Big(\frac{1}{\rho}\frac{\partial}{\partial\rho}+\frac{1}{\rho^2}\Big)+J_{\phi 0}^{+}\Big(\frac{1}{\rho^2}-k^2\Big)\Big\}A(\rho,\rho')+\Big\{J_{\rho'0}^{+}\Big(\frac{1}{\rho^2}-k^2\Big)+J_{\phi'0}^{+}\Big(\frac{1}{\rho}\frac{\partial}{\partial\rho}+\frac{1}{\rho^2}\Big)\Big\}B(\rho,\rho')\Big]=0. \quad (25)$$

The following values of $J_{\rho'0}^{+}$ and $J_{\phi\,0}^{+}$ in the aperture are obtained by combining (9) and (11):

$$J_{\rho'0}^{+}=-\Big(\frac{\epsilon}{\mu}\Big)^{1/2}$$

$$J_{\phi 0}^{+}=\Big(\frac{\epsilon}{\mu}\Big)^{1/2} \quad (26)$$

for $0<\rho'<a$.

Reduction of the Integral Equation for High Frequencies

It is desired to obtain an approximate solution of (24) and (25) for large values of ka. In this case, the significant regions for the integral equation are near the rim of the aperture. With a fixed vector ϱ for the point of observation on the screen, significant contributions to the integrals $A(\rho,\rho')$ and $B(\rho,\rho')$ in (24) and (25) correspond to two stationary values of ϕ', namely 0 and π.

In order to obtain the contribution to the integral

$$A(\rho,\rho')=\int d\phi'\cos^2\phi'\frac{\exp\,[ik(\rho^2+\rho'^2-2\rho\rho'\cos\phi')^{1/2}]}{(\rho^2+\rho'^2-2\rho\rho'\cos\phi')^{1/2}} \quad (27)$$

for ϕ' near 0, let the following variable be introduced:

$$\zeta=2\sin\frac{\phi'}{2}\qquad d\zeta=\Big(1-\frac{\zeta^2}{4}\Big)^{1/2}d\phi'. \quad (28)$$

The result of substitution is

$$A(\rho,\rho')=\int d\zeta\Big(1-\frac{\zeta^2}{2}\Big)^2\Big(1-\frac{\zeta^2}{4}\Big)^{-1/2}\cdot\frac{\exp\,[ik((\rho-\rho')^2+\rho\rho'\zeta^2)^{1/2}]}{[(\rho-\rho')^2+\rho\rho'\zeta^2]^{1/2}}. \quad (29)$$

After expanding the term

$$\Big(1-\frac{\zeta^2}{2}\Big)^2\Big(1-\frac{\zeta^2}{4}\Big)^{-1/2}$$

in a power series, taking infinite limits of integration and introducing the new variable

$$\zeta'=\frac{(\rho-\rho')^{1/2}}{|\rho-\rho'|}\zeta,$$

the contribution to the integral (29) from the neighborhood of $\phi'=0$ is

$$A_0(\rho,\rho')=\frac{1}{\sqrt{\rho\rho'}}\int_{-\infty}^{\infty}\Big[1-\frac{7}{8}\frac{|\rho-\rho'|^2}{\rho\rho'}\zeta'^2\cdots\Big]\cdot\frac{\exp\,[ik|\rho-\rho'|(1+\zeta'^2)^{1/2}]}{(1+\zeta'^2)^{1/2}}d\zeta'. \quad (30)$$

Since

$$H_0^{(1)}(kx)=-\frac{i}{\pi}\int_{-\infty}^{\infty}d\zeta'\frac{\exp\,[ikx(1+\zeta'^2)^{1/2}]}{(1+\zeta'^2)^{1/2}} \quad (31)$$

(30) becomes

$$A_0 = \frac{\pi i}{\sqrt{\rho\rho'}} H_0^{(1)}(k|\rho-\rho'|) + \frac{7\pi i}{8(\rho\rho')^{3/2}}\left[(|\rho-\rho'|)^2 H_0^{(1)}(k|\rho-\rho'|) + \frac{\partial^2}{\partial k^2} H_0^{(1)}(k|\rho-\rho'|)\right]. \quad (32)$$

Let the radial coordinates be referred to the rim of the aperture at $\rho=a$ by introducing the new variable x,

$$\rho = a + x \qquad \rho' = a + x'. \quad (33)$$

It follows from (32) that to the first order in x, x'

$$A_0 = \frac{\pi i}{a}\left[1 - \frac{x+x'}{2a}\right] H_0^{(1)}(k|x-x'|). \quad (34)$$

In order to get the contribution of (27) near $\phi'=\pi$, $\phi'=\pi+\phi$ is substituted. Thus,

$$A_\pi(\rho,\rho') = \int_0 d\phi \cos^2\phi \cdot \frac{\exp\left[ik\left((\rho+\rho')^2 - 4\rho\rho'\sin^2\frac{\phi}{2}\right)^{1/2}\right]}{\left[(\rho+\rho')^2 - 4\rho\rho'\sin^2\frac{\phi}{2}\right]^{1/2}}. \quad (35)$$

If $\cos^2\phi$ and

$$\left[(\rho+\rho')^2 - 4\rho\rho'\sin^2\frac{\phi}{2}\right]^{1/2}$$

are expanded in power series in ϕ and infinite limits of integration are taken, the value of the integral (35) near $\phi'=\pi$ becomes

$$A_\pi = \frac{e^{ik(\rho+\rho')}}{(\rho+\rho')}\int_{-\infty}^{\infty}\exp\left[-\frac{ik\rho\rho'\phi^2}{2(\rho+\rho')}\right]\cdot\left[1-\phi^2\left(1-\frac{\rho\rho'}{2(\rho+\rho')^2}\right)\cdots\right]d\phi$$

$$= \left[\frac{2\pi}{k\rho\rho'(\rho+\rho')}\right]^{1/2}\exp\left[ik(\rho+\rho') - i\frac{\pi}{4}\right]\cdot\left[1+\frac{i}{k}\left(\frac{\rho+\rho'}{\rho\rho'} - \frac{1}{2(\rho+\rho')}\right)+\cdots\right]. \quad (36)$$

If (33) is used in (36), it follows that to the first order in x, x'

$$A_\pi = \frac{\pi\alpha}{a}\exp\left[ik(x+x')\right]\left[1+\frac{7i}{4ka} - \frac{3}{4a}x - \frac{3}{4a}x'\right] \quad (37)$$

where

$$\alpha = (\pi ka)^{-1/2}\exp\left[2ika - i\frac{\pi}{4}\right]. \quad (38)$$

The sum of (34) and (37) is

$$A = \frac{\pi i}{a}\left(1 - \frac{x}{2a} - \frac{x'}{2a}\right)H_0^{(1)}(k|x-x'|) + \frac{\pi\alpha}{a}\exp\left[ik(x+x')\right]\left[1+\frac{7i}{4ka} - \frac{3}{4a}x - \frac{3}{4a}x'\right] \quad (39)$$

By a similar procedure, it can be shown that the value of the integral

$$B(\rho,\rho') = \int d\phi' \sin^2\phi' \cdot \frac{\exp\left[ik(\rho^2+\rho'^2-2\rho\rho'\cos\phi')^{1/2}\right]}{(\rho^2+\rho'^2-2\rho\rho'\cos\phi')^{1/2}} \quad (40)$$

near $\phi'=0$, is zero to the first order in x and x', and equals B_π near $\phi'=\pi$, where

$$B = B_\pi = -\frac{\pi\alpha}{a}\cdot\frac{2i}{ka}\exp\left[ik(x+x')\right]. \quad (41)$$

If in the integral equations (24) and (25), the radial coordinates are referred to the rim of the aperture as in (33); the values of A and B are substituted from (39) and (41); the substitution of the newly defined functions

$$F_1(x') = \left(\frac{\mu}{\epsilon}\right)^{1/2}\rho' J_{\rho'0}^{+}$$

$$F_2(x') = \left(\frac{\mu}{\epsilon}\right)^{1/2}\rho' J_{\phi'0}^{+} \quad (42)$$

is made in the range $x'>0$; and the values of $J_{\rho'0}^{+}$ and $J_{\phi'0}^{+}$ as given by (26) are used for $0<\rho'<a$, the following two equations are obtained for $x>0$:

$$\int_0^\infty dx' F_1(x') \left[\frac{\pi i}{a} \left(1 - \frac{x}{2a} - \frac{x'}{2a} \right) \frac{\partial^2}{\partial x^2} H_0^{(1)}(k \mid x - x' \mid) - \frac{\pi i}{2a^3} (x + x') \frac{\partial}{\partial x} H_0^{(1)}(k \mid x - x' \mid) \right.$$

$$\left. + \frac{\pi i}{a} \left(k^2 - \frac{1}{2a^2} - \frac{k^2}{2a} x - \frac{k^2}{2a} x' \right) H_0^{(1)}(k \mid x - x' \mid) + \frac{\pi \alpha}{a} \left(- \frac{ik}{2a} - \frac{5}{2a^2} - \frac{3ik}{4a} x - \frac{3ikx'}{4a} \right) e^{ik(x+x')} \right]$$

$$+ \int_0^\infty dx' F_2(x') \left[\frac{\pi i}{a^2} \left(1 - \frac{x}{2a} - \frac{x'}{2a} \right) \frac{\partial}{\partial x} H_0^{(1)}(k \mid x - x' \mid) - \frac{\pi i}{2a^3} H_0^{(1)}(k \mid x - x' \mid) \right.$$

$$\left. + \frac{\pi \alpha}{a^2} \left(ik - \frac{5}{2a} - \frac{3ik}{4a} x - \frac{3ik}{4a} x' \right) e^{ik(x+x')} \right]$$

$$= \int_{-\infty}^0 dx' \left[\pi i \left(1 - \frac{x}{2a} + \frac{x'}{2a} \right) \frac{\partial^2}{\partial x^2} H_0^{(1)}(k \mid x - x' \mid) - \frac{\pi i}{a} \left(1 + \frac{x'}{a} \right) \frac{\partial}{\partial x} H_0^{(1)}(k \mid x - x' \mid) \right.$$

$$\left. + \pi i k^2 \left(1 - \frac{x}{2a} + \frac{x'}{2a} \right) H_0^{(1)}(k \mid x - x' \mid) - \frac{3\pi \alpha i k}{2a} \left(1 + \frac{x'}{a} \right) e^{ik(x+x')} \right] \tag{43}$$

and

$$\int_0^\infty dx' F_1(x') \left[\frac{\pi i}{a^2} \left(1 - \frac{x}{2a} - \frac{x'}{2a} \right) \frac{\partial}{\partial x} H_0^{(1)}(k \mid x - x' \mid) - \frac{\pi i}{2a^3} H_0^{(1)}(k \mid x - x' \mid) \right.$$

$$\left. - \frac{\pi \alpha}{a^2} \left(ik + \frac{5}{2a} + \frac{3ik}{4a} x + \frac{3ik}{4a} x' \right) e^{ik(x+x')} \right]$$

$$+ \int_0^\infty dx' F_2(x') \left[- \frac{\pi i k^2}{a} \left(1 - \frac{x}{2a} - \frac{x'}{2a} \right) H_0^{(1)}(k \mid x - x' \mid) - \frac{\pi \alpha k^2}{a} \left(1 + \frac{7i}{4ka} - \frac{3x}{4a} - \frac{3x'}{4a} \right) e^{ik(x+x')} \right]$$

$$= \int_{-\infty}^0 dx' \left[\frac{\pi i}{a} \left(1 - \frac{x}{2a} + \frac{x'}{2a} \right) \frac{\partial}{\partial x} H_0^{(1)}(k \mid x - x' \mid) + \pi i \left[k^2 - \frac{1}{2a^2} - \frac{k^2}{2a} x + \left(\frac{k^2}{2a} - \frac{1}{2a^3} \right) x' H_0^{(1)}(k \mid x - x' \mid) \right. \right.$$

$$\left. \left. + \pi \alpha \left\{ k^2 + \frac{3ik}{4a} - \frac{5}{2a^2} - \left(\frac{3k^2}{4a} + \frac{3ik}{4a^2} \right) x + \left(\frac{k^2}{4a} - \frac{5}{2a^3} \right) x' \right\} e^{ik(x+x')} \right] \right]. \tag{44}$$

Fourier-Transform Solution of the Integral Equations

Two functions $R(x)$ and $S(x)$ which are both zero for $x > 0$ are added to the right-hand side of (43) and (44) respectively, in order to extend the range of validity of those equations to all values of x from $-\infty$ to ∞. A complex Fourier transformation is applied to (43) and (44) with respect to x. While taking the transforms of the terms containing the factor $e^{ik(x+x)}$, the integration with respect to x from 0 to ∞ is performed; on the other hand, the contributions of the integrals in the range of x from $-\infty$ to 0 are added to the transforms of $R(x)$ and $S(x)$ to yield, respectively, $\overline{R}(\zeta)$ and $\overline{S}(\zeta)$. The results, if only the first two orders of terms in ka are retained, are (ϵ-Im k)

$$\overline{F}_1(\zeta)(k^2 - \zeta^2)^{1/2} - \frac{i}{a} \overline{F}_1'(\zeta)(k^2 - \zeta^2)^{1/2}$$

$$- \frac{i}{2a} \overline{F}_1(\zeta) \frac{\partial}{\partial \zeta} (k^2 - \zeta^2)^{1/2} - \frac{\alpha i k}{4a} \frac{\overline{F}_1(-k)}{k - \zeta}$$

$$+ \frac{i}{a} \overline{F}_2(\zeta) \frac{\zeta}{(k^2 - \zeta^2)^{1/2}} + \frac{\alpha i k}{2a} \frac{\overline{F}_2(-k)}{k - \zeta}$$

$$= \frac{ai}{\zeta + i\epsilon} (k^2 - \zeta^2)^{1/2} + \frac{1}{2} \frac{1}{\zeta + i\epsilon} \frac{\partial}{\partial \zeta} (k^2 - \zeta^2)^{1/2}$$

$$+ \frac{1}{\zeta + i\epsilon} \frac{\zeta}{(k^2 - \zeta^2)^{1/2}} - \frac{3\alpha}{4} \frac{1}{k - \zeta} + \overline{R}(\zeta), \tag{45}$$

and

$$\frac{\overline{F}_2(\zeta)}{(k^2-\zeta^2)^{1/2}}+\frac{\alpha}{2}\frac{\overline{F}_2(-k)}{k-\zeta}-\frac{i}{ak^2}\overline{F}_1(\zeta)\frac{\zeta}{(k^2-\zeta^2)^{1/2}}$$
$$-\frac{i}{a}\frac{\overline{F}_2'(\zeta)}{(k^2-\zeta^2)^{1/2}}-\frac{i}{2a}\overline{F}_2(\zeta)\frac{\partial}{\partial\zeta}\frac{1}{(k^2-\zeta^2)^{1/2}}$$
$$+\frac{7i\alpha}{8ak}\frac{\overline{F}_2(-k)}{k-\zeta}-\frac{3\alpha i}{8a}\frac{\overline{F}_2'(-k)}{k-\zeta}$$
$$-\frac{3\alpha i}{8a}\frac{\overline{F}_2(-k)}{(k-\zeta)^2}+\frac{\alpha i}{2ak}\frac{\overline{F}_1(-k)}{k-\zeta}$$
$$=-\frac{ai}{\zeta+i\epsilon}\frac{1}{(k^2-\zeta^2)^{1/2}}+\frac{\alpha ia}{2k}\frac{1}{k-\zeta}$$
$$+\frac{1}{k^2}\frac{\zeta}{\zeta+i\epsilon}\frac{1}{(k^2-\zeta^2)^{1/2}}$$
$$-\frac{1}{2}\frac{1}{\zeta+i\epsilon}\frac{\partial}{\partial\zeta}\frac{1}{(k^2-\zeta^2)^{1/2}}$$
$$-\frac{\alpha}{2k^2}\frac{1}{k-\zeta}+\frac{3\alpha}{8k}\frac{1}{(k-\zeta)^2}+\overline{S}(\zeta), \tag{46}$$

where

$$\overline{F}_1(\zeta)=\int_0^\infty e^{-i\zeta x}F_1(x)dx$$
$$\overline{F}_2(\zeta)=\int_0^\infty e^{-i\zeta x}F_2(x)dx. \tag{47}$$

Primes in (45) and (46) signify derivatives.

An iterative procedure for solving the transform relations (45) and (46) starts from the developments

$$\overline{F}_1(\zeta)=\overline{F}_1^{(0)}(\zeta)+\overline{F}_1^{(1)}(\zeta),$$
$$\overline{F}_2(\zeta)=\overline{F}_2^{(0)}(\zeta)+\overline{F}_2^{(1)}(\zeta),$$
$$\overline{R}(\zeta)=\overline{R}^{0}(\zeta)+\overline{R}^{(1)}(\zeta),$$

and

$$\overline{S}(\zeta)=\overline{S}^{0}(\zeta)+\overline{S}^{(1)}(\zeta), \tag{48}$$

where

$$\overline{F}_1^{(0)}(\zeta)(k^2-\zeta^2)^{1/2}=\frac{ai}{\zeta+i\epsilon}(k^2-\zeta^2)^{1/2}+\overline{R}^{(0)}(\zeta) \tag{49}$$

and

$$\frac{\overline{F}_2^{(0)}(\zeta)}{(k^2-\zeta^2)^{1/2}}=-\frac{\alpha}{2}\frac{\overline{F}^{2(0)}(-k)-\frac{ia}{k}}{k-\zeta}$$
$$-\frac{ia}{\zeta+i\epsilon}\frac{1}{(k^2-\zeta^2)^{1/2}}+\overline{S}^{(0)}(\zeta). \tag{50}$$

After rewriting (49) in the form

$$\overline{F}_1^{(0)}(\zeta)(k-\zeta)^{1/2}-\frac{ia}{\zeta+i\epsilon}[(k-\zeta)^{1/2}-k^{1/2}]$$
$$=\frac{ia}{\zeta+i\epsilon}k^{1/2}+\overline{R}^{(0)}(\zeta), \tag{51}$$

it is seen that the left side is regular in the lower half-plane (Im $\zeta>$ Im k), and the right side is regular in the upper half-plane (Im $\zeta>-$Im k). Therefore an integral function is defined in the entire ζ-plane. Since both sides tend to zero at infinity in their respective half-planes the integral function vanishes, or

$$\overline{F}_1^{(0)}(\zeta)=\frac{ia}{\zeta+i\epsilon}\left(1-\left(\frac{k}{k-\zeta}\right)^{1/2}\right). \tag{52}$$

By setting $\zeta=-k$ and $\zeta=0$ in (52), it follows that

$$\overline{F}_1^{(0)}(-k)=-\frac{ai}{k}(1-2^{-1/2}) \tag{53}$$

$$\overline{F}_1^{(0)}(0)=-\frac{ia}{2k}. \tag{54}$$

Similarly, (50) may be rewritten in the form

$$\frac{\overline{F}_2^{(0)}(\zeta)}{(k-\zeta)^{1/2}}+\frac{ia}{\zeta+i\epsilon}\left(\frac{1}{(k-\zeta)^{1/2}}-\frac{1}{k^{1/2}}\right)$$
$$+\frac{\alpha}{2}\frac{(\overline{F}_2^{(0)}(-k)-ia/k)}{k-\zeta}(2k)^{1/2}$$
$$=-\frac{ia}{\zeta+i\epsilon}\frac{1}{k^{1/2}}-\frac{\alpha}{2}\left(\overline{F}_2^{(0)}(-k)-\frac{ia}{k}\right)$$
$$\cdot\frac{(k+\zeta)^{1/2}-(2k)^{1/2}}{k-\zeta}+(k+\zeta)^{1/2}\overline{R}^{(0)}(\zeta). \tag{55}$$

In this case the vanishing of the integral function leads to

$$\overline{F}_2^{(0)}(\zeta)=-\frac{ia}{\zeta+i\epsilon}\left(1-\left(\frac{k-\zeta}{k}\right)^{1/2}\right)$$
$$-\frac{\alpha}{2}\left(\overline{F}_2^{(0)}(-k)-\frac{ia}{k}\right)\cdot\left(\frac{2k}{k-\zeta}\right)^{1/2} \tag{56}$$

so that with $\zeta=-k$ and $\zeta=0$ in turn, it follows that

$$\overline{F}_2^{(0)}(-k)=\frac{ia}{k}\left[1-\frac{2^{1/2}}{1+\frac{\alpha}{2}}\right] \tag{57}$$

and

$$\overline{F}_2^{(0)}(0) = -\frac{ia}{2k} + \frac{ia}{k}\frac{\alpha}{1+\frac{\alpha}{2}}. \tag{58}$$

The substitution of $\overline{F}_2^{(0)}(-k)$ from (57) in (56) gives

$$\overline{F}_2^{(0)}(\zeta) = -\frac{ia}{\zeta + i\epsilon}\left(1 - \frac{(k-\zeta)^{1/2}}{k}\right) + \frac{ia}{k}\frac{\alpha}{1+\frac{\alpha}{2}}\left(\frac{k}{k-\zeta}\right)^{1/2}. \tag{59}$$

With (48) and (49) the next approximation for (45) is

$$\overline{F}_1^{(1)}(\zeta)(k^2-\zeta^2)^{1/2} = \overline{H}(\zeta) + \overline{R}^{(1)}(\zeta) \tag{60}$$

where

$$\begin{aligned}\overline{H}(\zeta) = {} & \frac{i}{a}\overline{F}_1^{(0)}(\zeta)(k^2-\zeta^2)^{1/2} \\ & + \frac{i}{2a}\overline{F}_1^{(0)}(\zeta)\frac{\partial}{\partial\zeta}(k^2-\zeta^2)^{1/2} \\ & + \frac{\alpha ik}{4a}\frac{\overline{F}_1^{(0)}(-k)}{k-\zeta} - \frac{i}{a}\overline{F}_2^{(0)}(\zeta)\frac{\zeta}{(k^2-\zeta^2)^{1/2}} \\ & - \frac{\alpha ik}{2a}\frac{\overline{F}_2^{(0)}(-k)}{k-\zeta} + \frac{1}{2}\frac{1}{\zeta+i\epsilon}\frac{\partial}{\partial\zeta}(k^2-\zeta^2)^{1/2} \\ & + \frac{1}{\zeta+i\epsilon}\frac{\zeta}{(k^2-\zeta^2)^{1/2}} - \frac{3\alpha}{4}\frac{1}{k-\zeta}.\end{aligned} \tag{61}$$

When use is made of (52), (53), (57) and (59), then (61) becomes

$$\begin{aligned}\overline{H}(\zeta) = {} & \frac{(k^2-\zeta^2)^{1/2}}{(\zeta+i\epsilon)^2} - \frac{k^{1/2}(k+\zeta)^{1/2}}{(\zeta+i\epsilon)^2} \\ & + \frac{k^{1/2}(k+\zeta)^{1/2}}{2(\zeta+i\epsilon)(k-\zeta)} - \frac{k^{1/2}}{2}\frac{1}{(k-\zeta)^2(k+\zeta)^{3/2}} \\ & + \frac{1}{k^{1/2}(k+\zeta)^{1/2}} - \frac{\alpha 2^{1/2}}{8}\left(1+\frac{4}{1+\frac{\alpha}{2}}\right)\frac{1}{k-\zeta} \\ & + \frac{k^{1/2}\alpha}{1+\frac{\alpha}{2}}\frac{1}{(k-\zeta)(k+\zeta)^{1/2}}.\end{aligned} \tag{62}$$

After the division of (60) by $\sqrt{k+\zeta}$ and the selection of terms regular in the lower (−) and upper (+) half-planes, it follows from the vanishing of the integral function that

$$\overline{F}_1^{(1)}(\zeta)(k-\zeta)^{1/2} = \left(\frac{\overline{H}(\zeta)}{(k+\zeta)^{1/2}}\right)_-. \tag{63}$$

Since

$$\left[\frac{1}{(\zeta+i\epsilon)^2}(k-\zeta)^{1/2}\right]_- = \frac{1}{\zeta^2}\left[(k-\zeta)^{1/2} - k^{1/2}\right] + \frac{1}{2\zeta k^{1/2}}$$

$$\left[\frac{1}{\zeta+i\epsilon}\frac{1}{k-\zeta}\right]_- = \frac{1}{k}\frac{1}{k-\zeta}$$

$$\left[\frac{1}{(k+\zeta)^2(k-\zeta)^2}\right]_- = \frac{(2k-\zeta)}{4k^3(k-\zeta)^2}$$

$$\left[\frac{1}{(k+\zeta)^{1/2}(k-\zeta)}\right]_- = \frac{1}{(2k)^{1/2}(k-\zeta)}$$

and

$$\left[\frac{1}{(k+\zeta)(k-\zeta)}\right]_- = \frac{1}{2k}\frac{1}{k-\zeta}, \tag{64}$$

it follows that $[\overline{H}(\zeta)/(k+\zeta)]_-$ is explicitly given by

$$\begin{aligned}\left(\frac{\overline{H}(\zeta)}{k+\zeta}\right)_- = {} & \frac{1}{\zeta^2}\left[(k-\zeta)^{1/2} - k^{1/2}\right] + \frac{1}{2\zeta k^{1/2}} \\ & + \frac{1}{2k^{1/2}}\frac{1}{k-\zeta} - \frac{(2k-\zeta)}{8k^{1/2}(k-\zeta)^2} \\ & - \frac{\alpha}{8k^{1/2}}\left(1+\frac{4}{1+\frac{\alpha}{2}}\right)\frac{1}{k-\zeta} \\ & + \frac{k^{1/2}\alpha}{1+\frac{\alpha}{2}}\frac{1}{2k(k-\zeta)}.\end{aligned} \tag{65}$$

With the omission of higher order terms in α, the principal part of $\overline{F}_1^{(1)}(0)$ turns out to be

$$F_1^{(1)}(0) = \frac{1}{8k^2} - \frac{\alpha}{8k^2}. \tag{66}$$

Hence

$$\overline{F}_1(0) = \overline{F}_1^{(0)}(0) + \overline{F}_1^{(1)}(0) = -\frac{ia}{2k} + \frac{1}{8k^2} - \frac{\alpha}{8k^2}. \tag{67}$$

Similarly, the next approximation for (46) is

$$\frac{\overline{F}_2^{(1)}(\zeta)}{(k^2-\zeta^2)^{1/2}} = -\frac{\alpha}{2}\frac{\overline{F}_2^{(1)}(-k)}{k-\zeta} + \overline{G}(\zeta) + \overline{S}^{(1)}(\zeta), \quad (68)$$

where

$$\begin{aligned}\overline{G}(\zeta) = {} & \frac{i}{ak^2}\overline{F}_1^{(0)}(\zeta)\frac{\zeta}{(k^2-\zeta^2)^{1/2}} + \frac{i}{a}\frac{\overline{F}_2'^{(0)}(\zeta)}{(k^2-\zeta^2)^{1/2}} \\ & - \frac{\alpha i}{2\alpha k}\frac{\overline{F}_1^{(0)}(-k)}{k-\zeta} + \frac{i}{2a}\overline{F}_2^{(0)}(\zeta)\frac{\partial}{\partial\zeta}\frac{1}{(k^2-\zeta^2)^{1/2}} \\ & - \frac{7i\alpha}{8ak}\cdot\frac{\overline{F}_2^{(0)}(-k)}{k-\zeta} + \frac{3\alpha i}{8a}\frac{\overline{F}_2'^{(0)}(-k)}{k-\zeta} \\ & + \frac{3\alpha i}{8a}\frac{\overline{F}_2^{(0)}(-k)}{(k-\zeta)^2} + \frac{1}{k^2}\frac{1}{(k^2-\zeta^2)^{1/2}} \\ & - \frac{1}{2(\zeta+i\epsilon)}\frac{\partial}{\partial\zeta}\frac{1}{(k^2-\zeta^2)^{1/2}}. \end{aligned} \quad (69)$$

Eqs. (52), (53), (57) and (59) are used to simplify (69) and the resulting equation for $\overline{G}(\zeta)$, up to linear terms in α, is

$$\begin{aligned}\overline{G}(\zeta) = {} & \frac{1}{k^{3/2}(k+\zeta)^{1/2}(k-\zeta)} - \frac{1}{(\zeta+i\epsilon)^2(k^2-\zeta^2)^{1/2}} \\ & + \frac{1}{k^{1/2}\zeta^2(k+\zeta)^{1/2}} + \frac{1}{2k^{1/2}\zeta(k+\zeta)^{1/2}(k-\zeta)} \\ & - \frac{1}{2k^{1/2}(k+\zeta)^{3/2}(k-\zeta)} - \left(\frac{1}{2k^2}+\frac{11\sqrt{2}}{32k^2}\right) \\ & \cdot\frac{\alpha}{k-\zeta} - \frac{\alpha}{2(k)^{1/2}}\frac{1}{(k-\zeta)^2(k+\zeta)^{1/2}} \\ & - \frac{\alpha\zeta}{2k^{1/2}(k-\zeta)^2(k+\zeta)^{3/2}} + \frac{3\sqrt{2}\alpha}{8k}\frac{1}{(k-\zeta)^2}. \end{aligned} \quad (70)$$

After the multiplications of (68) by $(k+\zeta)^{1/2}$ and the selection of terms regular in the lower $(-)$ and upper $(+)$ half-planes, it follows from the vanishing of the integral function that

$$\begin{aligned}\frac{\overline{F}_2^{(1)}(\zeta)}{(k-\zeta)^{1/2}} = {} & -\frac{\alpha}{2}\frac{(2k)^{1/2}}{k-\zeta}\overline{F}_2^{(1)}(-k) \\ & + [(k+\zeta)^{1/2}\overline{G}(\zeta)]_-. \end{aligned} \quad (71)$$

Since

$$\begin{aligned}\left[\frac{1}{(\zeta+i\epsilon)^2(k-\zeta)^{1/2}}\right]_- &= \frac{1}{\zeta^2}\left(\frac{1}{(k-\zeta)^{1/2}} - \frac{1}{(k)^{1/2}}\right) - \frac{1}{2\zeta k^{3/2}} \\ \left[\frac{1}{\zeta(k-\zeta)}\right]_- &= \frac{1}{k}\frac{1}{k-\zeta} \\ \left[\frac{1}{(k+\zeta)(k-\zeta)}\right]_- &= \frac{1}{2k(k-\zeta)} \\ \left[\frac{(k+\zeta)^{1/2}}{k-\zeta}\right]_- &= \frac{(2k)^{1/2}}{k-\zeta} \\ \left[\frac{\zeta}{(k-\zeta)^2(k+\zeta)}\right]_- &= \frac{k+\zeta}{4k(k-\zeta)^2} \\ \left[\frac{(k+\zeta)^{1/2}}{(k-\zeta)^2}\right]_- &= \left[\frac{(2k)^{1/2}}{(k-\zeta)^2} - \frac{1}{2(2k)^{1/2}(k-\zeta)}\right] \end{aligned} \quad (72)$$

it follows explicitly that

$$\begin{aligned}\frac{F_2^{(1)}(\zeta)}{(k-\zeta)^{1/2}} = {} & -\frac{\alpha}{2}\frac{(2k)^{1/2}}{k-\zeta}\overline{F}_2^{(1)}(-k) \\ & + \frac{5k^{-3/2}}{4(k-\zeta)} - \frac{1}{\zeta^2}\left(\frac{1}{(k-\zeta)^{1/2}} - \frac{1}{k^{1/2}}\right) \\ & + \frac{1}{2\zeta k^{3/2}} - \frac{\alpha k^{-3/2}}{k-\zeta}\left(2^{-1/2}+\frac{7}{8}\right) \\ & - \frac{\alpha k^{-1/2}}{(k-\zeta)^2}\left(-\frac{1}{8}+\frac{\zeta}{8k}\right). \end{aligned} \quad (73)$$

In particular, the special case $\zeta=-k$ in (73) gives

$$\begin{aligned}\overline{F}_2^{(1)}(-k) = {} & \frac{(2k)^{1/2}}{1+\frac{\alpha}{2}}\left[\left(\frac{9}{8}-2^{-1/2}\right)k^{-5/2}\right. \\ & \left. - \alpha k^{-5/2}\left(\frac{1}{2(2)^{1/2}}+\frac{3}{8}\right)\right]. \end{aligned} \quad (74)$$

After using (74) in (73), setting $\zeta=0$, and omitting higher order terms in α, the principal part of $\overline{F}_2^{(1)}(0)$ turns out to be

$$\overline{F}_2^{(1)}(0) = \frac{7}{8}k^{-2} - \frac{15}{8}\alpha k^{-2}. \quad (75)$$

Thus

$$\begin{aligned}\overline{F}_2(0) &= \overline{F}_2^{(0)}(0) + \overline{F}_2^{(1)}(0) \\ &= -\frac{ia}{2k} + \frac{ia}{k}\frac{\alpha}{1+\frac{\alpha}{2}} + \frac{7}{8}k^{-2} - \frac{15}{8}\alpha k^{-2}. \end{aligned} \quad (76)$$

The Transmission Coefficient

A quantity of physical interest in this problem is the transmission cross section of the aperture. It is defined as the ratio of the power passing through the aperture to the incident power density per unit area. The normalized transmission cross section or the transmission coefficient can be shown to be

$$\frac{\sigma}{\pi a^2} = 1 - \frac{1}{\pi a^2}\left(\frac{\mu}{\epsilon}\right)^{1/2} Re \int_S J_x^+(\rho')dS' \qquad (77)$$

Eq. (77) can be rewritten with the help of (6) and (42) in the form

$$\frac{\sigma}{\pi a^2} = 1 - \frac{1}{a^2} Re\left[\int_0^\infty F_1(x')dx' - \int_0^\infty F_2(x')dx'\right]$$
$$= 1 - \frac{1}{a^2} Re[\bar{F}_1(0) - \bar{F}_2(0)] \qquad (78)$$

The substitution of the values of $\bar{F}_1(0)$ and $F_2(0)$ from (67) and (76), respectively, in (78) gives

$$\frac{\sigma}{\pi a^2} = 1 - \frac{1}{\pi^{1/2}(ka)^{3/2}} \sin\left(2ka - \frac{\pi}{4}\right)$$
$$+ \frac{1}{(ka)^2}\left[\frac{3}{4} + \frac{1}{2\pi}\sin 2\left(2ka - \frac{\pi}{4}\right)\right]$$
$$- \frac{1}{(\pi)^{1/2}(ka)^{5/2}}\left[\frac{7}{4}\cos\left(2ka - \frac{\pi}{4}\right)\right.$$
$$\left. + \frac{1}{4\pi}\sin 3\left(2ka - \frac{\pi}{4}\right)\right] \qquad (79)$$

The first two terms of the transmission coefficient have been obtained previously by Chang[4] and Millar.[5] Millar had evaluated the coefficient of the $(ka)^{-2}$ term empirically as 0.70, which is quite close to the non-oscillatory part of the coefficient of $(ka)^{-2}$ in (79).

Numerical Results

The values of the transmission coefficients t_1, t_2 and t_3, which are obtained by adding respectively one, two, and three correction terms to the geometrical optics value, are tabulated in Table I, together with the value t calculated from the exact theory in the range of values $3 \leq ka \leq 10$. The values of t are taken from Millar's paper.[5] The values of $(t - t_3)$ given in the last column of the table show that the transmission coefficient with three correction terms as given (79) agrees with the one calculated from the exact theory to within about one per cent. Since the calculations from the exact theory may be unreliable beyond the second decimal place, more exact agreement of t_3 with t is not to be expected.

In Fig. 2, the transmission coefficients t_1, t_2, t_3 and t are compared for the range $0 \leq ka \leq 10$. Due to lack of accuracy in the calculations from the exact theory the transmission coefficient t, is omitted beyond $ka = 6$. From the graph it can be seen clearly that t_2 and t_3 are much better approximations to t than t_1 which was obtained by Chang.[4] It is further noted that both the position and the magnitude of the first maximum of the transmission coefficient approach the one given by the exact theory; and this poses an interesting unsolved problem: whether the sequence of graphs for t_1, t_2, t_3, $\cdots$ possesses any convergence property, even though the infinite series (79) for the transmission coefficient is believed to be divergent.

TABLE I

Numerical Comparison of Transmission Coefficients

$$t_1 = 1 - (\pi)^{-1/2}\frac{1}{(ka)^{3/2}}\sin\left(2ka - \frac{\pi}{4}\right)$$

$$t_2 = t_1 + \frac{1}{(ka)^2}\left[\frac{3}{4} + \frac{1}{2\pi}\sin 2\left(2ka - \frac{\pi}{4}\right)\right]$$

$$t_3 = t_2 - \frac{1}{(\pi)^{1/2}(ka)^{5/2}}\left[\frac{7}{4}\cos\left(2ka - \frac{\pi}{4}\right) + \frac{1}{4\pi}\sin 3\left(2ka - \frac{\pi}{4}\right)\right]$$

ka	t_1	t_2	t_3	t	$t-t_3$
3	1.09517	1.16358	1.13291	1.127	−0.006
4	0.94341	0.99981	0.98092	0.992	+0.011
5	0.98947	1.01687	1.03367	1.039	+0.005
6	1.03747	1.05643	1.05359	1.047	−0.007
7	0.98161	1.00004	0.99365	0.995	+0.001
8	0.98819	0.99783	1.00239	0.999	−0.003
9	1.02086	1.03037	1.03045	1.030	−0.000
10	0.99363	1.00219	0.99915	1.001	+0.002

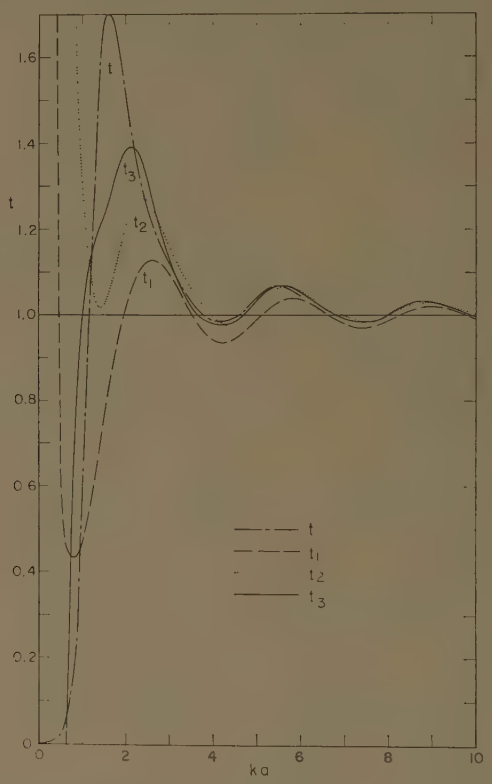

Fig. 2—Graphical comparison of transmission coefficients.

Acknowledgment

The authors are indebted to Prof. R. W. P. King for criticizing the manuscript. They also thank Miss B. Hamilton who carried out the numerical calculation.

High-Frequency Diffraction of Plane Waves by an Infinite Slit for Grazing Incidence*

S. R. SESHADRI† AND T. T. WU†

Summary—The scattering of plane electromagnetic waves of wave number k by an infinite slit of width $2a$ formed by two perfectly conducting coplanar screens of zero thickness is considered. In the limit of large ka and at grazing incidence, the asymptotic series for the transmission cross section per unit length of the slit is evaluated up to the order $(ka)^{-11/2}$.

Introduction

CONSIDER the problem of diffraction by an infinite slit formed by two perfectly conducting coplanar screens. A plane electromagnetic wave with its direction of propagation lying in a plane perpendicular to the screens is incident on the slit from one side of the two screens forming the slit. The earlier treatments of the problem, with the exception of that by Levine[1] have excluded the limiting case of grazing incidence, *i.e.*, the case in which the direction of the incident wave is parallel to the screens. In this report the special case for grazing incidence is investigated with the purpose of obtaining the first few terms in the asymptotic series for the transmission cross section for unit length of the slit.

The case for grazing incidence becomes physically more meaningful if the corresponding complementary problem of the infinite strip is considered. In that case the plane wave is incident edge-on the strip and the problem reduces to that of finding the total scattering cross section for unit length of the strip. Since it is convenient mathematically to deal with the infinite slit rather than the infinite strip, the problem of diffraction of plane waves by an infinite slit rather than by the infinite strip is treated. However, Babinet's principle makes it possible to obtain results for the problem of the infinite strip from those for the infinite slit, and vice versa.

It is possible to separate the problem of the diffraction of a plane electromagnetic wave by an infinite strip into two equivalent scalar problems: 1) the case when the magnetic vector is parallel to the edges of the strip, and 2) the case when the electric vector is parallel to the edges of the strip. In the first case, if a wave function is identified with the component of the magnetic vector parallel to the edges of the strip, then it is easily shown that the wave function satisfies the two-dimensional wave equation exterior to the screens. On the screens the normal derivative of the wave function vanishes. By the application of Green's theorem, the wave function at an arbitrary point may be written as the sum of the incident field and a scattered field. The scattered field is determined by the discontinuity of the wave function across the screens. For the case when the wave is incident edge-on the strip, symmetry considerations indicate that the wave function is the same on both sides of each of the two screens. Therefore, the discontinuity of the wave function across each of the two screens becomes zero, with the result that there is no scattered field. Consequently, by the principle of complementarity, it is easily inferred that the limiting value of the transmission cross section per unit length of an infinite slit is zero when the incident electric vector is parallel to the edges of the slit.

It remains, therefore, only to treat the case when the electric vector is parallel to the edges of the infinite strip. In this case the diffracted field is not zero and the total scattering cross section per unit length of the strip is calculable. As was stated before, for analytical reasons the treatment is in terms of the complementary problem of the infinite slit. The formulation of the problem is similar to that used by Levine.[1] The pair of simultaneous integral equations, which specify the transforms of the current distributions on the two screens and which were derived by Levine, are solved in a systematic manner and the first six terms in the high-frequency asymptotic series for the cross section are evaluated.

Formulation of the Problem

Consider the problem of edge-on scattering by an infinite strip. The incident plane electromagnetic wave is assumed to have its electric vector parallel to the edges of the strip [Fig. 1(a)]. If the x component of the electric vector is identified with a wave function $\psi_1(y, z)$, then it is readily seen that ψ_1 satisfies the scalar two-dimensional wave equation exterior to the strip, and obeys the Dirichlet boundary condition on the strip. Mathematically, it is convenient to treat the corresponding complementary problem and obtain the result for the strip by Babinet's principle. The complementary problem of the infinite slit is illustrated in Fig. 1(b). The incident wave has its magnetic vector parallel to the edges of the slit. If the x component of the magnetic field is set equal to the wave function $\psi_2(y, z)$, it may be

* Manuscript received by the PGAP, January 23, 1959. The research reported in this document was supported in part by the Air Force Cambridge Research Center under Contract AF19(604)-786 with Harvard University.

† Gordon McKay Labs., Harvard University, Cambridge, Mass. The work was carried out when Mr. Wu was a Junior Fellow of the Society of Fellows, Harvard University.

[1] H. Levine, "Diffraction by an Infinite Slit," Appl. Math. and Statistics Lab., Stanford University, Stanford, Calif., Tech. Rept. No. 61; 1957.

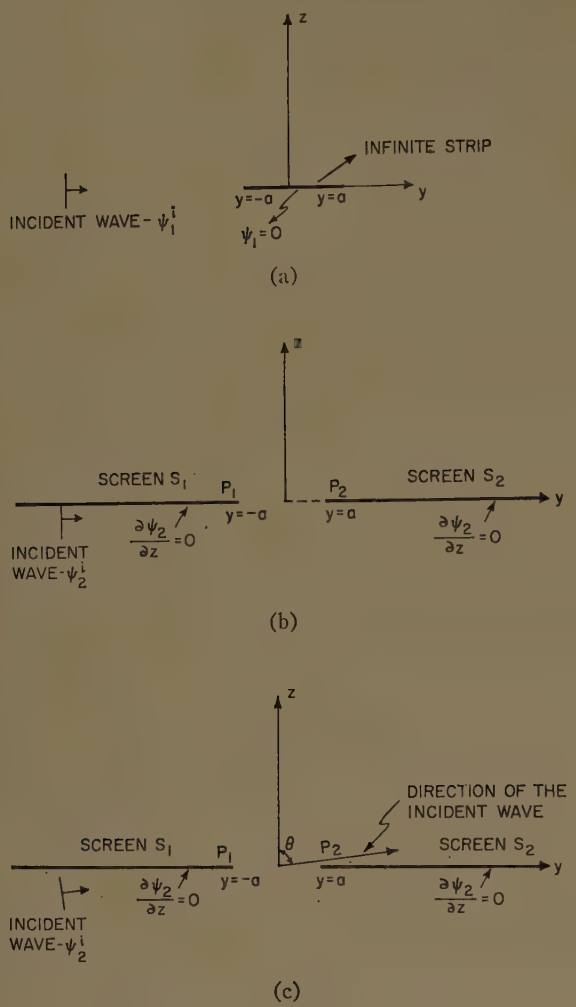

Fig. 1—Geometry of the problem.

shown that $\psi_2(y, z)$, in the region exterior to the screens, satisfies the wave equation

$$\left(\frac{\partial^2}{\partial y^2}+\frac{\partial^2}{\partial z^2}+k^2\right)\psi_2(y, z) = 0. \tag{1}$$

On the screens, the following boundary condition is satisfied:

$$\frac{\partial \psi_2}{\partial z}(y, 0) = 0. \qquad |y| > a \tag{2}$$

It is desired to obtain the solution for grazing incidence [Fig. 1(b)] as the limiting case of the solution for arbitrary incidence [Fig. 1(c)] in which the angle of incidence θ is allowed to go to its limiting value $\pi/2$ at a suitable stage in the calculations. Hence, the problem is formulated for arbitrary incidence. By application of Green's theorem, it may be shown that

$$\psi_2(y, z) = e^{ik(y \sin\theta + z\cos\theta)} + \int_{|y'|>a} dy' I(y') \left[\frac{\partial}{\partial y'}\frac{i}{4}H_0^{(1)}(k|\rho-\rho'|)\right]_{z'=0} \tag{3}$$

where

$$I(y) = \begin{Bmatrix} I_1(y), & y < -a \\ I_2(y), & y > a \end{Bmatrix} = \psi_2(y, 0^+) - \psi_2(y, 0^-). \tag{4}$$

The first term $e^{ik(y \sin\theta + z\cos\theta)}$ in (3) represents the incident field and the integral represents the scattered field.

Let the following transforms be defined:

$$\overline{P}_1(\zeta) = \int_{-\infty}^{0} e^{-i\zeta y} I_1(-a+y)dy \tag{5}$$

and

$$\overline{P}_2(\zeta) = \int_{0}^{\infty} e^{-i\zeta y} I_2(a+y)dy. \tag{6}$$

Then, by the use of the Wiener-Hopf procedure to (3), the following pair of simultaneous integral equations specifying the transforms $\overline{P}_1(\zeta)$ and $\overline{P}_2(\zeta)$ is obtained:

$$\frac{i}{2}\sqrt{k+\zeta}\,\overline{P}_1(\zeta) = \frac{\sqrt{k+k\sin\theta}}{\zeta - k\sin\theta}e^{-ika\sin\theta} + \frac{i}{2\pi}\int_k^\infty \frac{dt}{t+\zeta}\sqrt{t-k}e^{2ita}\overline{P}_2(-t) \tag{7}$$

and

$$\frac{i}{2}\sqrt{k+\zeta}\,\overline{P}_2(-\zeta) = \frac{\sqrt{k-k\sin\theta}}{\zeta + k\sin\theta}e^{ika\sin\theta} + \frac{i}{2\pi}\int_k^\infty \frac{dt}{t+\zeta}\sqrt{t-k}e^{2ita}\overline{P}_1(t). \tag{8}$$

It is convenient to make (7) and (8) dimensionless by the introduction of

$$Q_1(\zeta) = \frac{ik}{2}\sqrt{1+\zeta}\,\overline{P}_1(k\zeta) \tag{9}$$

and

$$Q_2(\zeta) = \frac{ik}{2}\sqrt{1+\zeta}\,\overline{P}_2(-k\zeta). \tag{10}$$

Then $Q_1(\zeta)$ and $Q_2(\zeta)$ satisfy the following simultaneous integral equations:

$$Q_1(\zeta) = \frac{\sqrt{1+\sin\theta}}{\zeta - \sin\theta}e^{-ika\sin\theta} + \frac{1}{\pi}\int_1^\infty \frac{dt}{t+\zeta}\left(\frac{t-1}{t+1}\right)^{1/2} e^{2ikat}Q_2(t) \tag{11}$$

$$Q_2(\zeta) = \frac{\sqrt{1-\sin\theta}}{\zeta + \sin\theta}e^{ika\sin\theta} + \frac{1}{\pi}\int_1^\infty \frac{dt}{t+\zeta}\left(\frac{t-1}{t+1}\right)^{1/2} e^{2ikat}Q_1(t). \tag{12}$$

Eqs. (11) and (12) are valid for all angles of incidence.

It is desired to carry out the solution of (11) and (12) only for the special case $\theta=\pi/2$. For $\theta=\pi/2$, (11) and (12) reduce to

$$Q_1(\zeta) = \frac{\sqrt{2}}{\zeta-1}e^{-ika} + \frac{1}{\pi}\int_1^\infty \frac{dt}{t+\zeta}\left(\frac{t-1}{t+1}\right)^{1/2} e^{2ikat}Q_2(t) \quad (13)$$

$$Q_2(\zeta) = \frac{1}{\pi}\int_1^\infty \frac{dt}{t+\zeta}\left(\frac{t-1}{t+1}\right)^{1/2} e^{2ikat}Q_1(t). \quad (14)$$

The main interest in this problem is the evaluation of the transmission cross section per unit length of the slit. It is easily shown[2] that the transmission cross section σ per unit length of the slit is given by the formula

$$\sigma = \frac{\sqrt{2}}{k}\operatorname*{Im}_{\zeta\to 1-}\left[e^{-ika}Q_2(-\zeta) - \frac{1}{\sqrt{1-\zeta}}\right]. \quad (15)$$

where $\operatorname*{Im}_{\zeta\to 1-}$ means the imaginary part in the limit $\zeta\to 1-$. It will be seen, after the solution for $Q_2(-\zeta)$ is obtained, that the singularity due to $1/\sqrt{1-\zeta}$ is exactly annulled by that contributed by $e^{-ika}\,Q_2(-\zeta)$.

Iterative Solution of the Integral Equations

It is convenient to reduce the pair of simultaneous integral equations (13) and (14) into two independent integral equations. This can be done by the method of symmetrical components. Let

$$Q_1(\zeta) = R(\zeta) + S(\zeta) \quad (16)$$

and

$$Q_2(\zeta) = R(\zeta) - S(\zeta). \quad (17)$$

By substituting (16) and (17) in (13) and (14), first by adding the two equations and then by subtracting one from the other, the following two independent integral equations are obtained:

$$R(\zeta) = \frac{1}{\sqrt{2}(\zeta-1)}e^{-ika} + \frac{1}{\pi}\int_1^\infty \frac{dt}{t+\zeta}\left(\frac{t-1}{t+1}\right)^{1/2} e^{2ikat}R(t) \quad (18)$$

and

$$S(\zeta) = \frac{1}{\sqrt{2}(\zeta-1)}e^{-ika} - \frac{1}{\pi}\int_1^\infty \frac{dt}{t+\zeta}\left(\frac{t-1}{t+1}\right)^{1/2} e^{2ikat}S(t). \quad (19)$$

[2] S. R. Seshadri, "Asymptotic Solutions of Some Electromagnetic Diffraction Problems," Ph.D. dissertation, Harvard University, Cambridge, Mass.; 1958. Also, "High-frequency diffraction of plane waves by an infinite slit I & II," *Proc. Nat. Inst. Sci. India*, vol. 25A, pp. 301–336; 1959.

It is desired to solve (18) first by the method of iteration. The zeroth-order solution is

$$[R(\zeta)]_0 = \frac{1}{\sqrt{2}(\zeta-1)}e^{-ika}. \quad (20)$$

With (18) and (20), the first-order solution becomes

$$[R(\zeta)]_1 = \frac{1}{\sqrt{2}(\zeta-1)}e^{-ika} + \frac{1}{\pi}\int_1^\infty \frac{dt}{t+\zeta}\left(\frac{t-1}{t+1}\right)^{1/2} e^{2ikat}\frac{e^{-ika}}{\sqrt{2}(t-1)}. \quad (21)$$

With the change of variable t to $1+is/2ka$, (21) may be reduced to

$$[R(\zeta)]_1 = \frac{1}{\sqrt{2}(\zeta-1)}e^{-ika} + \frac{1}{\sqrt{2\pi}}\left(\frac{i}{2ka}\right)^{1/2} e^{ika}R_1(\zeta), \quad (22)$$

where

$$R_1(\zeta) = -\int_0^\infty s^{-1/2}\left[\left(\frac{i}{2ka}\right)s + 1 + \zeta\right]^{-1} \cdot\left[\left(\frac{i}{2ka}\right)s + 2\right]^{-1/2} e^{-s}ds. \quad (23)$$

By substituting (22) in (18), the second-order solution is obtained as

$$[R(\zeta)]_2 = \frac{1}{\sqrt{2}(\zeta-1)}e^{-ika} + \frac{1}{\sqrt{2\pi}}\left(\frac{i}{2ka}\right)^{1/2} e^{ika}R_1(\zeta) + \frac{1}{\pi}\int_1^\infty \frac{dt}{t+\zeta}\left(\frac{t-1}{t+1}\right)^{1/2} e^{2ikat} \cdot\frac{1}{\sqrt{2\pi}}\left(\frac{i}{2ka}\right)^{1/2} e^{ika}R_1(t). \quad (24)$$

Note that $R_1(t)$ is regular at $t=1$. Hence, with a change of variable from t to $1+is/2ka$, (24) becomes

$$[R(\zeta)]_2 = \frac{1}{\sqrt{2}(\zeta-1)}e^{-ika} + \frac{1}{\sqrt{2\pi}}\left(\frac{i}{2ka}\right)^{1/2} e^{ika}R_1(\zeta) + \frac{1}{\sqrt{2\pi^2}}\left(\frac{i}{2ka}\right)^{2} e^{2ika}R_2(\zeta) \quad (25)$$

where

$$R_2(\zeta) = -\int_0^\infty ds\left[\frac{is}{2ka} + 1 + \zeta\right]^{-1} \cdot\left[\frac{is}{2ka} + 2\right]^{-1/2} s^{1/2}e^{-s}R_1\left(1 + \frac{is}{2ka}\right). \quad (26)$$

The iterative solution of (18) can be continued as far as is required. However, it is desired to evaluate only the first few terms in the high frequency asymptotic series for the cross section. It is seen from the solution of (18) that the first iteration introduces a factor $k^{-1/2}$ and each of the subsequent iterations introduces a factor of $k^{-3/2}$. Consequently, it is possible to obtain the first few terms in the series for the cross section even with the second-order solution of (18).

In a similar manner, the solution of (19) may be worked out, since (19) differs from (18) only in the sign before the integral. The solution of (19) may be written down by inspection. Thus,

$$[S(\zeta)]_2 = \frac{1}{\sqrt{2}(\zeta-1)} e^{-ika} - \frac{1}{\sqrt{2}\pi}\left(\frac{i}{2ka}\right)^{1/2} e^{ika} R_1(\zeta) + \frac{1}{\sqrt{2}\pi^2}\left(\frac{i}{2ka}\right)^{2} e^{3ika} R_2(\zeta) \tag{27}$$

where $R_1(\zeta)$ and $R_2(\zeta)$ are respectively given in (23) and (26).

With the help of (16), (25), and (27) it is deduced that

$$Q_1(\zeta) = \frac{\sqrt{2}}{\zeta-1} e^{-ika} + \frac{\sqrt{2}}{\pi^2}\left(\frac{i}{2ka}\right)^{2} e^{3ika} R_2(\zeta). \tag{28}$$

The substitution of (28) in (14) yields

$$Q_2(\zeta) = \frac{\sqrt{2}e^{-ika}}{\pi}\int_1^\infty \frac{dt}{t+\zeta}\,\frac{e^{2ikat}}{(t^2-1)^{1/2}} + \frac{\sqrt{2}}{\pi^3}\left(\frac{i}{2ka}\right)^{2} e^{3ika}\int_1^\infty \frac{dt}{t+\zeta}\left(\frac{t-1}{t+1}\right)^{1/2} \cdot e^{2ikat} R_2(t). \tag{29}$$

The use of (29) in (15) results in the following expression for σ:

$$\sigma = W_0 + W_1 \tag{30}$$

where

$$W_0 = \frac{\sqrt{2}}{k}\operatorname*{Im}_{\zeta\to 1_-}\left[\frac{\sqrt{2}e^{-2ika}}{\pi}\int_1^\infty \frac{dt}{t-\zeta}\,\frac{e^{2ikat}}{(t^2-1)^{1/2}} - \frac{1}{\sqrt{1-\zeta}}\right] \tag{31}$$

and

$$W_1 = -\operatorname{Im}\frac{e^{2ika}}{2\pi^3 k^3 a^2}\int_1^\infty \frac{dt}{(t^2-1)^{1/2}} e^{2ikat} R_2(t). \tag{32}$$

Evaluation of the Transmission Cross Section for Grazing Incidence

The determination of the series for the cross section σ involves the evaluation of the integrals W_0 and W_1. In the solution for $Q_1(\zeta)$ and $Q_2(\zeta)$, the contribution comes only from every other iteration. It is seen that the zeroth-order solution contributes terms starting with $(ka)^{-1/2}$ to the cross section. The second iterative solution contributes terms starting with $(ka)^{-7/2}$. It can be easily verified that the next-order solution will give rise to terms of order $(ka)^{-13/2}$. Hence, in the evaluation of the integrals, it is enough to retain terms up to order $(ka)^{-11/2}$.

Consider the evaluation of W_0. It is convenient to rewrite (31) as follows:

$$W_0 = \frac{\sqrt{2}}{k}\operatorname*{Im}_{\zeta\to 1_-}\left[\frac{\sqrt{2}e^{-2ika}}{\pi}\int_0^\infty \frac{dt}{t-\zeta}\,\frac{e^{2ikat}}{(t^2-1)^{1/2}} - \frac{1}{\sqrt{1-\zeta}}\right] - \operatorname*{Im}_{\zeta\to 1_-}\frac{2}{\pi k}e^{-2ika}\int_0^1 \frac{dt}{t-\zeta}\,\frac{e^{2ikat}}{(t^2-1)^{1/2}}. \tag{33}$$

Since

$$\int_1^\infty \frac{dt}{\sqrt{t^2-1}} e^{i2kat} = \frac{\pi i}{2} H_0^{(1)}(2ka), \tag{34}$$

it follows that

$$\left(\int_0^\infty - \int_0^1\right)\left[\frac{dt}{t-\zeta}\,\frac{e^{i2kat}}{\sqrt{t^2-1}}\right] = \pi ka e^{i2ka\zeta}\left(\int_0^\infty - \int_0^1\right)\left[e^{-i2ka\zeta t} H_0^{(1)}(2kat)dt\right]. \tag{35}$$

It can be shown that

$$\int_0^\infty e^{-i2ka\zeta t} H_0^{(1)}(2kat)dt = \frac{\left(1+\frac{2}{\pi}\sin^{-1}\zeta\right)}{2ka(1+\zeta)^{1/2}(1-\zeta)^{1/2}}. \tag{36}$$

With (35) and (36), (33) becomes

$$W_0 = \frac{\sqrt{2}}{k}\operatorname*{Im}_{\zeta\to 1_-}\left[\frac{e^{i2ka(\zeta-1)}}{\sqrt{2}(1+\zeta)^{1/2}(1-\zeta)^{1/2}}\left(1+\frac{2}{\pi}\sin^{-1}\zeta\right) - \frac{1}{\sqrt{1-\zeta}}\right] - \operatorname*{Im}_{\zeta\to 1_-} 2ae^{i2ka(\zeta-1)}\int_0^1 e^{-i2ka\zeta t} H_0^{(1)}(2kat)dt. \tag{37}$$

When the limit is taken, the first term vanishes, and hence it results that

$$\frac{W_0}{2a} = -\operatorname{Im}\int_0^1 e^{-i2kat} H_0^{(1)}(2kat)dt. \tag{38}$$

The integral in (38) can be evaluated explicitly with the result:

$$\frac{W_0}{2a} = -\operatorname{Im}\left[e^{-i2ka}\{H_0^{(1)}(2ka) + iH_1^{(1)}(2ka)\} - \frac{2}{\pi}\right]$$
$$= \frac{1}{\sqrt{2\pi}}\frac{2}{(ka)^{1/2}} - \frac{1}{\sqrt{2\pi}}\frac{1}{2^3}\frac{1}{(ka)^{3/2}} + \frac{1}{\sqrt{2\pi}}\frac{3}{2^3(ka)^{5/2}}$$
$$+ \frac{1}{\sqrt{2\pi}}\frac{15}{2^{12}(ka)^{7/2}} - \frac{1}{\sqrt{2\pi}}\frac{525}{2^{18}(ka)^{9/2}}$$
$$- \frac{1}{\sqrt{2\pi}}\frac{6615}{2^{22}(ka)^{11/2}}. \tag{39}$$

In order to evaluate W_1, it is necessary to evaluate $R_1(\zeta)$ and $R_2(\zeta)$ first, since the integrand in W_1 involves $R_2(t)$. Consider $R_1(\zeta)$ given in (23). It may be rewritten in the following way:

$$R_1(\zeta) = -\frac{1}{\zeta_0\sqrt{2}}\int_0^\infty s^{-1/2}\left[1+\frac{is}{2ka\zeta_0}\right]^{-1}$$
$$\cdot\left[1+\frac{is}{4ka}\right]^{-1/2} e^{-s}ds \tag{40}$$

where

$$\zeta_0 = 1 + \zeta. \tag{41}$$

In the asymptotic evaluation of $R_1(\zeta)$ and $R_2(\zeta)$, each term is an order $(ka)^{-1}$ lower than the preceding term. It is enough to keep terms of order up to $(ka)^{-2}$ only in $R_2(\zeta)$, since the higher-order terms of $R_2(\zeta)$ would contribute terms of order $(ka)^{-13/2}$ to the cross section. This, in turn, makes necessary the evaluation of $R_1(\zeta)$ only up to order $(ka)^{-2}$. The result of the asymptotic evaluation of (40), if only terms up to the order $(ka)^{-2}$ are retained, is

$$R_1(\zeta) = -\left(\frac{\pi}{2}\right)^{1/2}\frac{1}{\zeta_0} + \left(\frac{\pi}{2}\right)^{1/2}\left[\frac{i}{4ka\zeta_0^2} + \frac{i}{16ka\zeta_0}\right]$$
$$+ \left(\frac{\pi}{2}\right)^{1/2}\left[\frac{3}{16k^2a^2\zeta_0^3} + \frac{3}{64k^2a^2\zeta_0^2}\right.$$
$$\left. + \frac{9}{512k^2a^2\zeta_0}\right]. \tag{42}$$

Next, the value of $R_1(\zeta)$ for $\zeta = 1 + is/2ka$ is substituted in (26). With a procedure similar to that used in the evaluation of $R_1(\zeta)$, $R_2(\zeta)$ may be obtained as

$$R_2(\zeta) = \left[\frac{\pi}{8} - \frac{3\pi i}{32ka} - \frac{87\pi}{1024k^2a^2}\right]\frac{1}{\zeta_0}$$
$$- \left[\frac{3\pi i}{32ka} + \frac{27\pi}{256k^2a^2}\right]\frac{1}{\zeta_0^2} - \frac{15\pi}{128k^2a^2}\frac{1}{\zeta_0^3}. \tag{43}$$

By changing the variable t to $1+is/2ka$, (32) reduces to

$$W_1 = -\operatorname{Im}\frac{e^{4ika}}{4\pi^3k^3a^2}\left(\frac{i}{ka}\right)^{1/2}\int_0^\infty ds\, s^{-1/2}$$
$$\cdot e^{-s}\left[1+\frac{is}{4ka}\right]^{-1/2} R_2\left(1+\frac{is}{2ka}\right). \tag{44}$$

Substituting this value for $R_2(1+is/2ka)$ from (43), and simplifying the integrand in (44) by retaining only terms up to order $(ka)^{-2}$, (44) may be reduced to yield

$$\frac{W_1}{2a} = -\frac{\sin\left(4ka+\frac{\pi}{4}\right)}{128\pi^{3/2}(ka)^{7/2}} + \frac{21\cos\left(4ka+\frac{\pi}{4}\right)}{2048\pi^{3/2}(ka)^{9/2}}$$
$$+ \frac{861\sin\left(4ka+\frac{\pi}{4}\right)}{65{,}536\pi^{3/2}(ka)^{11/2}}. \tag{45}$$

With (30), (39) and (44), the first six terms in the asymptotic series for the transmission coefficient are obtained as follows:

$$t = \frac{\sigma}{2a} = \frac{1}{\sqrt{2\pi}}\frac{2}{(ka)^{1/2}} - \frac{1}{\sqrt{2\pi}}\frac{1}{8(ka)^{3/2}} + \frac{1}{\sqrt{2\pi}}\frac{3}{2^3(ka)^{5/2}}$$
$$+ \frac{1}{\sqrt{2\pi}}\frac{1}{(ka)^{7/2}}\left[\frac{15}{2^{12}} - \frac{\sin\left(4ka+\frac{\pi}{4}\right)}{64\sqrt{2\pi}}\right]$$
$$- \frac{1}{\sqrt{2\pi}}\frac{1}{(ka)^{9/2}}\left[\frac{525}{2^{18}} - \frac{21\cos\left(4ka+\frac{\pi}{4}\right)}{1024\sqrt{2\pi}}\right]$$
$$- \frac{1}{\sqrt{2\pi}}\frac{1}{(ka)^{11/2}}\left[\frac{6615}{2^{22}} - \frac{861\sin\left(4ka+\frac{\pi}{4}\right)}{32768\sqrt{2\pi}}\right]. \tag{46}$$

It is instructive to examine how the various terms in (46) arise, if the ray picture is used to interpret the phenomenon. It is known that the far field in the direction of the incident wave determines the transmission cross section. For the grazing incidence, no ray directly traverses the aperture. Hence there is no geometrical optics term in (46). The incident ray hitting the edge P_1 produces diffracted rays which, according to Keller's[3] theory, all lie in a plane perpendicular to the screens. The diffracted ray, from the edge P_1 traveling in the direction of the incident wave, is intercepted by the edge P_2 and, therefore, does not directly contribute to the far field in the forward direction. If the diffraction

[3] J. B. Keller, "Diffraction by an aperture," *J. Appl. Phys.*, vol. 28, pp. 426–444; April, 1957.

process is considered as a sequence of diffractions by the two half planes, then, in the solution (28), each iteration gives the effect of one more diffraction in the sequence. Only the rays diffracted at the edge P_2 *directly* contribute to the forward field and it is because of this fact that, in the iterative solution (28), only every other iteration contributes to the solution.

The incident ray and that ray diffracted by the edge P_1 proceeding in the incident direction are diffracted by the edge P_2. The first diffraction at P_2 reduces the order of the incident field by $(ka)^{-1/2}$. The field associated with the ray diffracted by P_2 is characterized by an infinite series in which each term is order $(ka)^{-1}$ lower than the preceding term. Consequently, the first diffraction at P_2 will contribute terms proportional to $(ka)^{-1/2}$, $(ka)^{-3/2}$, etc. to the cross section. Every subsequent diffraction at the edges reduces the order of the field by $(ka)^{-3/2}$. It is therefore evident that the second diffraction at P_2 will contribute terms proportional to $(ka)^{-7/2}$, $(ka)^{-9/2}$, etc. to the cross section. In the same manner, the third diffraction at P_2 will give rise to terms proportional to $(ka)^{-13/2}$, $(ka)^{-15/2}$, etc. The work of Levine was limited to finding the contribution from the rays diffracted once from P_2. Since the behavior of the subsequent diffractions at P_2 is different from that of the first diffraction and since Levine's work, in principle, cannot give the higher-order terms, this investigation was undertaken. Levine[1] had obtained the first two terms in (46).

Numerical values of the transmission coefficient (46) are obtained for the range $2 \leq ka \leq 10$ and are listed in Table I.

In Fig. 2 a graphical presentation of the transmission coefficient is given for the range $2 \leq ka \leq 10$. This curve approaches the value zero as ka is made indefinitely large.

TABLE I

TRANSMISSION COEFFICIENT FOR GRAZING INCIDENCE-*H* POLARIZATION

ka	*t*	*ka*	*t*	*ka*	*t*
2.0	0.548145	5.0	0.352448	8.0	0.279917
2.5	0.492579	5.5	0.336424	8.5	0.271683
3.0	0.451394	6.0	0.322399	9.0	0.264135
3.5	0.419073	6.5	0.309990	9.5	0.257182
4.0	0.392873	7.0	0.298917	10.	0.250751
4.5	0.371020	7.5	0.288951		

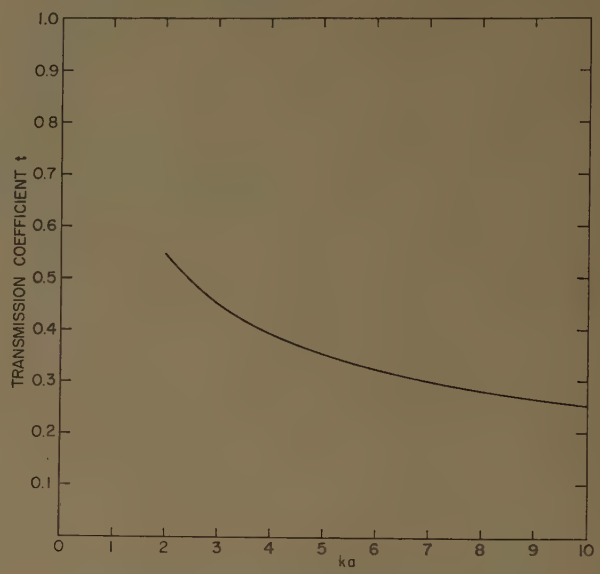

Fig. 2—Transmission coefficient as a function of *ka* for grazing incidence.

ACKNOWLEDGMENT

The authors are indebted to Prof. R. W. P. King for encouragement of this research and for his criticism of the manuscript.

The Calculation of Reflector Antenna Polarized Radiation*

LOUIS E. RABURN†

Summary—**A partly analytical process is described for calculating the far-zone patterns of reflector antennas which may have nonlinear polarization. Wave polarization equations are given for a focused but not necessarily symmetrical paraboloid. The process applies for any point-source feed whose radiation characteristics, including wave polarization, are known either by theory or measurements.**

Calculated and measured patterns are given for a fan-beam antenna whose reflector is 120 λ high and 30 λ wide. They agree well near the axis and agree qualitatively for off-axis angles of several beamwidths. The sources of errors are discussed.

Introduction

IT is well known that where a paraboloid reflector is fed by a linearly polarized electric dipole, the antenna system will radiate an appreciable amount of cross-polarized energy, assuming that the reflector surface is, for electrical purposes, a continuous sheet. This partial conversion of the wave polarization is caused by oblique reflections of the dipole's linearly polarized wave from the curved inner surface of the reflector.

This effect was first analyzed by Condon[1] and has been the subject of a recent study.[2] If the paraboloid is symmetrical about its axis and is illuminated symmetrically, the cross polarization is zero on axis and generally appears as a family of four sidelobes midway between the horizontal and vertical principal planes of the antenna. These lobes deserve consideration, since they lie close to the main beam and seriously degrade circular- and dual-mode polarized antennas. The procedure described herein was developed for calculating the secondary field polarization characteristics and patterns of various feed and reflector systems. It applies to one linear-polarization mode at a time but can be extended to the case of circular polarization, since this case can be split into two orthogonal linear-polarization modes which can be treated independently, with due regard for the time quadrature requirement at the feed aperture and in the far field.

This calculation procedure treats the radiation process of the antenna in three separate steps (see Fig. 1). 1) The far-zone field components of the primary feed element are assumed or measured. 2) These components are considered to propagate from the phase center point source of the primary feed to the reflector surface, and then to reflect into an assumed "aperture plane" with components which can be exactly calculated by simple trigonometric equations. 3) The far-zone radiation field components are then calculated as a function of angular direction by direct integration of the aperture-plane fields, with due allowance for time retardation.

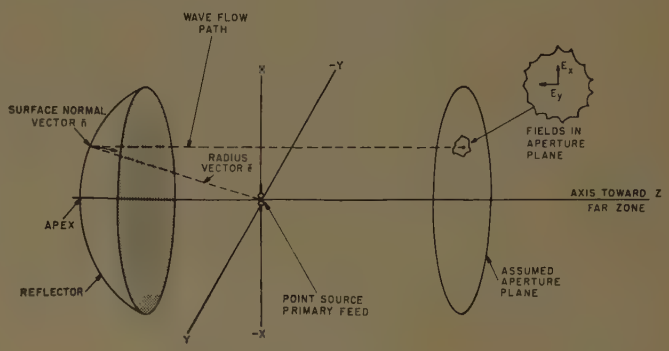

Fig. 1—Three reflector antenna components.

This process does not consider "spill-over," namely, the direct radiation of the primary feed in directions such that it is not intercepted by the reflector. The radiation field of this spill-over is directly related to the directive gain pattern of the primary feed in these directions, and, if appreciable, can be measured and superposed with proper phase on the far-zone fields due to the aperature-plane distribution calculated in step 3. Although this phase determination is a critical problem, it can be done to the precision of the known phase center location for the primary feed in the directions of spill-over and the focal location of the primary feed's phase center.

Practical primary feeds are usually not an elemental type whose far-zone field components are simply calculated, so it is necessary to construct an experimental model of the feed and measure these components. This experimental model can be constructed to any convenient scale factor and measured on a conventional short-span pattern range having a single-axis pedestal.

The equations for calculating the aperture-plane fields due to the primary feed field components are derived by a generalization of the vector trigonometry procedure previously used by Condon[1] and Silver[3] for the case of the fields reflected off a perfect conductor surface. This procedure is derived from geometric optics and employs two assumptions which should be quite suitable in most cases. The first assumption is that the reflector surface has such a gentle curvature that it can be considered as composed of many small reflector elements, each of which behaves as a flat plane reflector such that conventional laws of reflection are valid. In

* Manuscript received by the PGAP, May 25, 1959.
† Philco Corporation, Philadelphia, Pa.

[1] E. U. Condon, "Theory of Radiation from Paraboloid Reflectors," Westinghouse Res. Rept. SR 105; September, 1941.

[2] E. M. T. Jones, "Paraboloid reflector and hyperboloid lens antennas," IRE TRANS. ON ANTENNAS AND PROPAGATION, vol. AP-2, pp. 119–127; July 1954.

[3] S. Silver, "Microwave Antennas," M.I.T. Rad. Lab. Ser., McGraw-Hill Book Co., Inc., New York, N. Y., vol. 12, ch. 5.

other words, this procedure could not account for reflections from a thin metallic grating. The second assumption is that effects at the edge of the reflector can be neglected. This assumption is also a common one with considerable justification in the case of apertures over 10 wavelengths across.

Coordinate Systems

Three coordinate systems are used in the general procedure and in this section the systems and their applications are described. Two other coordinate systems are used in this section for convenience in deriving the expressions for a paraboloid's reflections. Fig. 2(a), (b) and (c) shows the three general systems and Fig. 2(d) shows the paraboloid's system used here. These coordinate systems were initially chosen for evaluation of a vertical dipole feed element and may seem most logical for this element, but they are equally valid for any other type of primary feed.

The first system is used in step 1 to express and, when necessary, to measure the primary feed's field components which illuminate the reflector. It is a conventional spherical one in (θ, ϕ, R), as far as point locations are concerned. Its origin is at the feed's phase center, its axis $(\theta=0/180°)$ vertical, and its aximuth zero $(\phi=0)$ toward the reflector's apex. The field vectors in the far-zone are functions of θ and ϕ but are defined as E_m and E_c rather than the conventional E_θ and E_ϕ. This is done because the latter components are ambiguous in the normally forbidden polar zones near $\theta=0$ and $\theta=\pi$. This type of ambiguity also occurs when an aircraft flies over the earth's North Pole and its course changes from due north to due south in an infinitesimal time, regardless of its flight path meridian. These field components have continuity through the polar zones for many feeds and these components are treated without ambiguity by the rectangular coordinate system shown in Fig. 2(d). The field vector E_m on the sphere's surface is aligned with a meridional great-circle $(\phi_1; \phi_1+180°)$ and is very similar to E_θ. The alignment of $+E_m$ is in the direction for increasing θ in the forward hemisphere $0<\theta<180°$. The other field vector on the sphere's surface, $+E_c$, is aligned perpendicular to E_m in the direction of increasing ϕ, so it is the counterpart to E_ϕ. If the feed's radiation in a given direction is linearly polarized, the E_m and E_c are in time-phase, and only their polarity remains to be determined. If the radiation is not linearly polarized, then the time-phase angle also must be determined. These fields and their polarizations can be simply measured with a scaled model feed on a short-span antenna range as described in the next section.

The second coordinate system is used in step 2 to express the calculated fields reflected into the aperture plane. It is a conventional rectangular system in $(X, Y,$ and $Z)$, [see Figs. 2(b) and 1]. The origin is on the reflector's axis with positive Z in the direction of propagation (forward), [see Fig. 2(b)]. The field vectors in the

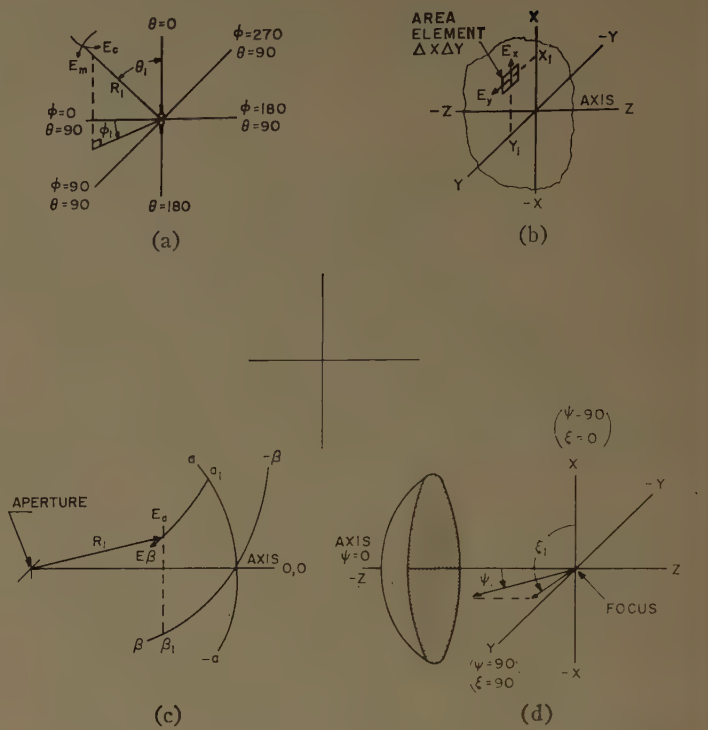

Fig. 2—Four coordinate systems with field components. (a) Spherical for primary feed. (b) Cartesian for aperture plane. (c) Modified spherical for secondary pattern. (d) Cartesian and spherical for paraboloid reflector.

aperture plane are functions of X, and Y, and are defined as E_x and E_y. The E_z component is neglected since, even if appreciable, it does not contribute significant radiation in the directions close to the Z axis. The E_x and E_y fields are defined to have positive polarity if their directions are in the direction of increasing X and Y coordinates, respectively. If the components E_x and E_y are in time-phase, the primary feed components E_m and E_c also will be in time-phase.

The third coordinate system is used in step 3 to express the far-field diffraction patterns which are calculated as the result of all the contributing aperture plane field components. It is a spherical one in (α, β, ρ) which is closely related to Mercator projection used in mapping. Its origin is on the axis of the aperture plane with its α axis vertical and its β axis horizontal. The far-zone secondary radiation field components are functions of α and β, and are defined as E_α and E_β. Again the polarity of these components is defined as positive when the fields are in the direction of increasing angles. These fields are those measured in a relative way on long span antenna range.

Step 1, Primary Feed Measurements

If the primary feed antenna differs from the three elemental types treated by Jones,[2] it is necessary to determine by measurements its radiation field characteristics in all directions subtended by the reflector. These characteristics are relative field components, wave polarization, and phase center coincidence.

The spherical coordinate system for the primary feed's field components is shown in Fig. 2(a). The field components are simply related to the polarization angle in every direction where the radiation for a particular feed mode is linearly polarized. (It has been found that several conventional linear-polarized feeds fulfill this requirement well in all directions subtended by the reflector.) In this linear-polarization case when the E_m and E_c components are measured, their relative polarity is determined by the direction of rotation which the maximum field, the vector sum of E_m+E_c, has from the meridian plane.

A suitable antenna range setup for measuring the far-field radiation characteristics of test feeds is shown in Fig. 3. This setup requires only a linear-polarized reference antenna, a single-axis pedestal, a tiltable yoke or support, a nonmetal vertical column, and several conventional items of microwave test equipment. The pattern plotting can be done either manually or automatically, depending upon available equipment and the accuracy desired.

The simple adjustable yoke on top of the column must provide as much tilt above and below the horizontal plane as the maximum horizontal plane angle "$\angle\phi$" subtended by the reflector. The test feed is mounted on its side so its vertical ($\theta=0/180°$) axis is horizontal. The angles of θ and ϕ provided by column rotation and yoke tilt, respectively, are (90, 0) when the reference antenna is on the $-Z$ axis of the illuminated reflector.

The field moments need be measured only for the values of θ and ϕ corresponding to match points or the centers of incremental areas in the aperture plane. The equations for calculating these values of θ and ϕ are given in the following section.

The reference antenna is first set for horizontal polarization and a relative directivity pattern of E_m as a function of θ for $\phi=0/180°$ is plotted by rotating the pedestal throughout the vertical plane angle subtended by the reflector. The reference antenna is then set for vertical polarization and a pattern of E_c vs θ is measured.

An appropriately chosen new meridian-pattern cut is then provided by tilting the test feed support mount on top of the column an amount ϕ_1. The relative directivity patterns for both polarizations of the reference antenna are then measured in path (ϕ_1;$\phi_1+180°$) without changing the power of the signal source of the receiver sensitivity. In like manner, the E_m and E_c fields are measured for all appropriate values of θ and ϕ which represent directions from the feed focus to incremental areas on the reflector, as well as other angles of interest where direct radiation may be appreciable.

If the feed differs from a simple dipole, it will have appreciable amounts of both E_m and E_c in some directions. Then either a shift in linear-polarization direction or else elliptical polarization is indicated. To determine

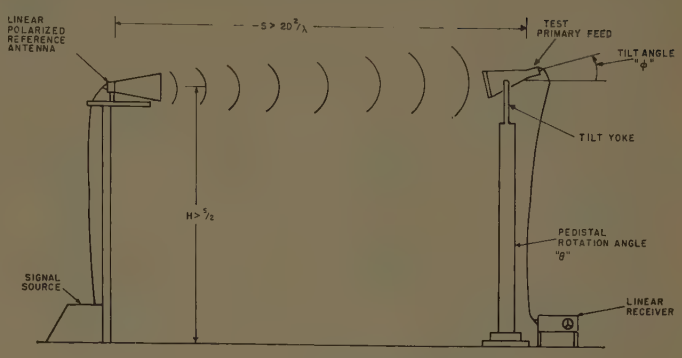

Fig. 3—Primary feed measuring setup.

which it is, rotate the reference antenna at least 180° on axis while observing the signal variation. If a very deep null is found for some alignment of the linearly polarized reference antenna, the feed's field is also linearly polarized. This is a convenient and reliable check on the primary feed when linear polarization is required, and it should be employed in all doubtful directions subtended by the reflector. Assuming that the radiation of the test feed is linearly polarized, the polarity relationship of the E_m and E_c field components is determined experimentally by noting whether the reference antenna must rotate clockwise or counterclockwise from the vertical position to reach the nearest null. If the former, E_m and E_c are of opposite polarity. If the latter, E_m and E_c have the same polarity.

Step 2, Aperture Plane Field Calculations

After the radiation field components of a specific primary feed have been determined, they are then used in analytical equations to calculate the aperture plane, (AP) field components for the specific type of reflector. The equations for a perfect paraboloid reflector with a point source primary feed at its focus have been derived in the Appendix.

These equations for the paraboloid are:

$$E_{ax} = \frac{E_M(\sin\theta + \cos\phi) - E_c(\cos\theta \sin\phi)}{1 + \sin\theta\cos\phi}\left(\frac{f}{r}\right)$$

$$E_{ay} = \frac{-E_m(\cos\theta \sin\phi) - E_c(\cos\phi + \sin\theta)}{1 + \sin\theta\cos\phi}\left(\frac{f}{r}\right)$$

where r is the distance from feed to reflector surface and f is the focal distance.

The calculation procedure is straightforward and not too tedious if only twenty or so points in the aperture plane are considered.

The integration process in step 3 requires the choice of nearly equal increments for the aperture-plane areas. Then the values (x, y) for the center of each area determine the corresponding vaules of (θ, ϕ) for measuring the feed's characteristics and calculating the AP fields.

These relations are

$$\theta = \cos^{-1} x/r$$

$$\phi = \sin^{-1} y/r \sin\theta$$

$$r = \left[x^2 + y^2 + \left(f - \frac{+x^2+y^2}{4f}\right)^2\right]^{1/2}.$$

Step 3, Far-Field Pattern Calculations

A general equation for the far-field (Fraunhofer) diffraction pattern of an illuminated aperture has been given by Silver.[3] This equation in the coordinate systems shown in Fig. 2(b) and (c), and assuming small values of α and β at range R gives

$$E_\alpha = F\int_A E_{ax} e^{+jk(x \sin\alpha_1 + y \sin\beta_1)} dxdy$$

$$E_\beta = F\int_A E_{ay} e^{+jk(x \sin\alpha_1 + y \sin\beta_1)} dxdy$$

$$F = \frac{je^{-jkR}}{\lambda R}$$

$$k = \frac{2\pi}{\lambda}.$$

These integral expressions can be solved either analytically or by incremental parts which synthesize the aperture plane. A convenient way to do the latter is with a distribution of discrete, illuminated rectangular elements of height ΔX_n and width ΔY_n. Then, near the axis:

$$E_\alpha = F\Sigma^n E_{ax} e^{+jk(X_n \sin\alpha_1 + y_n \sin\beta_1)} \frac{\sin H_n}{H_n} \frac{\sin W_n}{W_n}$$

$$E_\beta = F\Sigma^n E_{ay} e^{+jk(X_n \sin\alpha_1 + y_n \sin\beta_1} \frac{\sin H_n}{H_n} \frac{\sin W_n}{W_n}$$

$$H_n = \frac{\pi}{\lambda} \Delta X_n \sin\alpha \cos\beta$$

$$W_n = \frac{\pi}{\lambda} \Delta Y_n \sin\beta \cos\alpha.$$

The terms

$$\frac{\text{“sin } H_n\text{”}}{H_n} \quad \text{and} \quad \frac{\text{“sin } W_n\text{”}}{W_n}$$

are conventional for the diffraction pattern of the uniformly illuminated elemental areas. The dimensions ΔX_n and ΔY_n need not be the same in neighboring elements, and in fact, systematic errors are reduced if they are chosen unequal.

The choice of the quantity of area elements and their shapes is a matter of judgment, the required accuracy and the maximum off-axis angles required. If too few moments are used, they obviously cannot accurately represent with their finite steps actual field distributions which vary smoothly across the aperture plane. If too many moments are chosen the work in steps 1, 2 and 3 for each moment becomes prohibitive, especially if manual calculation is used in 3. Even when the IBM No. 650, a high-speed digital computer, is used in step 3, it lacks memory capacity and requires considerable programming and computing time. A Transac 5-2000 has more memory and should simplify the programming, but this type of machine is expensive to rent.

The general trend has been indicated by calculations for a modified dipole feeding an offset paraboloid with a −15 db taper. When the number of elements in height were increased from 4 to 8, the 3-db and 10-db vertical plane bandwidth did not change, the first cross-polarized side lobe level changed from −19 to −17 db, and the first direct-polarized side lobe level changed from approximately −34 db to −24 db. The radiation characteristics of most feeds vary smoothly enough with θ and ϕ so that quantitative engineering answers can be obtained in the main lobe and the first cross-polarized side lobes if the aperture plane is simulated by an 8 by 8 array of uniform elements. If quantitative data are also required on the first direct polarized side lobe which is further off axis, then more elements should be used.

No doubt, if the area elements could have arbitrary slopes in both the X and Y directions, these would approximate an actual taper illumination distribution much better than elements with uniform illumination. But the phase-step error would remain and expressions for the diffraction patterns of various elemental slopes would have to be derived.

A more elegant approach is to represent the two aperture-plane field distributions by linear polynomials whose terms are chosen for best fit by a digital computer. The area of the aperture plane is approximated by some analytical plane surface, and then the integration for the far-field is done analytically for each polynomial term. Then the computer is also used to calculate the values of the analytical functions for any special arguments not given in existing mathematical tables. This has been done for trapezoidal, elliptical, and one family of compound surfaces.[4] Another approach using an inverse matrix for machine computations has been described recently.[5]

Measured and Calculated Antenna Characteristics

This evaluation process was used to calculate the direct- and cross-polarized radiation patterns of a fan-beamed antenna with a sheet reflector. These calculated patterns are directly compared with the measured patterns for the same antenna. The measured patterns in the azimuth and elevation principal planes are shown in Figs. 4 and 5.

[4] B. Podolsky, AVCO Mfg. Corp., Crosley Div., Cincinnati, Ohio; unpublished memo.

[5] M. Hoffman, “The Utility of the Array Pattern Matrix for Linear Array Computation,” Philco Rept. PC-668.

Fig. 4—β (minor axis) patterns.

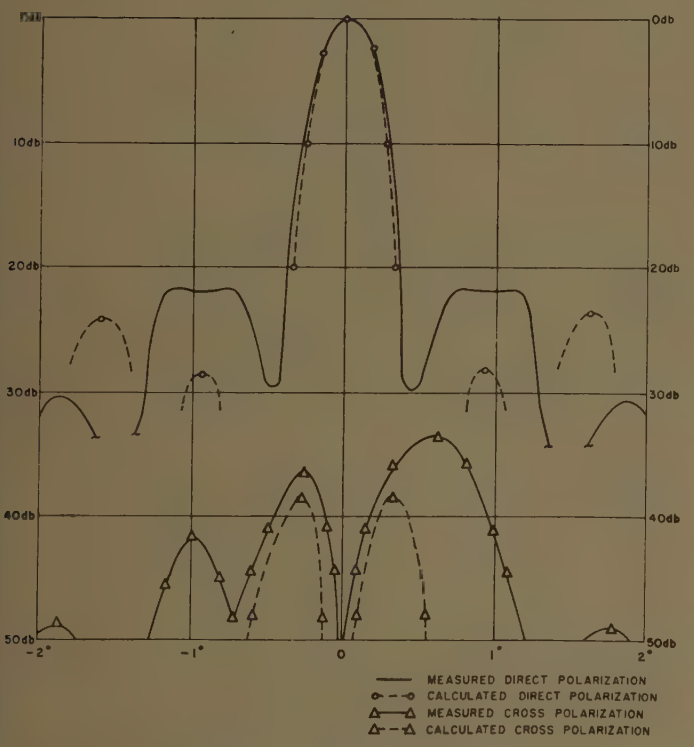

Fig. 5—α (major axis) patterns.

There was no measured cross-polarized radiation in the azimuth plane as would be expected since the antenna is symmetrical vertically.

The antenna as shown in Fig. 6 has an aperture plane which was approximated by 30 equal rectangular elements. The primary feed is an H-plane sectoral horn

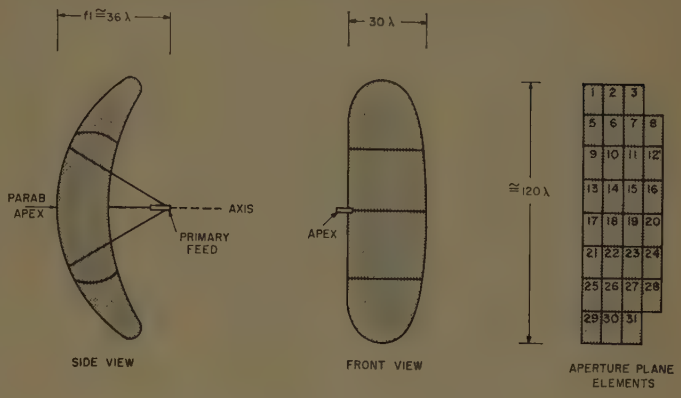

Fig. 6—Fan-beam antenna system.

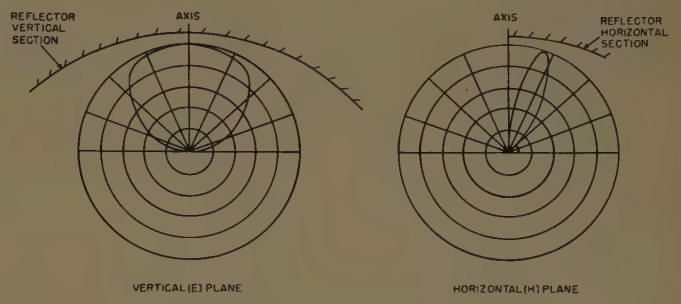

Fig. 7—Principal plane patterns of primary feed horn.

designed to illuminate the reflector only vertically polarized with an edge taper of about -15 db, and no special design attention had been given to its cross-polarization characteristics.

The far-zone radiation characteristics of the primary feed were measured as described above for step 1. Conventional E- and H-plane patterns for both E_m and E_c polarization were first measured for general reference and to give check points (see Fig. 7). The relative intensity of the E_m and E_c fields were then measured at angles representing the centers of the 30 elemental panels when projected on the reflector surface. These are shown in Fig. 8.

For step 2 the space attenuation factors and then the aperture-plane fields were calculated as described in the section on AP field calculations. The resulting E_{ax} and E_{ay} at the panel centers are also shown in Fig. 8.

For step 3 the secondary patterns were calculated in the vertical (α) and horizontal (β) principal planes. These calculations were done on an IBM 650 digital computer and the results were as follows: In the α plane, -3 db beamwidth 0.57°, -10 db beamwidth 1.0°, first cross-polarized sidelobe at ± 0.3,° and with a level of -39 db, first direct-polarized sidelobe at ± 1.6°, and a level -24 db. In the β plane, -3 db beamwidth $= 1.9$°, -10 db beamwidth $= 3.4$°, first direct-polarized sidelobe at ± 6°, and level -19 db. These significant parts of these calculated patterns are also shown in Figs. 4 and 5. They compare well with the measured patterns

Panel #	1 and 29	2 and 30	3 and 31	
θ at Center	19.1° 160.9°	20.9° 159.1°	25.7° 154.3°	
ϕ at Center	−12.5°	−35°	−52°	
E_m at Center 1)	0.20	0.35	0.240	
E_c at Center 1) 2)	0.016	0.11	0.141	
Space α at Center	0.66	0.65	0.64	
Calc. E_{ax}	0.13	0.15	0.11	
Calc. E_{ay}	+0.10 −0.10	+0.02 −0.02	+0.194 −0.194	
Panel #	5 and 25	6 and 26	7 and 27	8 and 28
θ at Center	36.2° 143.8°	37.5° 142.5°	40.1° 139.9°	43.5° 136.5°
ϕ at Center	−8.4°	−24.4°	−39°	−52°
E_M at Center 1)	0.24	0.51	0.39	0.21
E_c at Center 1) 2)	0.02	0.08	0.14	0.125
Space α at Center	0.79	0.78	0.76	0.72
Calc. E_{ax}	0.153	0.314	0.223	0.124
Calc. E_{ay}	+0.002 −0.002	+0.018 −0.018	−0.006 +0.006	+0.015 −0.015
Panel #	9 and 21	10 and 22	11 and 23	12 and 24
θ at Center	56.0° 124.0°	56.8° 123.2°	58.2° 121.8°	60.3° 119.7°
ϕ at Center	−7°	−20°	−33°	−45°
E_m at Center 1)	0.33	0.81	0.66	0.26
E_c at Center 1) 2)	0.002	0.003	0.10	0.06
Space α at Center	0.91	0.90	0.86	0.81
Calc. E_{ax}	0.275	0.64	0.49	0.19
Calc. E_{ay}	+0.004 −0.004	+0.043 −0.043	+0.008 −0.008	+0.000 −0.000
Panel #	13 and 17	14 and 18	15 and 19	16 and 20
θ at Center	78.4° 101.6°	78.6° 101.4°	79.1° 100.9°	79.8° 100.2°
ϕ at Center	−6°	−18°	−31°	−42°
E_m at Center 1)	0.355	0.88	0.78	0.31
E_c at Center 1) 2)	0.025	0.025	0.05	0.022
Space α at Center	0.99	0.97	0.91	0.86
Calc. E_{ax}	0.358	0.82	0.66	0.302
Calc. E_{ay}	+0.015 +0.015	+0.003 −0.003	−0.008 +0.008	−0.011 +0.011

Note: 1) Measured fields balanced for symmetry
2) Feed field linearly polarized to an ellipticity ratio exceeding 30 db and rotated from meridian C.C.W. in top half; C.W. in lower half of reflector.

Fig. 8—Illumination and aperture plane fields of fan-beam antenna.

only near the axis, and fair quantitative agreement exists in the first cross-polarized sidelobes in the α plane. Much better quantitative agreement for off-axis has been obtained by the analytic integration process. The other major sources of error are experimental measurements of E_m and E_c, and reflector imperfections. The dissymmetry in the α plane cross-polarization pattern may be caused by a known unsymmetrical deformation in the reflector surface.

Conclusions

A process for evaluating the pattern and polarization characteristics of reflector antennas has been described. This process checks out well with measurements for angles near the axis.

It is considered that patterns calculated by the incremental process agree well close to the axis, but give only qualitative agreement for off-axis angles of α greater than one beamwidth. The analytic process has given good agreement for off-axis angles of several beamwidths. Both calculation processes are subject to the following error sources:

1) Imperfections in the reflector surface.
2) Experimental errors in the E_m and E_c measurements.

Appendix

Reflection Expressions for Paraboloid

Assume that a large, gently curved reflector surface with an outward normal $\bar{n}$ is illuminated by a radiation field of electric intensity $\overline{E}$, propagating in the direction $\bar{\rho}$ from a point source. A surface current K flows on the reflector such that[6]

$$\overline{K} = \frac{2}{n}\lambda\,\bar{n}(x\bar{\rho}\times\overline{E})$$

$$= \frac{2}{n}\left[\bar{\rho}(\bar{n}\cdot\overline{E}) + \overline{E}\cos\Psi/2\right]\text{amps/m.} \qquad (1)$$

Then the field reflected into the aperture plane is

$$E_\alpha = \frac{-n}{2\cos\Psi/2}\,\overline{K}. \qquad (2)$$

Since the primary feed acts as a point source and is in free space with the spherical coordinate system of Fig. 2(a), the radiation field can be expressed by the arbi-

[6] S. Silver, "Microwave Antenna Theory and Design," McGraw-Hill Book Co., Inc., New York, N. Y., p. 134.

trary components E_m and E_c. These fields in the rectangular system of Fig. 2(d) are

$$\bar{E} = \bar{x}(-E_m \sin\theta) + \bar{y}(E_m \cos\theta \sin\phi + E_c \cos\phi) + \bar{z}(-E_m \cos\theta \cos\phi + E_c \sin\phi). \quad (3)$$

By inspection, the propagation unit vector is

$$\bar{\rho} = \bar{x} \cos\theta + \bar{y} \sin\theta \sin\phi - \bar{z} \sin\theta \cos\phi. \quad (4)$$

The unit normal for a paraboloid, using the spherical coordinate system of Fig. 4(d) is[5]

$$\bar{n} = \bar{z} \sin\Psi/2 \cos\xi = \bar{y} \sin\Psi/2 \sin\xi + \bar{z} \cos\Psi/2. \quad (5)$$

Table I, showing the coversion between this system and that in Fig. 2(a), can be written by inspection.

TABLE I

System	x/r	y/r	z/r
θ, ϕ	$\cos\theta$	$\sin\theta \sin\phi$	$-\sin\theta \cos\phi$
Ψ, ξ	$\sin\Psi \cos E$	$\sin\Psi \sin E$	$-\cos\Psi$

Then

$$\cos\Psi = \sin\theta \cos\phi \equiv Q; \quad \sin\Psi = \sqrt{(1+Q)(1-Q)}$$

$$\sin\Psi/2 = \sqrt{\frac{1-Q}{2}}; \quad \cos\Psi/2 = \sqrt{\frac{1+Q}{2}}$$

and

$$\cos\xi = \frac{\cos\theta}{\sqrt{(1+Q)(1-Q)}}; \quad \sin\xi = \frac{\sin\theta \sin\phi}{\sqrt{(1+Q)(1-Q)}}. \quad (6)$$

Using routine manipulations,

$$\bar{n}\cdot\bar{E} = E_m\left(\frac{\sin\theta \cos\theta \cos^2\phi}{\sqrt{2(1+Q)}} - \cos\theta \cos\phi \cos\Psi/2\right) + E_c\left(\frac{-\sin\theta \sin\phi \cos\phi}{\sqrt{2(1+Q)}} + \sin\phi \cos\Psi/2\right). \quad (7)$$

Completing the vector multiplication for $\bar{x}$ terms,

$$\left(\frac{n}{2}\right) K_x = E_m \cos\Psi/2\left(\frac{-\sin\theta - \cos\phi}{1+\sin\theta\cos\phi}\right) + E_c \cos\Psi/2\left(\frac{\cos\theta \sin\phi}{1+\sin\theta\cos\phi}\right) \quad (8)$$

so:

$$E_{ax} = \frac{E_m(\sin\theta + \cos\phi) - E_c(\cos\theta \sin\phi)}{1+\sin\theta\cos\phi}. \quad (9)$$

Completing the vector multiplication for $\bar{y}$ terms,

$$\left(\frac{n}{2}\right) K_y = E_m \cos\Psi/2\left(\frac{\cos\phi \sin\phi}{1+\sin\theta\cos\phi}\right) + E_c \cos\Psi/2\left(\frac{\sin\theta\cos\phi}{1+\sin\theta\cos\phi}\right) \quad (10)$$

so

$$E_{ay} = \frac{-E_m(\cos\theta \sin\phi) - E_c(\sin\theta + \cos\phi)}{1+\sin\theta\cos\phi}. \quad (11)$$

ACKNOWLEDGMENT

The development and measurements described herein have been assisted considerably by the following Crosley AVCO technical personnel: Dr. G. Bruck, Dr. B. Podolsky, L. Brueneman, J. Gruber, R. Schmidt, and G. Seward.

Maximum Angular Accuracy of Tracking a Radio Star by Lobe Comparison*

ROGER MANASSE†

Summary—**A general expression is derived for the maximum angular accuracy of tracking a radio star by lobe comparison (or monopulse). This angular accuracy depends on the input signal-to-noise ratio, the wavelength, the time-bandwidth product of signal integration, and the effective length of the antenna aperture. The maximum angular accuracy can be obtained, approximately, by performing a simple correlation of odd and even components of the antenna output. Angular accuracy formulas for simple antenna dishes or for interferometers appear as special cases of the general result.**

The Appendix discusses the interferometer technique in more detail, and the angular accuracy for the data processing technique used by M. Ryle is compared with that obtained from the optimum processing.

A NUMBER of situations exist in which it is desirable to obtain, with the aid of an antenna aperture of restricted size, very accurate angle measurements on a radiating noise source such as a radio star. For example, one might wish to use accurate angle measurements to study angle-of-arrival fluctuations introduced by propagation through the troposphere and/or the ionosphere. Another example might be the use of accurate angle measurements on stars for stellar navigation. It is the purpose of this paper to determine the maximum angular accuracy and the optimum signal processing in terms of a reasonable model for the angular accuracy problem which holds for an antenna aperture of arbitrary shape.

For the purpose of the analysis to follow, it is assumed that a radio star is a point source of noise. In the presence of external background noise and internal receiver noise we desire to estimate the apparent angular position of a radio star from the stellar noise waveform incident on the antenna aperture. The aperture is not necessarily simply connected, *e.g.*, it may consist of two or more disjoint coplanar areas. The antenna tracks the radio star and, thus, it may be assumed that the aperture plane is approximately normal to the direction of the star. The antenna is taken to operate only over a narrow band of frequencies, as usual, and the spectrum of the radio star is approximately flat over this band.[1] For simplicity we consider the estimation of the angle of arrival, denoted by θ, in one plane only. The generalization of the theory to two dimensions should be straightforward. θ is assumed to remain approximately constant during the measurement.

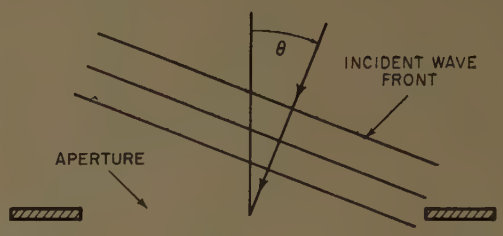

Fig. 1.

The lobe comparison technique[2] may be analyzed as follows. Construct two time outputs by taking the sum and difference of outputs corresponding to the two lobes of the lobe comparison scheme; *i.e.*, an even output $x_e(t)$ corresponding to a voltage gain pattern which is even in θ, and $x_o(t)$ corresponding to a voltage gain pattern which is odd in θ[2]. We define

$s(t) \equiv$ waveform from the radio star received by an antenna with unity gain.
$A_e(\theta) \equiv$ one-way even voltage gain pattern.
$A_o(\theta) \equiv$ one-way odd voltage gain pattern.
$n_e(t) \equiv$ noise waveform associated with $x_e(t)$.
$n_o(t) \equiv$ noise waveform associated with $x_o(t)$.

Then we may write

$$x_e(t) = A_e(\theta)s(t) + n_e(t)$$
$$x_o(t) = A_o(\theta)s(t) + n_o(t). \tag{1}$$

Because θ is assumed small, one may approximate

$$A_e(\theta) \approx A_e(0)$$
$$A_o(\theta) \approx A_o'(0)\theta. \tag{2}$$

So

$$x_e(t) = A_e(0)s(t) + n_e(t)$$
$$x_o(t) = A_o'(0)\theta s(t) + n_o(t). \tag{3}$$

In order to simplify the notation which follows, we set $A_e(0) = \alpha$ and $A_o'(0) = \beta$. Generally α and β are complex and give both an amplitude change and a phase shift of $s(t)$. Clearly the time origins of $x_e(t)$, $n_e(t)$, $x_o(t)$, $n_o(t)$ can be redefined so that α and β are real. Thus we may

* Manuscript received by the PGAP, January 5, 1959; revised manuscript received, June 22, 1959. The work reported in this paper was performed by Lincoln Lab., a center for research operated by Massachusetts Institute of Technology with the joint support of the U. S. Army, Navy, and Air Force.

† The MITRE Corp., Bedford, Mass.; formerly at Lincoln Lab., Mass. Inst. Tech., Lexington, Mass.

[1] The results of this paper may be extended to include a point source radiating a band of colored noise. For the stellar noise source the usable spectrum of noise is usually determined by the pass band of the receiver.

[2] Essentially this is the same as the so-called monopulse technique except that the received signal is not pulsed. The application of the monopulse technique to the radio astronomy problem has been suggested by Page [1].

assume without loss of generality that all quantities in (3) are real.

It is assumed that the received signal, the receiver noise and the background noise radiation are such that $s(t)$, $n_e(t)$, and $n_o(t)$ are statistically independent and behave as narrow-band-limited Gaussian noise with a rectangular shaped spectrum of width W centered about a frequency f_0. W represents the width of the signal band which is available for processing. The average power of $s(t)$, $\overline{s^2(t)}$, is denoted σ_s^2. $x_e(t)$ and $x_o(t)$ are assumed to have been normalized so that the average noise powers of $n_e(t)$ and $n_o(t)$ are both equal to σ_n^2, say. Both σ_s^2 and σ_n^2 are assumed to be known. The observation time is restricted to a short interval $(0, T)$ during which time it is assumed that θ is constant. We assume, furthermore, that $TW \gg 1$.

We wish to answer the following two questions. 1) Taking into account the statistical properties of $s(t)$, $n_e(t)$, and $n_o(t)$, how should $x_e(t)$ and $x_o(t)$ be processed in order to obtain the "best" estimate of θ? 2) What rms error in θ is obtained with this procedure? We shall use the probability approach as the method for estimating θ. The estimated value of θ will be that value which maximizes the *a posteriori* probability distribution over θ. The variance of this distribution will measure the error in estimating θ.

The received signal $s(t)$ may be written

$$s(t) = u(t) \cos 2\pi f_0 t + v(t) \sin 2\pi f_0 t, \tag{4}$$

where $u(t)$ and $v(t)$ are independent Gaussian noises with rectangular spectrum of width W centered at zero frequency. According to the sampling theorem, $u(t)$ and $v(t)$ may be represented by sampled values spaced $1/W$ apart in time. In the interval $(0, T)$, $s(t)$ may be (approximately) represented by the sampled values

$$s(t) \leftrightarrow (u^1, u^2, \cdots, u^{TW}, v^1, v^2, \cdots, v^{TW}).$$

We identify $u^i \equiv s^i$ and $v^i \equiv s^{i+TW}$, so that

$$s(t) \leftrightarrow (s^1, s^2, \cdots, s^{2TW}).$$

Similarly,

$$n_e(t) \leftrightarrow (n_e^1, n_e^2, \cdots, n_e^{2TW})$$
$$n_o(t) \leftrightarrow (n_o^1, n_o^2, \cdots, n_o^{2TW})$$
$$x_e(t) \leftrightarrow (x_e^1, x_e^2, \cdots, x_e^{2TW})$$
$$x_o(t) \leftrightarrow (x_o^1, x_o^2, \cdots, x_o^{2TW}).$$

It follows that

$$x_e^i = \alpha s^i + n_e^i \qquad (i = 1, 2, \cdots, 2TW) \tag{5}$$
$$x_o^i \leftrightarrow \beta\theta s^i + n_o^i.$$

For the joint probability distributions we have

$$P(s^1, s^2, \cdots, s^{2TW}) = \prod_{i=1}^{2TW} P(s^i)$$
$$P(n_e^1, n_e^2, \cdots, n_e^{2TW}) = \prod_{i=1}^{2TW} P(n_e^i)$$
$$P(n_o^1, n_o^2, \cdots, n_o^{2TW}) = \prod_{i=1}^{2TW} P(n_o^i) \tag{6a}$$

where for each i

$$P(s^i) = \frac{1}{\sqrt{2\pi\sigma_s^2}} e^{-s^{i2}/2\sigma_s}$$
$$P(n_e^i) = \frac{1}{\sqrt{2\pi\sigma_n^2}} e^{-n_e{}^{i2}/2\sigma_n}$$
$$P(n_o^i) = \frac{1}{\sqrt{2\pi\sigma_n^2}} e^{-n_o{}^{i2}/2\sigma_n^2}. \tag{6b}$$

We compute the conditional probability distribution over θ given $x_e(t)$ and $x_o(t)$ in the interval $(0, T)$, $P(\theta \,|\, x_e(t), x_o(t))$. Using Bayes' theorem,

$$P(\theta \,|\, x_e(t), x_o(t)) = \frac{P(x_e(t), x_o(t) \,|\, \theta) P(\theta)}{P(x_e(t), x_o(t))}, \tag{7}$$

where $P(\theta)$ is the *a priori* probability distribution over θ. Assuming that $P(\theta)$ is essentially constant in the region of interest,[3] and ignoring proportionality constants which are independent of θ, we have

$$P(\theta \,|\, x_e(t), x_o(t)) \sim P(x_e(t), x_o(t) \,|\, \theta)$$
$$\sim \int \cdots \int P(x_e^1, \cdots, x_e^{2TW}, x_o^1, \cdots, x_o^{2TW} \,|\, \theta, s^1, \cdots, s^{2TW}) \cdot P(s^1, \cdots, s^{2TW}) ds^1 \cdots ds^{2TW}$$
$$\sim \int \cdots \int P(x_e^1 \,|\, \theta, s^1) \cdots P(x_o^{2TW} \,|\, \theta, s^{2TW}) \cdot P(s^1) \cdots P(s^{2TW}) ds^1 \cdots ds^{2TW}$$
$$\sim \prod_{i=1}^{2TW} \int P(x_e^i \,|\, \theta, s^i) P(x_o^i \,|\, \theta, s^i) P(s^i) ds^i; \tag{8}$$

($\sim$ = "is proportional to"). From (5) and (6b) we have

$$P(x_e^i \,|\, \theta, s^i) \sim e^{-(x_e^i - \alpha s^i)^2/2\sigma_n^2},$$
$$P(x_o^i \,|\, \theta, s^i) \sim e^{-(x_o^i - \beta\theta s^i)^2/2\sigma_n^2}. \tag{9}$$

Substituting these in (8),

$$P(\theta \,|\, x_e(t), x_o(t)) \sim \prod_{i=1}^{2TW} \int_{-\infty}^{\infty} \exp\left[-\frac{1}{2\sigma_n^2} (x_e^i - \alpha s^i)^2 - \frac{1}{2\sigma_n^2} (x_o^i - \beta\theta s^i)^2 - \frac{s^{i2}}{2\sigma_s^2} \right] ds^i. \tag{10}$$

[3] This assumption will lead to an estimated value of θ which is the same as the *maximum likelihood* estimate.

The integral on the right-hand side can be evaluated using the relation

$$\int_{-\infty}^{\infty} e^{-az^2-bz-c}dz = \sqrt{\pi}e^{b^2/4a-1/2\ln a-c}, \tag{11}$$

where we identify

$$a = \frac{\alpha^2\sigma_s^2 + \sigma_n^2}{2\sigma_s^2\sigma_n^2}\left[1 + \frac{\beta^2\sigma_s^2\theta^2}{\alpha^2\sigma_s^2 + \sigma_n^2}\right],$$
$$b = -\frac{x_e^i\alpha}{\sigma_n^2} - \frac{x_o^i\beta\theta}{\sigma_n^2} \tag{12}$$

and c is a constant which does not depend on θ. We expand the exponent of e in a power series in θ and assume that for sufficiently small θ, terms of higher order than θ^2 may be neglected. Ignoring all proportionality factors independent of θ, (10) can be reduced to the following form, after some algebra.

$$P(\theta \mid x_e(t), x_o(t))$$
$$\sim \prod_{i=1}^{2TW} \exp\left\{\left[\frac{\sigma_s^2}{2\sigma_n^2(\alpha^2\sigma_s^2+\sigma_n^2)}\right]\cdot\left[\left(2x_e^i x_o^i\alpha\beta\right)\theta + \left(x_o^{i2}\beta^2 - \frac{x_e^{i2}\alpha^2\beta^2\sigma_s^2}{(\alpha^2\sigma_s^2+\sigma_n^2)} - \sigma_n^2\beta^2\right)\theta^2\right]\right\}$$
$$\sim \exp\left\{\left[\frac{\sigma_s^2}{2\sigma_n^2(\alpha^2\sigma_s^2+\sigma_n^2)}\right]\cdot\left[\left(4W\alpha\beta\int_0^T x_e(t)x_o(t)dt\right)\theta + \left(2W\beta^2\int_0^T x_o^2(t)dt - \frac{\alpha^2\beta^2\sigma_s^2 2W\int_0^T x_e^2(t)dt}{(\alpha^2\sigma_s^2+\sigma_n^2)} - 2TW\sigma_n^2\beta^2\right)\theta^2\right]\right\} \tag{13}$$

where we have used

$$\sum_{i=1}^{2TW}[\quad] = 2W\int_0^T[\quad]dt. \tag{14}$$

Because θ is very small and $2TW \gg 1$, the following approximations hold:

$$\int_0^T x_e^2(t)dt \approx \sigma_n^2T + \alpha^2\sigma_s^2T.$$
$$\int_0^T x_o^2(t)dt \approx \sigma_n^2T. \tag{15}$$

Substituting these in (13) gives

$$P(\theta \mid x_e(t), x_o(t)) \sim \exp\left\{\left[\frac{\sigma_s^2W\alpha\beta}{\sigma_n^2(\alpha^2\sigma_s^2+\sigma_n^2)}\right]\cdot\left[\left(2\int_0^T x_e(t)x_o(t)dt\right)\theta - \left(T\alpha\beta\sigma_s^2\right)\theta^2\right]\right\}. \tag{16}$$

The posterior probability distribution in θ is normal and the most probable value of θ, $\hat{\theta}$ say, is given by[4]

$$\hat{\theta} = \frac{\int_0^T x_e(t)x_o(t)dt}{T\alpha\beta\sigma_s^2}. \tag{17}$$

This very simple result says that we must compute the correlation between the even and odd outputs in order to make the best estimate of θ. Other methods of processing $x_e(t)$ and $x_o(t)$ can of course be used, but these can never give better results. The rms error in estimating θ, δ_θ say, may be computed directly from the coefficient of θ^2 in (16).

$$\delta_\theta = \frac{\left(1+\frac{\alpha^2\sigma_s^2}{\sigma_n^2}\right)^{1/2}}{\alpha\beta(\sigma_s^2/\sigma_n^2)\sqrt{2TW}}. \tag{18}$$

Because of the assumptions in (2), this expression does not take into account the possibility of angular ambiguities, though in practice they may occur. It is seen from (18) that α and β should be made as large as the antenna aperture allows in order to minimize δ_θ.[5] Denoting the total available signal power at the receiver $\alpha^2\sigma_s^2$ by P_s and the noise power in each output σ_n^2 by P_N, we have

$$\delta_\theta = \frac{\sqrt{1+P_s/P_N}}{(\alpha/\beta)(P_s/P_N)\sqrt{2TW}}. \tag{19}$$

Denote the antenna aperture by S, rectangular coordinates measured from the centroid of the aperture by ϵ and η, the aperture illumination function by $\mu(\epsilon, \eta)$, and the angles with respect to the aperture normal by θ and ϕ. The situation is shown in Fig. 2. The far-field voltage gain pattern is a function of θ and ϕ, $A = A(\theta, \phi)$, and for small θ and ϕ is related to the aperture function $\mu(\epsilon, \eta)$ and the wavelength λ as follows [3]:

$$A(\theta,\phi) = \frac{2\sqrt{\pi}}{\lambda}\frac{\int_S \mu(\epsilon,\eta)e^{j(2\pi/\lambda)(\epsilon\theta+\eta\phi)}d\epsilon d\eta}{\sqrt{\int_S |\mu(\epsilon,\eta)|^2 d\epsilon d\eta}}. \tag{20}$$

In (20) a constant phase shift of $A(\theta, \phi)$ corresponding to the time of propagation from the source to the origin of the receiving aperture has been ignored. From Schwarz's inequality

$$\left|\int f(z)g(z)dz\right| \le \left[\int |f(z)|^2dz\int |g(z)|^2dz\right]^{1/2} \tag{21}$$

it is easily seen that the maximum real value which $A(0, 0)$ can take is [3]

$$A(0,0)_{\max} = \frac{2\sqrt{\pi S}}{\lambda} \tag{22}$$

[4] For the normal probability distribution, the most probable estimate is also the estimate which has minimum variance.

[5] The problem of obtaining suitable $A_e(\theta)$ and $A_o(\theta)$ has been considered by Kirkpatrick [2].

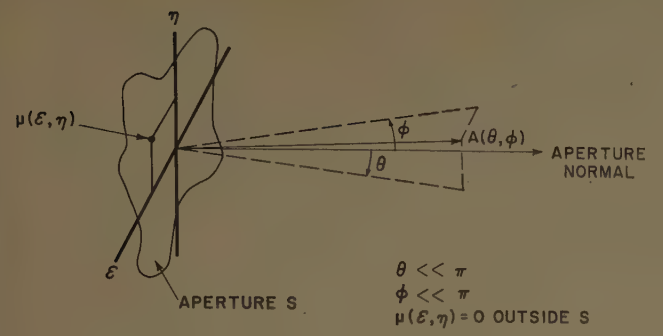

Fig. 2.

and is supplied by $\mu(\epsilon, \eta) = 1$. The maximum value of α is then

$$\alpha_{\max} = \frac{2\sqrt{\pi S}}{\lambda}. \tag{23}$$

Also,

$$\frac{\partial A(0,0)}{\partial \theta} = \frac{2\sqrt{\pi}\int_S \mu(\epsilon,\eta) j\left(\frac{2\pi\epsilon}{\lambda}\right) d\epsilon d\eta}{\lambda\sqrt{\int_S |\mu(\epsilon,\eta)|^2 d\epsilon d\eta}}. \tag{24}$$

From Schwarz's inequality it is easily seen that the maximum real value which this can take is [2]

$$\left[\frac{\partial A(0,0)}{\partial \theta}\right]_{\max} = \frac{2d_0\sqrt{\pi S}}{\lambda^2}, \tag{25}$$

where d_0 is a measure of the effective length of the antenna aperture (in the direction ϵ) and is defined by

$$d_0 = 2\pi\sqrt{\int_s \epsilon^2 d\epsilon d\eta / S}. \tag{26}$$

This maximum is supplied by the aperture function $\mu(\epsilon, \eta) = -j\epsilon$. The maximum value of β is then

$$\beta_{\max} = \frac{2d_0\sqrt{\pi S}}{\lambda^2}. \tag{27}$$

For these optimum values of α and β

$$\frac{\alpha_{\max}}{\beta_{\max}} = \frac{d_0}{\lambda}. \tag{28}$$

For various practical reasons (and perhaps some theoretical reasons) it is not possible to obtain the maximum values of α and β indicated in (23) and (27), but the above ratio is quite representative. For further details concerning α and β the reader is referred to Kirkpatrick's paper. Substituting (28) in (19), we have for the *optimum* angular accuracy,

$$\boxed{\delta_\theta = \frac{\lambda\sqrt{1 + P_s/P_N}}{d_0(P_s/P_N)\sqrt{2TW}}}. \tag{29}$$

It is interesting to note that at large values of P_s/P_N the expression for δ_θ becomes approximately

$$\delta_\theta \approx \frac{\lambda}{d_0\sqrt{\frac{2E}{N_0}}} \tag{30}$$

where we have defined

$E \equiv$ signal energy $= P_s T$,
$N_0 =$ noise power per cycle $= P_N/W$.

Eq. 30 has been derived previously by a different method for a signal which is known exactly [4]. It is expected that at large P_s/P_N the effect of the signal being unknown should be negligible, and therefore this agreement is not surprising.

For a rectangular aperture of length D, d_0 equals $\pi D/\sqrt{3}$ giving[6]

$$\delta_\theta = \frac{\sqrt{3}}{\pi}\left(\frac{\lambda}{D}\right)\frac{\sqrt{1 + P_s/P_N}}{(P_s/P_N)\sqrt{2TW}}. \tag{31}$$

The interesting fact about this expression is that for a sufficiently large $2TW$, P_s/P_N need not be large in order to obtain a good estimate of θ. Typical values might be $T = 0.01$ sec, $W = 10^6$ cps, $P_s/P_N = 0.1$, which give

$$\delta_\theta = 0.041\left(\frac{\lambda}{D}\right). \tag{32}$$

For a circular aperture of diameter D, d_0 equals $\pi D/2$, giving

$$\delta_\theta = \frac{2}{\pi}\left(\frac{\lambda}{D}\right)\frac{\sqrt{1 + P_s/P_N}}{(P_s/P_N)\sqrt{2TW}}. \tag{33}$$

For an interferometer system in which the aperture consists of two equal coplanar areas whose dimensions are small compared to their separation D, $d_0 \approx \pi D$ and

$$\delta_\theta = \frac{1}{\pi}\left(\frac{\lambda}{D}\right)\frac{\sqrt{1 + P_s/P_N}}{(P_s/P_N)\sqrt{2TW}}. \tag{34}$$

Appendix

Analysis of the Interferometer Technique

The receiving system consists of two similar receiving antennas, A and B, separated by a distance D which is large compared to their dimensions. The radio source is located at an angle θ as shown in Fig. 3.

[6] This expression for angular accuracy agrees with an expression derived by Hiller [5] using a different approach.

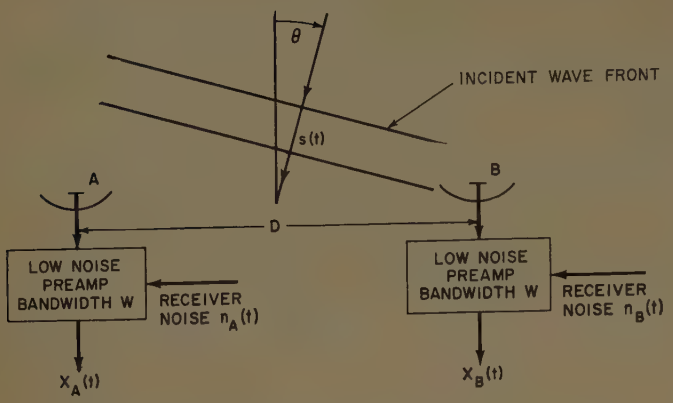

Fig. 3.

All the signal information is contained in the two outputs $x_A(t)$ and $x_B(t)$, which are the sum of signal and (external plus internal) noise. Further amplification which necessarily precedes the actual processing of $x_A(t)$ and $x_B(t)$ does not affect the inherent angular information, provided that no more noise is introduced. For this reason we ignore the scale factor changes introduced by the preamplifiers and all further amplifiers. The voltage gain of each antenna, denoted by $\sqrt{G}$, will be approximately independent of θ over the angular region of interest. Then we have

$$x_A(t) = \sqrt{G}s\left(t - \frac{D\sin\theta}{2c}\right) + n_A(t),$$

$$x_B(t) = \sqrt{G}s\left(t + \frac{D\sin\theta}{2c}\right) + n_B(t), \tag{35}$$

where c is the velocity of light. $s(t)$ is assumed to be very narrow-band and therefore may be written.

$$s(t) = \mathcal{E}(t)\cos(\omega t + \phi(t)), \tag{36}$$

where $\mathcal{E}(t)$ and $\phi(t)$ are slowly varying. Then we have approximately

$$s\left(t - \frac{D\sin\theta}{2c}\right) \approx \mathcal{E}(t)\cos\left(\omega t + \phi(t) - \frac{\pi D\sin\theta}{\lambda}\right),$$

$$s\left(t + \frac{D\sin\theta}{2c}\right) \approx \mathcal{E}(t)\cos\left(\omega t + \phi(t) + \frac{\pi D\sin\theta}{\lambda}\right). \tag{37}$$

This last approximation will be good providing that the difference in path length $D\sin\theta$ satisfies

$$D\sin\theta \ll c/W. \tag{38}$$

If it is not convenient to track the interferometer mechanically so that (38) is satisfied, then one can, in principle, track the interferometer electronically by appropriately delaying $x_A(t)$ or $x_B(t)$. The only theoretical disadvantage of the electronically scanned interferometer appears to be the somewhat shortened effective baseline.

From (37) we note the following two relations:

$$s\left(t - \frac{D\sin\theta}{2c}\right) + s\left(t + \frac{D\sin\theta}{2c}\right) = 2\cos\left(\frac{\pi D\sin\theta}{\lambda}\right)s(t),$$

$$s\left(t - \frac{D\sin\theta}{2c}\right) - s\left(t + \frac{D\sin\theta}{2c}\right) = 2\sin\left(\frac{\pi D\sin\theta}{\lambda}\right)s\left(t + \frac{3\lambda}{4c}\right). \tag{39}$$

Using these relations we take two orthogonal linear combinations of $x_A(t)$ and $x_B(t)$ to form $x_1(t)$ and $x_2(t)$.

$$x_1(t) = \frac{1}{\sqrt{2}}(x_A(t) + x_B(t))$$
$$= \sqrt{2G}\cos\left(\frac{\pi D\sin\theta}{\lambda}\right)s(t) + \frac{1}{\sqrt{2}}(n_A(t) + n_B(t)).$$

$$x_2(t) = \frac{1}{\sqrt{2}}(x_A(t) - x_B(t))$$
$$= \sqrt{2G}\sin\left(\frac{\pi D\sin\theta}{\lambda}\right)s\left(t + \frac{3\lambda}{4c}\right) + \frac{1}{\sqrt{2}}(n_A(t) - n_B(t)). \tag{40}$$

We identify

$$A_e(\theta) = \sqrt{2G}\cos\left(\frac{\pi D\sin\theta}{\lambda}\right),$$

$$A_o(\theta) = \sqrt{2G}\sin\left(\frac{\pi D\sin\theta}{\lambda}\right),$$

$$n_e(t) = \frac{1}{\sqrt{2}}(n_A(t) + n_B(t)),$$

$$n_o(t) = \frac{1}{\sqrt{2}}\left(n_A\left(t - \frac{3\lambda}{4c}\right) - n_B\left(t - \frac{3\lambda}{4c}\right)\right),$$

$$x_e(t) = x_1(t)$$

$$x_0(t) = x_2\left(t - \frac{3\lambda}{4c}\right). \tag{41}$$

For independent receiver noises and background noise radiation which varies slowly with angle, $n_e(t)$ and $n_o(t)$ will be uncorrelated on the average and will have equal average power. From the above relations there follow

$$x_e(t) = A_e(\theta)s(t) + n_e(t),$$
$$x_o(t) = A_o(\theta)s(t) + n_o(t). \tag{1}$$

For small values of θ we may approximate $\sin\theta \approx \theta$ and

$$A_e(\theta) \approx \sqrt{2G}\cos\frac{\pi D\theta}{\lambda} = A_e(0)\cos\frac{\pi D\theta}{\lambda},$$

$$A_o(\theta) \approx \sqrt{2G}\sin\frac{\pi D\theta}{\lambda} = A_e(0)\sin\frac{\pi D\theta}{\lambda}. \tag{42}$$

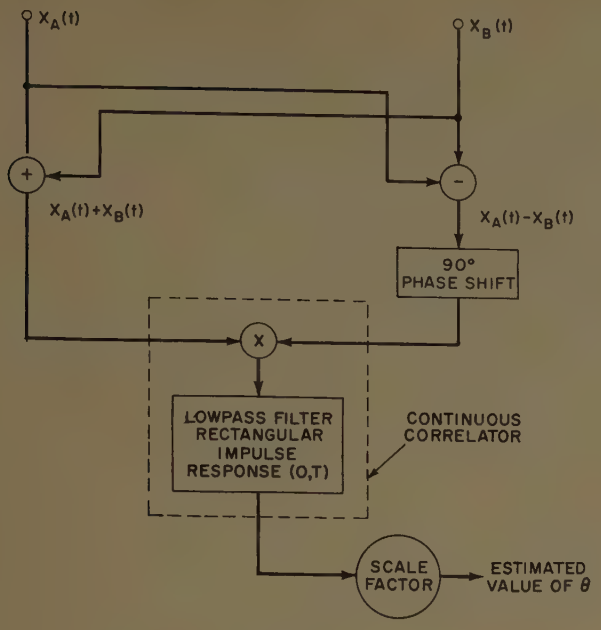

Fig. 4.

Using this approximation we have, furthermore,

$$\frac{A_o'(\theta)}{A_e(\theta)} = \frac{\pi D}{\lambda}. \tag{43}$$

Recalling that $d_0 = \pi D$ for the interferometer, we see that this ratio has the maximum theoretical value indicated by (28). It is seen that both $A_e(\theta)$ and $A_o(\theta)$ exhibit the fringe pattern characteristic of interferometers. Taken about $\theta = 0$ (or $\theta = k(\lambda/D)$, k integral), $A_e(\theta)$ represents the even pattern and $A_0(\theta)$ represents the odd pattern. Taken about $\theta = \frac{1}{2}(\lambda/D)$ (or $\theta = \frac{1}{2}(\lambda/D) + k(\lambda/D)$, k integral), $A_e(\theta)$ represents the odd pattern and $A_0(\theta)$ represents the even pattern. We assume, as before, that θ is sufficiently close to zero (or $k(\lambda/D)$), so that we may use the desired approximations

$$\left.\begin{aligned} A_e(\theta) &\approx A_e(0) \\ A_o(\theta) &\approx A_o'(0)\theta \end{aligned}\right\} \quad \text{or} \quad \left\{\begin{aligned} A_e(\theta) &\approx A_e\left(\frac{k\lambda}{D}\right) \\ A_o(\theta) &\approx A_0'\left(\frac{k\lambda}{D}\right)\left(\theta - \frac{k\lambda}{D}\right) \end{aligned}\right\} \tag{44}$$

on which (3) is based. As before we shall abbreviate $A_e(0) = \alpha$.

Subject to the assumptions noted above, the processing of $x_e(t)$ and $x_o(t)$ proceeds as indicated by (17) and the theoretical angular accuracy is given by (34). A schematic diagram for processing $x_A(t)$ and $x_B(t)$ is indicated in Fig. 4. Because x_A and x_B are very narrow-band, this system can easily be seen to be completely equivalent to the slightly simpler system shown in Fig. 5. The 90° phase shifter also is unnecessary if the origin for measuring θ is appropriately redefined.

In these equivalent systems it may prove convenient to use the estimated value of θ as an error correction

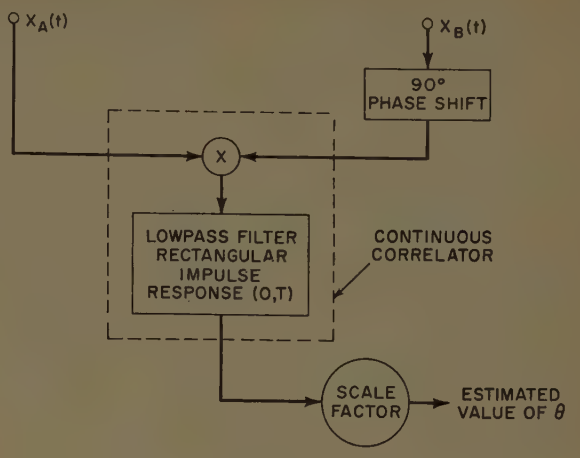

Fig. 5.

signal in a feedback loop to control a variable electronic delay in series with either $x_A(t)$ or $x_B(t)$. In this manner, the source would be tracked electronically, the value of θ would be kept small, and the approximations of (44) would remain valid, regardless of the source motion. From the delay-line setting and the θ correction signal, one could determine at any given moment the best estimate of the absolute angle of arrival.

It is interesting to compare the optimum angular accuracy given by (34) with that available from the signal processing technique introduced by Ryle [6] in his radio astronomy work using interferometers. Essentially, the Ryle processing technique can be described as follows: $x_A(t)$ and $x_B(t)$ are combined to form $x_e(t)$. From (1) and (42) we have for $x_e(t)$

$$x_e(t) = \alpha \cos\left(\frac{\pi D\theta}{\lambda}\right) s(t) + n_e(t). \tag{45}$$

Then one forms[7]

$$\int_0^T x_e^2(t)dt = \alpha^2 \cos^2\left(\frac{\pi D\theta}{\lambda}\right)\int_0^T s^2(t)dt + 2\alpha \cos\left(\frac{\pi D\theta}{\lambda}\right)\int_0^T s(t)n_e(t)dt + \int_0^T n_e^2(t)dt. \tag{46}$$

From a knowledge of $\int_0^T x_e^2(t)dt$ one can form an estimate of θ. We consider, particularly, the accuracy of estimating θ when θ has a value such that the Ryle system output (with switching) is near the null, *e.g.*,

$$\frac{\pi D\theta}{\lambda} \approx \frac{\pi}{4} \quad \text{or} \quad \theta \approx \frac{1}{4}\left(\frac{\lambda}{D}\right). \tag{47}$$

For the purpose of analysis we set

$$\theta = \frac{1}{4}\left(\frac{\lambda}{D}\right) + \theta', \tag{48}$$

[7] Actually, a switching technique is included to overcome the effect of drifts in amplifier gains.

where θ' is very small. Substituting (48) into (46) and neglecting second order terms, we have

$$\int_0^T x_e^2(t)dt \approx -\frac{\pi D\theta'}{\lambda}\alpha^2\int_0^T s^2(t)dt + \frac{1}{2}P_sT + P_NT + \chi_1 + \chi_2 + \chi_3 \approx -\frac{\pi D\theta'}{\lambda}P_sT + \frac{1}{2}P_sT + P_NT + \chi_1 + \chi_2 + \chi_3, \quad (49)$$

where we have defined

$$\chi_1 = \frac{1}{2}\alpha^2\int_0^T s^2(t)dt - \frac{1}{2}P_sT,$$

$$\chi_2 = \sqrt{2}\alpha\int_0^T s(t)n_e(t)dt,$$

$$\chi_3 = \int_0^T n_e^2(t)dt - P_NT. \quad (50)$$

By virtue of the central limit theorem and the fact that $2TW \gg 1$, the χ's are independent, normally distributed random variables with mean zero. These χ's represent unpredictable noise terms, and the best estimate of θ', $\hat{\theta}'$ say, is given by

$$\hat{\theta}' = \frac{-\lambda}{\pi DP_sT}\left[\int_0^T x_e^2(t)dt - \frac{1}{2}P_sT - P_NT\right]. \quad (51)$$

The variance in the estimation of θ', $\delta_{\theta'}^2$, is related to the variances of the χ's, $\delta_{\chi_1}^2$, $\delta_{\chi_2}^2$, and $\delta_{\chi_3}^2$, according to

$$\delta_{\theta'}^2 = \frac{\lambda^2}{(\pi DP_sT)^2}\left[\delta_{\chi_1}^2 + \delta_{\chi_2}^2 + \delta_{\chi_3}^2\right]. \quad (52)$$

The variance $\delta_{\chi_1}^2$ can be evaluated in the following manner. Express the integral over the interval $(0, T)$ as a sum of $2TW$ sampled values.

$$\chi_1 = \frac{1}{4W}\sum_{i=1}^{2TW}\xi_i^2 - \frac{1}{2}P_sT$$

where

$$\xi_i = \sqrt{2G}s^i = \alpha s^i. \quad (53)$$

Recall that $\alpha s(t)$ is the total available signal from the antenna aperture and that the average power of this signal is denoted P_s. The ξ_i are independent, normally distributed random variables with mean zero and variance P_s. A simple calculation then leads to the conclusion that the ξ_i^2 are independent random variables with mean P_s and variance $2P_s^2$. Recalling that for the addition of independent random variables the variance of the sum is the sum of the variances, we have

$$\delta_{\chi_1}^2 = \frac{P_s^2T}{4W}. \quad (54)$$

In a similar manner one can show that

$$\delta_{\chi_3}^2 = \frac{P_N^2T}{W}. \quad (55)$$

The evaluation of $\delta_{\chi_2}^2$ is somewhat different. The expression for χ_2 may be written as a sum

$$\chi_2 = \frac{1}{\sqrt{2W}}\sum_{i=1}^{2TW}\xi_i n_e^i. \quad (56)$$

For a fixed set of ξ_i, $\delta_{\chi_2}^2$ is easily computed.

$$\delta_{\chi_2}^2(\xi_i \text{ fixed}) = \frac{P_N}{2W^2}\sum_{i=1}^{2TW}\xi_i^2. \quad (57)$$

But since $2TW \gg 1$, it follows that we can approximate

$$\sum_{i=1}^{2TW}\xi_i^2 \approx 2TWP_s, \quad (58)$$

giving

$$\delta_{\chi_2}^2 = \frac{P_NP_sT}{W}. \quad (59)$$

Substituting these expressions for $\delta_{\chi_1}^2$, $\delta_{\chi_2}^2$, $\delta_{\chi_3}^2$ in (52) we obtain finally

$$\delta_\theta = \delta_{\theta'} = \frac{1}{\pi}\left(\frac{\lambda}{D}\right)\frac{\sqrt{1 + P_s/P_N + \frac{1}{4}(P_s/P_N)^2}}{(P_s/P_N)\sqrt{TW}}. \quad (60)$$

We compare this result with the optimum given by (34).

$$\frac{\delta_\theta(\text{Ryle})}{\delta_\theta(\text{optimum})} = \sqrt{2}\sqrt{\frac{1 + P_s/P_N + \frac{1}{4}(P_s/P_N)^2}{1 + P_s/P_N}}. \quad (61)$$

At small values of P_s/P_N, the region of most interest, the Ryle technique gives an accuracy which is $\sqrt{2}$ less than optimum.

Acknowledgment

The author is indebted to Dr. G. F. Hull, Jr. for pointing out this problem and to Dr. H. L. Kasnitz for helpful discussions relating to this work.

References

[1] R. M. Page, "Monopulse Radar," 1955 IRE Convention Record, pt. 8, pp. 132–134.
[2] G. M. Kirkpatrick, "Aperture illuminations for radar angle-of-arrival measurements," IRE Trans. on Aeronautical and Navigational Electronics, vol. ANE-3, pp. 20–24; September, 1953. See also, G. M. Kirkpatrick and O. E. Linderman, "Final Engineering Report on Angular Accuracy Improvement," Contract No. DA 36-039-sc-194, AD 46,849, August 1, 1952. (Not generally available.)
[3] S. Silver, "Microwave Antenna Theory and Design," M.I.T. Rad. Lab. Ser., McGraw-Hill Book Co., Inc., New York, N. Y., vol. 12, ch. 6; 1949.
[4] R. Manasse, "An Analysis of Angular Accuracies from Radar Measurements," Lincoln Lab., M.I.T., Lexington, Mass. Group Rept. 32-24; December, 1955.
[5] E. R. Hiller, Jr., "Available Source Information in Receiving Apertures," M.E.E. thesis, Mass. Inst. Tech., Cambridge; September, 1956. Also available as Tech. Rept. No. 3, Res. Lab. of Electronics, Mass. Inst. Tech., Cambridge; September, 1956.
[6] M. Ryle, "A new radio interferometer and its application to the observation of weak radio stars," *Proc. Roy. Soc. (London)*, vol. 211, pp. 351–375; March 6, 1952.

Experimental Studies of Meteor Echoes at 200 MC*

J. L. HERITAGE†, S. WEISBROD†, AND W. J. FAY†

Summary—**The paper describes experimental results of bistatic studies of meteor echoes at 200 mc using a high power source and highly directive antennas. The transmission paths studied ranged from 940 to 1800 km in length and included many off-great-circle paths. Diurnal burst rate curves are given for each path. Median duration of the VHF bursts is compared with theory. For certain paths, duty cycle and Doppler shift data are given. At some sites signals were received from ionization aligned with the Earth's magnetic field.**

Introduction

THE literature contains many reports on experimental studies of the characteristics of meteor bursts, both at forward and back scatter. These studies, however, were usually carried out in the 20- to 100-mc region, with antennas of only moderate directivity. Transmitters of moderate or low power were usually employed.

In 1957 an opportunity arose to carry out a fairly extensive forward scatter experiment at 200 mc using high power and highly directive antennas. Since the transmitter beams were fixed, the receiving units were made mobile and carried directive antennas. This arrangement made possible considerable departure from conventional great-circle transmission geometry while insuring that the region of the intersection of the transmitter and receiver beams provided a sensible majority of received signals.

Experimental Procedure

Apparatus

The receiving apparatus consisted of a pair of mobile units that could operate independently. Each contained a portable antenna and tower transported by a pickup truck, a set of receiving and recording equipment housed in a $2\frac{1}{2}$ ton truck, and a 5-kw power trailer. One of these stations on location is shown in Fig. 1. The antenna consisted of a four-by-four array of ten-element Yagi antennas, spaced at approximately one wavelength. The array had a 12° beamwidth between half-power points in the *E* plane and 13° in the *H* plane. The gain is 21.5 db over an isotropic source. The receiver pass band was 3 kc.

The transmitter, located in southern Texas, was high powered with pulse modulation. The transmission path was roughly from southeast to northwest, as shown in Fig. 2. Two transmitting beams, labeled "1" and "3," each with $2\frac{1}{2}$° elevation angle and offset from each other by 5° azimuth, were switched alternately at ten-minute intervals, doubling the number of paths under study.

Fig. 1—Receiving station in operation.

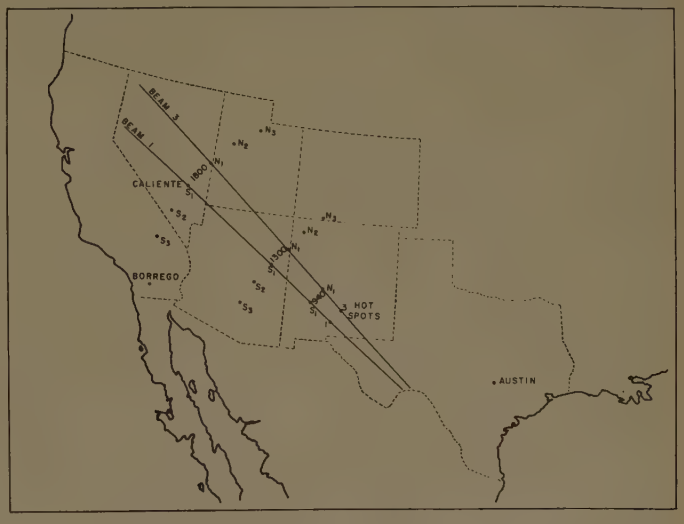

Fig. 2—Direction of beamed transmission and location of receiving sites.

The transmitting parameters cannot be given in more detail at this time. The system is capable of detecting electron columns of approximately 10^{11} electrons per meter line density.

Choice of Sites

In Fig. 2, the "hot spots" mark the intersection of the transmitter beams with a plane parallel to and 100 km above the Earth. Positions taken by the receiving stations are shown at 940, 1300, and 1800 km from the transmitter. The letters *S* and *N* designate sites south

* Manuscript received by the PGAP, February 3, 1959. This research was sponsored by Rome Air Dev. Center, Air Res. and Dev. Command, Griffiss AFB, N. Y., under Contract AF 30(602)-1624.

† Smyth Research Associates, San Diego 11, Calif.

and north of the great-circle paths of the transmitter beams. At all sites, the receiving antennas were pointed at the hot spot of the active transmitter beam. Having chosen a site on the great-circle path, for example, S_1–1300, the location of the S_2–1300 site was determined by specifying congruity between the triangles (S_1–hot spot 3 - transmitter) and (S_2–hot spot 1 - transmitter). The same method was used in determining site S_3 in relationship to S_2. The remaining sites were chosen in a similar manner. Since each location was occupied for a single 24-hour recording period, this method of site selection provided two days' data for all path configurations except the extreme off-great-circle paths.

The 1300-km series was made in November, 1957. Beam 3 malfunctioned during this test (only the beam 1 data is reported here). The 940-km observations were made in March, 1958, and the 1800-km series in May, 1958.

Experimental Results

Typical Signals

Parts of the record are shown in Fig. 3 to illustrate the typical meteor signals that were received. Below each signal trace is a time record received from WWV with increasing time from left to right. One-second intervals are marked by pulses protruding from the noise. Fig. 3(a) shows what is assumed to be two cases of reflections from overdense meteor trails; both exhibit a regular fading pattern of the envelope. Fig. 3(b) illustrates signals with a sharp rise time and slow fall, which approximate the classical shape of the Lovell-Clegg formula.[1] Many other types of signals were recorded that fit neither category; some of these are shown in Fig. 3(c). The two tall signals at the right of the illustration have fairly symmetric sides and are not unlike the bell shape of the Eshleman high-frequency formula.[2] The maximum amplitude of the bursts shown is of the order of 40 db above noise.

Two other distinct types of echoes are shown in Fig. 4. The first, illustrated in Fig. 4(a), is a signal classified as H_E scatter[3] and is characterized by a sharp rise, long decay time, and very ragged envelope. Fig. 4(b) shows a signal with long smooth envelope, which begins to exhibit a well defined fading pattern at its extremity. This signal occurred near the time of a meteor shower.

Burst Rate

For the burst rate analysis, all identifiable signals, exceeding 125 dbm and lasting less than 10 seconds, were counted. The burst rate found at the six 1300-km sites is shown in Fig. 5. Consideration of system sensitivity, size of the H plane area illuminated by the transmitting and receiving antenna beams, and the probability of specular alignment factor,[4] lead to a predicted average burst rate of 16 per minute. The observed rate varied from 4 to 31 bursts per minute and thus appeared to be in good quantitative agreement with the predictions. The site S_1–1300, located on the great-circle path of beam 1, exhibited a relatively low rate. The average rate increased rapidly with departure from the great-circle path and then gradually began to diminish beyond the S_2 and N_2 sites. The diurnal effects predictable from consideration of the motion of the Earth through space, in sweeping up more meteor particles on the morning side, and of the resulting concentration of meteor radiants toward the apex of the Earth's way, can be seen.[5]

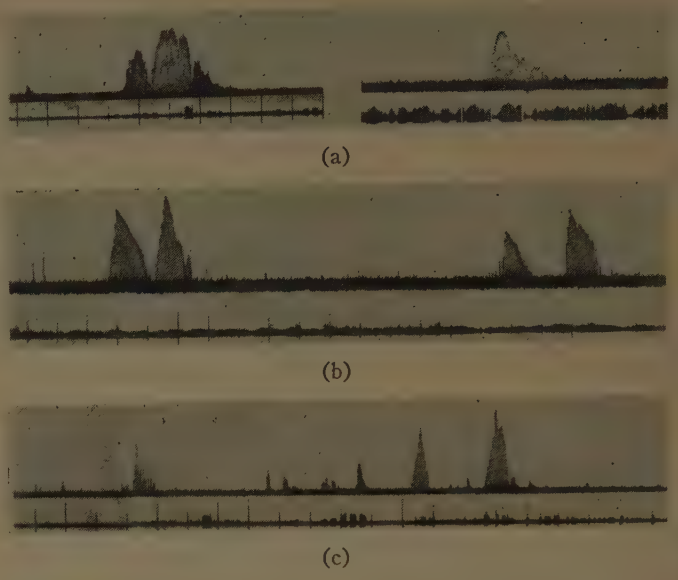

Fig. 3—Typical meteor signals. (a) Overdense meteor trails, (b) underdense meteor trails, (c) other types of meteor signals.

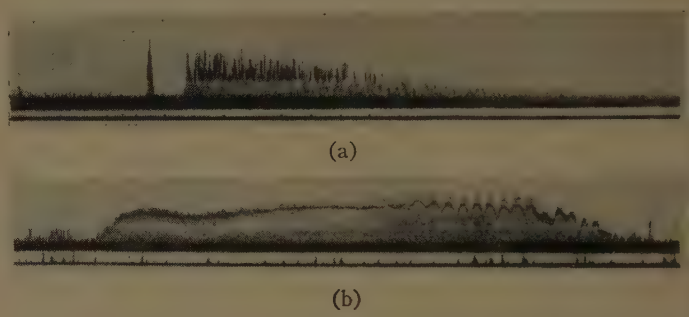

Fig. 4—Long signals. (a) H_E scatter, (b) overdense meteor trail.

[1] B. Lovell and J. A. Clegg, "Characteristics of radio echoes from meteor trails. I. The intensity of radio reflections and electron density in the trails," *Proc. Phys. Soc. A*, vol. 60, p. 491; 1948.

[2] V. R. Eshleman, "Short Wavelength Radio Reflection from Meteoric Ionization," Radio Propagation Lab., Stanford University, Stanford, Calif., Tech. Rept. No. 5; August 30, 1956.

[3] J. L. Heritage, S. Weisbrod, and W. J. Fay, "Evidence for a 200 mc ionospheric forward scatter mode associated with the Earth's magnetic field," *J. Geophys. Res.*, vol. 64, pp. 1235–1241; September, 1959.

[4] V. R. Eshleman and L. A. Manning, "Radio communication by scattering from meteoric ionization," Proc. IRE, vol. 42, pp. 530–537; March, 1954.

[5] V. R. Eshleman, "Directional characteristics of meteor propagation derived from radar measurements," Proc. IRE, vol. 45, pp. 1715–1724; December, 1957.

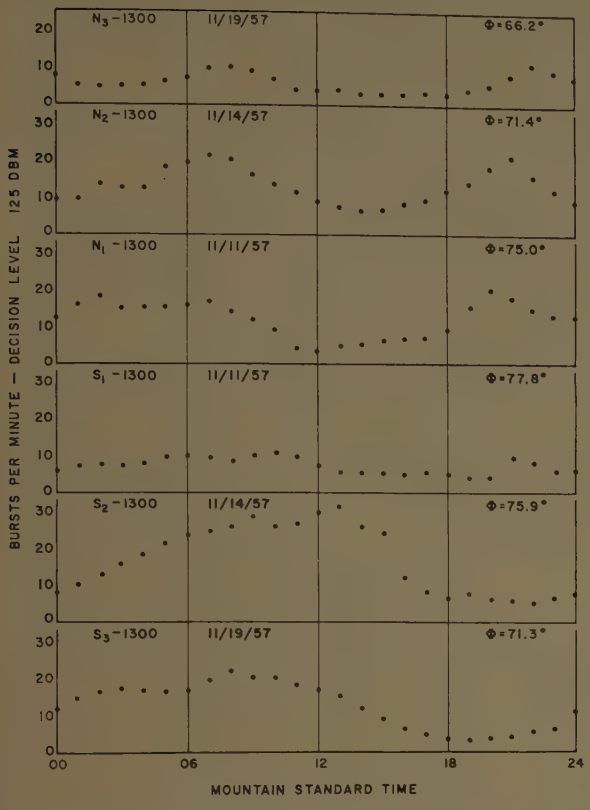

Fig. 5—Diurnal variation of burst rate for 1300-km sites.

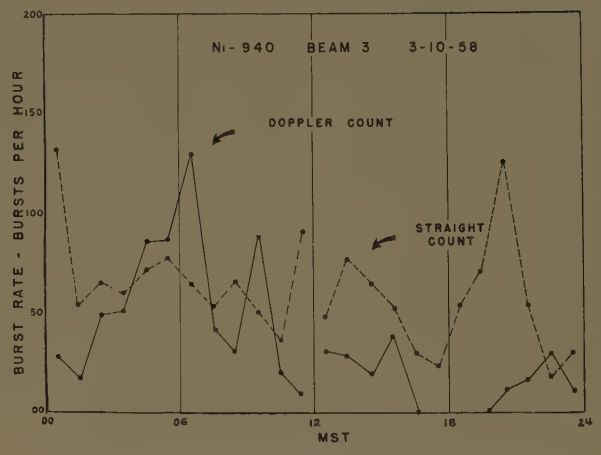

Fig. 6—Specular and Doppler burst rates on the great circle path at 940 km.

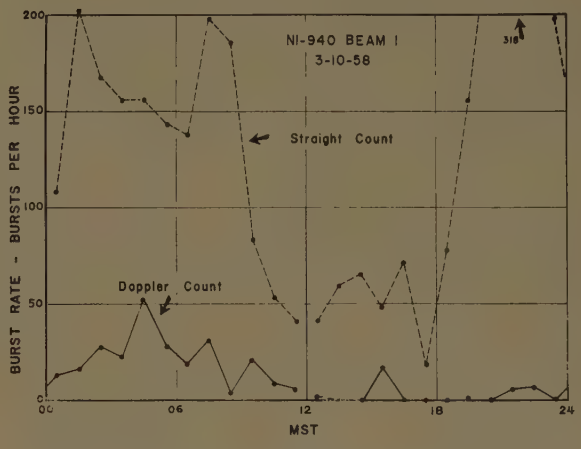

Fig. 7—Specular and Doppler burst rates slightly off the great-circle path at 940 km.

The N_1, N_2, and N_3 sites, all lying north and east of the main beam great-circle path, show an evening peak as expected from the radiant consideration. The S_2 and S_3 sites, lying south and west of the great circle, combine the predicted daytime and morning peaks due to radiant distribution to give a broad region of high-burst rate through the daytime and early morning. It should be remembered that each curve is only one day's data and that the N_1 and S_1 data are simultaneous, as are the N_2 and S_2 etc.

At 940 km, measurements were made on the great-circle path of beam 3. The diurnal burst rate for the on-circle path can be seen in Fig. 6 and for the off-circle path in Fig. 7. It is apparent that the burst rate is considerably lower at 940 km than at 1300 km. This difference is about what one would expect from the reduction in the H-plane area common to the antenna beams and from reduced probability of specular alignment. Comparison of the two figures indicates that the off-path specular or straight count considerably exceeds the on-path count.

Figs. 8 and 9 illustrate the diurnal variation in the burst rate for the 1800-km series. The curves are arranged to show the effect on burst rate as the half-scattering angle ϕ is decreased upon moving the receivers north and south away from the great-circle path. The two center graphs of each figure are averages for the two 24-hour periods during which the ϕ angles were repeated (as outlined in the experimental plan). As in the 1300-km series, the on-circle rates are relatively low, with rather dramatic increases found to either side. Comparison of the N_3 and S_3 curves shows the S_3 site considerably more active. It is possible that the S_3 count was influenced by inclusion of H_E scatter bursts.[3] The H_E scatter phenomenon is discussed briefly in the last section of this paper.

The time dependence of burst rate on scattering angle and site location off the great circle can be extracted more specifically from the basic curves of Figs. 8 and 9 by taking ratios. In the lower curve of Fig. 10, the ratio of burst rates is plotted for sites S_2 and S_1 using beams which have the same half-scattering angle ϕ. Although the sites differ somewhat geographically and the reception is on two different days, the ratio averages 1.5 to 1 through the day. The upper curve of Fig. 10 shows the ratio of burst rates for two sites having equal ϕ angles but disposed symmetrically on either side of the great-circle path. In the morning the southern site is favored

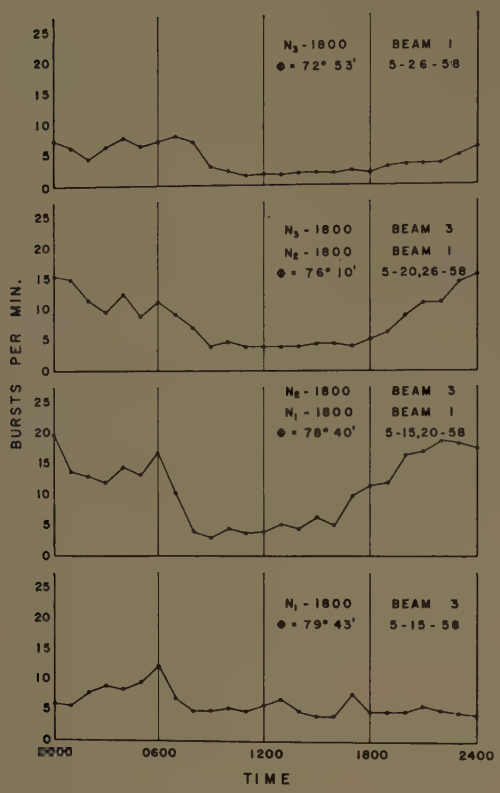

Fig. 8—Diurnal variation of burst rates for northern sites at 1800 km.

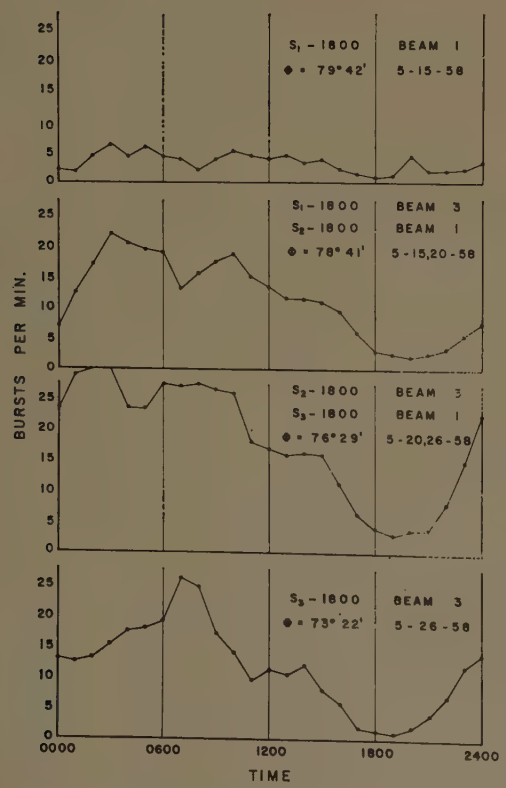

Fig. 9—Diurnal variation of burst rates for southern sites at 1800 km.

Fig. 10—Ratios of burst rates.

by 10 to 1 and in the evening the northern site dominates by about the same ratio.

Duty Cycle

One of the statistical quantities of interest for practical application is the fraction of time that signal is detectable. Fig. 11 shows a duty-cycle plot obtained from the 1300-km observations excluding bursts longer than 10 seconds. The duty-cycle curves are superimposed on a single chart to facilitate comparison between the various paths throughout the day. Only those sites with the largest duty cycle for the times indicated are shown. The general trend, as expected, follows the burst rate picture: the S sites dominate throughout the day, while the N sites take over in the evening and early morning.

Duration

Eshleman[2] developed an all-wavelength expression for the intrinsic duration τ for specular echoes, which is defined as the total energy contained in the pulse divided by the peak power. The transition wavelength and the intrinsic duration are functions of path geometry, meteor velocity, and physical properties of the medium. In Table I, computed values of τ are compared with experimental 1300-km results for the geometry of the S_1 and N_3 sites. The values of the transition wavelength are also tabulated and it is seen that the operating wavelength of 1.5 meters falls well within the theoretical transition region. The meteor velocity was assumed to be 40 km and the diffusion coefficient was taken as 4 m^2/second. In Table I, $\beta = 0°$ and $\beta = 90°$ refer to meteor trails in, and perpendicular to, the plane of propagation. For comparison with the calculated durations, the duration of bursts for morning and evening samples at the indicated sites were read and the median

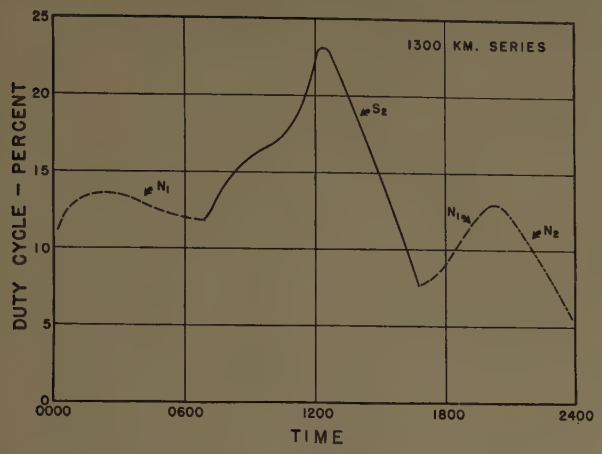

Fig. 11—Duty cycle, or per cent time that received signal exceeds a decision level of 125 dbm, at the 1300-km sites.

TABLE I

DURATION OF METEOR ECHOES

		Transition Wavelength in Meters		Calculated τ Eshleman Specular All λ		Measured τ Median	
Site	ϕ	$\beta=0°$	$\beta=90°$	$\beta=0°$	$\beta=90°$	0600	1800
S1-1300	77.84°	1.45	0.496	0.106	0.053	0.190	0.245
N3-1300	66.19°	2.38	1.03	0.059	0.023	0.115	0.200

values recorded. The method used was to read the duration 10 db down from the maximum. The segregation into morning and evening groups was to observe the effect of the generally higher morning velocities. The morning and evening values of τ at the great-circle site S_1 are approximately twice as large as the $\beta=0°$ calculation. This is good agreement considering that the classical low frequency formula gives values almost ten times smaller than the Eshleman formula. It can be shown that for very high frequencies the level at which the duration should be read is $(1+\pi^2)^{-1}$ or nearly 10 db down.[2] For the low-frequency exponential shape the level is exp (-1). Since most of the echoes that were observed lie between the two extremes, reading 6 or 7 db down might have resulted in better agreement with the calculated values. The significant point is that, as the receiving sites were changed from S_1 to N_3, the angle ϕ changed by almost 12° and both the calculated duration from the Eshleman all-wavelength formula and the observed duration dropped by about a factor of two. The low-frequency formula which involves secant^2 ϕ would require a decrease in duration by a factor of four. The observed afternoon values of τ are longer than the morning values, as might be expected from the lower values of meteor velocity.

Doppler Observations

At the 940-km site, both specular and Doppler-shifted signals were recorded. On the Doppler receiver, signals had to be 15 db stronger than the minimum detectable specular signals in order to register. The minimum Doppler shift measurable was ± 5 kc. In Fig. 6 the specular or straight count is compared with the Doppler count for the on-great-circle condition. Here the Doppler count exceeded the specular count near 0600. In Fig. 7 the same comparison is made for the off-great-circle condition. The specular count exceeds the Doppler count throughout the day. Even though the Doppler channel is less sensitive than the specular channel by more than an order of magnitude, the count of signals in both channels is still of the same order. This result implies that the echoing power of meteor ionization columns at 200 mc is not strongly dependent on aspect.

H_E Scatter

Signals of the type shown in Fig. 4(a) were found in increasing number as the receiving sites were moved progressively south of the great circle. They have never been seen on or north of the great-circle path. Special experiments performed in July, 1958, gave abundant evidence that this type of signal comes from ions, located in the hot spot, which are strung out along lines of the Earth's magnetic field. These signals were named H_E scatter and are treated in some detail in another paper.[3]

CONCLUSIONS

To summarize the important conclusions drawn from the experimental data:

1) Burst rates increased with increasing distance between 940 and 1300 km, but dropped again at 1800 km.
2) Lower burst rates and duty cycles were found *on* the great-circle path than *off* the path on either side. The increase is very rapid with departure from the great circle path, reaching a maximum near the N_2 and S_2 sites and then slowly decreasing.
3) The diurnal behavior of burst rate indicated that for 200-mc echoes the meteor columns retain enough aspect sensitivity to be influenced by radiant distribution.
4) Median duration of echoes compared favorably with Eshleman's theory of meteor echoes at VHF.
5) Comparison of burst rate in Doppler and specular channels of unequal sensitivity suggested that echoing power is not strongly dependent on aspect.

ACKNOWLEDGMENT

The authors wish to acknowledge the valuable assistance of A. C. Sheldon and H. R. Ahrens in obtaining the experimental data, and of L. A. Morgan, B. K. Crowley, V. S. South, H. D. Loucks, and N. A. Louie in the processing of the data.

Scattering by an Infinite Array of Thin Dielectric Sheets*

ROBERT E. COLLIN†

Summary—**By replacing each dielectric sheet in an infinite array of thin dielectric sheets by an infinitely thin polarization current sheet, a solution for the scattering of plane waves by such an array is obtained. The simplified periodic boundary value problem is rigorously solved by using bilateral Laplace transforms. Numerical results obtained compare favorably with those obtained by the Rayleigh-Ritz method.**

Introduction

An array of dielectric sheets as illustrated in Fig. 1 has interesting anisotropic properties.[1,2] For practical applications it is desirable to know the reflection and transmission coefficients for plane waves incident on the interface. Various approximate techniques are available for evaluating these parameters. In particular, for arbitrary thickness of the sheets the approximate solution based on an application of the Rayleigh-Ritz method is readily obtained.[3] When the electric field is everywhere parallel to the sheets and the plane of incidence is either in the yz plane or xz plane one may obtain another approximate solution valid for the case when the thickness t is much smaller than the spacing or period s of the sheets. For this approximation, each dielectric sheet is replaced by an infinitely thin polarization current sheet located at the center of the original sheet. The resulting boundary value problem can be rigorously solved by the Wiener-Hopf or related function-theoretic techniques.[4,5,6] The solution gives expressions for the reflection and transmission coefficients which are readily evaluated in terms of the eigenvalues or propagation constants for the problem.

Eigenfunctions in Dielectric Sheet Region

The periodic array of dielectric sheets is assumed to occupy the whole half space $z>0$. The spacing between sheets is s and the thickness of each sheet is t. The relative dielectric constant of each sheet is κ. Also the free space-dielectric sheet interface is assumed to be located

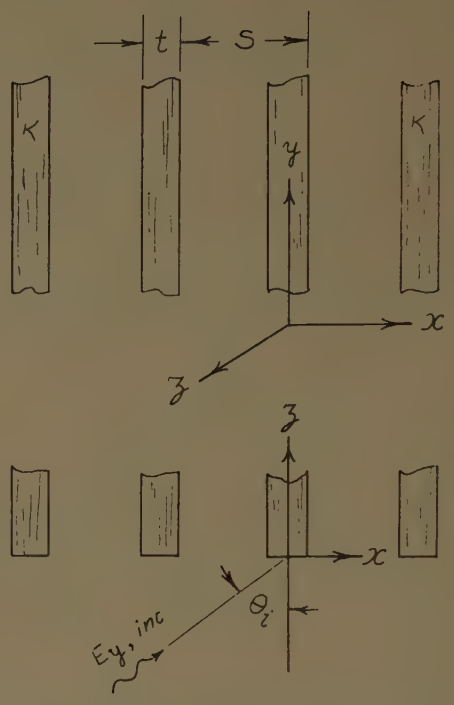

Fig. 1—Infinite array of thin dielectric sheets.

in the xy plane at $z=0$. If the electric field in the incident TEM wave in the region $z<0$ has only a y component and the plane of incidence is in the xz plane, the electric field everywhere will have only a y component. Maxwell's curl equation for the magnetic field $\boldsymbol{H}$ may be written as

$$\nabla \times \boldsymbol{H} = j\omega\epsilon_0\kappa(x)\boldsymbol{E} = j\omega\epsilon_0\boldsymbol{E} + \chi_e j\omega\epsilon_0\boldsymbol{E}, \qquad (1)$$

where $\chi_e=\kappa-1$ and is the electric susceptibility of the dielectric. The term $j\omega\epsilon_0\chi_e\boldsymbol{E}$ may be regarded as a polarization current density. When the sheets are very thin, the electric field E_y is approximately constant across each sheet. The total polarization current in each sheet is then given by

$$J_p = j\omega\epsilon_0\chi_e t E_y(x = ns),\ n = 0, \pm 1, \cdots, \qquad (2)$$

where $E_y(x=ns)$ is the value of the electric field at the center of the sheet located at $x=ns$. To a first approximation, each sheet may thus be replaced by an infinitely thin polarization crrrent sheet with a surface density given by (2). At such a current sheet, the tangential components of the magnetic field are discontinuous. The line integral of the magnetic field $\boldsymbol{H}$ around a small contour running parallel to the z axis and on adjacent sides of the current sheet shows that the discontinuity in H_z is given by

$$H_z^+ - H_z^- = -J_p = -j\omega\epsilon_0\chi_e t E_y. \qquad (3)$$

* Manuscript received by the PGAP, August 8, 1958. This work was supported by Case Inst. of Tech. Res. Fund under Grant No. 190.

† Elect. Engrg. Dept., Case Inst. Tech., Cleveland, Ohio.

[1] R. E. Collin, "A simple artificial anisotropic dielectric medium," IRE Trans. on Microwave Theory and Techniques, vol. MTT-6, pp. 206–209; April, 1958.

[2] H. S. Kirschbaum and S. Chen, "A method of producing broad band circular polarization employing an anisotropic dielectric," IRE Trans. on Microwave Theory and Techniques, vol. MTT-5, pp. 199–203; July, 1957.

[3] R. E. Collin, "Properties of Slotted Dielectric Interfaces," IRE Trans. on Antennas and Propagation, vol. AP-7, pp. 62–73; January, 1959.

[4] J. F. Carlson and A. E. Heins, "The reflection of an electromagnetic plane wave by an infinite set of plates," *Quart. Appl. Math.*, vol. IV, pp. 313–329; January, 1947.

[5] S. N. Karp, "An application of Sturm-Liouville theory to a class of two-part boundary value problems," *Proc. Camb. Phil. Soc.*, vol. 53, pt. 2, pp. 368–381; April, 1957.

[6] F. Berz, "Reflection and refraction of microwaves at a set of parallel metallic plates," *Proc. IEE*, vol. 98, pt. III, pp. 47–55; January, 1951.

If the incident electric field in the region $z<0$ is given by

$$E_{\text{inc}} = A_0 e^{-jhx-\Gamma_0 z}, \tag{4}$$

where $h=k_0 \sin\theta_i$, $\Gamma_0=jk_0\cos\theta_i$, k_0 is the free space wave number and θ_i is the angle of incidence measured from the interface normal; then the electric field in the region $z>0$ must have this same progressive change in phase with x. The electric field for $z>0$ can be represented by an infinite number of normal modes propagating or being attenuated in the positive z direction. In view of the periodic nature of the medium, the electric field is of the following form for $z>0$:[7]

$$E_y = \sum_{m=0}^{\infty} B_m F_m(x) e^{-\gamma_m z}$$

$$= e^{-jhx} \sum_{m=0}^{\infty} B_m \phi_m(x) e^{-\gamma_m z}, \tag{5}$$

where ϕ_m is a periodic function of x with period s; *i.e.*, $\phi_m(x)=\phi_m(x+ns)$. Provided that the spacing s obeys the following relation, all γ_m except γ_0 are real so that only one mode propagates,

$$s < \frac{\lambda_0}{\sqrt{\kappa} + |\sin\theta_i|}, \tag{6}$$

where λ_0 is the free space wavelength.

Each normal mode function F_m is a solution of the following:

$$\frac{d^2F_m}{dx^2} + (\gamma_m^2 + k_0^2)F_m = 0 \tag{7}$$

and must be a continuous function of x and must also satisfy the boundary condition (3). Each normal mode function may be constructed from the independent even and odd solutions of (7). Thus, let

$$F_m(x) = \cos l_m x + c_m \sin l_m x, \qquad 0 < x \leq s. \tag{8}$$

The corresponding solution for $s<x\leq 2s$ must be $e^{-jhs}[\cos l_m(x-s)+c_m \sin l_m(x-s)]$ since $\phi_m=e^{jhx}F_m$ is periodic. The propagation constant γ_m is given by

$$\gamma_m^2 = l_m^2 - k_0^2. \tag{9}$$

Continuity of E_y at $x=s$ gives the following condition on l_m and the coefficient c_m:

$$\cos l_m s + c_m \sin l_m s = e^{-jhs}. \tag{10}$$

The magnetic field H_z is given by $(j/\omega\mu_0)(\partial E_y/\partial x)$ and hence the boundary condition (3) at $x=s$ imposes the further condition,

$$k_0^2\chi_e t e^{-jhs} = l_m c_m(e^{-jhs} + \cos l_m s) - l_m \sin l_m s. \tag{11}$$

[7] R. E. Collin, "Reflection and transmission at a slotted dielectric interface," *Can. J. Phys.*, vol. 34, pp. 398–411; April, 1956.

From (10) and (11) the following solution for c_m is obtained:

$$c_m = (e^{-jhs} - \cos l_m s)\operatorname{cosec} l_m s \tag{12}$$

and also the following eigenvalue equation,

$$\cos hs = \cos l_m s - \frac{\chi_e k_0^2 t}{2l_m} \sin l_m s. \tag{13}$$

The following is the rigorous eigenvalue equation:[7]

$$\cos hs = \cos l_m(s-t)\cos\sqrt{l_m^2+\chi_e k_0^2}\,t$$

$$- \frac{2l_m^2+\chi_e k_0^2}{2l_m\sqrt{l_m^2+\chi_e k_0^2}} \sin l_m(s-t)\sin\sqrt{l_m^2+\chi_e k_0^2}\,t. \tag{14}$$

An expansion of (14) in powers of t shows that it is identical to (13) to terms up to and including t^2. This suggests that replacing each sheet by an infinitely thin polarization current sheet may be valid for values of t greater than first anticipated.

The transverse magnetic field for the dominant mode is given by $-(|\gamma_0|/k_0)Y_0E_y=H_x$ where $Y_0=\sqrt{\epsilon_0/\mu_0}$. Thus the power flow per section of unit height in the positive z direction is

$$P_t = \frac{1}{2}\int_0^s \frac{|\gamma_0|}{k_0} Y_0 E_y E_y^* dx = Y_0 \frac{|\gamma_0|}{k_0} |B_0|^2 \frac{s}{2\sin^2 l_0 s}$$

$$\left[1 - \cos hs\cos l_0 s + \frac{\sin l_0 s}{l_0 s}(\cos hs - \cos l_0 s)\right]. \tag{15}$$

There is also a component of the Poynting vector in the x direction.

Eigenfunctions in Free Space Region

In the region $z<0$, there is an incident wave

$$A_0 e^{-jhx-\Gamma_0 z} \tag{16a}$$

and, in addition, a reflected wave

$$R_1 A_0 e^{-jhx+\Gamma_0 z}, \tag{16b}$$

plus an infinite number of evanescent modes given by

$$\sum_{n=-\infty}^{\infty}{}' A_n \exp -j\left(h+\frac{2n\pi}{s}\right)x + \Gamma_n z, \tag{16c}$$

where R_1 is the reflection coefficient and

$$\Gamma_n^2 = \left(h+\frac{2n\pi}{s}\right)^2 - k_0^2 \tag{17}$$

and the prime in (16c) means omission of the term $n=0$.

The solution to the interface problem is obtained by equating the tangential electric and magnetic fields in the interface plane $z=0$. This gives two infinite sets of equations which may be solved by function-theoretic methods for the amplitude coefficients A_n and B_m.[6] A more straightforward solution in this case may be obtained by means of bilateral Laplace transforms.

Bilateral Laplace Transform Solution

Let $\psi(x, z)$ represent the y component of the electric field for all values of x and z. This function has the following properties.

1) It is continuous at all points.
2) The normal derivative of ψ, *i.e.*, $\partial\psi/\partial x$ is discontinuous across each polarization current sheet for $z>0$.
3) The normal derivative $\partial\psi/\partial z$ is continuous at $z=0$, *i.e.*, at the free space-dielectric sheet interface.
4) ψ satisfies the periodicity condition $e^{jhz}\psi(x, z) = e^{jh(x+ns)}\psi(x+ns, z)$ for all z.
5) As $z\to-\infty$, ψ is asymptotic to $e^{-\Gamma_0 z}+R_1 e^{\Gamma_0 z}$ where R_1 is the complex reflection coefficient and Γ_0 is pure imaginary.
6) As $z\to+\infty$ the asymptotic form of ψ is $e^{-\gamma_0 z}$ where γ_0 is pure imaginary. If the dielectric has a small amount of loss, then γ_0 has a small positive real part. Such a small positive real part will be assumed but the effect of dielectric loss on the other modes will be neglected.
7) At each polarization current sheet edge, *i.e.*, at $z=0$, $x=ns$, both ψ and $\partial\psi/\partial z$ are finite. This is readily demonstrated by expanding the fields in terms of cylindrical coordinates in the vicinity of each edge and putting in the appropriate boundary conditions.
8) For $z>0$, ψ is of the form (5) while for $z<0$, it is of the form given by (16a)–(16c). These properties are sufficient to permit the unique construction of the bilateral Laplace transform of $\psi(x, z)$ and therefore enable the rigorous solution of the problem to be obtained.

Let the bilateral Laplace transform of $\psi(s, z)$ be $e^{-jhs}G(w)$, where

$$G(w) = \frac{e^{jhs}}{2\pi j}\int_{-\infty}^{\infty}\psi(s, z)e^{wz}dz \tag{18}$$

and the factor e^{jhs} is introduced only for later convenience. For arbitrary values of x, let the transform of $\psi(x, z)$ be $g(x, w)$, where

$$g(x, w) = \frac{1}{2\pi j}\int_{-\infty}^{\infty}\psi(x, z)e^{wz}dz. \tag{19}$$

The inversion of this recovers the function $\psi(x, z)$, *i.e.*,

$$\psi(x, z) = \int_c g(x, w)e^{-wz}dw, \tag{20}$$

where c is a contour as yet to be determined. Eq. (19) defines $g(x, w)$ as an analytic function of w in that region of the complex $w=u+jv$ plane for which the integral is absolutely convergent. In view of the asymptotic forms of ψ as $|z|\to\infty$, it is readily deduced that the strip of analyticity is the infinite strip $0<u<Re\,\gamma_0$. It is assumed that γ_0 has a small positive real part arising from dielectric loss so as to provide a finite width strip of analyticity. This is done to facilitate the analysis and after the solution has been obtained, γ_0 will again be taken as pure imaginary. Thus the inversion contour c will be a contour parallel to the jv axis in the w plane and in the strip of analyticity. When $z>0$ an examination of (20) shows that the contour c may be closed in the right half w plane. The integral may be evaluated in terms of its residues at the poles in the right half plane and must give a form for the field such as that given by (5). Therefore, $g(x, w)$ must have simple poles at $w=\gamma_0, \gamma_1, \cdots, \gamma_m \cdots$ in the right half plane.

When $z<0$, the contour c can be closed in the left half plane and in order to obtain the form (16a)–(16c) for the field, $g(x, w)$ must have simple poles at $w=\pm j|\Gamma_0|$ on the imaginary axis and at $w=-\Gamma_n$, $n=\pm1, \pm2, \cdots$ in the left half plane.

In addition to the above properties, $g(x, w)$ must be a solution of

$$\frac{d^2g}{dx^2} + (w^2+k_0^2)g = 0 \tag{21a}$$

and must satisfy the periodicity condition,

$$e^{jhx}g(x, w) = e^{jh(x+s)}g(x+s, w) \tag{21b}$$

as well as being a continuous function of x.

In $0<x\leq s$ let

$$g(x, w) = A(w)\cos\sqrt{w^2+k_0^2}x + B(w)\sin\sqrt{w^2+k_0^2}x$$

which is the general solution of (21a). For $s<x\leq 2s$, the solution is simply

$$e^{-jhs}\left[A\cos\sqrt{w^2+k_0^2}(x-s) + B\sin\sqrt{w^2+k_0^2}(x-s)\right].$$

From the continuity condition at $x=s$, one gets

$$Ae^{-jhs} = Ge^{-jhs} = A\cos\sqrt{w^2+k_0^2}s + B\sin\sqrt{w^2+k_0^2}s.$$

Thus,

$$A(w) = G(w) \tag{22a}$$

and

$$B(w) = G(w)\frac{e^{-jhs}-\cos\sqrt{w^2+k_0^2}s}{\sin\sqrt{w^2+k_0^2}s}. \tag{22b}$$

Hence, in the region $0<x\leq s$, the field $\psi(x, z)$ is given by

$$\psi(x, z) = \int_c e^{-wz}G(w)\left[\cos\sqrt{w^2+k_0^2}x + (e^{-jhs}-\cos\sqrt{w^2+k_0^2}s)\frac{\sin\sqrt{w^2+k_0^2}x}{\sin\sqrt{w^2+k_0^2}s}\right]dw, \tag{23a}$$

and for $s<x\leq 2s$ by

$$\psi(x, z) = \int_c e^{-wz}G(w)e^{-ihs}\left[\cos\sqrt{w^2+k_0^2}(x-s)\right.$$

$$+ (e^{-ihs} - \cos\sqrt{w^2+k_0^2}s)\cdots$$

$$\left.\cdot\frac{\sin\sqrt{w^2+k_0^2}(x-s)}{\sin\sqrt{w^2+k_0^2}s}\right]dw. \quad (23b)$$

The solution may be continued periodically in the same fashion to give the solution for all values of x. When $x=s$, (23) reduces to the expression obtained by inverting (18).

For $z>0$, $\psi(x, z)$ must satisfy the boundary condition (3), *i.e.*,

$$\left.\frac{\partial\psi}{\partial x}\right|_{s-}^{s+} = -k_0^2\chi_e t\psi(s, z)$$

while for $z<0$, $\partial\psi/\partial x$ must be continuous at $x=s$. Using (23a) and (23b), the above boundary conditions impose the following conditions on $G(w)$:

$$\int_c e^{-wz}G(w)\left[\cos\sqrt{w^2+k_0^2}s - \cos hs\right.$$

$$\left.- \frac{\chi_e k_0^2 t\sin\sqrt{w^2+k_0^2}s}{2\sqrt{w^2+k_0^2}}\right]$$

$$\cdot\frac{\sqrt{w^2+k_0^2}}{\sin\sqrt{w^2+k_0^2}s}dw = 0, \qquad z>0, \quad (24a)$$

$$\int_c e^{-wz}G(w)[\cos\sqrt{w^2+k_0^2}s - \cos hs]$$

$$\cdot\frac{\sqrt{w^2+k_0^2}}{\sin\sqrt{w^2+k_0^2}s}dw = 0, \qquad z<0. \quad (24b)$$

Now for $z>0$, the contour c in (24a) may be closed in the right half plane. Thus $G(w)$ must cancel the poles of $(\sin\sqrt{w^2+k_0^2}s)^{-1}$ in the right half plane in order for the integral to vanish. It was postulated earlier that $G(w)$ would have poles at $w=\gamma_m$, $m=0, 1, \cdots$ in the right half plane. These poles, however, do not contribute to the integral in (24a) since the numerator contains the eigenvalue equation for γ_m and, hence, vanishes at $w=\gamma_m$.

In (24b) the contour c may be closed in the left half plane. The integral will vanish provided that $G(w)$ also cancels the poles of $(\sin\sqrt{w^2+k_0^2}s)^{-1}$ in the left half plane. Again, the numerator contains the eigenvalue equation for Γ_n so the poles of $G(w)$ at $w=\pm\Gamma_0, -\Gamma_n$, $n=\pm 1, \cdots$, do not contribute to the integral.

At this time it is convenient to relabel the eigenvalues Γ_n according to the following scheme:

$$\Gamma_0^2 = h^2 - k_0^2,$$

$$\Gamma_n^2 = \left(\frac{(n+1)\pi}{s} - h\right)^2 - k_0^2, \qquad n = 1, 3, 5, \cdots$$

$$\Gamma_n^2 = \left(\frac{\eta\pi}{s} + h\right)^2 - k_0^2, \qquad n = 2, 4, 6, \cdots.$$

Thus, the eigenvalues for n odd are those original eigenvalues which corresponded to negative values of n. An examination of (13) shows that for m large one has

$$\cos hs = \cos l_m s$$

and hence the eigenvalue γ_m approaches Γ_m.

In view of the required properties of $G(w)$ it is readily seen that a suitable form for $G(w)$ is the following:

$$G(w) = p(w)\frac{\sin\sqrt{w^2+k_0^2}s}{\sqrt{w^2+k_0^2}}$$

$$\cdot\left[(w^2-\Gamma_0^2)(w-\gamma_0)\prod_{n=1}^{\infty}\frac{(w+\Gamma_n)(w-\gamma_n)}{\Gamma_n^2}\right]^{-1}, \quad (25)$$

where $p(w)$ is as yet an undetermined integral function of w. This integral function may be determined from a consideration of the asymptotic form of $G(w)$ as $|w|\to\infty$.

Consider the infinite product expansion of

$$\cos\sqrt{w^2+k_0^2}s - \cos hs.$$

The zeros of this function occur at $w=\pm\Gamma_n$ and the value of the function at $w=0$ is $\cos k_0 s - \cos hs$ and, hence, by standard procedures one gets

$$\cos\sqrt{w^2+k_0^2}s - \cos hs$$

$$= (\cos k_0 s - \cos hs)\prod_{n=0}^{\infty}\frac{\Gamma_n^2 - w^2}{\Gamma_n^2}.$$

Since

$$\prod_{n=1}^{\infty}\frac{(w+\Gamma_n)(w-\gamma_n)}{\Gamma_n^2}$$

differs from

$$\prod_{n=1}^{\infty}\frac{\Gamma_n^2 - w^2}{\Gamma_n^2}$$

by a bounded function, one sees that the asymptotic form of $G(w)$ is

$$G(w)\sim\frac{p(w)\sin ws}{w^2(\cos ws - \cos hs)}, \quad |w|\to\infty. \quad (26)$$

In view of the property (7) of the function ψ, the transform must be asymptotic to w^{-2} as $|w|\to\infty$ and therefore $p(w)$ is simply a constant whose value can be determined in terms of the amplitude of the incident wave. The transform $G(w)$ is thus uniquely determined and therefore $g(x, w)$ and $\psi(x, z)$ may be found.

Reflected and Transmitted Wave Amplitudes

An examination of (16a), (16b) and (23a) shows that the residue of the integrand in (23a) at the pole $w=\Gamma_0$ gives the incident wave in the region $z<0$ while the residue at the pole $w=-\Gamma_0$ gives the reflected wave in the region $z<0$. These waves are given by

$$A_0 e^{-jhx-\Gamma_0 z} = r(\Gamma_0)e^{-jhx-\Gamma_0 z}, \tag{27a}$$

$$R_1 A_0 e^{-jhx+\Gamma_0 z} = r(-\Gamma_0)e^{-jhx+\Gamma_0 z}, \tag{27b}$$

where $r(\Gamma_0)$ is the residue of $G(w)$ at $w=\Gamma_0$; *i.e.*,

$$r(\Gamma_0) = \lim_{w\to\Gamma_0} (w-\Gamma_0)G(w)$$

and similarly for $r(-\Gamma_0)$. The complex reflection coefficient R_1 is given by

$$R_1 = \frac{r(-\Gamma_0)}{r(\Gamma_0)} = \frac{\Gamma_0-\gamma_0}{\Gamma_0+\gamma_0}\prod_{n=1}^{\infty}\frac{\Gamma_n+\Gamma_0}{\gamma_n+\Gamma_0}\frac{\gamma_n-\Gamma_0}{\Gamma_n-\Gamma_0} = \frac{|\Gamma_0|-|\gamma_0|}{|\Gamma_0|+|\gamma_0|}e^{j\alpha_1}, \tag{28a}$$

where the angle α_1 is given by

$$\alpha_1 = 2\sum_{n=1}^{\infty}\left[\tan^{-1}\frac{|\Gamma_0|}{\Gamma_n} - \tan^{-1}\frac{|\Gamma_0|}{\gamma_n}\right]. \tag{28b}$$

The latter result for R_1 follows because all γ_m and Γ_n are real except γ_0 and Γ_0 which are now taken as pure imaginary quantities.

From (23a) it is seen that the transmitted wave is given by the residue of the integrand at the pole $w=\gamma_0$. Thus for $0\leq x\leq s$, the transmitted wave is

$$B_0F_0(x)e^{-\gamma_0 z} = -r(\gamma_0)\cdot\left[\cos l_0x + (e^{-jhs}-\cos l_0 s)\frac{\sin l_0x}{\sin l_0 s}\right]e^{-\gamma_0 z}, \tag{29}$$

where $r(\gamma_0)$ is the residue of $G(w)$ at the pole $w=\gamma_0$. The minus sign arises because the integration is taken in a clockwise sense around the contour c. If the transmission coefficient T is defined as the ratio B_0/A_0, it is given by

$$T = -\frac{r(\gamma_0)}{r(\Gamma_0)} = \frac{2\Gamma_0}{\Gamma_0+\gamma_0}\frac{h\sin l_0 s}{l_0\sin hs}\cdot\prod_{n=1}^{\infty}\frac{(\Gamma_n+\Gamma_0)}{(\Gamma_n+\gamma_0)}\frac{(\gamma_n-\Gamma_0)}{(\gamma_n-\gamma_0)} = |T|e^{j\alpha_t}, \tag{30}$$

where the phase angle α_t is given by

$$\alpha_t = \sum_{n=1}^{\infty}\left[\left(\tan^{-1}\frac{|\Gamma_0|}{\Gamma_n}+\tan^{-1}\frac{|\gamma_0|}{\gamma_n}\right) - \left(\tan^{-1}\frac{|\Gamma_0|}{\gamma_n}+\tan^{-1}\frac{|\gamma_0|}{\Gamma_n}\right)\right] \tag{31}$$

since Γ_n, γ_n are real except γ_0 and Γ_0. The amplitudes of all the higher order modes may be similarly determined from the residues of $G(w)$ at the appropriate poles.

For a wave incident from the region $z>0$ it is only necessary to remove the pole at $w=\Gamma_0$ in $G(w)$ and to introduce a new pole at $w=-\gamma_0$ which will give rise to the incident wave. Thus the factor $w-\Gamma_0$ in (25) is replaced by $(w+\gamma_0)$. The reflection coefficient for a wave incident from $z>0$ is readily found to be given by

$$R_2 = \frac{|\gamma_0|-|\Gamma_0|}{|\gamma_0|+|\Gamma_0|}e^{j\alpha_2}, \tag{32a}$$

where α_2 is given by

$$\alpha_2 = 2\sum_{n=1}^{\infty}\left[\tan^{-1}\frac{|\gamma_0|}{\gamma_n} - \tan^{-1}\frac{|\gamma_0|}{\Gamma_n}\right]. \tag{32b}$$

An examination of (28), (31), and (32) shows that

$$\angle R_1 + \angle R_2 = \pi + 2\angle T, \tag{33}$$

a result which may be deduced by more elementary means from the properties of the scattering matrix of a lossless two-terminal pair network.[8]

The difference between the incident and reflected power in the z direction per unit height for a width s along the x coordinate is

$$P_i - P_r = \tfrac{1}{2}Y_0|A_0|^2\frac{|\Gamma_0|}{k_0}\frac{4|\Gamma_0\gamma_0|}{|\Gamma_0+\gamma_0|^2}s \tag{34}$$

and is equal to the transmitted power P_t given by (15). These relations may be used to compute the modulus of the transmission coefficient $|T|$ since B_0 in (15) is equal to TA_0. One may show formally that this gives the same value for $|T|$ as (30) does. The Appendix gives the derivation for the particular case when $h=0$, *i.e.*, for normal incidence.

A Numerical Example

Numerical results were computed for the following typical parameters, $\kappa=2.56$, $\theta_i=30^0$, $s=\lambda_0/2$, $\lambda_0=3.14$ cm, by using the theoretical formulas given here as well as for two- and three-term approximations based on an application of the Rayleigh-Ritz method. Fig. 2 compares the approximate values of the first propagation constant $|\gamma_0|$ in the dielectric slab medium as obtained by the two methods. The Rayleigh-Ritz method gives a result which is a lower bound while the eigenvalue equation (13) gives a result which is greater than the true value. For values of t/s up to 0.2, the difference between the two is less than 3 per cent. Both methods give the modulus of the reflection coefficient as $(\gamma_0-\Gamma_0)/(\gamma_0+\Gamma_0)$. Fig. 3 compares the values of the reflection coefficient angles α_1 and α_2. Since these angles are proportional to the reactive energy stored in the evanescent modes at the interface, the Rayleigh-Ritz method gives results which are too small since only a few of the higher order modes are taken into account.

[8] B. A. Lengyel, "A note on reflection and transmission," *J. Appl. Phys.*, vol. 22, pp. 263–264; March, 1951

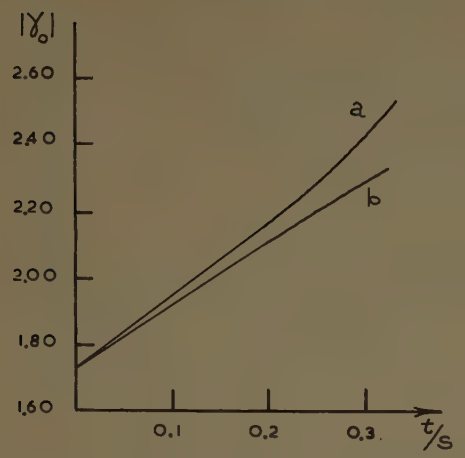

Fig. 2—Propagation constant in dielectric sheet medium for $\kappa=2.56$, $\theta_i=30°$, $S=0.5\lambda_0$, $\lambda_0=3.14$ cm.
(a) Transform solution (13).
(b) Two-term Rayleigh-Ritz solution.

Conclusion

By replacing each dielectric sheet by an infinitely thin polarization current sheet, a rigorous solution to the problem of diffraction by an array of thin dielectric sheets was obtained. Numerical results compare favorably with those obtained by an application of the Rayleigh-Ritz method.

Appendix

The modulus of the transmission coefficient for normal incidence as given by (30) may be shown to be equal to that computed from power flow considerations by making use of the following two relations. The first relation required is

$$\frac{2(1-\cos l_0 s)}{l_0^2 s^2} = \prod_{n=2,4\cdots}^{\infty}\left(1-\frac{l_0^2 s^2}{n^2\pi^2}\right)\cdot\prod_{n=1,3\cdots}^{\infty}\left(1-\frac{l_0^2 s^2}{(n+1)^2\pi^2}\right)$$

which is readily established by expanding the left-hand side into an infinite product. Similarly, the following result may be obtained by eliminating the term $\chi_e k_0^2$ from the eigenvalue equation (13) for l_0 and l_n;

$$g(w) = \frac{\sin l_0 s}{l_0 s}(1-\cos ws) - \frac{\sin ws}{ws}(1-\cos l_0 s)$$

$$= (\cos l_0 s - 1)\prod_{n=0}^{\infty}\left(1-\frac{w^2}{l_n^2}\right)$$

after expanding the equation as an infinite product. The second relation required is obtained by taking the limit of $g(w)/(w^2-l_0^2)$ as w tends to l_0 to get

$$\frac{1}{2}\left(1+\frac{\sin l_0 s}{l_0 s}\right) = \prod_{n=1}^{\infty}(1-l_0^2/l_n^2).$$

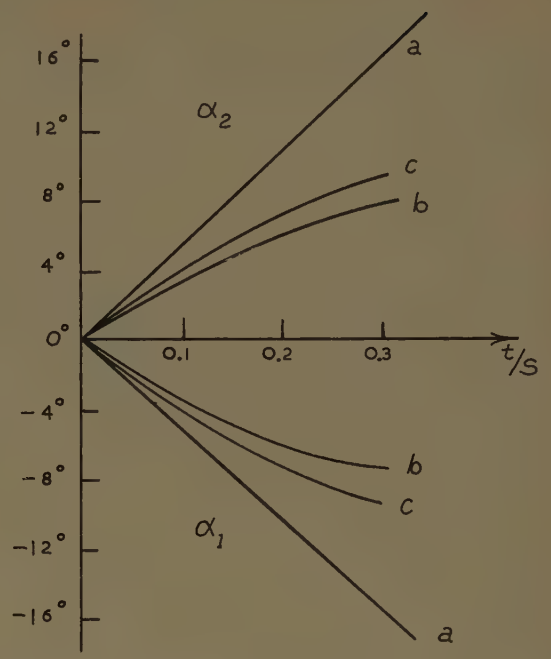

Fig. 3—Reflection coefficient angles α, and α^2 for $k=2.56$, $\theta_j=30°$, $S=0.5\ \lambda_0$, $\lambda=3.14$ cm.
(a) Transform solution.
(b) Two-term Rayleigh-Ritz solution.
(c) Three-term Rayleigh-Ritz solution.

Reciprocity Theorems for Electromagnetic Fields Whose Time Dependence Is Arbitrary*

W. J. WELCH†

Summary—Two reciprocity theorems are derived which are valid for fields whose sources may have arbitrary time dependence. The first theorem involves the electromagnetic potentials, and the second is in terms of the electric and magnetic fields directly. In both cases, it is necessary to make use of the advanced as well as the retarded solutions to Maxwell's equations. Some properties of the theorems are discussed, and, as an application, the second theorem is used to derive a variational expression for scattering of electromagnetic waves from a perfect conductor.

Introduction

ONE of the most simple and yet useful deductions from Maxwell's equations is Lorentz' reciprocity theorem. This theorem, which is valid for fields whose time dependence is simple harmonic, may be written in the following form:

$$\nabla\cdot[(\boldsymbol{E}_1\times\boldsymbol{H}_2)-(\boldsymbol{E}_2\times\boldsymbol{H}_1)] = (\boldsymbol{E}_2\cdot\boldsymbol{J}_1-\boldsymbol{H}_2\cdot\boldsymbol{K}_1)-(\boldsymbol{E}_1\cdot\boldsymbol{J}_2-\boldsymbol{H}_1\cdot\boldsymbol{K}_2),$$

where $\boldsymbol{J}$ and $\boldsymbol{K}$ are electric and magnetic current sources, respectively, and the numerical subscripts distinguish the two sets of sources and their respective fields. Rumsey has used this theorem to define an electromagnetic "reaction" between sources and fields, and has shown how it may be systematically applied to simplify and solve many problems in electromagnetic theory.[1]

The purpose of this paper is to present two reciprocity relations which are valid for sources whose time dependence is arbitrary. As an application, the second of the two theorems will be used to derive a variational principle for scattering by a perfect conductor.

For reference, Maxwell's equations and the definitions of the electromagnetic potentials used in this paper are presented below.

$$\nabla\times\boldsymbol{E}=-\frac{\partial\boldsymbol{B}}{\partial t}\quad\text{(I)};\qquad \nabla\times\boldsymbol{H}=\boldsymbol{J}+\frac{\partial\boldsymbol{D}}{\partial t}\quad\text{(II)}$$

$$\nabla\cdot\boldsymbol{J}+\frac{\partial\rho}{\partial t}=0. \qquad \text{(III)}$$

Because

$$\nabla\cdot\boldsymbol{B}=0, \qquad \text{(IV)}$$

we may write

$$\boldsymbol{B}=\nabla\times\boldsymbol{A}, \qquad \text{(V)}$$

where $\boldsymbol{A}$ is the vector potential. After substituting (V) into (I), we may define the scalar potential as follows:

$$\boldsymbol{E}+\frac{\partial\boldsymbol{A}}{\partial t}=-\nabla\phi. \qquad \text{(VI)}$$

Then, with the requirement that

$$\nabla\cdot\boldsymbol{A}+\frac{1}{c^2}\frac{\partial\phi}{\partial t}=0,$$

$$\nabla^2\boldsymbol{A}-\frac{1}{c^2}\frac{\partial^2\boldsymbol{A}}{\partial t^2}=-\mu\boldsymbol{J} \qquad \text{(VII)}$$

and

$$\nabla^2\phi-\frac{1}{c^2}\frac{\partial^2\phi}{\partial t^2}=-\frac{\rho}{\epsilon}. \qquad \text{(VIII)}$$

Theorem I

Suppose that existing in free space are two sources of electromagnetic fields, (J_a, ρ_a) and (J_b, ρ_b), which have finite extent and integrable singularities as functions of space and time. The vector and scalar potentials for such sources will be the following:[2]

$$\boldsymbol{A}(r,t)=\frac{\mu}{4\pi}\int\frac{\boldsymbol{J}\left(t-\frac{R}{c},\,r'\right)dv'}{R};$$

$$\phi(r,t)=\frac{1}{4\pi\epsilon}\int\frac{\rho\left(t-\frac{R}{c},\,r'\right)dv'}{R}. \qquad (1)$$

$$\tilde{\boldsymbol{A}}(r,t)=\frac{\mu}{4\pi}\int\frac{\boldsymbol{J}\left(t+\frac{R}{c},\,r'\right)dv'}{R};$$

$$\tilde{\phi}(r,t)=\frac{1}{4\pi\epsilon}\int\frac{\rho\left(t+\frac{R}{c},\,r'\right)dv'}{R}. \qquad (2)$$

$R=|r-r'|$. The tildes are used to denote the so-called "advanced" potential solutions as distinct from the retarded potentials, (1). Both the retarded and advanced potentials are proper solutions to Maxwell's equations, but the advanced solution is usually discarded as having no physical meaning because it does not satisfy the causality principle. However, the advanced potential is often useful from a mathematical point of view, and one

* Manuscript received by the PGAP, April 30, 1959. This work was sponsored in part by the Office of Naval Research.

† Dept. Elec. Engrg., University of California, Berkeley.

[1] V. H. Rumsey, "Reaction concept in electromagnetic theory," *Phys. Rev.*, vol. 94, pp. 1483–1491; June, 1954.

[2] W. Panofsky and M. Phillips, "Classical Electricity and Magnetism," Addison Wesley, Reading, Mass., p. 214; 1955.

can even form a physical picture of it. For example, it represents either a wave radiating outward from the source with time running backward or a wave collapsing on its source with time going forward.

Reciprocity between sources a and b is expressed by the following:

$$\int\int_{V_b} (\boldsymbol{A}_a \cdot \boldsymbol{J}_b - \phi_a \rho_b) dv dt = \int\int_{V_a} (\tilde{\boldsymbol{A}}_b \cdot \boldsymbol{J}_a - \tilde{\phi}_b \rho_a) dv dt. \quad (3)$$

V_a and V_b represent the volumes occupied by the sources a and b, respectively. Notice that the potentials on one side of the equation are advanced potentials. The notation may be considerably simplified by the introduction of "four-vectors" for the sources and potentials.

$$S_\nu = (\boldsymbol{J}, jc\rho); \qquad A_\nu = \left(\boldsymbol{A}, j\frac{\phi}{c}\right); \qquad \nu = 1, 2, 3, 4. \quad (4)$$

In terms of these quantities, (3) becomes the following:

$$\int\int_{V_b} A_\nu{}^a S_{\nu b} dv dt = \int\int_{V_a} \tilde{A}_\nu{}^b S_\nu{}^a dv dt. \quad (5)$$

By convention, the index ν is to be summed.

The proof of (3) is straightforward. Let $\sum_\nu{}^a(\boldsymbol{r}, \omega)$ be the Fourier transform of $S_\nu{}^a(\boldsymbol{r}, t)$.

$$\sum_\nu^a (\boldsymbol{r}, \omega) = \frac{1}{\sqrt{2\pi}} \int_{-\infty}^{\infty} S_\nu{}^a(\boldsymbol{r}, t) e^{-j\omega t} dt;$$

$$S_\nu{}^a(\boldsymbol{r}, t) = \frac{1}{\sqrt{2\pi}} \int_{-\infty}^{\infty} \sum_\nu^a (\boldsymbol{r}, \omega) e^{j\omega t} d\omega. \quad (6)$$

Similarly, $\sum_\nu^b(\boldsymbol{r}, \omega)$, $\tilde{\Gamma}_\nu{}^a(\boldsymbol{r}, \omega)$, and $\tilde{\Gamma}_\nu{}^b(\boldsymbol{r}, \omega)$ are the transforms of $S_\nu{}^b(\boldsymbol{r}, t)$, $A_\nu{}^a(\boldsymbol{r}, t)$, and $\tilde{A}_\nu{}^b(\boldsymbol{r}, t)$, respectively. $\boldsymbol{r}$ represents the coordinates of source a and $\boldsymbol{r}'$ the coordinates of source b. Parseval's formula for the Fourier transform is the following:[3]

$$\int_{-\infty}^{\infty} F_1(t) F_2(t) dt = \int_{-\infty}^{\infty} G_1(\omega) G_2(-\omega) d\omega, \quad (7)$$

where the $G(\omega)$ functions are the transforms of the $F(t)$ functions. From this it follows that

$$\int\int_{V_b} A_\nu{}^a S_\nu{}^b dv' dt = \int_{-\infty}^{\infty} \int_{V_b} A_\nu{}^a(\boldsymbol{r}', t) S_\nu{}^b(\boldsymbol{r}', t) dv' dt$$

$$= \int_{-\infty}^{\infty} \int_{V_b} \Gamma_\nu{}^a(\boldsymbol{r}', \omega) \sum_\nu^b (\boldsymbol{r}', -\omega) dv' d\omega. \quad (8)$$

The transformed potential functions are given in terms of the transformed sources by the usual formulas.

$$\Gamma_\nu{}^a(\boldsymbol{r}', \omega) = \frac{\mu}{4\pi} \int_{V_a} \frac{\sum_\nu^a (\boldsymbol{r}, \omega) e^{-jKR} dv}{R};$$

$$R = |\boldsymbol{r} - \boldsymbol{r}'|, \; K = \omega/c. \quad (9)$$

[3] E. C. Titchmarsh, "Introduction to the Theory of Fourier Integrals," Oxford University Press, New York, N. Y., p. 50; 1937.

$$\tilde{\Gamma}_\nu{}^b(\boldsymbol{r}, \omega) = \frac{\mu}{4\pi} \int_{V_b} \frac{\sum_\nu^b (\boldsymbol{r}', \omega) e^{jKR} dv'}{R}. \quad (10)$$

Let $-\omega$ be substituted for ω in (10).

$$\tilde{\Gamma}_\nu{}^b(\boldsymbol{r}, -\omega) = \frac{\mu}{4\pi} \int_{V_b} \frac{\sum_\nu^b (\boldsymbol{r}', -\omega) e^{-jKR} dv'}{R}. \quad (11)$$

Now, (9) is substituted into (8).

$$\int_{-\infty}^{\infty} \int_{V_b} \Gamma_\nu{}^a(\boldsymbol{r}', \omega) \sum_\nu^b (\boldsymbol{r}', -\omega) dv' d\omega$$

$$= \int_{-\infty}^{\infty} \int_{V_b} \left[\frac{\mu}{4\pi} \int_{V_a} \frac{\sum_\nu^a (\boldsymbol{r}, \omega) e^{-jKR}}{R} dv \right] \sum_\nu^b (\boldsymbol{r}', -\omega) dv' d\omega$$

$$= \int_{-\infty}^{\infty} \int_{V_a} \sum_\nu^a (\boldsymbol{r}, \omega) \left[\frac{\mu}{4\pi} \int_{V_b} \frac{\sum_\nu^b (\boldsymbol{r}', -\omega) e^{-jKR}}{R} dv' \right] dv d\omega$$

$$= \int_{-\infty}^{\infty} \int_{V_a} \sum_\nu^a (\boldsymbol{r}, \omega) \tilde{\Gamma}_\nu{}^b(\boldsymbol{r}, -\omega) dv d\omega.$$

The last step resulted from a substitution of (11) for the term in the square brackets. Again Parseval's formula may be applied.

$$\int_{-\infty}^{\infty} \int_{V_a} \sum_\nu^a (\boldsymbol{r}, \omega) \tilde{\Gamma}_\nu{}^b(\boldsymbol{r}, -\omega) dv d\omega$$

$$= \int_{-\infty}^{\infty} \int_{V_a} S_\nu{}^a(\boldsymbol{r}, t) \tilde{A}_\nu{}^b(\boldsymbol{r}, t) dv dt. \quad (12)$$

This demonstrates the validity of (3). This reciprocity theorem could also have been written with the tildes over the a fields instead of the b fields.

$$\int\int_{V_b} (\tilde{\boldsymbol{A}}_a \cdot \boldsymbol{J}_b - \tilde{\phi}_a \rho_b) dv dt = \int\int_{V_a} (\boldsymbol{A}_b \cdot \boldsymbol{J}_a - \phi_b \rho_a) dv dt. \quad (13)$$

The only restrictions on the theorem are that the sources be in free space and that their Fourier transforms exist. Written in the form (5), it is clear that the reciprocity integral, $\int\int A_\nu{}^a S_\nu{}^b dv dt$, is a quantity which is invariant under a Lorentz transformation. Both A_ν and S_ν transform like four-vectors under a Lorentz transformation, and their scalar product must be an invariant; $dv dt$ is also an invariant. This means, of course, that the integral may be calculated in an arbitrary coordinate system which is uniformly translating and will always yield the same number. Eq. (5) is also the appropriate reciprocity relation for scalar fields which satisfy the wave equation, such as the sound-wave field. In this case, A_ν would be replaced by the velocity potential ϕ, and S_ν would be replaced by the source of sound waves.

Theorem II

The second relation involves the electric and magnetic fields directly, rather than the electromagnetic potentials. One may speak of advanced electric and magnetic fields as those derived from advanced potentials by the usual process of differentiation, (VI) and (V). These fields naturally satisfy Maxwell's equations, as do the retarded fields. Let there be two sources of electromagnetic fields, (J_a, K_a) and (J_b, K_b). J is electric current density, and K is magnetic current density, introduced for added generality. Then the following reciprocity statement holds:

$$\int\int (E_a \cdot J_b + H_a \cdot K_b) dv dt = -\int\int (\tilde{E}_b \cdot J_a + \tilde{H}_b \cdot K_a) dv dt. \quad (14)$$

Notice two things. First, there is a minus sign in front of one of the integrals, and second, the tildes could just as well be placed over the a fields as over the b fields. This relation could be proved by the method used for Theorem I. However, with the addition of magnetic current and because the electric and magnetic fields are not given so simply in terms of the sources, that method would be laborious, and it will be convenient to prove (14) in another way.

Let the fields due to (J_a, K_a) be retarded fields and those due to (J_b, K_b) be calculated in the advanced sense. Both satisfy Maxwell's equations.

$$\nabla \times E_a + \frac{\partial B_a}{\partial t} = -K_a; \quad \nabla \times \tilde{E}_b + \frac{\partial \tilde{B}_b}{\partial t} = -K_b.$$
$$\nabla \times H_a - \frac{\partial D_a}{\partial t} = J_a; \qquad \nabla \times \tilde{H}_b - \frac{\partial \tilde{D}_b}{\partial t} = J_b. \quad (15)$$

After expanding the divergence of $(E_a \times \tilde{H}_b + \tilde{E}_b \times H_a)$ and substituting from (15), we find that

$$\begin{aligned}
&\nabla \cdot (E_a \times \tilde{H}_b + \tilde{E}_b \times H_a) \\
&= \tilde{H}_b \cdot \nabla \times E_a - E_a \cdot \nabla \times \tilde{H}_b + H_a \cdot \nabla \times \tilde{E}_b - \tilde{E}_b \cdot \nabla \times H_a \\
&= \tilde{H}_b \cdot \left(-\frac{\partial B_a}{\partial t} - K_a\right) - E_a \cdot \left(\frac{\partial \tilde{D}_b}{\partial t} + J_b\right) \\
&\quad + H_a \cdot \left(-\frac{\partial \tilde{B}_a}{\partial t} - K_b\right) - \tilde{E}_b \cdot \left(\frac{\partial D_a}{\partial t} + J_a\right) \\
&= -\mu \frac{\partial}{\partial t}[\tilde{H}_b \cdot H_a] - \epsilon \frac{\partial}{\partial t}[\tilde{E}_b \cdot E_a] \\
&\quad - [(E_a \cdot J_b + H_a \cdot K_b) + (\tilde{E}_b \cdot J_a + \tilde{H}_b \cdot K_a)]. \quad (16)
\end{aligned}$$

Next, we integrate both sides of (16) over a volume which contains both sources and over a time interval $T_1 < t < T_2$. Then, with the application of the divergence theorem to the left-hand side, it follows that

$$\begin{aligned}
\int_{T_1}^{T_2} \int_V [(E_a \cdot J_b + H_a \cdot K_b) + (\tilde{E}_b \cdot J_a + \tilde{H}_b \cdot K_a)] dv dt \\
= -\int_{T_1}^{T_2} \int_S (E_a \times \tilde{H}_b + \tilde{E}_b \times H_a) \cdot n dS dt \\
- \int_V \mu H_a \cdot \tilde{H}_b dv \Big|_{T_1}^{T_2} - \int_V \epsilon E_a \cdot \tilde{E}_b dv \Big|_{T_1}^{T_2}. \quad (17)
\end{aligned}$$

Let T_1 be some time prior to the sources and T_2 some time after the sources are both off. At time T_1 the retarded fields are everywhere zero, and at time T_2 the advanced fields are everywhere zero. Therefore, for this choice of T_1 and T_2, the two volume integrals on the right hand side of (17) vanish identically. Next, an inspection of (17) shows that the value of the surface integral is independent of the size or shape of the surface, so long as the surface is large enough to enclose completely both sources. Let the surface be a large sphere of radius R. Then, if, for example, $R \gg c(|T_1| + |T_2|)$, the retarded field will not reach the surface S during the interval $T_1 < t < T_2$, and the surface integral will be identically zero. It follows then that if the integrations over space and time completely enclose the sources,

$$\int\int [(E_a \cdot J_b + H_a \cdot K_b) + (\tilde{E}_b \cdot J_a + \tilde{H}_b \cdot K_a)] dv dt = 0, \quad (18)$$

and if we divide the integral into two parts,

$$\int\int (E_a \cdot J_b + H_a \cdot K_b) dv dt = -\int\int (\tilde{E}_b \cdot J_a + \tilde{H}_b \cdot K_a) dv dt. \quad (19)$$

It is convenient to use Rumsey's "reaction" notation for the scalar products.[1]

$$\langle a, b \rangle = \int\int (E_a \cdot J_b + H_a \cdot K_b) dv dt \quad (20)$$

$$\langle \tilde{b}, a \rangle = \int\int (\tilde{E}_b \cdot J_a + \tilde{H}_b \cdot K_a) dv dt. \quad (21)$$

Then (14) may be written as

$$\langle a, b \rangle = -\langle \tilde{b}, a \rangle. \quad (22)$$

Suppose that the volume of integration in (17) enclosed only one of the sources, say a, even though the time integration enclosed both sources. It is clear from (17) that (22) would still be valid with

$$\langle a, b \rangle = \int\int_S (E_a \times \tilde{H}_b + \tilde{E}_b \times H_a) \cdot n dS dt. \quad (23)$$

There are two assumptions implicit in the proof of (14): first, ϵ and μ are assumed to be simple scalar functions of position; and second, the conductivity of the space is taken to be zero. The second restriction is not as serious as it sounds, for as long as the extent of the conductivity is finite, its effect can be lumped with the electric current sources, J. On the other hand, if the space is partially bounded by ideal conductors, (14) is still valid because the surface integral vanishes on the surface of a perfect conductor.

Eq. (14) has the following properties. Although the integrals which occur in (14) are not Lorentz invariant as are those in (3), (14) will probably be more useful for boundary value problems. This is because it involves the electric and magnetic fields directly rather than the potentials. Eqs. (20) and (21) may be regarded as the "reaction" between two sources of arbitrary time dependence. Notice that (20) and (21) have the dimensions of energy. As a matter of fact, it can be shown that $\langle a, a\rangle$, the self reaction or self energy of a source, is always a negative number. It appears to be the total energy radiated by the source. If source b were an impulsive unit electric dipole of the form $J_b = i\delta(r-r_0)\delta(t-t_0)$, then the reaction $\langle a, b\rangle$ would just be the i component of the a electric field at (r_0, t_0), $E_{ai}(r_0, t_0)$.

It should be clear why the advanced fields must be used in one of the integrals (20) or (21) in order that (22) be valid. Suppose that both sources a and b are of short-time duration. It can be arranged that the wave emanating from a in the usual retarded sense will reach source b just as the latter turns on. Then $\langle a, b\rangle$ will have some value other than zero. At this time, source a has long since turned off. The only way in which the wave leaving b can arrive at source a while the latter is on is by going backward in time. Thus, the wave from b must be an advanced wave.

As an application, (22) will be used in the next section to derive a variational expression for scattering from a perfect conductor.

Variational Formulation for Scattering

Suppose that a source, J_h, is radiating in the presence of a perfect conductor S, as shown in Fig. 1. (Since we are dealing with a perfect conductor, we need not consider magnetic current in this section.) We wish to know what the field scattered by S is. To proceed, following the method developed by Rumsey,[1] we place a test source J_g at the point of observation and consider the reaction between the test source and the scattered field. If J_g is an impulsive unit electric dipole of the form described in the preceding section, then this reaction is a measure of the instantaneous scattered electric field at the point of observation. It will be necessary to employ the advanced field associated with the test source J_g in order to use (22) and obtain the stationary expression for the scattered field.

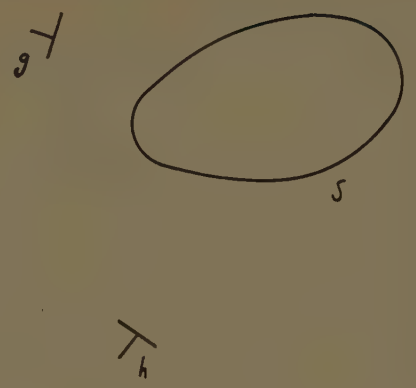

Fig. 1.

In the absence of the scatterer, space is described by ϵ_0, μ_0, and with the scatterer present by ϵ, μ_0 and σ. Let J_g be zero for the moment. The total field due to J_h will be found by solving Maxwell's equations for the retarded fields.

$$\nabla \times \boldsymbol{E}_{Th} = \frac{\partial \boldsymbol{B}_{Th}}{\partial t} = -\frac{\partial}{\partial t}(\mu_0 \boldsymbol{H}_{Th}), \tag{24}$$

$$\nabla \times \boldsymbol{H}_{Th} = \frac{\partial \boldsymbol{D}_{Th}}{\partial t} + \sigma \boldsymbol{E}_{Th} + \boldsymbol{J}_h$$

$$= \frac{\partial}{\partial t}(\epsilon_0 \boldsymbol{E}_{Th}) + \left[\sigma + (\epsilon - \epsilon_0)\frac{\partial}{\partial t}\right]\boldsymbol{E}_{Th} + \boldsymbol{J}_h. \tag{25}$$

Let

$$\boldsymbol{J}_b = \left[\sigma + (\epsilon - \epsilon_0)\frac{\partial}{\partial t}\right]\boldsymbol{E}_{Th}.$$

Then $(\boldsymbol{E}_{Th}, \boldsymbol{H}_{Th})$ appears to be the field resulting from J_b and J_h in free space. J_b is a current equivalent to the scatterer (in fact, it is the current induced on the scatterer) and we can now apply superposition in free space. Let $(\boldsymbol{E}_b, \boldsymbol{H}_b)$ be the field due to J_b and $(\boldsymbol{E}_h, \boldsymbol{H}_h)$ be the field due to J_h. Then $\boldsymbol{E}_{Th} = \boldsymbol{E}_h + \boldsymbol{E}_b$, and $\boldsymbol{H}_{Th} = \boldsymbol{H}_h + \boldsymbol{H}_b$. $(\boldsymbol{E}_b, \boldsymbol{H}_b)$ is thus the field scattered from the obstacle S due to J_h. Because S is assumed an ideal conductor, J_b flows only on the surface of S. Furthermore, the usual boundary condition for a perfect conductor applies

$$\boldsymbol{n} \times (\boldsymbol{E}_h + \boldsymbol{E}_b) = 0 \tag{26}$$

on S.

Next, we let $J_h = 0$ and consider the advanced field due to J_g in the presence of the scatterer.

$$\nabla \times \tilde{\boldsymbol{E}}_{Tg} = -\frac{\partial \tilde{\boldsymbol{B}}_{Tg}}{\partial t} = -\frac{\partial}{\partial t}(\mu_0 \tilde{\boldsymbol{H}}_{Tg}), \tag{27}$$

$$\nabla \times \tilde{\boldsymbol{H}}_{Tg} = \frac{\partial \tilde{\boldsymbol{D}}_{Tg}}{\partial t} + \sigma \tilde{\boldsymbol{E}}_{Tg} + \boldsymbol{J}_g$$

$$= \frac{\partial}{\partial t}(\epsilon_0 \tilde{\boldsymbol{E}}_{Tg}) + \left[\sigma + (\epsilon - \epsilon_0)\frac{\partial}{\partial t}\right]\tilde{\boldsymbol{E}}_{Tg} + \boldsymbol{J}_g. \tag{28}$$

Let

$$J_a = \left[\sigma + (\epsilon - \epsilon_0)\frac{\partial}{\partial t}\right]\tilde{E}_{Tg}.$$

In this case, $(\tilde{E}_{Tg}, \tilde{H}_{Tg})$ appears to be the advanced field resulting from J_a and J_g in free space. We apply superposition as before, letting $(\tilde{E}_a, \tilde{H}_a)$ be the field due to J_a and $(\tilde{E}_g, \tilde{H}_g)$ be the field due to J_g. $\tilde{E}_{Tg}=\tilde{E}_g+\tilde{E}_a$, $\tilde{H}_{Tg}=\tilde{H}_g+\tilde{H}_a$, and $(\tilde{E}_a, \tilde{H}_a)$ is the scattered field for the advanced solution to the scattering problem. Again, because S is assumed to be a perfect conductor, J_a flows only on the surface of S. In this case, the appropriate boundary condition on S is the following:

$$n \times (\tilde{E}_a + \tilde{E}_g) = 0. \tag{29}$$

With both J_h and J_g present, the effect of the scatterer is given by J_b and J_a in free space. It should be noted that either retarded or advanced fields may be calculated from the four currents J_h, J_b, J_g, J_a. However, it is important to bear in mind how J_b and J_a are defined and how $\tilde{E}_a$ and E_b are defined. Neither $n\times(\tilde{E}_h+\tilde{E}_b)$ nor $n\times(E_g+E_a)$ is zero on S.

Let J_g be a delta function in both space and time.

$$J_g = i\delta(r - r_0)\delta(t - t_0).$$

Then

$$\langle b, g\rangle = \int E_b \cdot J_g dvdt = E_{bi}(r_0, t_0), \tag{30}$$

where i is a unit vector; $\langle b, g\rangle$ is then the quantity in which we are interested and we will now find a stationary expression for it.

J_b is a source which flows only on the surface of S. Therefore, from (29),

$$\langle \tilde{g}, b\rangle = \int \tilde{E}_g \cdot J_b dvdt = -\int \tilde{E}_a \cdot J_b dvdt = -\langle \tilde{a}, b\rangle. \tag{31}$$

J_a is also a surface source, and from (26),

$$\langle h, a\rangle = \int E_h \cdot J_a dvdt = -\int E_b \cdot J_a dvdt = -\langle b, a\rangle. \tag{32}$$

It follows from the reciprocity theorem (22) that

$$\langle b, g\rangle = -\langle \tilde{g}, b\rangle, \tag{33}$$

$$\langle b, a\rangle = -\langle \tilde{a}, b\rangle. \tag{34}$$

The combination of (31), (33), and (34) yields the following:

$$\langle b, g\rangle = -\langle \tilde{g}, b\rangle = \langle \tilde{a}, b\rangle = -\langle b, a\rangle. \tag{35}$$

With the substitution of (32),

$$\langle b, g\rangle = \langle h, a\rangle. \tag{36}$$

Eqs. (33), (35), and (36) are three expressions for $\langle b, g\rangle$, the quantity of interest. In the external scattering problem, E_g, $\tilde{E}_g$, E_h, and $\tilde{E}_h$ are known, whereas J_a and J_b are unknown. An expression which is homogeneous in both a and b and which is equal to $\langle b, g\rangle$ is obtained by multiplying together (33) and (36) and dividing by (35).

$$\langle b, g\rangle = \frac{\langle h, a\rangle\langle \tilde{g}, b\rangle}{\langle b, a\rangle} = \frac{\int\int E_h \cdot J_a dvdt \int\int \tilde{E}_g \cdot J_b dvdt}{\int\int E_b \cdot J_a dvdt}$$

$$= \frac{\int\int E_h \cdot J_a dvdt \int\int \tilde{E}_g \cdot J_b dvdt}{\int\int\int J_b \cdot \Gamma \cdot J_a dv' dvdt}. \tag{37}$$

Γ is the free-space retarded vector Green's function. This is the formula for the scattered field. It is clear that the amplitudes of J_a and J_b cancel from the numerator and denominator of the fraction and can have no effect on the answer. It is shown in the Appendix that (37) is stationary with respect to variations of J_a and J_b about their true values. This means that a reasonable guess for the functional forms of J_a and J_b should, when substituted into (37), lead to an even more reasonable estimate of the scattered field. More precisely, if the errors in the choices of J_a and J_b are $0(\epsilon)$ and $0(\eta)$ respectively, then the error in the calculation of $\langle b, g\rangle$ will be $0(\epsilon\eta)$. Because the location of J_g is quite arbitrary, (37) may be used to find the scattered field everywhere in space resulting from J_h. Eq. (37) is very similar to formulas which have been derived for fields whose time dependence is periodic, $e^{j\omega t}$. The essential difference is that in (37) the time dependence of the illuminating source, J_h, is arbitrary.

For certain types of approximate variational calculations, such as the determination of quantum mechanical energy levels or resonant frequencies of a cavity, it is possible to know *a priori* that the resulting error will be always positive or always negative. In these cases the result of any particular approximate calculation is either an upper or a lower bound on the true value, upper or lower depending on the sign of the error. This added feature is, of course, very important. Dolph[4] has shown, however, that this property is not obtained when one performs variational calculations for exterior wave scattering using the usual formulations for time periodic fields. Eq. (37) also fails in this respect. To see this, we must investigate the second variation of (37).

$$\delta^2\langle b, g\rangle = 2\langle \delta b, \delta a\rangle - \frac{2\langle b, \delta a\rangle\langle \delta b, a\rangle}{\langle b, a\rangle}. \tag{38}$$

[4] C. L. Dolph, "A saddle point characterization of the schwinger stationary points in exterior scattering problems," *J. Soc. Ind. Appl. Math.*, vol. 5, pp. 89–104; September, 1957.

For small variations, the error incurred in any particular calculation is proportional to the second variation, (38). In order that the answer be a bound on the true value of the quantity being calculated, $\delta^2\langle b, g\rangle$ must have the same algebraic sign for all possible variations δa and δb. Suppose that for a particular calculation $\delta a = \alpha$ and $\delta b = \beta$. Then an evaluation of (38) would result in some number, say N. $\delta^2\langle b, g\rangle = N$. Now consider another calculation in which $\delta a = \alpha$ and $\delta b = -\beta$. Then, by inspection of (38), we see that $\delta^2\langle b, g\rangle = -N$. In general then, (37) fails to give a bound for the scattered field.

J_h may be chosen to be a point dipole with a delta function time dependence. In this case, (37) will give an approximation to both the time and space parts of the Green's function for the scattering problem. From this, one may obtain the scattered field resulting from an arbitrary illuminating source.

Appendix

Eq. (37) may be written as $\langle b, a\rangle\langle b, g\rangle = \langle h, a\rangle\langle \tilde{g}, b\rangle$. Then,

$$(\langle \delta b, a\rangle + \langle b, \delta a\rangle)\langle b, g\rangle + \langle b, a\rangle\delta\langle b, g\rangle = \langle h, \delta a\rangle\langle \tilde{g}, b\rangle + \langle h, a\rangle\langle \tilde{g}, \delta b\rangle$$

$$\langle b, a\rangle\delta\langle b, g\rangle = -\langle b, g\rangle\langle \delta b, a\rangle - \langle b, g\rangle\langle b, \delta a\rangle + \langle b, \delta a\rangle\langle b, g\rangle - \langle b, g\rangle\langle \bar{a}, \delta b\rangle$$

$$= -\langle b, g\rangle\langle \delta b, a\rangle + \langle b, g\rangle\langle \delta b, a\rangle = 0.$$

Both the boundary conditions and the reciprocity theorem were employed above. Also, the variations in J_a and J_b were required to be surface distributions.

Acknowledgment

The author gratefully acknowledges the contributions of Prof. V. H. Rumsey, Prof. S. Silver, M. C. Horton, and N. Kusnezeov.

Frequency Scintillations of Satellite Signals Before and After the Argus Experiments*

P. R. ARENDT†

Summary—**Satellite signals are effected by frequency scintillations in the same manner as radio star emissions. Therefore, the Doppler shift of such signals suffers fluctuations. These alterations are a function of the variations of the electron density distribution along the radio-ray path under observation. The number and the magnitude of these scintillations are used to measure the roughness of the ionosphere (formation of a scintillation index). The paper deals with the alteration of the established scintillation index during a time interval in August and September, 1958, *i.e.*, before, during, and after the well known Argus experiments. The observations indicate that no long-living ionospheric inhomogeneities were produced within the zones of the ionosphere which could be checked from our ground station.**

IT has been shown that satellite signals are effected by scintillations in the same manner as radio star emissions.[1] Since the satellites are moving fast, their signals suffer from a broad Doppler shift, which is described by the known equation,

$$\frac{f_T}{f_R} = 1 \mp \frac{b}{v},$$

where f_T is the transmitted frequency, f_R is the received frequency, b is the velocity of the satellite relative to the observer, and v is the phase velocity of the propagation of the radio signal; v is connected to the refractive index n of the medium by the following definition:

$$n = \frac{c}{v},$$

where c is the velocity of light in free space. b is also a function of n. Thus, it is obvious that fluctuations of n will create corresponding alterations of the observed frequency f_R. Now, since n is a function of the electron density of the medium, it is evident that inhomogeneities of the ionosphere along the signal ray path will be reflected by deviations of the observed frequency from a

* Manuscript received by the PGAP, August 21, 1959.
† Inst. for Exploratory Res., U. S. Army Signal Res. and Dev. Lab., Fort Monmouth, N. J.
[1] H. P. Hutchinson and P. R. Arendt, "Ionospheric scintillations of satellite signals," *Proc. 10th Interntl. Astronaut. Cong.*, London, Eng.; May, 1959 (to be published).

smooth Doppler curve. The longer the signal travels within the ionosphere the greater is the probability of observing the integrated effect of perturbations along the ray path. Therefore, most of the frequency scintillations will be observed during the incoming or outgoing period of a Doppler measurement. Fig. 1 is an example of this type of observation.

However, such scintillations have been observed at any moment of a satellite's passage. It has also been found that higher frequencies (in the 100-mc range) are less sensitive to scintillations than at 20 or 40 mc. Further, strong and multiple scintillations have been observed for rather long periods of several weeks. These intervals are preceded and followed by others which are quiet and during which no scintillations occur. Since this trend is in line with the above concept of the origin of the scintillations, the number and magnitude of these frequency deviations are used for a measure of the ionospheric roughness of the propagation path under observation. Figs. 2 and 3 give examples of various types of scintillations. On some days, the scintillations (on 20 mc), were so strong and manyfold that it became impossible to make an observation of the Doppler shift.

Some of the periods of strong scintillation activity could be correlated to extreme solar activity. For example, during a period shortly before and after June 8, 1958, strong scintillations with Sputnik III (δ, 1958) were observed on 20 mc. During the same time, special solar activity was reported. In the case of Fig. 3, effects of solar flares and short wave fadeouts have been reported from 1653 GMT to 1707 GMT in the White Sands observations on 200 mc. This time coincides exactly with the scintillations in Fig. 3. However, other observations of the same period were made in which there were no scintillations during solar activity; for example, during orbit 332 of Sputnik III on June 8, 1958. But on the same day, exceptional strong scintillations were observed during the prior orbit 331, in spite of the fact that the solar activity was reportedly "milder" at that time. On the other hand, a day which was reported "quiet" with respect to solar activity, brought no scintillations at all (orbits 341 and 346 on June 9, 1958).

Various periods of strong scintillation effects have occurred; for example, during the second half of December, 1958, scintillations similar to the ones during the reported period in June, 1958 were found.

With the assumed, but unestablished, correlation to solar activity in mind, the recently published Argus[2] experiment offered some chance for a more detailed investigation. In this experiment, nuclear radiation was released in outer space high above the earth's dense atmosphere by various atomic bursts (on August 27 and 30, and September 6, 1958). Since the status of the iono-

[2]White House Press Release, March 26, 1959.

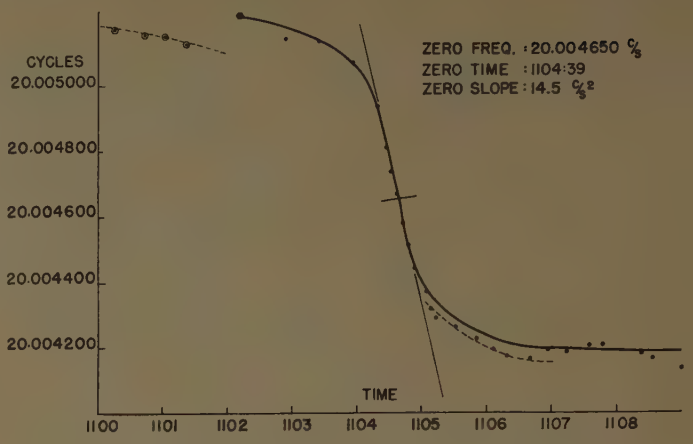

Fig. 1—Doppler curve of Sputnik III at its perigee (217-km altitude at 11 04.8 GMT) at 20 mc.

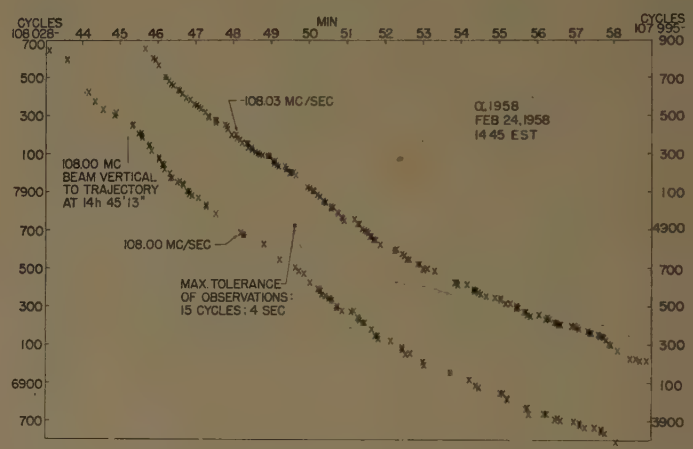

Fig. 2—Part of a Doppler curve of Explorer I at 108.00 and 108.03 mc; the frequency deviations are multiples of the observational tolerance.

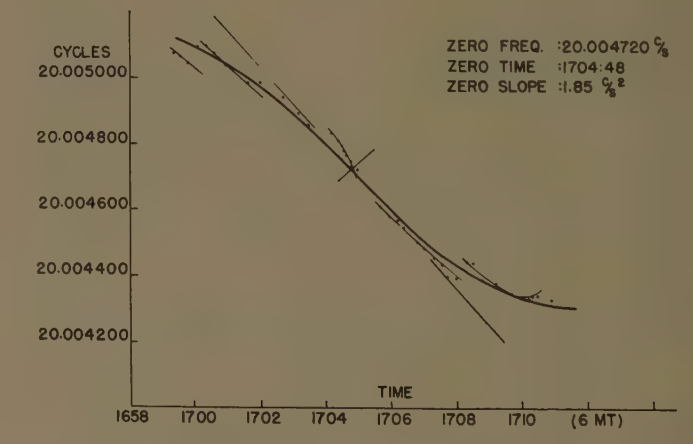

Fig. 3—Doppler curve of Sputnik III during a N to S passage, changing altitude from 570 to 990 km; at zero time in 740-km altitude.

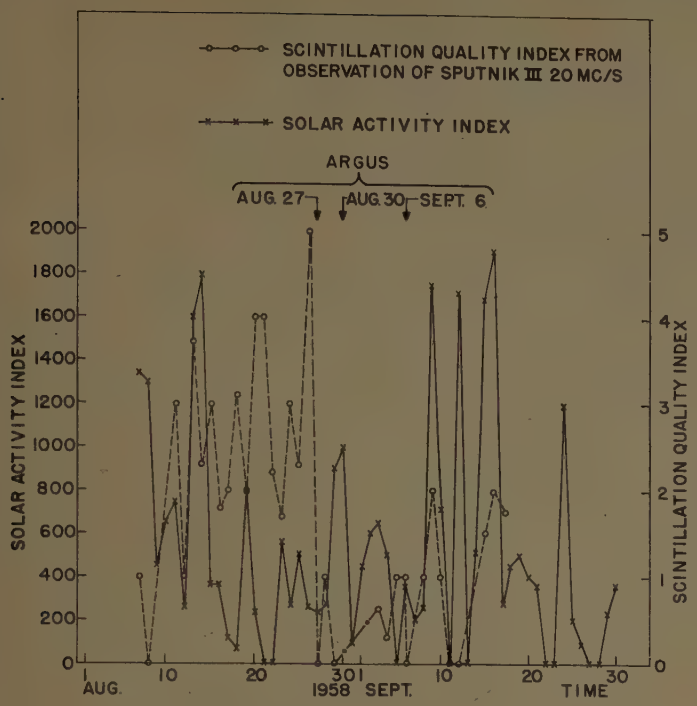

Fig. 4—Scintillation quality index compared with solar activity index.

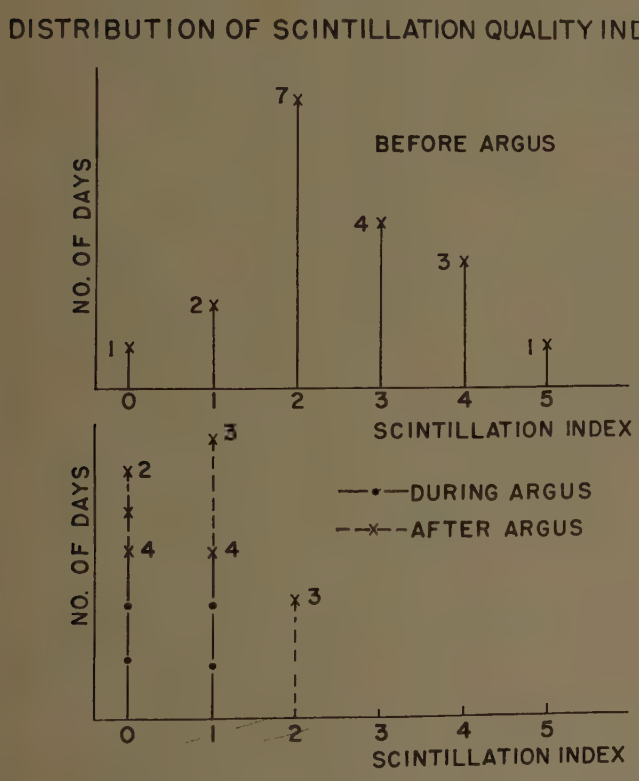

Fig. 5—Histograms of scintillation quality index.

sphere would have been influenced by these experiments, at least for the period of the experiments and possibly for some time thereafter (for some weeks), a certain influence of the Argus experiments on the observation of the scintillation of satellite signals could be expected. *A priori*, it is an open question whether the Argus experiment would multiply or reduce the number of scintillations. The question is whether such an experiment produces rather a smooth distribution of electrons or a very heterogeneous one over the area under investigation.

Since the lower frequencies are more sensitive with respect to the inhomogeneities of the ionosphere than the higher frequencies, the signals from Sputnik III on 20 mc were chosen. This frequency was found to be very convenient as an indication of whether the ionosphere contains more or less inhomogeneities.

The first inspection of the data indicates that a smooth distribution existed during the period after Argus, or in other words, that a naturally rough distribution was smoothed (see Fig. 4). It is obvious that there were strong scintillations before August 27 (the day that the first of the three Argus explosions were performed) but very few scintillations during or after Argus. During the period from August 2 to August 25 there were observed 75 Sputnik orbits. Only 13 of these orbits were nearly free from scintillations; that is 17.3 per cent. From August 27 through September 23, another 37 orbits were observed; 19 orbits of these or 57.7 per cent were nearly free from scintillations. Moreover, the orbits of that latter period showed very few scintillations per passage in contrast to the first period in which most orbits had many scintillations. During the period before Argus, the number of days in which scintillations occurred was randomly distributed over the various groups of a qualitatively measured scintillation intensity (daily index). However, during and shortly after Argus, the maximum of this distribution was obviously shifted to a very low scintillation intensity (see histograms of Fig. 5). A direct comparison of the solar intensity with this qualitatively measured scintillation intensity showed no correlation. Strong solar activity was observed between August 11 and August 20, as well as between September 9 and 19. However, the scintillation intensity decreased after August 27 (see Fig. 4).

In addition to the above, a more exact investigation of the data was tried. For this purpose, the qualitative scintillation index was replaced by a quantitative one. This was done by using a planimeter and measuring the area above and below the smooth Doppler curve limited by a system of straight lines which connect the successive points of measurements (see Fig. 6). Then, this area was defined as the scintillation index. The method is somewhat arbitrary because it assumes an equal number of observations per unit time. However, it was accepted in view of the fact that the frequency measurements on Doppler shifts were normally performed every two seconds. The results of this type of classification are given in the distribution of Fig. 7, which again indicates the trend to a higher scintillation index during the time before Argus.

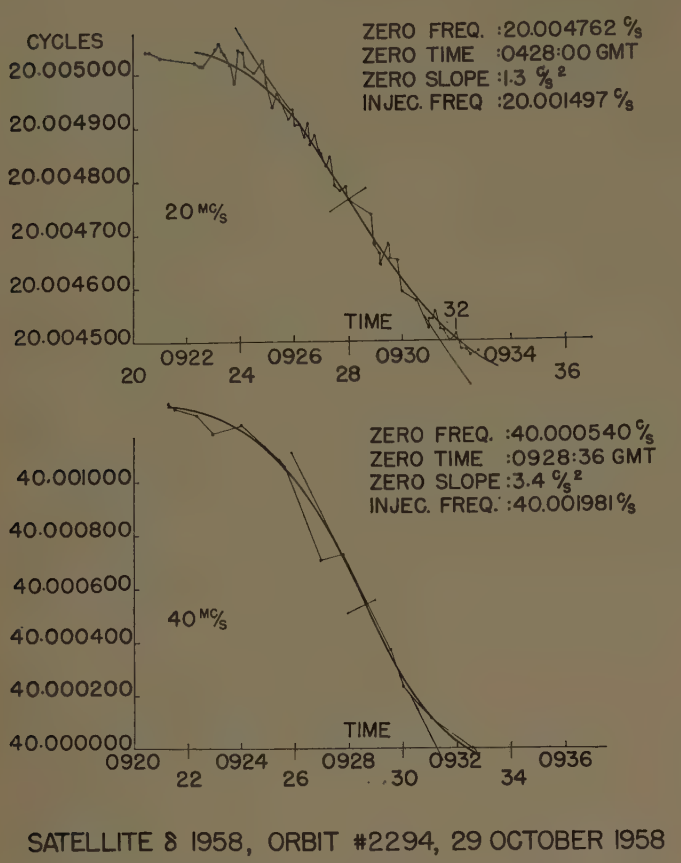

Fig. 6—Area of quantitative scintillation index; Doppler curves of Sputnik III on 20 mc and on 40 mc.

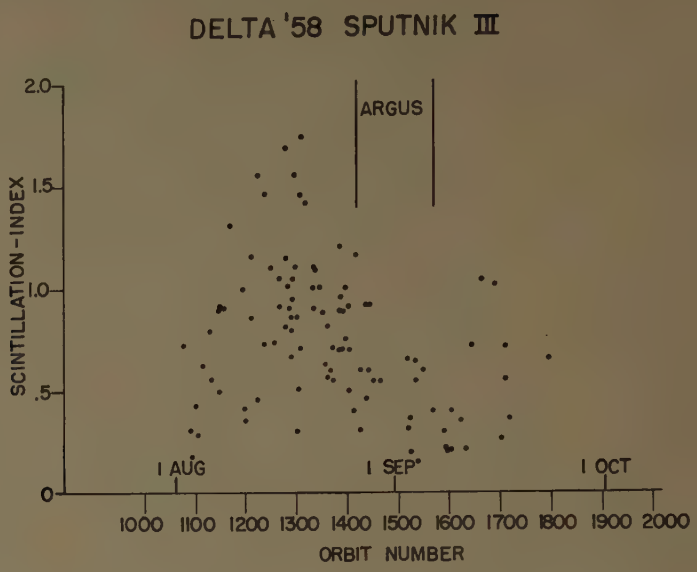

Fig. 7—Distribution of scintillation index before and after Argus.

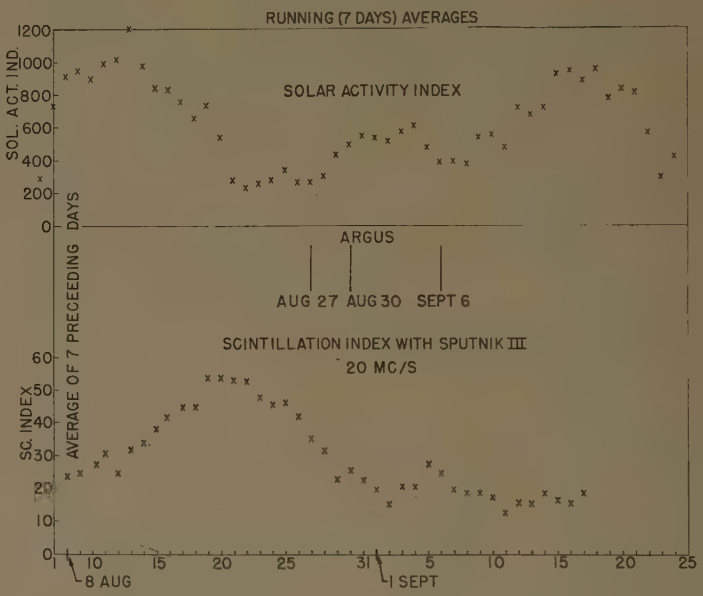

Fig. 8—Running (7 days) averages of solar activity index and of quantitative scintillation index.

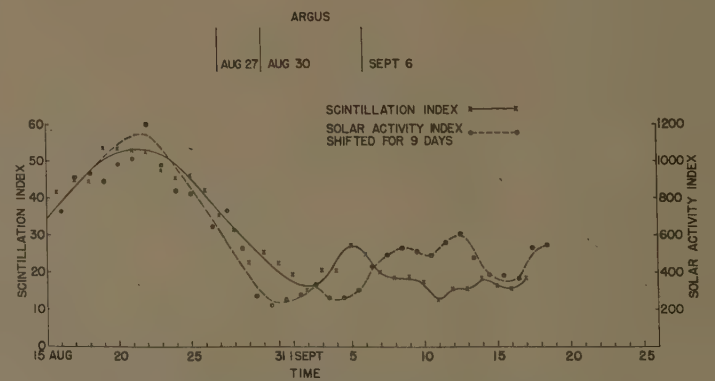

Fig. 9—Apparent correlation of solar activity and scintillation after arbitrary time shift.

For a comparison of this scintillation index with solar activity, a running daily average (over 7 days) was used. A measure of the solar activity was gained from the solar activity index published from High Altitude Observatory on Sacramento Peak Observatory optical measurements. The result is shown in Fig. 8 which indicates a remarkable smoothing of the daily fluctuations demonstrated in Figs. 4 and 7.

Again, the curves of Fig. 8 do not establish a direct correlation. The curve of the scintillation index indicates that the Argus experiment did not produce additional disturbance in the ionosphere (close to the area of the observed satellite tracks). If correlation between solar activity and scintillation index had been established, it might be concluded from a comparison of both curves in Fig. 8 that the Argus experiment smoothed the ionosphere rather than created inhomogeneities. However, such a conclusion cannot be drawn yet.

In order to test whether some kind of formal correlation could be established, the upper curve of Fig. 8 was shifted far forward in time (for 9 days) until a rather good correlation was obtained, at least for the first half of the observed period. The result of this shift is shown in Fig. 9. Now, the optical observed solar activity index appears to be in good correlation with the scintillation index for the time before Argus. During Argus and

thereafter, the trend of the two curves goes in opposite directions. Thus, this figure underlines the previous result, that there was no correlation to solar activity observed for the time during and after Argus.

What is the physical meaning which is connected to the rather arbitrary shift of 9 days? A shift for about 11 days, *i.e.*, for an entire solar cycle, was tried, but, in this case there was much less correlation, as can be easily guessed from Fig. 9. Further, significance of the used optical solar index has to be considered. This index measures all types of optical visible solar activity independently, whether or not this activity creates particle streams reaching the earth, whether the flares observed originate particles, ultraviolet radiation, or *X*-rays, etc. We had assumed first that this divergence could be compensated, at least in part, by the use of the 7-day running average. However, it should be considered that the electromagnetic wave effects for day-time solar activity are immediately felt in the ionosphere under observation, and that particle streams get active in the outer spheres of the earth's environment at least within two days after emission at the sun. Thus, these arguments lead back to the original concept of a comparison of daily averages of the two indices, respectively, which leads to the concept demonstrated by Fig. 4.

Furthermore, one has to consider that the satellite used for measuring purposes travels in different zones from one orbit to the next one. This means that the satellite's radio emission is propagated, within various parts of the ionosphere. These parts will be affected, to a rather varied degree, by the solar activity, thus explaining the above mentioned observation of a great variability in the scintillation index of successive passages.

Condensing the observations it can be stated that sometimes there is a good correlation between optical observed solar activity and frequency scintillations and at other times there is no correlation. Therefore, a much greater statistical volume of data, than that reported here, of observations made during a few weeks is necessary, in order to determine the manner in which the ionospheric inhomogeneities observed by frequency scintillations are related to specific solar events. These statistics must cover the position of the satellite and of the path of propagation at the time of observation. Future investigations should also consider that it might be easier to find a correlation to inhomogeneities of the magnetic field of the earth than to search for a direct correlation with optical observations of the sun.

With respect to the Argus experiment, it has been clearly observed that additional long-living ionospheric inhomogeneities were not produced within the zones of the ionosphere under observation during the measurements.

Acknowledgment

The author wishes to thank the members of the USASRDL Astro-Electronics Division's radio receiving station in Deal, N. J., where the satellite signal recordings used in this paper were performed. The recording operations were under the supervision of L. D. Manamon and D. R. Wills. The frequency measurements were made in the Frequency Control Division under the supervision of H. D. Tanzman. The quantitative scintillation index was measured by 1st Lt. R. Leach. The data on solar activity were communicated by H. F. Bush of USARPA. The author is much indebted to all mentioned and to many other members of USASRDL, especially Dr. E. M. Reilley and H. P. Hutchinson for their helpful advice and assistance.

Correction

F. S. Holt and A. Mayer, authors of "A Design Procedure for Dielectric Microwave Lenses of Large Aperture Ratio and Large Scanning Angle," which appeared on pages 25–30 of the January, 1957, issue of these Transactions, have requested that the following corrections to their paper be noted.

In (5c) on page 28, the equal sign after X_{2k} should be replaced by a plus sign, and in (5d), the argument of the tangent function should be $(\psi_{2k}+\phi_{2k})$.

On page 29, in (6f) the first tan $(\bar{\psi}_{2k-1}+\bar{\phi}_{2k-1})$ should be sec $(\bar{\psi}_{2k-1}+\bar{\phi}_{2k-1})$, and the algebraic sign before the term $(\overline{X}_{2k-1}-X_f)$ should be negative.

Antenna Image Quality Evaluation Part I—By an Optical Simulation Method*

J. J. MYERS†

Summary—**An optical simulation method was used to study the effect of aperture illumination on image quality for a high resolution antenna. It was determined that an illumination close to uniform yields the best image, as measured by the similarity of the image to the object when similarity was judged by a group of human observers. The techniques used are described, and the results of the evaluation of a typical class of illuminations are given.[1]**

Introduction

SYSTEM performance requirements for radar systems or other radio mapping systems sometimes dictate the use of antennas that are very large in terms of both wavelength and physical size. Some of the problems inherent in constructing large antennas may make it impracticable to build an antenna as large as desired. It is of considerable importance, therefore, that illumination of the maximum available aperture be done in the optimum manner in order to obtain the best image[2] that the antenna can give, as measured by a suitable criterion.

The most direct experimental method for determining the effect of aperture illumination on the quality of the image is to construct an antenna, or set of antennas, to vary the illumination, and to measure by some suitable means the effect upon image quality. This method is both expensive and time-consuming if the study is to be extensive. In practice, it probably would not be used for an exhaustive study of aperture illumination, although in specific instances it might be feasible.

An alternative method, which is more convenient, is to simulate the antenna imaging process, form suitable images, and judge their quality, taking into account the limitations of the simulation procedure. If the simulation method is sufficiently simple and flexible, a wide range of illumination may be studied relatively quickly and at small cost.

Many studies[3–5] have been made of photographic picture quality as related to the aperture illumination (lens characteristics) used in the imaging process. These studies have investigated largely the effects of lens aberrations. The effects upon image quality of resolution, scale, and contrast, has been the subject of study[6] from the standpoint of aerial photography, and the effect of aperture size (and to a limited extent, aperture illumination) upon the recognizability of certain types of ground targets has been studied for antennas.[7]

The study reported here was made to measure semiquantitatively the effect of aperture illumination on image quality and to try to get a clue to what constitutes the "best" illumination for an antenna for mapping purposes. Crucial to such an evaluation is the choice of a criterion of quality. A separate paper[8] discusses mathematical image quality criteria that are applicable in antenna theory, but still unanswered by any such discussion is the relationship between the results of applying a particular mathematical criterion and the results obtained when a competent observer judges image quality.

A nonmathematical criterion of quality was used for this experiment, *viz.*, the ability of a group of observers to identify correctly certain forms in images presented to them for assessment. The criterion seems appropriate since it is this kind of measurement of quality that is invoked in identifying features in a map. The choice of this criterion avoided the need to make a choice from among the mathematical criteria. In practice, special considerations not concerned with image quality might dictate the use of an illumination that is nonoptimum in an image-quality sense.

Experimental Method

Photographic film images of selected types of objects were formed through an off-focus lens system in front of which was placed a mask whose density varied as a func-

* Manuscript received by the PGAP, April 25, 1959; revised manuscript received, October 12, 1959. The research reported here was made possible through the support extended to the University of Illinois Control Systems Lab. jointly by the Depts. of the Army, Navy, and Air Force, under Signal Corps Contract DA-36-039-SC-56695, D/A Sub-Task 3-99-06-111. The material in this paper was abstracted from a dissertation submitted in partial fulfillment of the requirements for the Ph.D. degree at the University of Illinois, Urbana, Ill.

† Hoffman Science Center, Santa Barbara, Calif. Previously at Coordinated Science Lab. (formerly the Control Systems Lab.), University of Illinois, Urbana, Ill.

[1] More detail about the experimental work than is given here may be found in J. J. Myers, "Optical Simulation of Antenna Images," Control Systems Lab., University of Illinois, Urbana, Rept. No. R-109; 1958.

[2] The term "image" is used throughout this paper in the optical sense, that is, meaning the "picture" of some object or set of objects after reception by an antenna system and after linear detection or processing.

[3] M. W. Baldwin, Jr., "The subjective sharpness of simulated TV images," *Bell Sys. Tech. J.*, vol. 19, pp. 563–586; October, 1940.

[4] P. Croce, "Étude d'une méthode de filtrage des images optiques," Ph.D. dissertation, University of Paris, France; 1954.

[5] G. C. Higgins and L. A. Jones, "The nature and evaluation of the sharpness of photographic images," *J. Soc. Mot. Pic. Telev. Engrs.*, vol. 58, pp. 277–290; April, 1952.

[6] "Criteria for Detection and Recognition of Photographic Detail," Boston University, Boston, Mass., Tech. Note No. 69, pt. 1; September, 1950.

[7] R. D. Rawcliffe, W. W. Lichtenberger, and H. V. Krone, "Optical Simulation of Radar Resolution, Control Systems Lab., University of Illinois, Urbana, Rept. R-111; 1958. Accepted for publication in *J. Opt. Soc. Am.*

[8] J. J. Myers, "Antenna Image Quality Criteria," Control Systems Lab., University of Illinois, Urbana, Rept. No. R-108; 1958. To be published.

tion of the radius. This variation was the same as the power radiation pattern of the antenna simulated. The images so formed were "smeared" in the same way that an antenna image is smeared because of the finite aperture and the corresponding aperture illumination. By using different masks, several different antenna radiation patterns were simulated corresponding to the several aperture illuminations chosen for evaluation. A human observer then passed judgment on the quality of the resulting images according to the particular criterion of image quality chosen.

The method employed appears to have been developed largely during the studies of Rawcliffe *et al.*,[7] although the use of off-focus imaging (without weighting of the entrance pupil by means of masks) is a common technique employed to investigate sharpness in optical or photographic images. Contributions to the technique resulted from this study. They were the means for making masks of arbitrary density and the development of a method of forming random objects for image-making.

The masks used corresponded to aperture illuminations given by the class $(1+A\cos 2\pi x/L)$, where x is the radial aperture coordinate, L is the antenna diameter, and A is an aperture illumination parameter defined over the interval $(-1, 1)$. Five illuminations of the class, including the two extremes given by values of $A=\pm 1.0$, were used. This class of illuminations was used because it contains both uniform illumination $(A=0)$ and a "cosine squared" illumination $(A=1.0)$. It contains also a "sine squared" illumination $(A=-1.0)$ which approaches a two-element interferometer in main lobe half-power width and in sidelobe level. Finding the optimum of this class of illuminations does not imply that the optimum of all illuminations has been found. However, since this class yields patterns from the extremes of high sidelobe and narrow main beam to low sidelobes and broad main lobe, it is reasonable to expect that the optimum of all illuminations should not be too much different from that found.

At the outset of the experiment it was apparent that very small differences in image quality would not be readily detected and hence that five points would be a sufficient number to construct a useful curve of image quality vs aperture illumination.

Image Formation

A focussed, aberration-free imaging system maps points in the object plane into corresponding areas of the image plane. If the imaging system is defocussed, the image of a point object broadens and there is a transition from a Fraunhofer diffraction image to a Fresnel image. The Fresnel pattern is an approximate image of the aperture of the system, with spurious response at edge transitions of the image caused by diffraction at the edges of the aperture. The shape of the image and distribution of intensity in it may be changed by varying the shape and density of the aperture. For example, if a square aperture whose density is a function of radius is placed in front of a lens, the image of a point will also be a square and the light intensity in the image will vary in approximately the same way that the density of the mask varies; that is, the point image will reproduce the mask shape and intensity.

In the point image formed through such an optical system there is distortion because of diffraction effects. However, if the system is sufficiently off focus, then these effects are small compared to the off-focus effects, and the image is a sufficiently good reproduction of the mask used. For a circular mask of uniform transmission, the light intensity across the main disk of the off-focus image is to the first approximation constant. Neglecting the small diffraction effects (small in terms of the scale of the off-focus image), the transfer function[9] of this uniform disk is approximately the Fourier transform of a rectangular distribution, *viz.*, of the form $(1/x \sin x)$. Thus, the transfer function of the in-focus imaging system is modified by defocussing and by the use of a mask. The transmission of the mask required is approximately the power radiation pattern of the antenna simulated.

In the experiment images of selected objects were formed on photographic film. The objects used consisted of film transparencies illuminated from behind by a uniform light field. A camera with mask in front of the lens was mounted with the lens at a distance of approximately its focal length from the object. The image of the object was recorded on photographic film placed a short distance from the focal plane of the camera. This off-focus distance was not critical and depended on the degree of smearing desired. However, to minimize diffraction effects, sufficient spreading of the image was used to make the scale of the distorted image large in comparison with the scale of the main lobe of the diffraction image of the camera when focussed.

Masks[10]

The masks made for the experiment constituted the entrance pupil of the camera used in making images. They were made of photographic film that was exposed appropriately so that the curve of transmission as a function of radial distance from the center of the mask was the same as the power radiation pattern curve of the antenna that was being simulated. In Fig. 1 the five antenna radiation patterns simulated and the corresponding measured density of the associated mask are plotted.

The choice of proper over-all mask size was made on the basis of experimental data that showed the optimum size to minimize undesired diffraction effects. Since the mask size was limited, it was not possible to include a complete diffraction pattern (which would, in fact, ex-

[9] The transfer function of an optical system is the Fourier transform of the point object intensity diffraction image, or spread function. In antenna theory the transfer function is the Fourier transform of the power radiation pattern.

[10] A detailed description of the method of making the masks is given in the original report (see footnote 1) from which this paper has been taken.

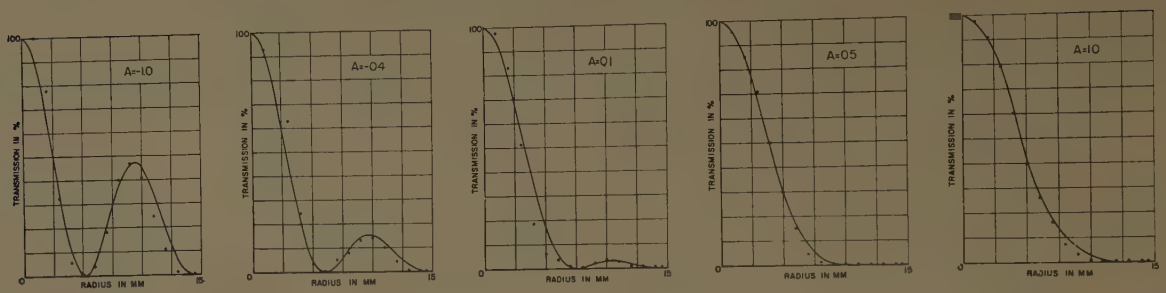

Fig. 1—Transmission of masks used in forming images. The solid lines are calculated data, and the dots are measured data. A is the aperture illumination parameter.

tend to infinity). The masks were made to include only the first sidelobes of the antenna radiation pattern since higher order sidelobes were not so important in their smearing effect as the first sidelobes (their presence for the $A = -1.0$ case and perhaps for $A = -0.4$ would further degrade the image and thus would exaggerate the result obtained). The total light transmission range in the mask was about 200:1, which gave the opportunity to include sidelobes greater than about -23 db.

Objects

Objects that were not simple geometric forms, *e.g.*, converging lines, squares, etc., and whose spectra were reasonably broad were used for image making. Rows of random Roman capital letters on a background of random shapes of the same density (Fig. 2) were used.[11] Upon direct viewing, most or all of the letters could be read in spite of the obscuring effect of the random shapes; when distorted by the off-focus camera and mask, the letters in the image were less legible and from 12 per cent to 92 per cent could be identified, depending upon the amount of distortion and skill of the observer.[12] A choice of Roman letters on a random background was made based upon the fact that, in general, the objects imaged through an antenna consist of random type radiators whose angular size, shape, position, and reflectivity or luminance cannot be predicted. It also was desirable to have readily identifiable object forms to avoid difficulties in experimental scoring.

The random background chosen corresponded to random radiators and not to receiver noise. That is, it was spatial "noise" and so was smoothed in the imaging process in the same way that the letters were smeared. The background corresponded, roughly speaking, in a radar map to geometrical shapes, such as airfields, amidst random return. Both the background and the letters were high-contrast object forms (greater than 1000:1).

[11] Two interesting experiments have been reported involving the recognition of forms against complex backgrounds. Although different information was desired than that desired from the present experiment, the studies are relevant. They are footnote 6, and R. M. Boynton and W. R. Bush, "Recognition of forms against a complex background," *J. Opt. Soc. Am.*, vol. 46, pp. 758–764; September, 1956.

[12] In the reproduction process, the image of Fig. 2 has been distorted so that its legibility is poorer than in the original film transparency used in the evaluation.

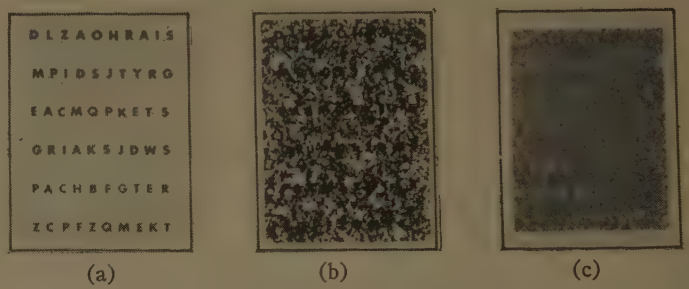

(a) (b) (c)

Fig. 2—(a) Unobscured letters used in forming objects. (b) Typical object. (c) Typical image made from it.

Technique

Formation of Images

For assessment by the observers, 25 different images were made using the method described above. Five images for each of the five different aperture illuminations were formed, the five for any illumination differing from each other only in the registration between letters and the random background. The values for the aperture illumination factor, A, were -1.0, -0.4, 0.1, 0.5, and 1.0 (see Fig. 1).

The average contrast of each image made was approximately the same as that of each of the other 24 images. Each undeveloped film containing the latent image was given the same photographic processing, and each developed image was mounted between glass sheets and identified by a random number.

The objects used in forming the images consisted of *negatives* of the objects reproduced in Fig. 2 so that the image film as viewed by the observers contained dark letters on a mottled background. It has been experimentally determined previously that white letters on a mottled background were unsatisfactory.

Observers

Five subjects were used for the experiment. Each was believed to have had about the same incentive in helping to make the results significant. All were graduate or former graduate students, and none had poor eyesight, although one wore glasses. Each subject was given the same training by having him view initially a series of five images without his knowing that the results of his evaluation of these images would not be used in the final scoring.

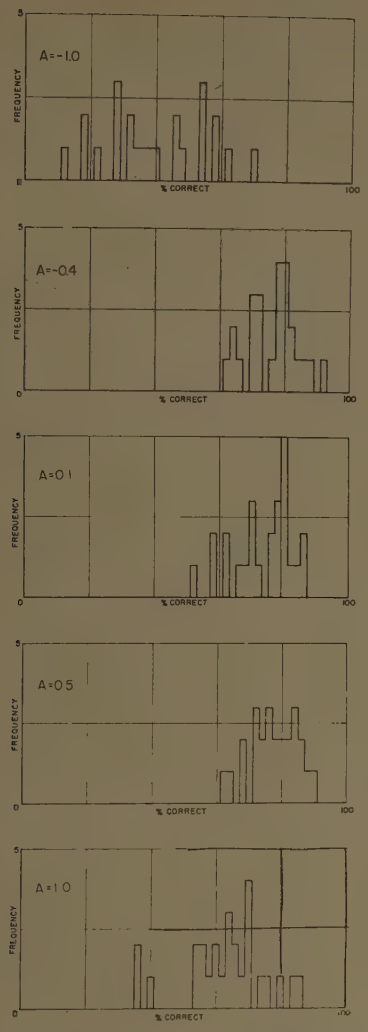

Fig. 3—Experimental results of image assessment. Each graph gives the results of 25 observations from five observers, each assessing five images. *A* is the aperture illumination parameter.

Method of Viewing Images

The images were illuminated from behind for viewing. The light level was controllable by the observer to suit his own preference. At the beginning of the sessions, each observer was presented with a set of printed instructions that were not changed during the course of the observations. At each evaluation session (observers were used one at a time) the subject was seated in a darkened room in isolation and was given whatever time he desired to try to identify each of the letters in each of the five images presented to him in a particular order during that session. A low-power reading glass was supplied for him to use or not as he chose. He chose the viewing distance, magnification, and light level that he found best. A single session varied in length, but averaged about 30 minutes per observer. Subsequent sessions about a day apart were held until all images had been evaluated.

Earlier sessions run by projecting images one at a time on a screen for simultaneous viewing by a diverse group were unsuccessful and the results inconclusive because of both the conditions of viewing and, it is believed, a lack of adequate incentive on the part of some members of the group. Individual viewing of the images by carefully selected subjects as adopted for the test was much more successful.

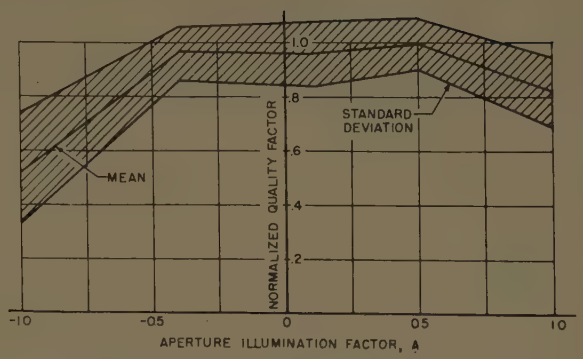

Fig. 4—Relative image quality as determined by five observers. The data have been normalized so that a quality factor of 1.0 represents the best illumination of the class.

Experimental Design

The experimental plan involved a 5×5×5 "Latin square" design[13] in which all of the variables were randomized such that each of the 25 images was presented to each of the five subjects in a different order. At each session five images made with five different aperture illuminations and each with a different letter-background registration were presented one at a time.

Scoring

The individual scores for each image were obtained by noting the percentage of correct identifications. Erroneous identification was counted the same as no identification. Subjects were advised in the instructions that there would be no penalty for incorrect identification, but each was urged not to guess. To avoid reduction of dynamic range of the data because of subjects' remembering certain key letters, the key letters were not counted in the scoring. Out of a possible 60 letters, 50 were used in the actual scoring.

Results and Discussion

The results of the 125 image analyses are given in the histograms of Fig. 3 and the curves of Fig. 4. The histograms show the frequency distribution of correct identification for each of five different aperture illuminations. From these data the mean and the standard deviation of the observations were determined. The results are plotted in the over-all quality curve of Fig. 4.

Observer learning was investigated by having each subject re-assess at the conclusion of the experiment the first five images he had examined. He was not aware that he had seen the images before. Out of a possible 250 correct identifications, the average for the five observers

[13] A. L. Edwards, "Experimental Design in Psychological Research," Rinehart and Co., New York, N. Y., ch. 16; 1950.

during the first trial was 148 as compared to 198 for the second trial. This difference indicates the extent of learning during the experiment. However, the design of the experiment was such as to avoid bias from this cause. Analysis of the differences between performance of the five subjects showed these to be caused by chance rather than to some "real" difference between observers.

No significant statistical difference between the images, corresponding to values of the aperture illumination factors 0.5, 0.1, and -0.4, were found.[14] However, a distinct degradation in image quality for the two extremes as compared to the center values was found. The flatness of the curve of the mean in Fig. 4 suggests that image quality is relatively insensitive to the aperture illumination factor.

In an independent experiment reported in a companion paper,[15] a uniform aperture illumination was found to be close to optimum. This result coincides grossly with the general conclusion that may be drawn from this optical experiment, *viz.*, that a uniform illumination yields an image whose quality is close to the best that can be obtained.

It might reasonably be argued that the results of the experiment would have been different had there been used different objects, such as those with a continuous range of intensities rather than the black-white objects used. This objection is a valid one because certainly smearing of low-intensity objects due to sidelobe energy from nearby objects with higher intensity would only be found with a more or less continuous range of intensities in the object. However, it is believed that the differences would be ones of degree only and that, in spite of the high contrast of the objects used, the results obtained do not differ greatly in form from the results that would have been obtained with a continuous range of intensities.

[14] The results obtained here are directly applicable to circular apertures.

[15] J. J. Myers, "Antenna image quality evaluation Part II—by a mechanical observer," this issue, p. 83.

Conclusion

The experiment has shown that it is possible to evaluate the effect of aperture illumination on image quality by an optical simulation method. It was found that image quality by optical viewing is not highly sensitive to aperture illumination. This finding suggests that very subtle differences in aperture illuminations, and hence in antenna patterns, could not be evaluated by the method.

It is concluded that a nearly uniform aperture illumination is best when the greatest similarity between the image and object is the measure of "best." This conclusion has been reached by other workers by intuitive means. To the author's knowledge, this is the first experimental verification of the conclusion.

Acknowledgment

The author wishes to acknowledge that the optical simulation was suggested by J. P. Ruina, based on work by R. D. Rawcliffe *et al.*;[7] he also wishes to express appreciation to B. D. Elliott for his assistance with the experiments, to Dr. H. W. Simaiko for help in planning the testing phase of the experiment, to J. W. Cummings and C. W. Morris of the photo laboratory for their help and great patience, and to the other members of the Control Systems Laboratory who participated in the experiment as subjects.

Antenna Image Quality Evaluation Part II—By a Mechanical Observer*

J. J. MYERS†

Summary—**A digital computer was used as a mechanical observer to evaluate antenna image quality as a function of the aperture illumination for a high resolution antenna. An illumination close to uniform was found to yield an image that was best as measured by the ease with which the mechanical observer was able to analyze the images. A description of the logical design of the observer and the results of applying it to the analysis of a typical class of illuminations are given.[1]**

Introduction

A COMPANION paper[2] describes results of an experiment that was undertaken to measure the effect of aperture illumination on antenna image[3] quality. That experiment used human observers to determine quality of simulated antenna images. An independent experiment that would eliminate the variability of humans was felt desirable; accordingly, an experiment was devised using ILLIAC[4] as an observer to assess simulated images, and the results are reported here.

In contrast to a human observer, a mechanical observer is for all practical purposes a perfectly constant observer and can be made to apply any chosen criterion of quality in a constant manner. In particular, the application of the criterion can be completely invariant with changes in antenna aperture illumination and with time. As compared with a human observer, an MO (mechanical observer) is more constant, is not subject to fatigue, is much faster, requires no training, and is independent of the physiological and psychological factors that influence a human observer. Further, since the criteria applied by the MO are subject to precise numerical control, very small differences in images and hence image quality that arise from small changes in aperture illumination are observable.

No attempt was made in the development of the MO to design an optimum observer; that problem was outside the scope of the present study. Instead, attention was concentrated on making the observer satisfactory for the study, flexible, and reasonably efficient.

The use of an MO for image evaluation is reasonable in light of the tendency today to mechanize as many system functions as possible, including the observer or decision-maker. If an antenna image is ultimately to be analyzed by mechanical means, then the system parameters, including aperture illumination, should be chosen to allow the desired information to be obtained from the image with the greatest ease. Accordingly, although the mechanical observer developed for this study may not represent an optimum type for a practical system, mechanical evaluation is justifiable. The results obtained from the experiment give a great deal of insight into how the performance of an MO is affected by the antenna pattern of the system.

Task of Mechanical Observer

The problem presented to the MO was that of analyzing, or "deconvolving"[5] into its constituent parts, a given waveform constituting the (simulated) image being assessed. The images were nearly perfect in the sense that they were obtained analytically and computed numerically to a high degree of precision. For the analyses, images of the same representative class used for the related theoretical[6] and experimental studies[2] were chosen, *viz.*, the class of illuminations given by $(1+A \cos 2\pi x/L)$, where x is the aperture coordinate, L is the antenna length, and A is an aperture illumination parameter defined over the interval $(-1, 1)$. Throughout the analyses nothing except the aperture illumination factor A was changed in measuring the effectiveness of deconvolution as a function of the aperture illumination.

It may be shown that there is no unique solution possible in the deconvolution process since there is an infinite set of possible target[7] configurations that could give rise to any image. However, since it was not re-

* Manuscript received by the PGAP, April 25, 1959; revised manuscript received, October 12, 1959. The research reported here was made possible through the support extended to the University of Illinois Control Systems Lab. jointly by the Depts. of the Army, Navy, and Air Force under Signal Corps Contract DA-36-039-SC-56695, D/A Sub-Task 3-99-06-111. The material in this paper was abstracted from a dissertation submitted in partial fulfillment of the requirements for the Ph.D. degree at the University of Illinois, Urbana, Ill.

† Hoffman Sci. Ctr., Santa Barbara, Calif. Formerly at Coordinated Science Lab. (formerly Control Systems Lab.), University of Illinois, Urbana, Ill.

[1] More detail about the experimental work than is given here may be found in J. J. Myers, "Assessment of Antenna Image Quality by a Mechanical Observer," Control Systems Lab., University of Illinois, Urbana, Rept. R-110; 1958.

[2] J. J. Myers, "Antenna image quality evaluation, Part I—By an optical simulation method," this issue, p. 78.

[3] The term "image" is used throughout this paper in the optical sense, that is, meaning the "picture" of some object or set of objects after reception by an antenna system and after linear detection or processing.

[4] The University of Illinois' digital computer.

[5] The manufactured term "deconvolution" is used because it is descriptive of the inverse operation by which the image was obtained, *i.e.*, the inverse of convolution of the antenna pattern and the object distribution.

[6] J. J. Myers, "Antenna Image Quality Criteria," Control Systems Lab., University of Illinois, Urbana, Rept. R-108; 1958. To be published.

[7] Borrowing a term from radar, the word "target" is used to denote a radiating or reradiating object which gives rise to a corresponding image, even though the "target" is in fact a self-luminous object, such as a radio star.

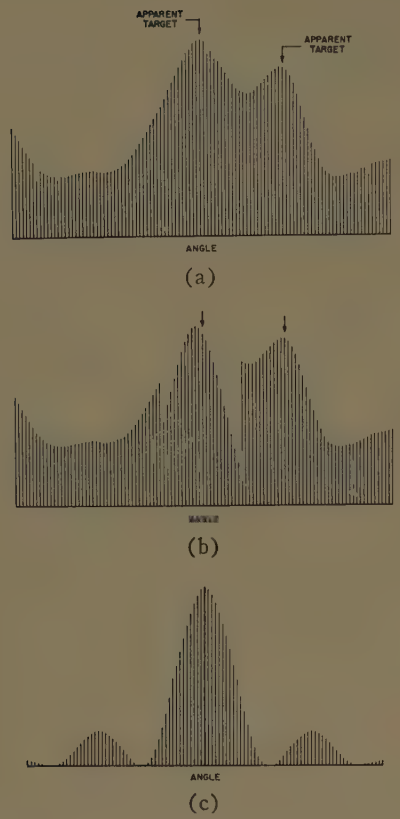

Fig. 1—Representation of manufactured data used by the mechanical observer. (a) Section of typical image showing two probable targets. (b) Same image section after subtraction of interfering contributions in vicinity of the largest target due to nearby targets. (c) Reference antenna pattern.

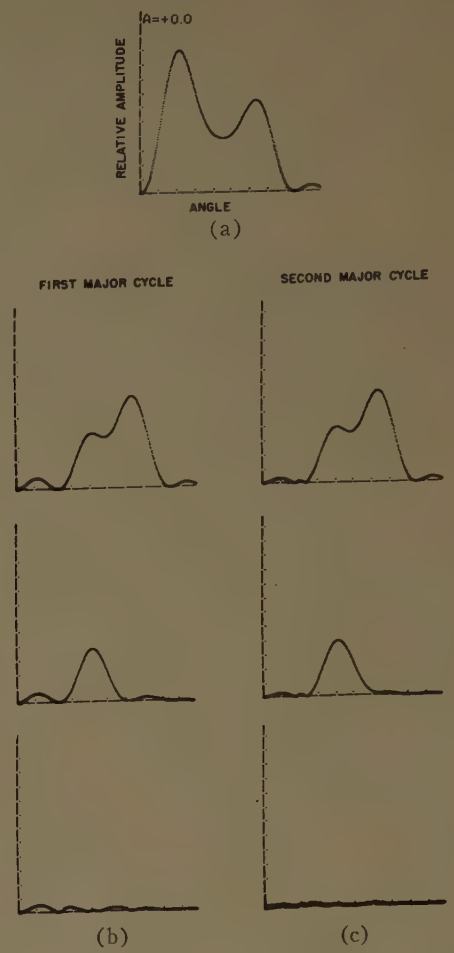

Fig. 2—Photographs showing the essence of the "deconvolution" process used by the mechanical observer. (a) Image of three point targets. (b) Successive removal of targets by early estimates. (c) Final removal of targets with improved estimates. Two bottom graphs show residual after removal of all targets.

quired of the MO that it perform a perfect deconvolution of the image, a satisfactory analysis for purposes of this study was obtained for an appropriate variety of target dispositions.

In assessing the quality of the images, the MO was "unaware" of the contents of the image beyond knowing that it was formed by convolution of a given antenna pattern and some unknown quantity and disposition of *point* targets, the image being described by a set of values of ordinates, *e.g.*, Fig. 1, equispaced across the image. For purposes of assessment by the MO, the best image was that one which was most easily deconvolved.

The MO developed[8] has potential use in the practical analysis of real data such as that obtained from a radio telescope. Although the MO was applied to analyzing artificial images, no restriction to artificial data is thereby implied.

Procedure

Manufactured Images

The image produced by a scanning antenna is in the form of an output voltage that varies with time as the antenna scans a set of radiating or reradiating objects. When point objects that radiate incoherently with respect to each other are scanned, the antenna output power is the sum of the powers due to each object individually. One may manufacture such images by linearly summing the responses of a given imaging system to some assumed distribution of point targets.

For the purpose of forming images for mechanical analysis by the MO, this method of image manufacture was employed. The actual computations were made by ILLIAC according to a program prepared for the purpose. In Fig. 1 a representation of the type of data manufactured is shown, and in Fig. 2 photographs of the ILLIAC cathode-ray tube output for typical images are reproduced.

The calculation of the image by ILLIAC was done on an ordinate-by-ordinate basis. Following computation of the image, a reference antenna power radiation pattern [Fig. 1(c)] was computed in the same manner. This reference pattern was used by the MO as described below.

If the MO were used on real data instead of on manufactured images, the values of the received signal

[8] The MO consisted of ILLIAC and a suitable program that gave rules of observation, such as might be given a human observer performing the analysis in the same (although much slower) way.

at equal time intervals and the measured values of the antenna radiation pattern at the same intervals would be entered into the appropriate places of the memory.[9]

Observer Design

The MO design was based on a curve-fitting technique by means of which the images of the individual targets were successively removed from the original image until the residual was reduced to some arbitrarily chosen threshold. The curve-fitting was applied first in successive stages of approximation to the largest target of the image; when the best estimates of its position and amplitude were determined, the image of this target was removed from the original image and the process was continued until all targets had been located. When the blending or smearing of one target's image into another was not great, deconvolution of the image was done easily and accurately by the MO; when the blending was severe, deconvolution was poorer until, for an excessive amount of blending, the MO was unable to analyze the image into its component targets satisfactorily. The essentials of the deconvolution process used[10] are:

1) The approximate positions of suspected targets were determined by a simple peak-picking technique. The largest of such suspected targets was then assumed to be the largest target present.
2) In order to minimize the smearing effect on this largest target caused by nearby targets, the nearby targets were removed to leave a more or less well-defined peak that was assumed to be a more nearly true representation of the largest target.
3) The reference antenna pattern was fitted to this largest target on a least-squares basis. The best fit was taken as defining tentatively the true location of that target. The estimated target size and location were saved for later use.
4) This largest target was then removed from the original image (meanwhile preserving elsewhere in the computer memory the original image).
5) The entire process of steps 1) through 4) was repeated successively on the remaining image to find the next largest target and so on, until finally there remained no potential targets greater than the threshold that had been chosen.
6) Following the removal of all targets above the threshold, the steps 1) through 5) were repeated using the target estimates obtained previously. Upon applying the curve-fitting procedure a second time, the resulting estimates of position and amplitude of the targets were improved because better estimates of nearby targets were available for step 2).

Fig. 2 shows the deconvolution of a three-target image indicating the condition of the image at each subtraction step. At the top is a typical image.[11] In the left-hand column are the results of going through the first major cycle of the deconvolution process where targets are being removed in decreasing order of their amplitudes. It may be noted in the bottom graph that the residual remaining is not insignificant and that it exists because of inaccurate estimates of the true sizes and positions of the targets.

The result of going through the second major cycle of the deconvolution process is shown in the right-hand column. It may be seen that the residual left after subtracting each of the three targets present is appreciably less than the residual left in the earlier steps of the first major cycle. In some cases, further repetitions of the steps of the second major cycle could have reduced the residual to an arbitrarily low level. However, for the purposes intended, there was little reason to look for extremely small residuals. In practice, the threshold was set to allow a residual of 10 per cent.

The method chosen for curve-fitting was the univariate,[12] or one-at-a-time, method of arriving at a minimum corresponding to the best fit. The sum of the squares of the differences between the ordinates of the target and ordinates of the main lobe of the reference antenna pattern was used as a measure of the fit. When this sum had been reduced as low as possible by varying the parameters, the fitting process was terminated. During a fitting cycle, each of the parameters was varied one at a time until the sum of the square of the differences was minimized.

Observer Errors

Errors in the deconvolution process arose only from inexact estimates of the target locations and sizes, since ILLIAC does essentially perfect subtraction. An analysis of deconvolution errors showed that it is more important that the amplitude estimates be good than that the position estimates be good.

Observer Operation

Prior to using the MO, an image and a power radiation pattern of the antenna being simulated were manufactured. Before starting the actual image analysis, the MO measured the beamwidth at the 90 per cent amplitude point and at the half-power point, and measured the highest sidelobe level to set a threshold for selection of neighboring peaks. After setting various constants on the basis of these measurements, the main MO pro-

[9] The value of the deconvolution technique in a practical case would be limited by the accuracy with which the actual radiation pattern were known. In radio astronomy, the radiation pattern is in general not well known and hence, in judging the applicability of the results obtained, account would have to be taken of the uncertainty in the knowledge of the actual pattern.

[10] The deconvolution process employed for the MO is complex and is described in more detail elsewhere; see footnote 1.

[11] Throughout this evaluation noise-free images were used. The MO contained provisions for handling noisy images and was, in fact, used extensively on them.

[12] G. E. P. Box and K. B. Wilson, "On the experimental attainment of optimum conditions," *J. Roy. Stat. Soc.*, vol. 13B, pp. 1–45; 1951.

gram took over. At each stage where an estimate of the presence of a target was made, the results were punched on tape. By means of a display (on a Memotron long-persistence cathode-ray tube) it was possible to watch the course of the deconvolution and to see which target was found and subtracted at each point in the process.

Experimental Design and Scoring

It was determined experimentally that the accuracy with which deconvolution of images was carried out was directly proportional to the number of trials made during the curve-fitting procedure. That this proportionality should exist is seen when it is recognized that the number of trials is dependent upon the flatness of the minimum being sought and upon the correctness of the initial estimate of the value of parameters associated with the minimum. In turn, the correctness of the original estimates of the best values for the parameters used to start the curve-fitting was inversely proportional to the degree of blending of the images of the individual targets; *i.e.*, a large amount of blending led to poor first estimates. Also, the more the blending, the flatter the minimum on the three-dimensional surface over which the best-fit search was carried out.

The total number of trials required to reduce the residual in the image to the 10 per cent level was taken as the measure of the quality of the image. The number of trials for deconvolving two-target images, averaged over the target spacings varying from those which gave essentially perfect deconvolution to those which were impossible for the MO to deconvolve, was used as a measure of over-all image quality. The validity of this procedure was verified experimentally by deconvolving images containing a large number of randomly disposed targets of random amplitude and noting that the number-of-trials measure correlated well with the accuracy with which the targets were located.

If the MO knew that the image were made up of the responses from two targets alone, then it would be a relatively simple matter to deconvolve the results with a high precision, regardless of the target spacing or relative amplitudes. Inasmuch as this knowledge was not imparted to the MO, it made its own determination of the number of targets present. In some cases it decided that it could not deconvolve with acceptable precision and hence it found no targets; in other cases it found either fewer or more targets than actually were present. Finding other than the correct number of targets implied a partially unsatisfactory deconvolution and this was reflected in the number of trials required to reduce the residual to the threshold chosen.

The MO was applied to the analysis of images formed using values of the illumination parameter, A, of -1.0, -0.5, 0, 0.5, and 1.0. Target spacings varying from Rayleigh[13] for $A=1.0$ to about $\frac{2}{3}$ Rayleigh for $A=-1.0$ and target amplitude ratios of 1:1, 1:2, and 1:5 were used. This range of spacings was chosen since spacings greater than these were almost perfectly deconvolvable regardless of the aperture illumination, whereas small spacings were not analyzable by the MO for all illuminations.

[13] The Rayleigh spacing criterion of optics (see Myers, footnote 6).

Results

A total of 108 analyses of images were made in arriving at the data and conclusions discussed below. The results are presented in the plots of Figs. 3 and 4.

Fig. 3 shows, as a function of target spacing for each of the five aperture illuminations, the number of trials required to deconvolve the image. All data do not extend over the entire range of target spacings because of catastrophic failures, that is, failure of the MO to find targets. For example, in the 1:1 amplitude plots the individual curves terminate at about that point where further decreasing of the distance between the targets results in no data; *i.e.*, the MO finds no targets. This failure to find targets occurs when the shape of the composite image due to the two targets becomes too broad in the main-lobe region for the MO to determine that there is a legitimate target present.

The over-all summary curves of the image assessment performed are found in Fig. 4 for target amplitude ratios of 2:1 and 5:1.[14] Fig. 4(a) gives the over-all quality obtained by taking the average of the data of Fig. 3 over the target spacing used, and also shows the average difficulty of deconvolving the images analyzed. As plotted, the data have been normalized so that unity represents the best performance relative to the data displayed. It is quite clear that the optimum performance occurs for that aperture illumination which is nearly uniform, *i.e.*, near to $A=0$.[15]

Fig. 4(b) shows resolution curves as a function of aperture illumination factor. These curves, representing the locus of minima from plots intermediate between those of Fig. 3 and Fig. 4(a), have been normalized so that unity represents the best illumination of the class. As would be expected, the best resolution occurs for $A=-1.0$. The broken portion of the 5:1 curve indicates that for normalized quality factor less than about 0.4 (which occurs for target spacings *greater* than 1.0), the resolvability by the MO measure is independent of aperture illumination. This is to say that for such target spacings the MO was able to resolve the targets almost perfectly, regardless of the aperture illumination.

The result of Fig. 4 indicating that best resolvability indeed occurs for the narrowest beamwidth (*viz.*, for $A=-1.0$) in part validates the results obtained for over-all image quality by showing that the analysis of image quality was not in error from the resolution aspect.

[14] For 1:1 target amplitude ratios, insufficient data was obtainable to allow plotting the same curves.

[15] The results obtained here apply to any separable aperture distribution.

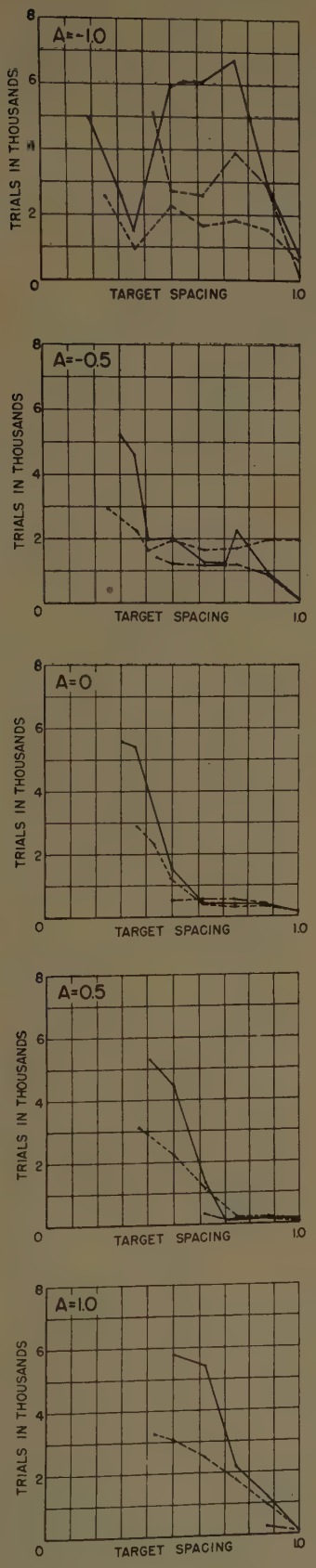

Fig. 3—Experimental results of image assessment. The number of trials required by the mechanical observer to "deconvolve" images of two point targets of various amplitude ratios are given. Target spacing is expressed in units of Rayleigh Spacing for a "cosine-squared" illumination.

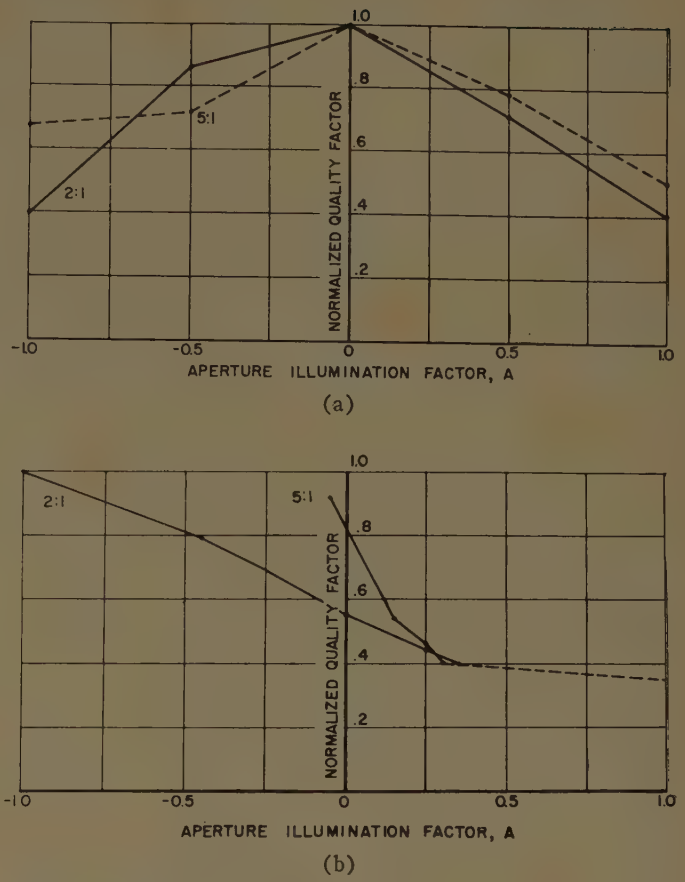

Fig. 4—(a) Relative image quality as determined by mechanical observer for two ratios of target amplitudes. (b) Resolution quality as determined by mechanical observer. Each curve has been normalized so that a quality factor of 1.0 represents the best illumination of the class.

Conclusions

It is evident from the data that there is a significant difference between the various illuminations used insofar as the resulting deconvolvability of the image is concerned. Hence, there is to be expected a significant variation in performance of a mechanical observer as a function of the aperture illumination used.

The data show that a uniform aperture illumination is close to optimum. This result agrees with the result obtained in the optical experiment of the companion paper in this issue[2] although the two experiments were quite different and would not necessarily be expected to yield the same result.

Acknowledgment

The author wishes to acknowledge that the use of ILLIAC for assessing quality of antenna images was suggested by Professor J. P. Ruina. Appreciation is expressed to D. L. Bitzer for his help given during the early stages of development of the program for the mechanical observer.

Transmission-Line Missile Antennas*

RONOLD KING†, C. W. HARRISON, JR.‡, AND D. H. DENTON, JR.‡

Summary—**A class of protruding rocket antennas of low silhouette is analyzed in terms of an approximately equivalent circuit that consists of a shunt-driven transmission line terminated in a reactor at each end. Expressions for the currents in the several parts of the circuit are used to determine the Poynting vector and from this the radiation resistance referred to the current in the generator. The reactance is obtained from transmission-line formulas.**

SEVERAL of a class of externally carried telemetry antennas for missiles are shown in Figs. 1–4. These and a number of other related types may be analyzed in terms of a shunt-driven section of transmission line that is terminated in a reactor at each end. The method is essentially that used by Storer and King[1] to determine the radiation resistance of a two-wire line when driven at one end and arbitrarily terminated at the other.

The generalized, approximately equivalent circuit is shown in Fig. 5. Parallel wires of radius a, length s, and separated by a distance b between centers are terminated in impedances Z_0 at $z=0$ and Z_s at $z=s$. The notation, $w=s-z$, is used. An impedanceless generator with EMF V^e is connected across the line at $z=s_1$ or $w=s_2$. The currents in the line are $I_{z1}(z)$ when $0\leq z\leq s_1$ and $I_{z2}(w)$ when $0\leq w\leq s_2$. The currents in the generator and in Z_0 and Z_s are, respectively, I_g, $I_0=I_{z1}(0)$ and $I_s=I_{z2}(0)$. The currents in the two sections of the line are given by[2]

$$I_{z1}(z) = -I_g\left\{\frac{\cosh(\gamma s_2+\theta_s)\sinh(\gamma z+\theta_0)}{\sinh(\gamma s+\theta_0+\theta_s)}\right\} \qquad 0\leq z\leq s_1 \quad (1)$$

$$I_{z2}(w) = I_g\left\{\frac{\cosh(\gamma s_1+\theta_0)\sinh(\gamma w+\theta_s)}{\sinh(\gamma s+\theta_0+\theta_s)}\right\} \qquad 0\leq w\leq s_2 \quad (2)$$

where the terminal functions θ_0 and θ_s are defined by[3]

$$\theta_i = \rho_i + j\Phi_i = \coth^{-1}(Z_i/Z_c), \quad i=0 \text{ or } s, \quad (3)$$

and the propagation constant is $\gamma=\alpha+j\beta$. For low-loss lines and terminations $\theta_0\doteq j\Phi_0$, $\theta_s\doteq j\Phi_s$, and $\gamma\doteq j\beta$.

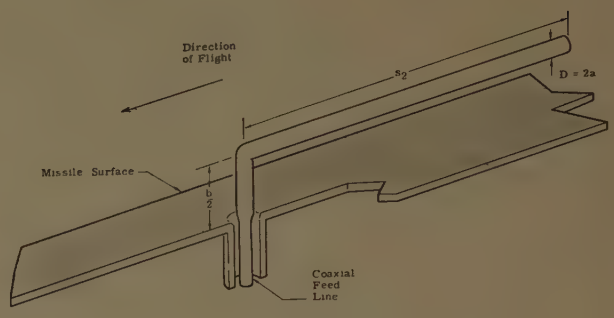

Fig. 1—Inverted L antenna-transmission line.

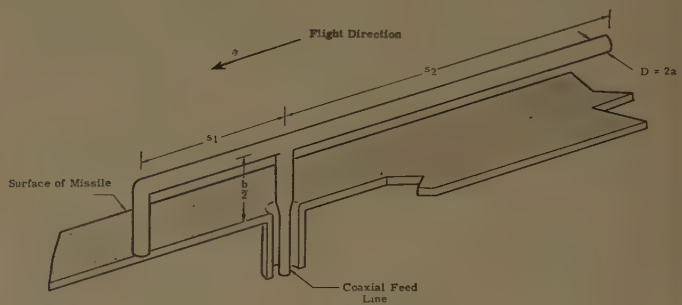

Fig. 2—Shunt-driven inverted L antenna-transmission line with open end.

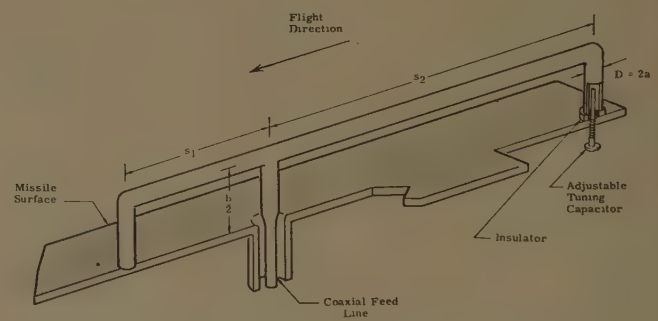

Fig. 3—Shunt-driven inverted L antenna-transmission line with capacitive end loading.

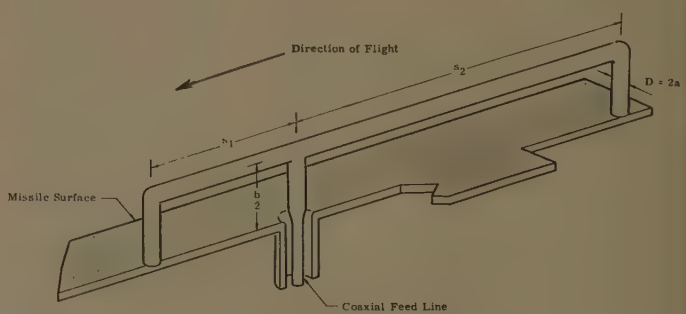

Fig. 4—m antenna-transmission line.

* Manuscript received by the PGAP, May 4, 1959; revised manuscript received, October 22, 1959. A greatly expanded version of this paper appeared as Sandia Corp. Tech. Memo. No. 436-58(14) dated November 20, 1958.

† Consultant to Sandia Corporation, Albuquerque, N. M., and Gordon McKay Professor of Applied Physics, Harvard University, Cambridge, Mass.

‡ Sandia Corporation, Albuquerque, N. M.

[1] J. E. Storer and R. W. P. King, "Radiation resistance of a two-wire line," PROC. IRE, vol. 39, pp. 1408–1412; November, 1951.

[2] R. W. P. King, "Transmission-Line Theory," McGraw-Hill Book Co., Inc., New York, N. Y., ch. 4, sec. 3; 1955. See formulas (8) and (10) with W_x^e/Z_c replaced by I_g.

[3] *Ibid.*, ch. 2, sec. 15.

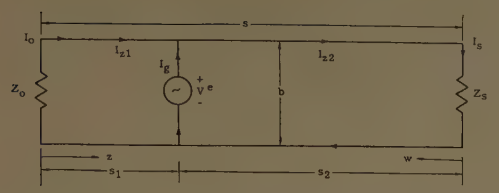

Fig. 5—Equivalent circuit of shunt-driven transmission line terminated in impedances of arbitrary value.

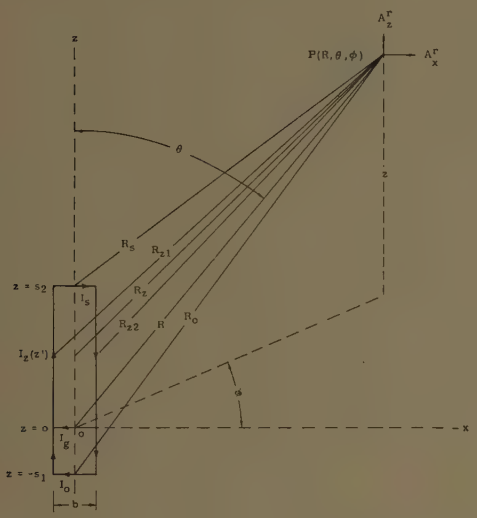

Fig. 6—Coordinate system used in calculating the radiation resistance of a shunt-driven transmission line.

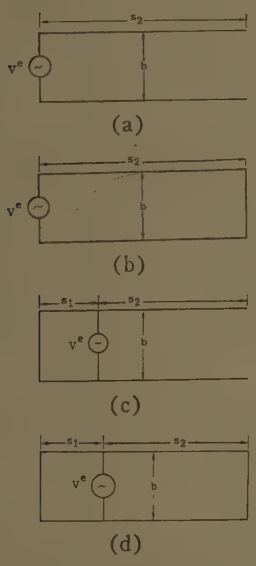

Fig. 7—Special forms of the shunt-driven line.

The currents in the line as given by (1) and (2) and the currents I_g, I_0, and I_s may be substituted in the integrand of general integrals[4] for the components A_z^r and A_z^r of the far-zone vector potential. The coordinates are shown in Fig. 6. These rectangular components may then be combined to obtain the polar components A_θ^r and A_ϕ^r which occur in[5,6]

$$S_R = \frac{\omega^2}{2\zeta_0}\left[|A_\theta^r|^2 + |A_\phi^r|^2\right] \tag{4}$$

for the radial Poynting vector. In (4), $\zeta_0 \doteq 120$ ohms. The total power radiated is obtained from the integral of S_R over a great sphere, and the radiation resistance referred to I_g is this power divided by $I_g^2/2$. The result in ohms is

$$R^e = 30\beta^2 b^2 \left\{\frac{1}{2}\left[1 + \left(\frac{K_0}{\sin\Phi_0}\right)^2 + \left(\frac{K_s}{\sin\Phi_s}\right)^2\right] - \left[K_0\frac{\sin\beta s_1}{\beta s_1} + K_s\frac{\sin\beta s_2}{\beta s_2}\right] - \left(\frac{K_0}{\sin\Phi_0}\right)\left(\frac{K_s}{\sin\Phi_s}\right)\cos(\Phi_0+\Phi_s)\frac{\sin\beta s}{\beta s}\right\}, \tag{5}$$

where

$$\left(\frac{K_0}{\sin\Phi_0}\right) = \frac{\cos(\beta s_2 + \Phi_s)}{\sin(\beta s + \Phi_0 + \Phi_s)}, \tag{6}$$

$$\left(\frac{K_s}{\sin\Phi_s}\right) = \frac{\cos(\beta s_1 + \Phi_0)}{\sin(\beta s + \Phi_0 + \Phi_s)}. \tag{7}$$

The general formula (5) is readily applied to specific antennas.

1) End-driven open-end section of line.—For the structure shown in Fig. 7(a) $\Phi_0 = \Phi_s = 0$, $s_1 = 0$, and $s_2 = s$. It follows that

$$R^e = \frac{30\beta^2 b^2}{\sin^2\beta s_2}\left\{1 - \frac{\sin 2\beta s_2}{2\beta s_2}\right\}. \tag{8}$$

2) End-driven closed-end section of line.—For the circuit shown in Fig. 7(b) $\Phi_0 = 0$, $\Phi_s = \pi/2$, $s_1 = 0$, and $s_2 = s$. The radiation resistance is

$$R^e = \frac{30\beta^2 b^2}{\cos^2\beta s_2}\left\{1 - \frac{\sin 2\beta s_2}{2\beta s_2}\right\}. \tag{9}$$

This formula agrees with results previously obtained by Storer and King.[1]

[4] See for example R. W. P. King, "Theory of Linear Antennas," Harvard University Press, Cambridge, Mass., ch. I, sec. 7, (15).

[5] *Ibid.*, ch. 1, sec. 10.

[6] S. A. Schelkunoff, "A general radiation formula," Proc. IRE, vol. 27, p. 662; October, 1939.

3) Shunt-driven line with an open and a short-circuited termination.—This circuit is shown in Fig. 7(c). For it, $\Phi_0 = \pi/2$ and $\Phi_s = 0$. The radiation resistance is

$$R^e = \frac{30\beta^2 b^2}{\cos^2 \beta s}\left\{\frac{1}{2}\left[\cos^2 \beta s + \sin^2 \beta s_1 + \cos^2 \beta s_2\right] - \cos \beta s \cos \beta s_2 \frac{\sin \beta s_1}{\beta s_1}\right\} \qquad (\cos \beta s \neq 0). \quad (10)$$

(Note that the restriction, $\cos \beta s \neq 0$, which is imposed on (10), is a consequence of the fact that ohmic losses in the line have been neglected. With some additional complication they may be included and a more general formula obtained.) If $\beta s_2 = \pi/2$, (10) reduces to the very simple form

$$R^e = 30\beta^2 b^2 \qquad (11)$$

for all values of s_1. Hence, s_1 may be adjusted to obtain a desired input reactance without affecting the input resistance.

4) Shunt-driven line with short-circuited terminations.—For the circuit in Fig. 7(d), $\Phi_0 = \Phi_s = \pi/2$ and the radiation resistance is

$$R^e = \frac{30\beta^2 b^2}{\sin^2 \beta s}\left\{\frac{1}{2}\left(\sin^2 \beta s + \sin^2 \beta s_1 + \sin^2 \beta s_2\right) - \left(\frac{s_1^2 + s_1 s_2 + s_2^2}{\beta s s_1 s_2}\right) \sin \beta s \sin \beta s_1 \sin \beta s_2\right\} \qquad (\sin \beta s \neq 0). \quad (12)$$

If reactive terminations other than short or open circuits are used, Φ_0 and Φ_s may be evaluated from (3). Specific formulas are in the literature.[3]

Since the radiation resistance given in general by (5) is the driving point resistance if ohmic losses in the conductors are neglected, the impedance is readily obtained by adding to R^e the reactance across the terminals of the generator. The result is simply

$$Z_{in} = R^e + j\left(\frac{X_1 X_2}{X_1 + X_2}\right), \qquad (13)$$

where

$$X_1 = -Z_c \cot (\beta s_1 + \Phi_0), \qquad (14)$$

$$X_2 = -Z_c \cot (\beta s_2 + \Phi_s). \qquad (15)$$

The characteristic impedance is given by

$$Z_c = \frac{\zeta_0}{\pi} \ln \left[\frac{b}{2a}\left(1 + \sqrt{1 - \left(\frac{2a}{b}\right)^2}\right)\right]. \qquad (16)$$

Note that (13) does not include any reactive contribution to Z_{in} by the short bridge containing the generator.

If the antennas are constructed of conductors with other than circular cross section, the equivalent radius may be computed.[7,8] When thick wires are involved, the physical dimensions may differ somewhat from the electrical dimensions because of the inadequate treatment of the corners. It is to be noted that X_1 and X_2 as defined in (14) and (15) are the apparent input reactances that include terminal-zone corrections to Φ_0 and Φ_s where required.[9]

Quite accurate results should be obtained from (5) if $b \leq 0.1\lambda$. For greater spacings the accuracy diminishes, since the conditions of transmission-line theory and the assumption that the currents in the shunt elements have uniform amplitudes are not well satisfied.

[7] C. Flammer, "Equivalent Radii of Thin Cylindrical Antennas with Arbitrary Cross Sections," Stanford Res. Inst., Menlo Park, Calif., Project No. 188, Tech. Rept. No. 4; March, 1950.
[8] King, *op. cit.*, footnote 4, pp. 16–20.
[9] King, *op. cit.*, footnote 2, ch. 2, sec. 20, and ch. 5, sec. 12.

Radiation Pattern Synthesis with Sources Located on a Conical Surface*

A. ISHIMARU† AND G. HELD†

Summary—**This paper presents various methods of synthesizing sources placed on a conical surface to produce a prescribed radiation pattern. The sources considered are a series of electric dipoles placed in free space on the surface of the cone around a set of circumferences. These circumferences are equidistant from each other, and the dipoles are oriented in the circumferential direction with no circumferential variation in intensity and phase.**

A successive approximation method is employed to obtain the source function for those sources which are placed in a region where the circumferences measure approximately less than two wavelengths. For sources placed in the region where the circumference is less than approximately $(4/3)\pi$ wavelengths, an expansion formula of the product of the Bessel and exponential functions is employed. When the sources are located far from the cone tip, a method utilizing the maximum points of the Bessel function is used to compute the source function. In considering the beamwidth and the sidelobe level, the Tchebycheff pattern with the tapering effect is employed. Numerical examples are given to illustrate the effectiveness of the methods.

Introduction

THE PROBLEM of determining the sources required to produce a prescribed pattern has been discussed in the past for the linear array,[1–5] the line source, the rectangular aperture,[6–8] and the circular aperture.[9] The sources in these cases are all placed on a line or on a plane, and this particular geometry makes it possible to employ the familiar techniques of Fourier series, Tchebycheff polynomials, and Fourier transforms. However, when the sources are located on a curved surface, the above-mentioned techniques cannot be readily applied because of the complex expressions of the radiation field.

The purpose of the present work is to study various methods of determining the sources located on a conical surface in free space required to produce a prescribed radiation pattern. The sources are assumed to be composed of electric dipoles oriented in the circumferential direction. These dipoles are located on circumferences which are equidistant from each other (see Fig. 1). The number of dipoles around the cone are assumed to be infinitely large, and all the dipoles on a circumference are fed in phase. The radiation field then comes out to be a nonorthogonal series involving the product of Bessel and exponential functions. The synthesis problem is then reduced to that of finding the coefficients of this series in order to produce a prescribed radiation field.

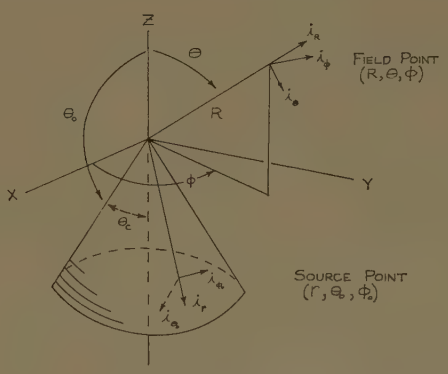

Fig. 1—Field point and source point.

Alternatively,[10] it is possible to employ a formal technique of the Hertz potential and to express the far zone fields by means of two scalar functions representing TE and TM modes. The potential functions are then expanded in the infinite series of harmonic functions, and the source intensities are given as the solutions of an infinite system of linear equations for the infinite number of unknowns. The application of this technique to the practical problem requires the knowledge of the convergence of the elements of the equations, thus approximating an infinite equation with a finite number of equations. Since the definite criterion of this convergence is not established, the practical application of this approach seems very difficult in view of the error considerations. In the present work, we propose to employ

* Manuscript received by the PGAP, June 13, 1959. This work was supported by the AF Cambridge Res. Ctr. under Contract No. AF-19(604)1381, and by Hughes Aircraft Co., Culver City, Calif.

† Dept. of Electrical Engineering, University of Washington, Seattle.

[1] C. L. Dolph, "A current distribution for broadside arrays which optimizes the relationship between width and sidelobe level," PROC. IRE, vol. 34, pp. 335–348; June, 1956.

[2] D. Barbiere, "A method for calculating the current distribution of Tchebycheff arrays," PROC. IRE, vol. 40, pp. 78–82; January, 1952.

[3] R. H. DuHamel, "Optimum patterns for endfire arrays," PROC. IRE, vol. 41, pp. 652–659; May, 1953.

[4] D. R. Rhodes, "The optimum linear array for a single main beam," PROC. IRE, vol. 41, pp. 793–794; June, 1953.

[5] R. L. Pritchard, "Discussion on optimum patterns for endfire arrays," IRE TRANS. ON ANTENNAS AND PROPAGATION, vol. AP-3, pp. 40–43; January, 1955.

[6] P. M. Woodward, "A method of calculating the field over a plane aperture required to produce a given polar diagram," *J. IEE (London) A*, pt. 3, vol. 93, pp. 1554–1558; 1946.

[7] T. T. Taylor, "Design of line-source antennas for narrow beamwidth and low sidelobes," IRE TRANS. ON ANTENNAS AND PROPAGATION, vol. AP-3, pp. 16–28; January, 1955.

[8] J. L. Yen, "On the synthesis of line-sources and infinite strip-sources," IRE TRANS. ON ANTENNAS AND PROPAGATION, vol. AP-5, pp. 40–46; January, 1957.

[9] C. T. A. Johnk, "Synthesis of Aperture Antennas," Engrg. Exper. Sta., Univ. of Ill., Urbana, AF 33(616)-310, R-112-110-SR-6F2, Tech. Rept. No. 1; October, 1954.

[10] H. Unz, "Determination of a current distribution over a cone surface which will produce a prescribed radiation pattern," IRE TRANS. ON ANTENNAS AND PROPAGATION, vol. AP-6, pp. 182–186; April, 1958.

an approximation method which does not depend on the harmonic series, and is simple and effective in evaluating the source as well as in considering the error and convergence properties.

Three approaches are discussed in this paper, each of them applying to a particular range of the source location. When the sources are in the range of the conical surface where the circumference is approximately equal to or less than two wavelengths, a successive approximation method is used to compute the source strength. When the sources are in the range where the circumference is less than approximately $(4\pi)/3$ wavelengths, a new expansion formula for the product of Bessel and exponential functions is devised. When the sources are located farther away from the tip, a method utilizing the maximum points of the Bessel function is used to compute the source function.

The present work is confined to the problem of synthesizing the source in free space to produce a prescribed pattern, and the important problems of physically realizing such a source and of interactions between sources are not treated here.

Electric Dipoles Oriented in Circumferential Direction

Let us assume that the sources are composed of electric dipoles located on a conical surface oriented in ϕ_0 direction (see Fig. 1).

$$J = Ji_{\phi_0}, \quad \text{and} \quad J_m = 0 \tag{1}$$

$$J = \sum_n \sum_m P_{nm} \frac{\delta(r - r_n)\delta(\phi_0 - \phi_m)\delta(\theta - \theta_0)}{r_n^2 \sin \theta_0}. \tag{2}$$

P_{nm} in this equation has the dimensions of current times length, and is the strength of the dipole at (r_n, ϕ_m, θ_0). The electric dipole moment is given by $P_{nm}/j\omega$. The far-zone fields are then given by

$$E_\theta = -j\frac{\omega\mu}{4\pi R} e^{-jkR} F_\theta$$

$$E_\phi = -j\frac{\omega\mu}{4\pi R} e^{-jkR} F_\phi \tag{3}$$

$$F_\theta = \int_v J \cdot i_\theta e^{jkri_r \cdot i} dv$$

$$= \sum_n \sum_m P_{nm} \cos\theta \sin(\phi - \phi_m) e^{jkr_n \cos\gamma_m} \tag{4}$$

$$F_\phi = \int_v J \cdot i_\phi e^{jkri_r \cdot i_r} dv$$

$$= \sum_n \sum_m P_{nm} \cos(\phi - \phi_m) e^{jkr_n \cos\gamma_m} \tag{5}$$

where

$$\cos\gamma_m = \cos\theta\cos\theta_0 + \sin\theta\sin\theta_0\cos(\phi - \phi_m). \tag{6}$$

When the number of dipoles around the cone is increased indefinitely, the series expression approaches the integral in the limit, provided that the length of each dipole is decreased so that A_n is finite as $s \to \infty$ in

$$A_n(\phi_m) = sP_{nm} \tag{7}$$

where s is the number of dipoles around the cone.

Therefore, the synthesis problem is reduced to that of finding $A_n(\phi_0)$ to produce a prescribed radiation pattern, and the actual strength of a finite number of dipoles is given by (7).

Let us assume that the source function $A_n(\phi_0)$ is expressed in a Fourier series around the cone

$$A_n(\phi_0) = \sum_{h=-\infty}^{\infty} A_{nh} e^{jh\phi_0}. \tag{8}$$

The substitution in (4) and (5) and the integration with respect to ϕ_0 yield

$$f_\phi(\theta, \phi) = \sum_n \sum_h A_{nh}(-j^h) e^{jh\phi} \cos\theta h \frac{J_h(Z_n)}{Z_n} \cdot e^{jkr_n \cos\theta_0 \cos\theta} \tag{9}$$

$$F_\phi(\theta, \phi) = \sum_n \sum_m A_{nh}(-j^h) e^{jh\phi} j \frac{dJ_n(Z_n)}{dZ_n} e^{jkr_n \cos\theta_0 \cos\theta} \tag{10}$$

where

$$Z_n = kr_n \sin\theta_0 \sin\theta. \tag{11}$$

If all the dipoles are placed with rotational symmetry and fed in phase around the cone so that $A_{nh} = 0$ for all $h \neq 0$, we get

$$F_\theta = 0$$

$$F_\phi = \sum_n A_n j J_1(Z_n) e^{jkr_n \cos\theta_0 \cos\theta}. \tag{12}$$

The field pattern $y(\theta, \phi)$ is then given by

$$y(\theta, \phi) = \sqrt{|F_\theta|^2 + |F_\phi|^2} \tag{13}$$

$$= \left| \sum_n A_n J_1(Z_n) e^{jkr \cos\theta_0 \cos\theta} \right|. \tag{14}$$

It may be noted that the radiation field becomes zero at $\theta = 0$ and at π because of $J_1(Z_n)$, and this system may be useful for a broadside antenna (which has a main beam at $\theta = \pi/2$).

When the phase shift of the dipoles is 2π around the cone, $A_{nh} = 0$ for $h \neq 1$ and we have $J_1(Z_n)/Z_n$ and $d/dZ_n(J_1(Z_n))$ in F_θ and F_ϕ, which yield the circularly polarized field at $\theta = 0$; and this can be used for an end-fire antenna[11] (which has a main beam at $\theta = 0$).

[11] A. Ishimaru and G. Held, "Radiation Pattern Synthesis with Sources Located on a Conical Surface," AF Cambridge Res. Ctr., Bedford, Mass., Rept. No. AFCRC-TN-58-177, ASTIA Doc. No. AD 152420; April, 1958.

It can also be shown[11] that, if a finite number of dipoles is used, the correction terms involve $J_{s-|h|}$ and decrease as s is increased because of the increased order of the Bessel function.

Successive Approximation Method

We wish to determine A_n in (14) to produce a prescribed $y(\theta)$. In this section we shall deal with the sources located in the region of the conical surface where the circumference is equal to or less than two wavelengths.

The method is based on a series expansion of the Bessel function, and in this region it can be seen that the first two terms of the expansion are significant. We take an odd number of sources and the phase of the center element is chosen as the reference. Then, letting

$$kr_n \cos\theta_c = nZ_0$$
$$Z_0 \cos\theta = x, \tag{15}$$

we get

$$J_1(kr_n \sin\theta_c \sin\theta) = \sin\theta[a_n + b_n x^2] \tag{16}$$

where

$$a_n = \frac{n \tan\theta_c Z_0}{2}\left(1 - \frac{(n \tan\theta_c Z_0)^2}{8}\right) \tag{17}$$

$$b_n = \frac{n \tan\theta_c Z_0}{2}\,\frac{(n \tan\theta_c)^2}{8}. \tag{18}$$

The radiation field is expressed by

$$y(\theta) = \sin\theta \left| \sum_n A_n(a_n + b_n x^2) e^{-jnx} \right|. \tag{19}$$

Let

$$y(\theta) = \sin\theta f(\theta),\ n = m + n_0, \tag{20}$$

and r_0 in (15) be the location of the center element. Then

$$f(x) = f_1(B, x) + f_2(B, h, x) \tag{21}$$

$$f_1(B, x) = B_0 + \sum_{m=1}^{M} (B_{-m} + B_m)\cos mx + \sum_{m=1}^{M} j(B_{-m} - B_m)\sin mx \tag{22}$$

$$f_2(B, h, x) = x^2\left[B_0 h_0 + \sum_{m=1}^{M} (B_{-m}h_{-m} + B_m h_m)\cos mx + \sum_{m=1}^{M} j(B_{-m}h_{-m} - B_m h_m)\sin mx\right] \tag{23}$$

where

$$B_m = A_m a_m$$
$$h_m = \frac{b_m}{a_m}. \tag{24}$$

The successive approximation method will be used in the following manner. Letting

$$f(x) - f_2(B, h, x) = f_1(B, x) \tag{25}$$

we obtain the first approximation $B^{(1)}$ by neglecting f_2 and writing

$$f(x) = f_1(B^{(1)}, x). \tag{26}$$

The second approximation $B^{(2)}$ is obtained by

$$f(x) - f_2(B^{(1)}, h, x) = f_1(B^{(2)}, x). \tag{27}$$

In a like manner, the $n+1$th approximation is obtained by

$$f(x) - f_2(B^{(n)}, h, x) = f_1(B^{(n+1)}, x). \tag{28}$$

It can be seen that if $B^{(n)}$ is a convergent sequence, then it converges to the desired solution.

Since f_1 and f_2 are linear with B, we can use the correction terms to simplify the procedure. Thus, letting

$$B^{(n+1)} = B^{(n)} + C^{(n+1)} \tag{29}$$

we get

$$-f_2(C^{(n)}, h, x) = f_1(C^{(n+1)}, x). \tag{30}$$

The right-hand side of this equation is a finite Fourier series, as seen from (22), and the coefficients are given by Euler's formula to obtain the best approximation in the least mean square sense.

The evaluation of those coefficients C_m may be simplified by the use of matrix notation.

Thus, let

$$C_+^{(n)} = \begin{bmatrix} C_0^{(n)} \\ C_1^{(n)} \\ \cdot \\ \cdot \\ C_M^{(n)} \end{bmatrix} \qquad C_-^{(n)} = \begin{bmatrix} C_0^{(n)} \\ C_{-1}^{(n)} \\ \cdot \\ \cdot \\ C_{-M}^{(n)} \end{bmatrix}$$

$$h_+ = \begin{bmatrix} h_0 & & & \\ & h_1 & & 0 \\ & & \cdot & \\ & 0 & & h_M \end{bmatrix} \qquad h_- = \begin{bmatrix} 0 & & & \\ & h_{-1} & & \\ & & h_{-2} & 0 \\ & & 0 & \cdot \\ & & & h_{-M} \end{bmatrix}$$

$$K = \begin{bmatrix} K_{00} & K_{01} \cdots K_{0M} \\ \cdot \\ \cdot \\ \cdot \\ K_{M0} & \cdots & K_{MM} \end{bmatrix}$$

$$L = \begin{bmatrix} L_{00} & L_{01} \cdots L_{0M} \\ \cdot \\ \cdot \\ \cdot \\ L_{M0} & \cdots & L_{MM} \end{bmatrix} \tag{31}$$

where

$$K_{mm} = -\frac{2}{3}\pi^2$$

$$K_{mm} = -(-1)^{m+n}\frac{1}{(m-n)^2} \qquad m \neq n$$

$$L_{00} = -\frac{2}{3}\pi^2$$

$$L_{mm} = -(-1)^{m+n}\frac{4}{(m+n)^2}. \tag{32}$$

Using these matrices we get the matrix equation to compute the source function

$$C_+^{(n+1)} = \tfrac{1}{2}[Kh_+C_+^{(n)} + Lh_-C_-^{(n)}] \tag{33}$$

$$C_-^{(n+1)} = \tfrac{1}{2}[Lh_+C_+^{(n)} + Kh_-C_-^{(n)}]. \tag{34}$$

This method of successive approximation can be valid only if the sequence $C^{(n)}$ is convergent. The approximate criterion of this convergence was developed previously,[11] and this determines the maximum distance of the source from the tip when the cone angle and the axial separation are given. For example, if the axial separation is a half wavelength, $kr_{\max}\sin\theta_c = 2.45$.

It must also be noted that an error is introduced by taking only a finite number of Fourier expansion. The approximate estimation of the error can be made[11] and it is seen that the error is mostly determined by $B_M^{(n)}$, which, in turn, depends on the highest-order term of the Fourier expansion of the prescribed radiation pattern. Therefore, in order to reduce the error, the radiation field should be prescribed in such a manner that the Fourier coefficients decrease as fast as possible with increasing order. This means that it is desirable that the prescribed pattern should be smooth and that it should not have too narrow a beamwidth.

As an example of the application of this method, let us consider a definite numerical case. Suppose that the prescribed pattern is given by

$$y(\theta) = \sin\theta[1-(\cos\theta-\tfrac{1}{2})^2] \qquad \text{for } 0 \leq \theta \leq 120°$$

$$= 0 \qquad \text{for } 120° \leq \theta \leq 180°. \tag{35}$$

Let us see how this pattern can be synthesized by five dipole sources with an axial separation of a quarter wavelength. Previously, the above method has been used to evaluate the coefficients up to the second approximation.[11]

Both the prescribed and the synthesized patterns are shown in Fig. 2. The error is estimated to be about 0.05, and this is in good agreement with the actual calculation except at $\theta = 120°$, where the higher harmonics errors are concentrated.

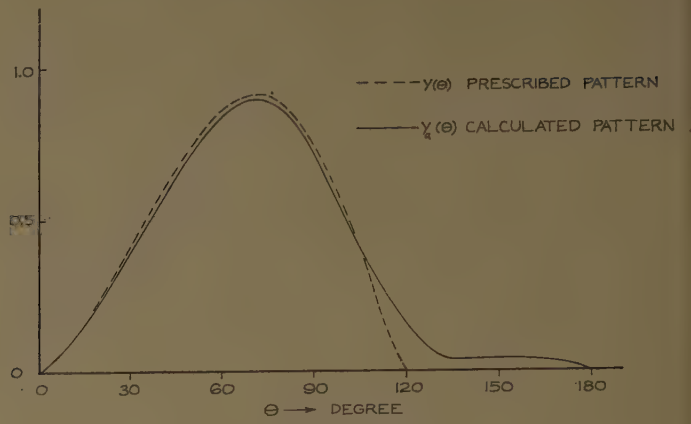

Fig. 2—Example of arbitrary pattern.

Successive Approximation Method II

When the range of the source location extends beyond the region mentioned in the previous section, the approximate expression (16) is no longer valid and it is necessary to employ other methods. An expansion formula has been devised for our purpose, and a brief description will be given here.

Let us consider a function

$$f(\cos\theta) = \frac{1}{\sin\theta}J_v(Z\sin\theta)e^{jZ_0\cos\theta}. \tag{36}$$

If $f(\cos\theta)$ satisfies the Dirichlet conditions, it can be expanded in a Fourier series;

$$f(\cos\theta) = \sum_{m=-\infty}^{\infty} C_m e^{jm\pi\cos\theta}. \tag{37}$$

The evaluation of the coefficients is carried out by Gegenbauer's integral formula for the product of two cylindrical functions.[12]

$$C_m = \frac{\pi}{2}\left\{J_{v/2}\left(\frac{\sqrt{Z^2+(Z_0-m\pi)^2}+(Z_0-m\pi)}{2}\right)\right.$$

$$\left. J_{v/2}\cdot\left(\frac{\sqrt{Z^2+(Z-m\pi)^2}-(Z_0-m\pi)}{2}\right)\right\}. \tag{38}$$

It can be shown that the Dirichlet conditions require $v \geq 1$. When $v = 1$, we have a simple expression

$$C_m = \frac{1}{Z}[(-1)^m\cos Z_0 - \cos\sqrt{Z^2+(Z_0-m\pi)^2}]. \tag{39}$$

[12] W. Magnus and F. Oberhettinger, "Formulas and Theorems for the Functions of Mathematical Physics," Chelsea Publishing Co., New York, N. Y., p. 32; 1954.

Let us take an odd number of sources and choose the phase of the center element as a reference. The separation along the axis between the sources is a half wavelength. Employing the expansion, we can write the radiation field as

$$y(\theta) = \sum_{K=-N}^{N} A_K J_1(kr_K \sin\theta_c \sin\theta) e^{ikr_K \cos\theta_c \cos\theta}$$
$$= \sin\theta f(\theta) \tag{40}$$

$$f(\theta) = \sum_{K=-n}^{N} A_K \sum_{m=-\infty}^{\infty} C_{mK} e^{im\pi\mu} \tag{41}$$

where $\mu = \cos\theta$ and A_k is a complex conjugate of the source intensity. (This is chosen in order to use θ_c instead of θ_0.) It can easily be verified that if the sources are placed in the region where the circumference is smaller than $4\pi/3$ wavelengths, the magnitude of C_{KK} is greater than the other coefficients C_{mk}, $m \neq k$.

We let

$$f(\mu) = f_1(A, \mu) + f_2(A, \mu) \tag{42}$$

$$f_1(A, \mu) = \sum_{K=-N}^{N} A_K C_{KK} e^{iK\pi\mu} \tag{43}$$

$$f_2(A, \mu) = \sum_{K=-N}^{N} A_K \sum_{m \neq K} C_{mK} e^{im\pi\mu}. \tag{44}$$

The successive approximation method will be used in a manner similar to that in the previous section.

Letting

$$A_K^{(n+1)} = A_K^{(n)} + C_K^{(n+1)} \tag{45}$$

$$C^{(n)} = \begin{pmatrix} C_{-N}^{(n)} \\ C_{-(N-1)}^{(n)} \\ \vdots \\ C_0^{(n)} \\ \vdots \\ C_N^{(n)} \end{pmatrix} \qquad D = \begin{pmatrix} 0 & d_{-N,-(N-1)} \cdots d_{N,N} \\ \cdot & 0 \\ \cdot & \cdot \quad 0 \\ \cdot & \cdot \quad \cdot \\ d_{N,-N} & \cdots \quad 0 \end{pmatrix}$$

$$d_{Kh} = \frac{C_{Kh}}{C_{KK}}. \tag{46}$$

We obtain the matrix relationship

$$C^{(n+1)} = -DC^{(n)}. \tag{47}$$

The error consideration may be made in a manner similar to the previous section, and the magnitude of the higher harmonics terms of the prescribed pattern will be the major contribution to the magnitude of the error.

As an example, let us choose the sources located at

$$kr_n \cos\theta_c = \frac{\pi}{2} + n\pi, \qquad n = 0, 1, 2, 3, 4$$
$$\theta_c = 14^\circ\, 2'. \tag{48}$$

We prescribe the radiation pattern by using the Tchebycheff polynomial of degree 2 with the specified sidelobe level of 19.1 db. Therefore,

$$y(\theta) = \sin\theta \left[\frac{5}{18} e^{-i\pi\cos\theta} + \frac{4}{9} + \frac{5}{18} e^{i\pi\cos\theta} \right]. \tag{49}$$

It may be noted that the first approximation computed from this yields $A_0^{(1)} = A_4^{(1)} = 0$, which is desirable for error reduction. Using the matrix equation (47), the second approximation $A_n^{(2)}$, $n = 0, 1, 2, 3, 4$ are computed.[13] Both $y(\theta)$ and the calculated patterns are shown in Fig. 3, and the improvement of the second approximation over the first approximation can easily be seen in the reduction of the beamwidth and the sidelobe level. This computation was carried out on an IBM 650.

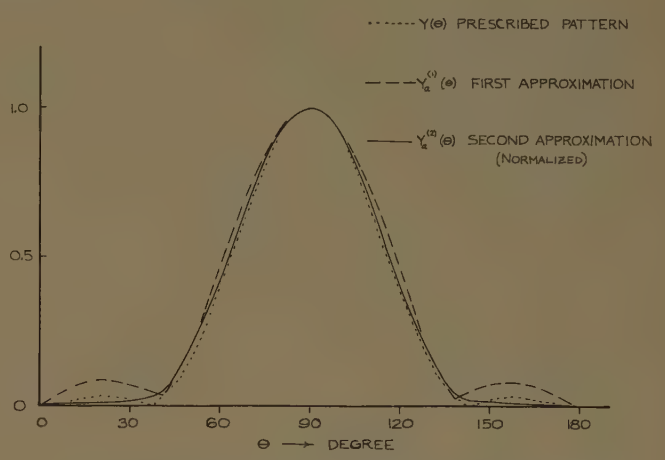

Fig. 3—Example of broad-side tapered Tchebycheff pattern.

Sources Distant from the Cone Tip

When the sources are located farther away from the cone tip, the successive approximation methods described in the previous sections are no longer applicable, because the radiation pattern includes the wider range of the Bessel function and the main beam is directed in the direction further away from $\theta = \pi/2$.

In order to produce a desired pattern, we consider the suitable choice of the source location which will yield considerable amount of radiation in the desired direction. At the same time, we can suppress the sidelobes by a suitable choice of source intensity and phase.

Let us first consider the synthesis of a broadside pattern. At $\theta = \pi/2$, the Bessel function J_1 has a maximum when $kr_n \sin\theta_c = 1.84$. (This case is included in the previous section.) The next maximum of $|J_1|$ occurs at 5.33. Therefore, the broadside pattern may be obtained if we place the sources around this distance in such a manner that the fields are added at $\theta = \pi/2$ and cancelled by

[13] For details of the numerical techniques involved, see Ishimaru and Held, *op. cit.*

each other in the other directions. In particular, since J_1 is maximum at the angle where $kr_n \sin\theta_c \sin\theta = 1.84$, we wish to suppress the sidelobe at this angle as much as possible.

As an example, we consider three sources where the center one is placed at such a distance that kr sin $\theta_c = 5.33$. The other two sources are a half wavelength away from the center source along the cone axis. The cone angle $\theta_c = 7°8'$.

The radiation field is given by

$$y(\theta) = \left| A_{-1}J_1(Z_{-1}\sin\theta)e^{i\pi\cos\theta} + A_0J_1(Z_0\sin\theta) + A_1J_1(Z_{+1}\sin\theta)e^{-i\pi\cos\theta}\right| \quad (50)$$

where

$$Z_{\pm 1} = 5.33 \pm \frac{\pi}{8}. \quad (51)$$

In order to suppress the sidelobe we need to consider the pattern behavior near θ_s where $Z_0 \sin\theta_s = 1.84$. At this angle, we have

$$y(\theta_s) = h_0[A_{-1}U_{-1}e^{i\pi\cos\theta_s} + A_0 + A_1U_1e^{-i\pi\cos\theta_s}] \quad (52)$$

where

$$h_0 = J_1(Z_0\sin\theta_s)$$

$$U_1 = U_{-1} = 1 - \frac{(\Delta\sin\theta_s)^2}{2} + \frac{1}{2}\left(\frac{\Delta}{Z_0}\right)^2$$

$$\Delta = \frac{\pi}{8}. \quad (53)$$

Now the source strength will be chosen such that (52) represents the Tchebycheff pattern. Consider

$$Y_T(\theta) = \frac{T_2(x)}{T_2(x_0)}$$

$$T_2(x) = 2x^2 - 1$$

$$x = x_0\cos\left(\frac{\pi\cos\theta}{2}\right). \quad (54)$$

Let us choose

$$T_2(x_0) = 19. \quad (55)$$

Comparing (54) with (52), we get A_{-1}, A_0, A_1.[13] The sidelobe level is expected to be

$$\left|\frac{J_1(Z_0\sin\theta_s)}{J_1(Z_0)}\,\frac{1}{T_2(x_0)}\right| = 0.0884 \quad (56)$$

which is 20.1 db down.

The beamwidth can be shown as almost equal to that of the Tchebycheff pattern, which is 41.4° in this example.

The synthesized pattern is shown in Fig. 4. It can be seen that the values of the beamwidth and the sidelobe level we obtained are approximately equal to the values expected from the theory.

A similar technique can be employed to synthesize the pattern whose main beam is directed at an arbitrary angle θ_p. The synthesized pattern $y_a(\theta)$ for $\theta_p = 60°$ and Tchebycheff pattern $y_t(\theta)$ are shown in Fig. 5. It can be observed that the sidelobe level of the computed pattern is 18.9 db, which is in close agreement with the expected sidelobe level of the Tchebycheff pattern.

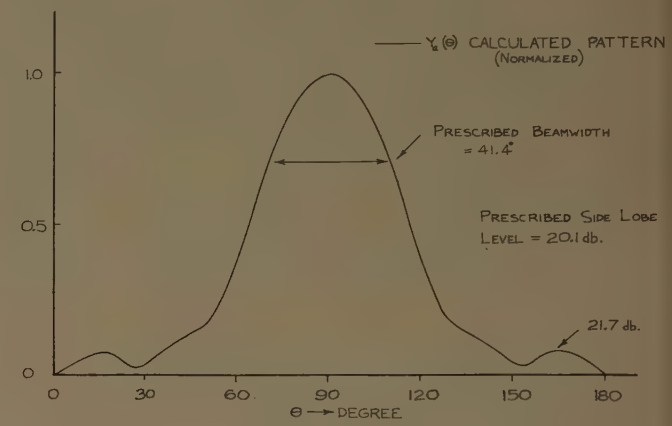

Fig. 4—Example of broad-side pattern.

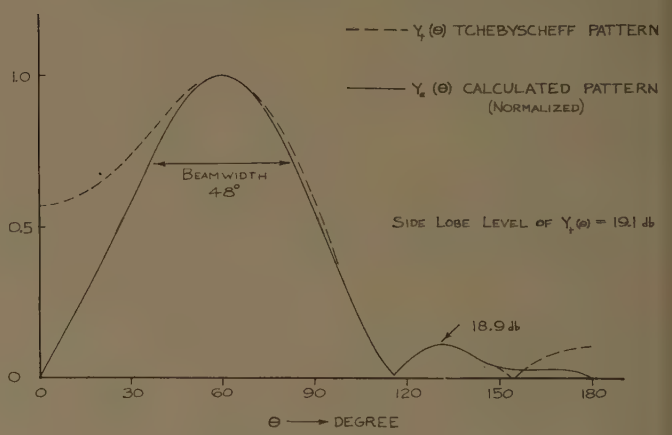

Fig. 5—Example of pattern with main lobe at 60°.

Acknowledgment

The assistance of the University of Washington Computer Laboratory in the numerical calculations is acknowledged.

A Slot with Variable Coupling and Its Application to a Linear Array*

RAYMOND TANG†

Summary—The importance of a waveguide linear array capable of producing many different radiation patterns has led to the development of a slot radiator with variable coupling. An array of such radiators can be used as a laboratory apparatus for the evaluation of aperture distributions, or as a ground-painting reconnaissance antenna operable at many different altitudes. The slot radiator consists of a longitudinal slot centered in the broad face of a rectangular waveguide. An adjustable iris excites the slot by introducing controlled asymmetry in the waveguide fields. The theory of operation and the characteristics of this variable coupling slot are presented. These characteristics are shown in curves usable for design purposes. A detailed discussion is given of the technique used in determining the range of conductances of this slot. The control of coupling available is demonstrated by measured radiation patterns on a 12-element array in which the conductance values are varied to obtain sidelobe ratios from 10 to 34 db. The method used in obtaining the aperture distributions for these radiation patterns is also presented.

Introduction

An array which will produce many different radiation patterns is of considerable interest. Such an array could be very useful, for example, as a laboratory apparatus for the investigation of various aperture distributions or as a ground-painting reconnaissance antenna operable at many different altitudes. An array with variable radiation patterns has been developed, and it is the purpose of this paper to describe the radiating elements used in this array and their performance characteristics.

The radiation patterns of an array are controllable when the excitation of the elements of the array are individually adjustable. The variable amplitude element shown in Fig. 1 consists of an adjustable iris and a longitudinal slot cut along the centerline of the broad face of a rectangular waveguide. A linear array of these elements radiates no second-order beams[1] because all the longitudinal slots are positioned collinearly and spaced $\lambda g/2$ apart. The theory of operation of this combination of adjustable iris and longitudinal slot is based on the fact that a longitudinal slot will radiate an amount which is dependent on the distance the slot is displaced from the electrical centerline of the guide. The position of this electrical centerline can be shifted by lateral displacement of the iris inside the waveguide. Consequently, the longitudinal slot will radiate when the iris inside the waveguide is laterally displaced, and the amount of radiation will be determined by this displacement.

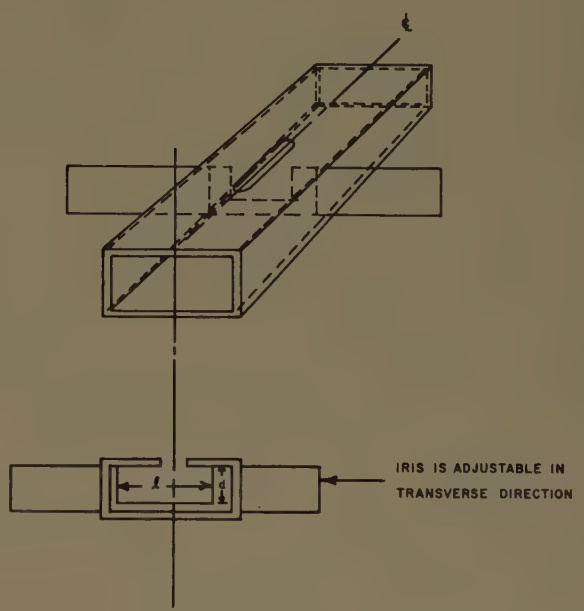

Fig. 1—Slot radiator with sliding iris.

General Properties of the Slot-Iris Combination

A series of measurements performed on this unit element brought out a number of interesting and useful properties of the slot-iris combination. The conductance of the element remains approximately constant over a wide range of frequencies, thus offering broad-band operation. The normalized susceptance at 9375 mc can be held to a variation of only from 0 to 0.01 as the iris is displaced from 0.030 to 0.075 inch. The conductance variation of the element with changes in iris position is proportional to the conductance variation which results when a slot alone is displaced from the centerline. Conductance of the element also varies with the iris dimensions.

With a resonant combination of iris and slot, the element maintains its conductance over a broad band of frequencies. The slot by itself can be represented by an

* Manuscript received by the PGAP, June 13, 1959; revised manuscript received, October 13, 1959.
† Microwave Lab., Hughes Aircraft Co., Culver City, Calif.
[1] H. Gruenberg, "Second order beams of slotted waveguide arrays," *Canad. J. Phys.*, vol. 31, pp. 55–59; 1955.

equivalent series RLC circuit across the waveguide,[2] and similarly the iris by itself can be considered an equivalent parallel LC circuit. Thus, the combination of slot and iris is equivalent to a series RLC circuit in parallel with a parallel LC circuit across the waveguide [see Fig. 1(b)]. The susceptances of these two circuits vary oppositely with frequency and hence tend to cancel each other over a large frequency range. Fig. 2 shows this broadband behavior in an element which has a slot on the centerline and an iris resonant by itself at 0.040-inch displacement.

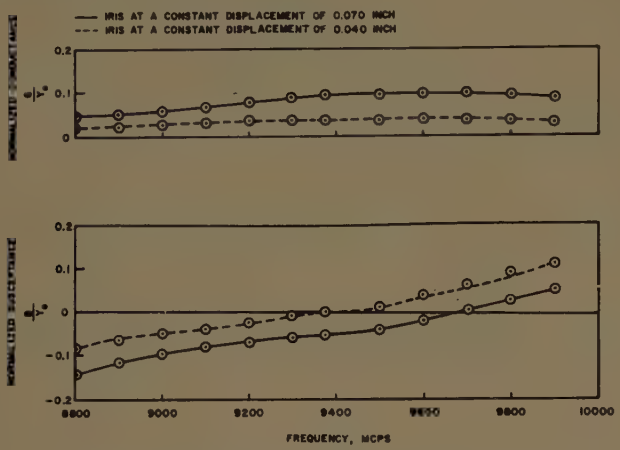

Fig. 2—Variation with frequency of the components of admittance of a unit element.

Measurements of Slot-Iris Characteristics

Susceptance measurements were made on the unit element for a wide range of iris displacement and for several iris shapes. When the iris used is resonant by itself at its symmetrical position, the measured normalized susceptance of the unit element varied from 0 to −0.09 as the iris was displaced 0.08 inch from its symmetrical position. This variation is shown in curve I of Fig. 3. However, when the iris used is resonant by itself at 0.04 inch from its symmetrical position, then the unit element remains approximately resonant for a range of iris displacement from 0.03 inch to 0.075 inch, as shown in curve II of Fig. 3. The conductance variation over this range of iris displacement is sufficient for many aperture distributions.

This wide range of useful iris displacement is due to the relatively constant level of susceptance; the susceptances introduced by the iris and by the slot tend to cancel each other when the iris is displaced from the symmetrical position. This cancelling effect is evident from the forms of curves III and IV of Fig. 3; curve III shows the measured susceptance of an iris vs its displacement when no slot is present, and curve IV shows the measured susceptance of a slot vs its physical displacement when no iris is present. The latter curve was

[2] W. H. Watson, "The Physical Principles of Waveguide Transmission and Antenna Systems," Oxford University Press, London, Eng.; 1947.

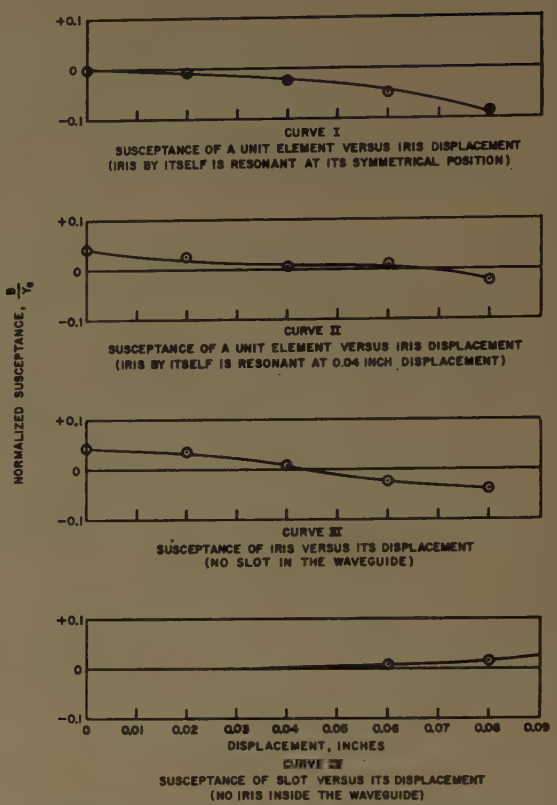

Fig. 3—Susceptance of the unit element for a wide range of iris displacement and for several iris shapes.

calculated from the experimental results given by Stegen.[3]

The conductance of the element was determined by the following two-step procedure.

1) A curve of relative power coupled through the slot vs iris displacements is obtained by direct measurement (see Fig. 4).
2) From this curve the ratio of conductances at two different iris displacements is calculated from the ratio of relative coupled power at these iris displacements. The calculation makes use of an equation derived from the equivalent circuit of the unit element with a matched load termination:

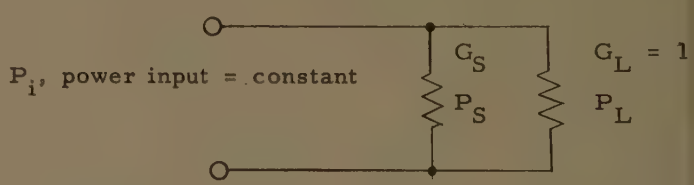

where

G_S = normalized conductance of the slot of the unit element,
P_S = power coupled from the slot of the unit element,
G_L = normalized conductance of the matched load,
P_L = power in the matched load.

[3] R. J. Stegen, "Slot radiators and arrays," *Radio-Electronic Engrg.*; January, 1952.

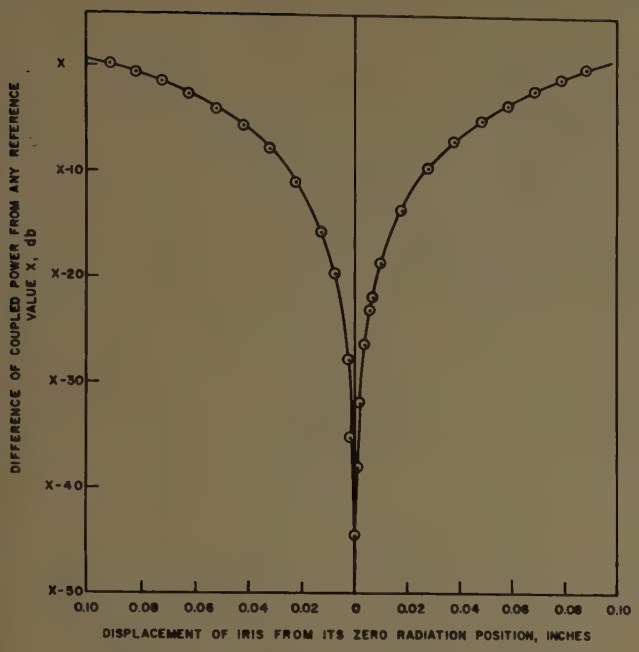

Fig. 4—Relative coupled power vs iris displacement.

Since

$$P_S = \frac{G_S}{G_S + 1} P_i,$$

$$\frac{G_S}{G_S + 1} = \frac{P_S}{P_i},$$

then

$$\frac{\dfrac{G_1}{G_1 + 1}}{\dfrac{G_2}{G_2 + 1}} = \frac{\dfrac{P_1}{P_i}}{\dfrac{P_2}{P_i}}$$

and

$$\left(\frac{G_1}{G_2}\right)\left(\frac{G_2 + 1}{G_1 + 1}\right) = \frac{P_1}{P_2},$$

where G_1 and P_1 are the conductance of, and the coupled power from, the slot when the iris is in one position; and G_2 and P_2 are corresponding values for the other iris position.

The absolute conductance values at different iris displacements can be determined from this equation if one absolute value of conductance at one fixed position of the iris is known. This reference value of conductance is established by a measurement (with a traveling probe in a slotted waveguide) of the conductance for a 0.08-inch iris displacement. The 0.08-inch iris displacement is used for the reference value rather than a smaller displacement, because of the inherent difficulties in measuring very low conductances. In addition, on the test setup the conductance due to the leakage power through the vertical slots on the edge walls became comparable to the conductance of the unit element for small iris displacements. The measured values of the conductances are shown in curve I of Fig. 5.

Comparison of the conductance variation of a unit element with that of a slot substantiates the directly proportional relationship between the displacement of the iris and the displacement of the slot. This relationship is shown by curves I–III of Fig. 5. Curve I shows the effect of iris displacement on the conductance variation of a slot fixed on the centerline of the broad face of an X-band waveguide. Curve II shows the conductance variation of a slot vs its physical displacement off the centerline of the broad face of an X-band waveguide with the iris fixed symmetrically with respect to the centerline. Curve II was calculated with this fixed symmetrical iris so that the waveguide dimensions in curves I and II are the same, and a comparison of curves I and II can be made. Curve III shows the conductance variation of a slot vs its physical displacement off the centerline of the broad face of a waveguide with no iris present.

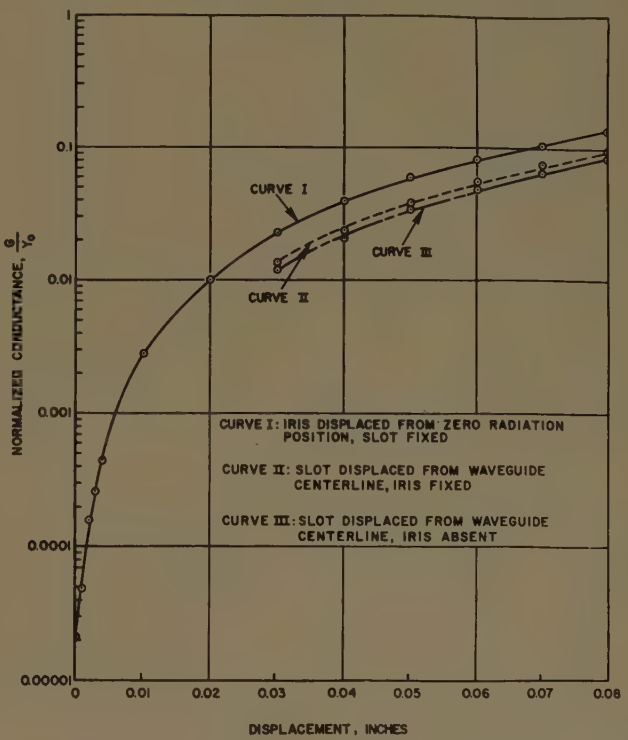

Fig. 5—Conductance-displacement relationship of the slot and iris.

The normalized conductances in curves II and III are related by a constant ratio of Y_0/Y_{01}, where Y_0 is the waveguide admittance with no iris and Y_{01} is the admittance of a waveguide having the dimensions of the iris.

Conductance variation of the unit element may also be obtained by changes in the dimensions of the resonant iris rather than by physical displacement of the iris. The field configuration around the slot changes with variation in the dimensions of the resonant iris, and this variation changes the conductance of the unit element. Fig. 6 shows conductance variation with

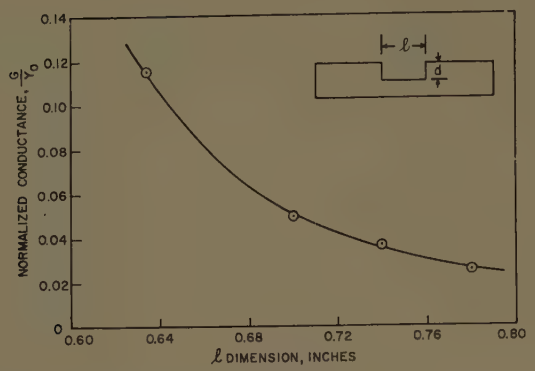

Fig. 6—Slot conductance vs iris length, l. The corresponding d dimension required to maintain resonance at 0.040-inch displacement is shown in Fig. 7.

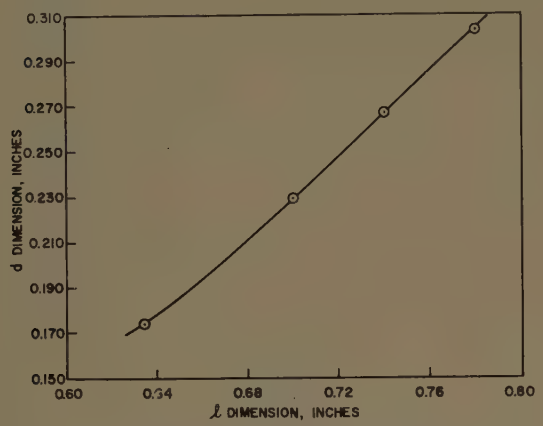

Fig. 7—Relationship between l and d iris dimensions for resonance at 0.040-inch displacement.

change in dimensions for an iris which is always resonant and maintains a constant displacement of 0.040 inch from its symmetrical position. The resonant iris dimensions, which are shown in Fig. 7, are interesting because they point out an approximate linear relationship between the dimensions of the inductive and capacitive strips required to maintain resonance.

Experimental 12-Element Array

For further tests on the unit element, a resonant array of twelve elements was constructed. By changes of iris displacement, the aperture distribution was adjusted for sidelobe levels of 10, 13.5, 20, 30, and 40 db. The resulting radiation patterns are shown in Fig. 8. A horn was used to reduce the E-plane beamwidth of the array. The aperture distributions of these patterns were obtained in one of two ways:

1) From the conductance distribution, the corresponding iris displacements were determined from the conductance curve (Fig. 5) for a unit element. This approach was taken in setting the conductance distributions for the 10- and 13.5-db sidelobe ratios. Table I shows a tabulation of iris displacements for these sidelobe ratios.

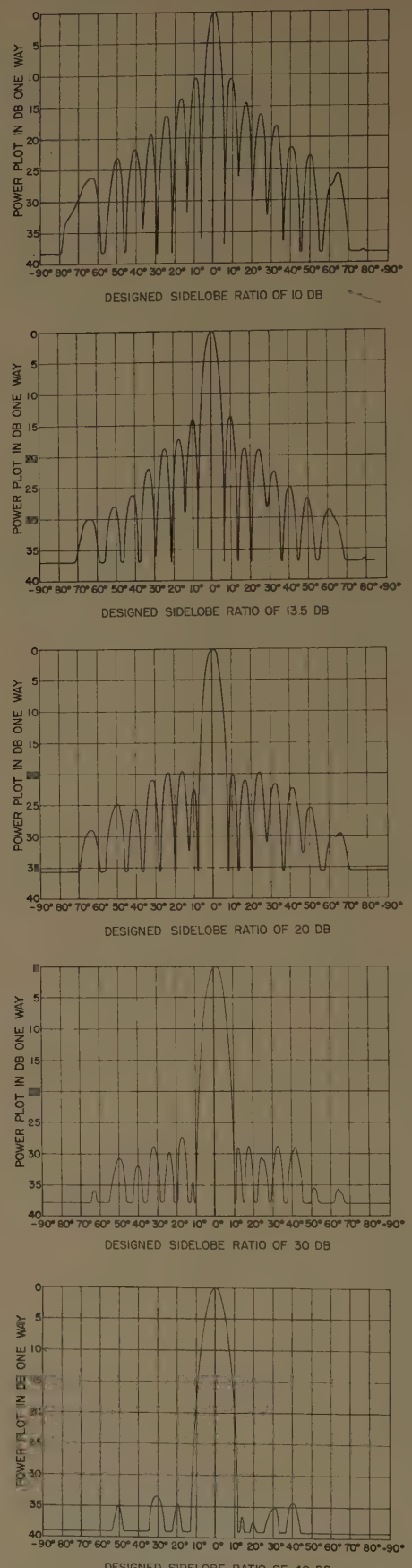

Fig. 8—Radiation patterns of sliding-iris 12-element array.

TABLE I

IRIS DISPLACEMENTS VS SIDELOBE RATIOS IN A 12-ELEMENT ARRAY

Element	10-db sidelobe ratio		13.5-db sidelobe ratio		20-db sidelobe ratio		30-db sidelobe ratio		40-db sidelobe ratio	
	Conductance	Iris Displacement	Conductance	Iris Displacement	Conductance	Iris Displacement	Conductance	Iris Displacement	Conductance	Iris Displacement
1	0.1370	+0.080	0.137	+0.080	0.0697	+0.056	0.0096	+0.019	0.0019	+0.008
2	0.0968	−0.066	0.137	−0.080	0.0419	−0.041	0.0194	−0.028	0.0088	−0.018
3	0.0714	+0.056	0.137	+0.080	0.0688	+0.055	0.0449	+0.043	0.0292	+0.034
4	0.0552	−0.048	0.137	−0.080	0.0978	−0.067	0.0797	−0.060	0.0653	−0.053
5	0.0465	+0.042	0.137	+0.080	0.1226	+0.076	0.1146	+0.073	0.1071	+0.071
6	0.0416	−0.041	0.137	−0.080	0.1370	−0.080	0.1370	−0.080	0.1370	−0.080
7	0.0416	+0.041	0.137	+0.080	0.1370	+0.080	0.1370	+0.080	0.1370	+0.080
8	0.0465	−0.042	0.137	−0.080	0.1226	−0.076	0.1146	−0.073	0.1071	−0.071
9	0.0552	+0.048	0.137	+0.080	0.0978	+0.067	0.0797	+0.060	0.0653	+0.053
10	0.0714	−0.056	0.137	−0.080	0.0688	−0.055	0.0449	−0.043	0.0292	−0.034
11	0.0968	+0.066	0.137	+0.080	0.0419	+0.041	0.0194	+0.028	0.0088	+0.018
12	0.1370	−0.080	0.137	−0.080	0.0697	−0.056	0.0096	−0.019	0.0019	−0.008

2) From the power distributions, the irises were adjusted until the desired coupled power from each slot was measured. This method was used to obtain the 20-, 30-, and 40-db sidelobe ratios.

The maximum deviation of the measured ratios from the designed sidelobe ratios was 0.5 db for the 10-, 13.5- and 20-db radiation patterns. However, the deviation increased to 2.5 and 6.5 db for the designed 30- and 40-db radiation patterns. The reasons for this greater deviation are:

1) The variation from the desired aperture distribution due to the random error in the placement of the iris. In fact, it has been theoretically derived by statistical methods[4] and experimentally verified that, for a 24-element *X*-band ordinary slot array manufactured with a 0.002-inch tolerance, the probable highest sidelobes are a) 19 db for a 20-db array, b) 27 db for a 30-db array, and c) 32 db for a 40-db array.
2) The variation in phase due to the random errors in the slot spacing and slot length.
3) The leakage power coupled through the vertical slots on the narrow walls by the irises. However, this leakage can be almost completely eliminated by shielding the irises with metal tape.

[4] L. L. Bailin and M. J. Ehrlich, "Factors Affecting the Performance of Linear Arrays," Res. Labs., Hughes Aircraft Co., Culver City, Calif., Tech. Memo. No. 263; December, 1951.

CONCLUSION

The variable-amplitude element consisting of a slot and iris offers a means of obtaining many aperture distributions from a single array. Measurements show that this element has the following limitations: 1) maximum conductance is limited by the maximum iris displacement that still maintains a resonant circuit; 2) minimum conductance is limited to a value at which leakage power from the vertical slot is an appreciable portion of the total conductance. Within these limits many possibilities exist for applications of the element in arrays with variable aperture distributions. Experiments will be continued to adapt this unit element for the design of a two-dimensional array which can be used as a variable altitude ground-painting reconnaissance.

ACKNOWLEDGMENT

The author is indebted to L. A. Kurtz for his many helpful suggestions and consistent guidance during the course of this work, to L. A. Gustafson for his encouragement and support, and to H. W. Marlin, who assisted in performing the measurements.

communications

Theory of Equilibrium Electron and Particle Densities Behind Normal and Oblique Hypersonic Shock Waves in Air*

C. A. ROBERTS†, W. B. SISCO‡, AND J. M. FISKIN†

Summary—The quantitative changes in propagation, antenna impedance, radar cross section, breakdown, and emissivity characteristics resulting from hypersonic plasmas depend on the electrons and heavier particles present. To determine these number densities for normal and oblique shocks, aerothermodynamic theory is applied to relate macroscopic properties on both sides of the shock front by means of the flow conservation equations. Composition and energy of the shocked air at assumed velocities, densities, and temperatures are then obtained using the law of mass action and the principles of statistical quantum mechanics until the conservation equations are satisfied.

Introduction

VEHICLES whose characteristic cross section is large compared to the mean free path of the air molecules will be surrounded by an ionized layer when traveling at hypersonic speeds. This sheath will modify 1) EM propagation constants, 2) vehicle antenna impedances, 3) radar cross sections, 4) air breakdown properties, and 5) noise levels. These quantitative changes are determined from a detailed knowledge of the electron and heavier particle number density distribution together with the energy level population.

Aerothermodynamics

Relationships between aerothermodynamic properties on both sides of the normal shock front and to each other are given by the flow conservation equations and the equation of state.

$$\rho_0 U_0 = \rho_1 U_1 \text{ (mass flow)}, \tag{1}$$

$$P_1 - P_0 = \rho_0 U_0 (U_0 - U_1) \text{ (momentum flow)}, \tag{2}$$

$$E_{m_0} + \rho_0 \tau_0 + 1/2 U_0^2 = E_{m_1} + P_1 \tau_1 + 1/2 U_1^2 \text{ (energy flow)}, \tag{3}$$

$$PV = \sum_j n_j k T \text{ (equation of state)}; \tag{4}$$

where

ρ = density (weight/unit volume) $= 1/\tau$,
τ = specific volume,
U = streamwise flow velocity,
P = pressure,
E_m = internal energy/unit mass,
V = volume,
n_j = number of particles of jth species,
k = Boltzmann's constant,
t = temperature.

Zero subscripts indicate the unshocked or ambient air; one subscripts signify the shocked air. The qualitative relationships between these quantities are shown in Fig. 1. For oblique and swept swing shocks, (1)–(3) are applicable provided U_0 and U_1 are replaced by their components normal to the shock front. A typical shock-wave surrounding a blunt body is shown in Fig. 2.

Composition and Energy

The composition (number density) depends on the shocked air temperature (T_1), density (ρ_1), or pressure (P_1), and on the chemical reactions taking place. For EM considerations, equilibrium reactions used below 5000° K are

$$N_2 \rightleftarrows N + N, \tag{5}$$

$$O_2 \rightleftarrows O + O, \tag{6}$$

$$NO \rightleftarrows N + O, \tag{7}$$

$$NO \rightleftarrows NO^+ + e^-. \tag{8}$$

* Manuscript received by the PGAP, March 3, 1959; revised manuscript received, July 8, 1959.
† Douglas Aircraft Co., Inc., Long Beach, Calif.
‡ National Engineering Science Co., Pasadena, Calif.; formerly with Douglas Aircraft Co., Inc.

→Initial state		→Shocked state
U_0	(Streamwise flow velocity)	$U_1 < U_0$
ρ_0	(Density $= 1/\tau_0$ (specific volume)$^{-1}$	$\rho_1 > \rho_0$
P_0	(Pressure)	$P_1 > P_0$
T_0	(Temperature)	$T_1 > T_0$
E_{m0}	(Internal energy per unit mass)	$E_{m1} > E_{m0}$

Shock front

Fig. 1—Flow through a shock front.

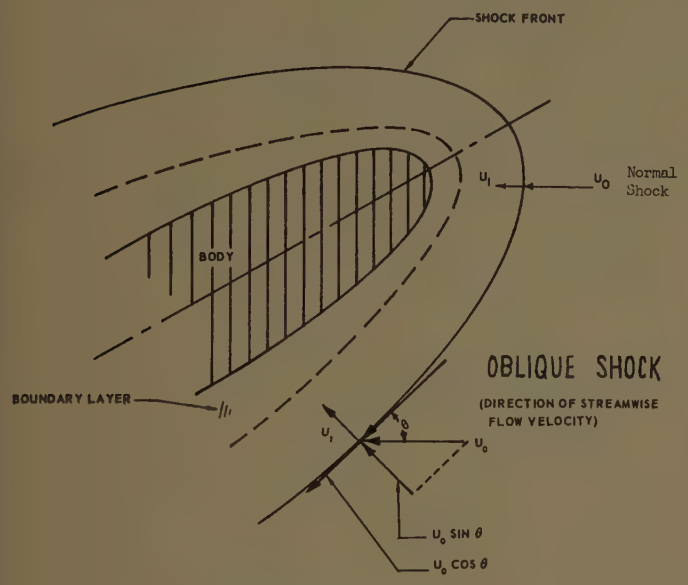

Fig. 2—Shock wave geometry.

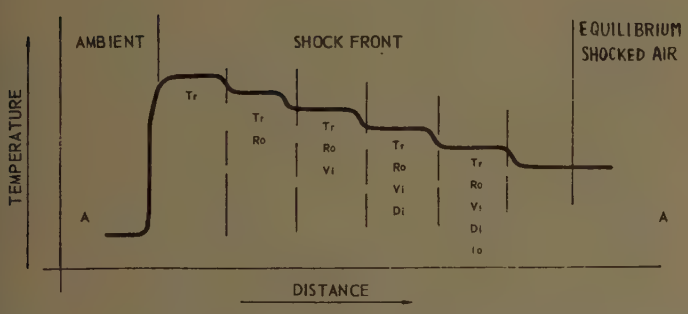

Fig. 3—The shock front cross section illustrating excitation of various energy modes. Tr = translation, Ro = rotation, Vi = vibration, Di = dissociation, and Io = ionization.

Associated with each reaction is an equilibrium constant that is related to the partition functions and the composition by the law of mass action.

$$K_5 = \frac{[N][N]}{[N_2]} = \frac{(PF)_N (PF)_N}{(PF)_{N_2}} \left(\frac{1}{\rho_{dr} L}\right) e^{-Q_5/kT}, \quad (9)$$

$$K_6 = \frac{[O][O]}{[O_2]} = \frac{(PF)_O (PF)_O}{(PF)_{O_2}} \left(\frac{1}{\rho_{dr} L}\right) e^{-Q_6/kT}, \quad (10)$$

$$K_7 = \frac{[N][O]}{[NO]} = \frac{(PF)_N (PF)_O}{(PF)_{NO}} \left(\frac{1}{\rho_{dr} L}\right) e^{-Q_7/kT}, \quad (11)$$

$$K_8 = \frac{[NO^+][e^-]}{[NO]} = \frac{(PF)_{NO} + (PF)e^-}{(PF)_{NO}} \left(\frac{1}{\rho_{dr} L}\right) e^{-Q_8/kT}; \quad (12)$$

where

K = equilibrium constant,
ρ_{dr} = ratio of actual density to standard density,
L = number of air atoms at standard density,
Q = energy of dissociation, formation and ionization,
[ ] = ratio of number of particles of a particular species to total number of air atoms present.

The partition function (PF) is

$$(PF) = \sum_i g_i e^{-\epsilon_i/kT} \quad (13)$$

where

g_i = degeneracy of ith energy level
ϵ_i = ith energy level.

Eq. (13) can be expressed as the product of specific partition functions related to each energy mode.

$$(PF) = (PF)_{\text{translational}} \times (PF)_{\text{rotational}} \times (PF)_{\text{vibrational}} \times (PF)_{\text{electronic}}. \quad (14)$$

The (PF) is obtained from the theory of statistical quantum mechanics and experimental spectroscopic data.[1] When calculated they yield the equilibrium constants. Three additional equations are also required:

$$2[N_2] + [N] + 2[O_2] + [O] + 2[NO] + 2[NO^+] = 1 \text{ (mass conservation)}, \quad (15)$$

$$\frac{2[N_2] + [N] + [NO] + [NO^+]}{2[O_2] + [O] + [NO] + [NO^+]} = 3.71 \text{ (material balance conservation)}, \quad (16)$$

$$[NO^+] = [e^-] \text{ (charge conservation)}. \quad (17)$$

Eqs. (9)–(12) and (15)–(17) constitute a set of simultaneous equations and are solved for the concentrations, [ ].

Total energy, E_{m_1}, of the shocked air is

$$E_{m_1}(\text{total}) = E_{\text{particle}} + E_{\text{diss}}, - E_{\text{form}}, + E_{\text{ion}}, \quad (18)$$

where E_{particle} includes all of the energy modes (see Fig. 3). The population of the energy states is

$$n_i = \frac{g_i e^{-\epsilon_i/kT}}{\sum_i g_i e^{-\epsilon_i/kT}}, \quad (19)$$

where n_i = number of particles in ith energy state.

Iterative Solution

Shocked air concentrations and energy are obtained from assumed values of T_1, ρ_1, and U_1. This process is repeated until the aerothermodynamic conservation equations are satisfied for a given ambient altitude (ρ_0) and velocity (U_0).

[1] C. A. Roberts, W. B. Sisco, and J. M. Fiskin, Douglas Aircraft Co., Inc., Long Beach, Calif., Engrg. Rept. No. LB-25872; 1958.

A Theorem Regarding the Commutation of Antenna Rotations*

L. P. BOLGIANO, JR.†

Summary—**Ordinarily when an antenna is rotated successively about mutually perpendicular earth-fixed axes such as axes pointing up, north, and west, the order in which the successive rotations are made cannot be reversed without obtaining a very different final antenna orientation. This paper gives an analytic proof that the same final antenna orientation can always be obtained with the rotation order reversed as with the rotations performed in correct order. To accomplish this it is necessary when reversing the order of rotation only to also reidentify the axes of rotation. The required reidentification is obtained by considering the axes as detached from the earth and permitted to turn with the antenna as would lines painted on the antenna before the rotations are begun.**

IT IS well known that one cannot reverse the order in which successive rotations of an antenna about orthogonal fixed axes are performed without obtaining an entirely different final antenna orientation. We wish to point out that if, in addition to reversing the order of the successive rotations, the axes of rotation are beforehand reidentified as axes fixed to the antenna (such as lines painted on the antenna), then the same final antenna orientation will be obtained with the order of the rotations reversed. The converse statement permitting changing from antenna axes to fixed axes is equally valid and perhaps the more useful theorem.

It is often convenient to visualize the aiming of an antenna as the result of successive rotations about two perpendicular ground-plane axes and a polarization axis. For example, a radiometer antenna might be aimed at the sun by pointing it upwards and then rotating it first about its ground-plane axes, as required by time of day and time of year, and then about its polarization axis so as to receive a desired polarization. This commutation theorem then provides a convenient means for converting these rotations to earth-fixed axes either for drafting convenience or for facilitating the use of matrix algebra to reduce a larger number of rotations to the usual minimum of three successive rotations.

The mathematical basis of this equivalence corresponds to the dual interpretation of any rotation matrix as either rotating a vector with respect to fixed base coordinates, or alternatively rotating the base coordinate axes with respect to which a stationary vector's components are reckoned. As an example consider an antenna with a rectangular ground plane initially lying flat on the ground with its long axis north-south so as to beam the antenna straight up. Three mutually perpendicular lines may be imagined as painted on the antenna, one along the major ground-plane axis (pointing north), one along the minor ground-plane axis (pointing west), and a third along the polarization axis (pointed up). To permit distinguishing clockwise and counterclockwise rotations, let these orthogonal lines painted on the antenna be assigned directions corresponding to the right-hand choice north-west-up before rotation. Imagine also an arrow pointing in any convenient direction painted on the antenna so that its components in the north-west-up directions can be used to specify different antenna orientations as the antenna is rotated. The argument which will now be given is general and does not require the reader to visualize the precise orientation of the antenna or the axes and arrow painted on it. It is necessary only to note that these markings on the antenna permit any rotation of the antenna to be specified in two alternative ways either 1) by stating the change in the north-west-up components of the arrow painted on the antenna or 2) by stating the change in the components along the axes painted on the antenna of some vector which stays fixed in space during the rotation.

Now suppose that the antenna is rotated through an angle α about its short ground-plane axis. This rotation causes the lines painted on the antenna to assume a new position in space. We can therefore speak of two distinct sets of coordinate axes, set 1 being the north-west-up axes originally coincident with the painted lines and set 2 being the new orientation of these lines. The vector defined in space by the new orientation of the arrow painted on the antenna has components y_1, y_2, y_3 along the axes of set 2 identical to those the arrow originally had along the north-west-up axes. This vector has different components x_1, x_2, x_3 along the axes of set 1. This alternate component representation is conveniently represented as a matrix product $Y=AX$ where X and Y denote column matrices with elements x_1, x_2, x_3 and y_1, y_2, y_3, respectively, and A is a square matrix which converts the components of any vector along the axes of set 1 into those along the axes of set 2.

Next let the antenna be rotated through an angle β about its long ground-plane axis. The painted lines now define a third set of axes we denote as set 3. The new vector defined by the painted arrow in its new position has new components z_1', z_2', z_3'; y_1', y_2', y_3'; and x_1', x_2', x_3' along the axes of sets 3, 2, and 1, respectively. Again we can represent the new component transformation by a matrix equation $Z'=BY'$. By the previous paragraph, $Y'=AX'$; since the painted arrow always has the same components along the painted lines, $Z'=Y$.

* Manuscript received by the PGAP, May 28, 1959. This work was supported by a Frederick Gardner Cottrell grant from the Research Corporation.

† University of Delaware, Newark Del.

Combining these gives $Y=BAX'$. Continuing the same reasoning, if C is a matrix converting the components of any vector relative to set 3 into those relative to another set 4 defined by rotating the antenna an angle γ about its polarization axis, then we can write $Y=CBAX''$. The elements of X'' are the north-west-up components of the vector defined by the final position of the painted arrow, and the elements of Y have become the components of this vector relative to coordinate set 4.

By matrix algebra, $X''=A^{-1}B^{-1}C^{-1}Y$. This can be interpreted as meaning that if the antenna had first been turned so that the painted arrow's north-west-up components were changed from Y to $C^{-1}Y$, then turned again so as to change its north-west-up components to $B^{-1}C^{-1}Y$, and finally turned so as to change the north-west-up components of the arrow to $A^{-1}B^{-1}C^{-1}Y$, the identical final antenna orientation would have resulted. But this amounts precisely to rotating the antenna successively through the angles γ, β, and α about up, north, and west axes, respectively. Since the same relative movement between an object and a set of axes is caused either by turning the object one way or the axes the opposite way, the inverse matrices mean that each rotation of the antenna should be performed in the same sense (clockwise or counterclockwise) as before. The proof is the same regardless of which axes the rotations α, β, and γ are about, and it can be extended to any number of successive rotations by mathematical induction.

ACKNOWLEDGMENT

The writer wishes to acknowledge the valuable assistance of V. W. Richard and K. A. Richer of the Aberdeen Proving Ground Ballistic Research Laboratories.

Radiation Fields of Circular Loop Antennas by a Direct Integration Process*

E. J. MARTIN, JR.†

Summary—**Starting from the radiation characteristics of a differential current element, the vector potential produced by a single-turn circular loop antenna is formulated in terms of a general loop current by a direct integration process. Evaluation of the resulting integrals for a limited number of specific loop current distributions leads to generalized expressions for both the standing-wave and traveling-wave cases. Radiation fields can be found from the integrated vector potential expressions. This technique represents only a slight modification of the one used by Sherman, but it extends his work in such a way that the results are equivalent to those obtained by Knudsen in a somewhat different manner.**

IN 1944, Sherman[1] investigated the general case of a circular loop antenna with nonuniform standing-wave and traveling-wave current distributions. On the basis of his analysis, he concluded that the field of the general loop could be determined only on the axis of the loop and in a plane perpendicular to the axis. The invalidity of this conclusion was later demonstrated by Knudsen,[2] who considered a "quasi-array" composed of a finite number of tangential dipoles and then obtained the final field equations through a limiting process in which the number of dipoles is allowed to approach infinity.

It is our purpose here to point out that it is possible to develop the field equations for the general case of a circular loop with uniform or nonuniform standing-wave current distribution or traveling-wave current distribution through a method of integration that is very similar to the one used by Sherman. The primary difference between this procedure and the one used by Sherman is that attention is focused on the vector potential during integration; the electric and magnetic fields are subsequently found from the integrated vector potential. This technique results in field expressions which describe the loop antenna at any point in space and are, in fact, identical with the results obtained by Knudsen when account is taken of the form of the time variation of the assumed current distribution. It is therefore demonstrated that the methods of Sherman and Knudsen are essentially equivalent.

Consider a "linear, thin-wire" radiator of differential length $dl=ad\phi$ situated at an azimuthal angle ϕ from some arbitrary reference point on the circumference of a circle of radius a, which lies ln the XY plane with its center at the origin (Fig. 1). This radiator may be thought of as comprising a differential segment of a

* Manuscript received by the PGAP, April 27, 1959; revised manuscript received, October 9, 1959. This paper is based on the author's M.S. thesis, "An Approximation of the Helical Beam Antenna," submitted to the Graduate School, University of Kansas, Lawrence; May, 1956.

† Midwest Research Institute, Kansas City, Mo.

[1] J. B. Sherman, "Circular loop antennas at ultrahigh frequencies," PROC. IRE, vol. 32, pp. 534–537; September, 1944.

[2] H. L. Knudsen, "The field radiated by a ring quasi-array of an infinite number of tangential or radial dipoles," PROC. IRE, vol. 41, pp. 781–789; June, 1953.

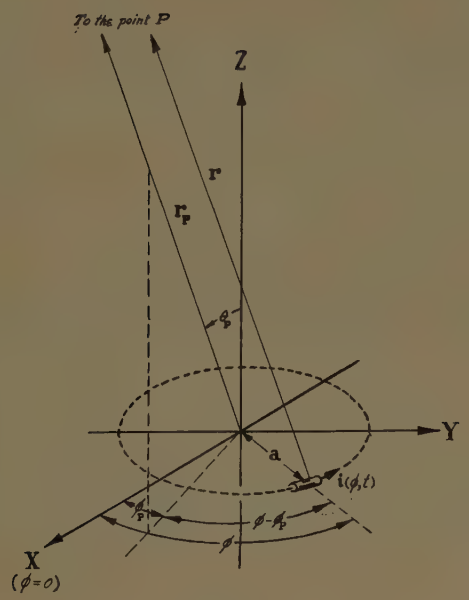

Fig. 1.

single-turn circular loop which is defined by the circle of radius a. Let the differential radiator carry a current $i(\phi, t) = I(\phi)\epsilon^{j\omega t}$. If a *fixed* point of observation P, at which the fields are to be determined, has coordinates r_p, θ_p, ϕ_p, such that P is far away from the loop, the distance r_p (which is measured from the origin to the point P) and the distance r (which is measured from the differential segment under consideration to the point P) are measured along virtually parallel lines. Consequently, r may be expressed in terms of r_p as

$$r = r_P - a \sin \theta_P \cos (\phi - \phi_P). \tag{1}$$

Upon recalling the form of the vector potential that is produced by a differential current element, one can refer to the diagram of Fig. 2, which is a projection of Fig. 1 on the XY plane, and also to Fig. 3, which presents an enlarged perspective view of the various vector components at the point of observation, in order to see that the vector potential at P due to the differential segment of the loop at ϕ can be expressed as

$$d\mathbf{A} = \frac{\mu a}{4\pi r_p}\epsilon^{j(\omega t - kr_p)}\left\{\left[\frac{-\mathbf{r}}{\sin\theta_p} - \mathbf{\Theta}\cos\theta_p\right]\sin\phi' + \mathbf{\Phi}\cos\phi'\right\} I(\phi)\epsilon^{j\gamma\cos\phi'}d\phi'. \tag{2}$$

Here

$\mathbf{r}$, $\mathbf{\Theta}$, $\mathbf{\Phi}$ = spherical-coordinate unit vectors at the point P,

$\phi' = (\phi - \phi_x)$ and consequently $d\phi' = d\phi$,

and the substitutions $k = \omega/c$ and $\gamma = ka \sin\theta_p$ have been made in order to simplify the notation. Summation of the contributions from all differential segments, which

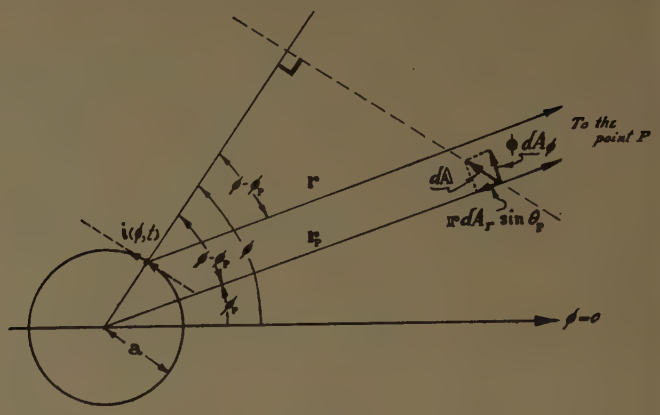

Fig. 2.

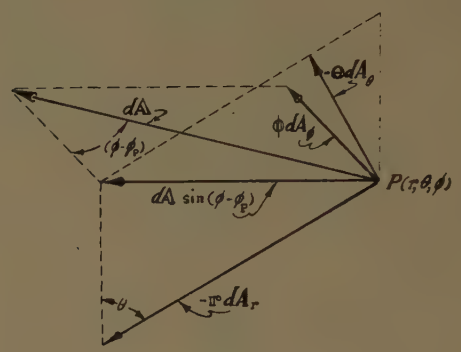

Fig. 3.

together comprise the circular loop, will now give the total vector potential at P. However, before this can be accomplished, it is necessary that the current, designated simply by $I(\phi)$ in (2), be more specifically defined.

Following the technique used by Sherman and Knudsen, we first assume a standing-wave current distribution such that

$$I(\phi) = I\left\langle \begin{matrix} \cos n\phi \\ \text{or} \\ \sin n\phi \end{matrix} \right\rangle. \tag{3}$$

This selection allows us to integrate the right side of (2) between the limits $-\phi_p$ and $2\pi - \phi_p$ and to evaluate the resulting integrals by means of the Sommerfeld integral expression for Bessel functions in precisely the same manner as discussed by Knudsen. The results show that the total vector potential at P is

$$\mathbf{A} = j^n\left[\frac{-j\mu K\epsilon^{-jkr_p}}{2r_p}\right] \cdot \left\{\left[\frac{\mathbf{r}}{\sin\theta_p} + \mathbf{\Theta}\cos\theta_p\right]\frac{2n\left\langle \begin{matrix}\sin n\phi \\ \cos n\phi\end{matrix}\right\rangle}{\gamma} J_n(\gamma) + \mathbf{\Phi}\left\langle \begin{matrix}\cos n\phi \\ \sin n\phi\end{matrix}\right\rangle [J_{n-1}(\gamma) - J_{n+1}(\gamma)]\right\}, \tag{4}$$

where the notation is further simplified by the substitution $K=\frac{1}{2}aI\epsilon^{j\omega t}$. For the case of an assumed traveling-wave current distribution

$$I(\phi) = I\epsilon^{-jn\phi}, \tag{5}$$

the vector potential is found to be

$$\mathbf{A} = j^n\left[\frac{-j\mu K\epsilon^{-j(kr_p+n\phi)}}{2r_p}\right]\left\{\left[\frac{\mathbf{r}}{\sin\theta_p}+\mathbf{\Theta}\cos\theta_p\right]\frac{j2n}{\gamma}J_n(\gamma) + \mathbf{\Phi}[J_{n-1}(\gamma)-J_{n+1}(\gamma)]\right\}. \tag{6}$$

Since the selection of the point of observation is made in a completely arbitrary manner, the subscripts on r and θ in (4) and (6) can be dropped, once the integration is complete. The electric and magnetic field components can now be obtained from the vector potential through the use of the vector relations. $\mathbf{E}=(1/j\omega\mu\epsilon)\boldsymbol{\Delta}(\boldsymbol{\Delta}\cdot\mathbf{A})-j\omega\mathbf{A}$ and $\mathbf{H}=1/\mu(\boldsymbol{\Delta}\times\mathbf{A})$. Appropriate combinations of the resulting field equations can be used to determine completely the fields produced by a circular loop with any assumed or measured current distribution.

Refraction of VHF Signals at Ionospheric Heights*

S. WEISBROD† AND L. COLIN‡

Summary—**It is not generally realized that while the refractive error due to the troposphere rapidly decreases with the elevation angle, its ionospheric counterpart behaves very differently. For target heights which are small or comparable to the Earth's radius the ionosphere refractive error initially increases with the elevation angle, attains the maximum value at elevation angles on the order of 100 milliradians and then gradually decreases. The size of this increase decreases with the distance from the Earth and at astronomical distances the initial slope of the ionospheric error at grazing incidence is zero. At ionospheric heights the elevation angle at which the ionosopheric bending is maximum is roughly proportional to the square root of the layer height.**

This somewhat unexpected behavior of ionospheric bending is examined and sample computations are made using realistic models of ionosphere and troposphere.

WITH the advent of the space age, the subject of refraction of VHF signals passing through the ionosphere has become extremely important. Tropospheric refraction has been investigated for many years, and it is generally known that it decreases rapidly with an increase in the elevation angle, and becomes virtually negligible for angles of elevation greater than 10° or 15°. What apparently is not generally known or appreciated is that ionospheric refraction behaves in a much different manner. For target heights within the ionosphere, the refractive error due to the ionosphere increases with elevation angle, attains a maximum value at elevation angles between 100 and 200 mr, and then gradually decreases.

The significance of this fact is that the total refractive error falls off more slowly than one might expect from a study of tropospheric bending. Furthermore, it is even possible under some conditions for the refractive error to increase with elevation angle. Since this has obvious implications in the problem of radio tracking of space vehicles, this subject has been investigated by the authors in detail, and the results are summarized below. A detailed treatment of this subject is now being prepared for publication.

First, let us briefly summarize the basic equations which govern the refractive bending. The amount of bending suffered by a ray passing through a layer bounded by heights h_j and h_k, and whose index of refraction varies linearly from n_j to n_k, is given by[1]

$$\gamma_{jk} = \frac{2(N_j - N_k)\times 10^{-6}}{\tan\beta_j + \tan\beta_k} \tag{1}$$

where

γ_{jk} = refractive bending in radians,
$N=(n-1)\times 10^6$,
β = co-angle of incidence,
N (troposphere) $=(77.6/T)(P+4810\ e/T)$,
T = absolute temperature in degrees Kelvin,
P = total atmospheric pressure in millibars,
e = water pressure in millibars,
N (ionosphere) $=4.03(N_e/f^2)\times 10^{-6}$,
N_e = electron density per cubic meter,
f = frequency in mc.

Fig. 1 illustrates the refractive geometry.

* Manuscript received by the PGAP, August 25, 1959; revised manuscript received, October, 1959. This work has been supported by the Rome Air Development Center, Griffiss AFB, Rome, N. Y., under Contract AF 30(602)-1624.

† Smyth Research Associates, San Diego, Calif.
‡ Rome Air Dev. Center, Griffiss AFB, Rome, N. Y.

[1] S. Weisbrod and L. J. Anderson, "Simple methods of computing tropospheric and ionospheric refractive effects on radio waves," PROC. IRE, vol. 47, pp. 1770–1777; October, 1959.

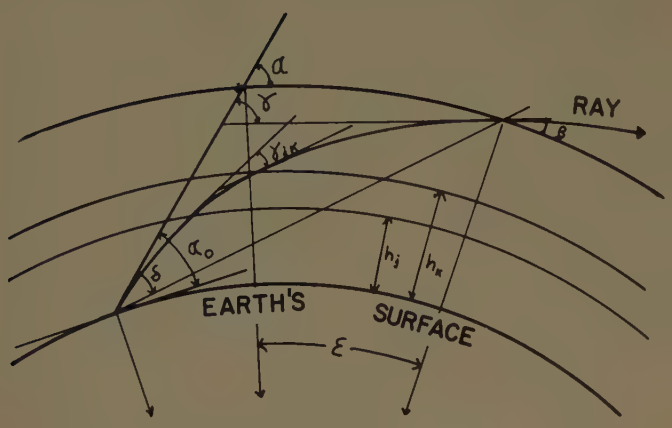

Fig. 1—Geometry of refraction.

Contribution to γ due to the passage through other layers is directly additive. The total bending is thus given by

$$\gamma = \sum_{k=0} \frac{2(N_k - N_{k+1}) \times 10^{-6}}{\tan \beta_k + \tan \beta_{k+1}} . \tag{2}$$

The summation in (2) is carried out over the tropospheric and the ionospheric layers.

It is frequently convenient to describe the refractive error in terms of the angle subtended from the earth's center between the refracted and the unrefracted rays. This angle, ϵ, is given by

$$\begin{aligned} \epsilon &= \gamma - (\alpha - \beta) \\ &\approx \gamma - (N_0 - N) \times 10^{-6} \cot \alpha \end{aligned} \tag{3}$$

where N_0 = the surface value of the refractive index, and N = the value of the refractive index at the point of interest.

The elevation angle error, δ, can be conveniently described in terms of ϵ:

$$\delta = \frac{\epsilon \tan \alpha}{\epsilon + \tan \alpha - \tan \alpha_0} . \tag{4}$$

According to (4), the contributions to δ due to tropospheric and ionospheric refraction are not directly additive. However, it turns out that as long as ϵ is much less than $\tan \alpha - \tan \alpha_0$, which is usually the case, very little error is introduced if the two contributions are added directly.

We should also note that at astronomic distances all three quantities, γ, ϵ, and δ, are equal.

Eqs. (1)–(4) form the basis of a simple and a very convenient method for computing refractive bending. The numerical work can be greatly shortened with the aid of special charts—one for the troposphere and one for the ionosphere. Details of this method are described elsewhere.[1]

Let us now investigate the behavior of δ as a function of α_0. Since the general expressions are extremely cumbersome, the approach used here consists of three steps. First, we will consider $d\delta/d\alpha_0$ for the case of tangentially departing ray. Secondly, we will derive an expression for α_0 under which the ionospheric contribution to δ is maximum. Third, we will construct plots of δ vs α_0 based on realistic models of the troposphere and the ionosphere.

Since the tropospheric and the ionospheric contributions to the refractive bending are going to be examined separately, subscripts "t" and "i" will be used to differentiate the two cases.

If a constant radial index gradient is assumed, $d\delta/d\alpha_0$ can be readily evaluated for the special case of $\alpha_0 = 0$. The slope of δ_t for any target height above the troposphere is

$$\left.\frac{d\delta_t}{d\alpha_0}\right|_{\alpha_0=0} = \frac{-2N_0 \times 10^{-6}}{(\epsilon_t + \tan \alpha_T)^2} \tag{5}$$

where α_T = the co-angle of incidence at the top of the troposphere.

For the case of a target in the ionosphere, the rate of change of δ_i with respect to α_0 is

$$\left.\frac{d\delta_i}{d\alpha_0}\right|_{\alpha_0=0} = \frac{\epsilon_i \tan \alpha}{(\epsilon_i + \tan \alpha)^2} . \tag{6}$$

The significant fact that these equations show is that, at grazing incidence, δ_t always decreases with α_0 whereas δ_i always increases. It is interesting to determine the condition for which the slope of the total δ becomes positive. It can be shown that

$$\left.\frac{d\delta}{d\alpha_0}\right|_{\alpha_0=0} = \frac{\epsilon_i \tan \alpha - 2N_0 \times 10^{-6} \tan^2 \alpha \cot^2 \alpha_T}{(\epsilon + \tan \alpha)^2} \tag{7}$$

where $\delta = \delta_i + \delta_t$ and $\epsilon = \epsilon_i + \epsilon_t$.

For the purpose of the estimate, we may assume the following parameters: height of the troposphere = 10 km, base of the F layer = 200 km, semithickness of the F layer = 100 km.

Under these conditions, (7) becomes positive when the ionospheric error δ_i is about 50 times the tropospheric error δ_t. In other words, the peak ionospheric refractive index would have to be about 500 times the tropospheric surface value. For typical N_0 values of 290 to 325 N units, and typical plasma frequencies of 10 to 15 mc, the signal frequency would have to be below 20 or 30 mc before the δ slope would become positive. We might also add that, under these conditions, the high-frequency assumptions used in deriving the above equations begin to break down, and, consequently, these estimates are only approximate. Also, at these frequencies other ionospheric effects, such as magneto-ionic splitting, absorption, and a possibility of total reflection, become the predominant effects so that refractive errors have only a limited significance in practical applications. Thus, we can conclude that, normally, the initial value of $d\delta_t/d\alpha_0$ is much greater than that of $d\delta_i/d\alpha_0$, so that the total elevation angle error decreases with α_0. The initial positive slope of δ_i causes the total δ at ionospheric heights to fall off much more slowly than one might expect from the study of the tropospheric bending alone. More will be said about this later.

Now that we have established that the slope δ_i is positive at grazing incidence, it would be interesting to estimate at what values of α_0 the maximum δ_i occurs.

Assuming linear variation of refractive index in the ionosphere, and also noting that at ionospheric heights ϵ is much less than $\tan \alpha_2 - \tan \alpha_1$ and that $\tan \alpha$ is approximately equal to $\tan \beta$, (1)–(4) yield

$$\delta_i = \frac{|N_i|_2(\tan \alpha_2 - \tan \alpha_1)}{(\tan \alpha_2 + \tan \alpha_1)(\tan \alpha_2 - \tan \alpha_0)} \qquad (8)$$

where the subscripts 1 and 2 refer to the values at the base and the top of the ionospheric layer.

Setting the derivative of (8) with respect to α_0 equal to zero results in a lengthy expression which can be greatly simplified by correctly assuming that the required value of α_0 is small so that

$$\sin 2\alpha_2 \pm \sin 2\alpha_1 \approx 2 \sin (\alpha_2 \pm \alpha_1)$$

and

$$\sin 2\alpha_2 - \sin 2\alpha_0 \approx 2 \sin (\alpha_2 - \alpha_0).$$

The value of α_0, which results in the maximum value of δ_i, turns out to be

$$\sin \alpha_0 \approx [(\rho^2 - a^2)/(4\rho^2 - a^2)]^{1/2} \qquad (9)$$

where

a = Earth's radius
ρ = distance from the Earth's center to the base of the layer.

From (9), it is seen that the value of α_0 for maximum δ_i is roughly proportional to the square root of the height of the bottom edge of the layer. For typical F-layer parameters, one would expect the maximum error to occur for values of α_0 between 100 and 200 mr.

The expressions derived so far were based on very simplified models of the troposphere and ionosphere, since otherwise the equations would not have been trackable. It will be interesting to plot δ vs α_0 for the case of more realistic models of the earth's atmosphere. For the case of the tropospheric refraction, the values of δ_t are based on a typical radiosonde data. To compute the ionospheric refraction, we picked a model which is analytically defined by

$$N_e/N_m = 1 - (1 - \sigma)^2 \qquad 0 \le \sigma \le 1$$
$$= \operatorname{sech} \tfrac{1}{4}\pi(\sigma - 1) \qquad 1 \le \sigma \le \infty \qquad (10)$$

where

N_m = the maximum electron density,
$\sigma = (h - h_0)/y_m$,
h = height above the ground,
h_0 = height of the base of the layer,
$y_m = h_m - h_0$,
= half-thickness of the layer,
h_m = height of the maximum electron density.

The lower portion of this distribution is parabolic, while the upper one resembles the Chapman distribution but it is a little thicker and the total electron content above the maximum is three times greater than below it.[2]

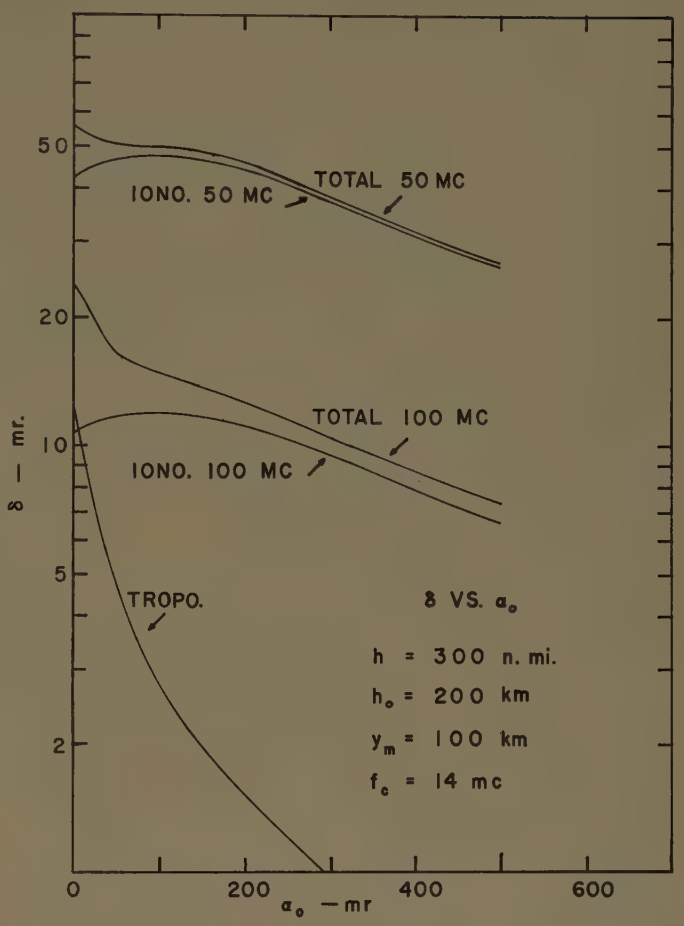

Fig. 2.

Fig. 2 is the plot of δ_t, δ_i, and δ vs α_0. The ionospheric parameters are: $h_0 = 200$ km, $y_m = 100$ km, critical frequencies of the layer = 14 mc, the signal frequency is 50 and 100 mc, and the target height is 300 nautical miles. The behavior of δ_i vs α_0 is as it might have been anticipated from the previous discussion. The elevation angle error increases with α_0, reaches a maximum value for α_0 around 100 mr, and then gradually falls off. The total δ decreases all the time, but, at 50 mc, there is a pronounced shoulder when the ionospheric refraction takes over.

In general, it appears that, for very low angles of elevation, the tropospheric refraction will predominate.

Acknowledgment

The authors wish to acknowledge the assistance of the various staff members of Smyth Research Associates. In particular, we are indebted to L. A. Morgan, H. D. Loucks, and L. J. Anderson for the expression relating the angle of elevation with the maximum ionospheric refractive error.

[2] J. B. Evans, *Proc. Phys. Soc. (London) B*, vol. 69, p. 953; 1956.

Modified Luneberg Lens for Defocused Source*

DAVID K. CHENG†

Summary—**A spherical Luneberg lens has the property of focusing the rays from a point source on the surface of the lens into a collimated beam on the diametrically opposite side of the lens. In microwave applications a point source on the surface of the lens is usually not obtained. Curves are given for the required index of refraction for a modified Luneberg lens which possesses the same collimating property for a point source located at a small distance outside of the lens.**

A SPHERICAL Luneberg lens having an index of refraction obeying the relation[1]

$$n(r) = \sqrt{2 - r^2} \tag{1}$$

where r is the normalized radial dimension, $0 \leq r \leq 1$, has the well-known property of focusing the rays from a point source on the surface of the lens into a collimated beam on the diametrically opposite side of the lens. Because of its adaptability to wide-angle scan with no change in the diffraction pattern, the Luneberg lens is of considerable interest to antenna engineers. A number of modifications to the Luneberg lens have been proposed.[2–5]

In microwave applications a point source on the surface of a lens is difficult to obtain. An electromagnetic horn, for example, does not have its phase center in its aperture plane. It has been found[6] that the E-plane phase center of an E-plane sectoral horn and the H-plane phase center of an H-plane sectoral horn usually lie at the back of the aperture plane (inside the horn). This effect is more pronounced for long horns with large flare angles. We are then often faced with a situation where the effective point source is located *outside* of a Luneberg lens even when the mouth of the horn touches the lens surface. A Luneberg lens with a defocused source gives rise to aperture phase errors.[7] This paper furnishes two curves showing how the index of refraction function as given in (1) should be modified in order that an effective point source outside of the lens would yield a plane wavefront on the diametrically opposite side of the lens.

Following Luneberg's notation, we write the index of refraction function n in the following form:

$$n = \epsilon^{\omega(nr,a)} \tag{2}$$

where

$$\omega(nr, a) = \frac{1}{\pi}\int_{nr}^{1} \frac{\sin^{-1}(t/a)}{\sqrt{t^2 - (nr)^2}}\, dt. \tag{3}$$

a is the normalized distance of the point source from the center of the spherical lens. For the true Luneberg case, $a = 1$ (source on lens surface), and

$$\omega(nr, 1) = \frac{1}{\pi}\int_{nr}^{1} \frac{\sin^{-1} t}{\sqrt{t^2 - (nr)^2}}\, dt = \frac{1}{2}\ln\left[1 + \sqrt{1 - (nr)^2}\right]. \tag{4}$$

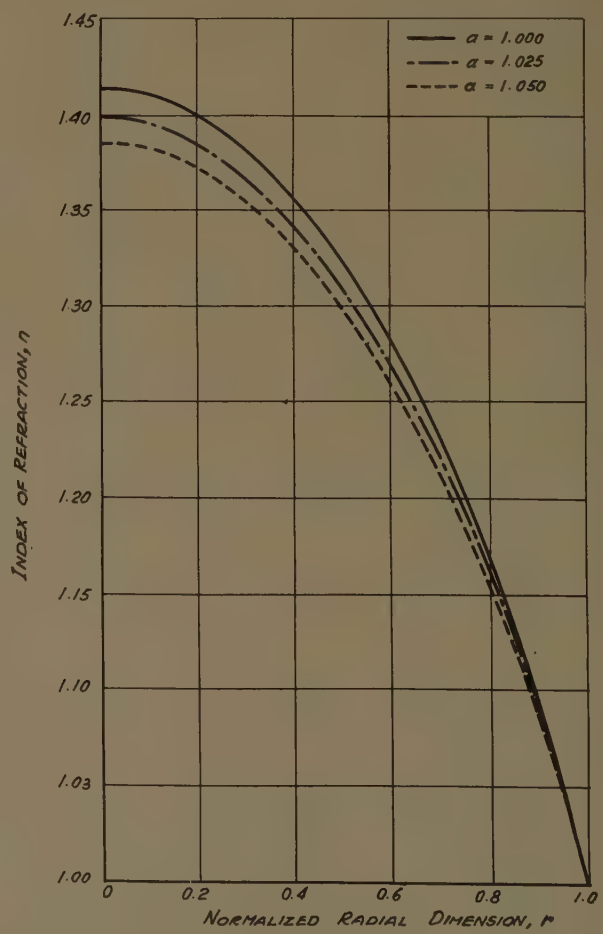

Fig. 1—Modified indices of refraction for defocused Luneberg lenses

* Manuscript received by the PGAP, July 10, 1959.
† Elec. Engrg. Dept., Syracuse University, Syracuse, N. Y.

[1] R. K. Luneberg, "The Mathematical Theory of Optics" (mimeographed notes), Brown University, Providence, R. I., sec. 29; 1944.
[2] A. F. Kay, "Spherically symmetric lenses," IRE TRANS. ON ANTENNAS AND PROPAGATION, vol. AP-7, pp. 32–38; January, 1959.
[3] J. E. Eaton, "On spherically symmetric lenses," IRE TRANS. ON ANTENNAS AND PROPAGATION, vol. AP-4, p. 66; December, 1952.
[4] J. Brown, "Microwave wide-angle scanner," *Wireless Eng.*, vol. 30, pp. 250–255; October, 1953.
[5] A. S. Gutman, "Modified Luneberg lens," *J. Appl. Phys.*, vol. 25, pp. 855–859; July, 1954.
[6] Y. Y. Hu, "Phase Centers of Electromagnetic Horns," Res. Inst., Syracuse University, Syracuse, N. Y. Final Rept. on Contract No. AF 30(602)-926 with Rome Air Dev. Ctr.; September 30, 1954.
[7] D. K. Cheng and P. A. Grusas, "Defocus characteristics of the Luneberg lens," *Proc. NEC*, vol. 12, pp. 898–904; 1956.

Substitution of (4) in (2) yields directly the relation given in (1).

When the source is outside of the lens, $a=1+\epsilon$, $\epsilon>0$, we write (3) as follows:

$$\omega(nr,a)=\frac{1}{\pi}\int_{nr}^{a}\frac{\sin^{-1}(t/a)}{\sqrt{t^2-(nr)^2}}dt-\frac{1}{\pi}\int_{1}^{a}\frac{\sin^{-1}(t/a)}{\sqrt{t^2-(nr)^2}}dt$$

$$=\frac{1}{2}\ln\left[1+\sqrt{1-(nr/a)^2}\right]$$

$$-\frac{1}{\pi}\int_{1}^{a}\frac{\sin^{-1}(t/a)}{\sqrt{t^2-(nr)^2}}dt. \qquad (5)$$

Substitution of (5) in (2) gives

$$n=\left[1+\sqrt{1-(nr/a)^2}\right]^{1/2}$$

$$\exp\left[-\frac{1}{\pi}\int_{1}^{a}\frac{\sin^{-1}(t/a)}{\sqrt{t^2-(nr)^2}}dt\right]. \qquad (6)$$

Unfortunately the integral appearing in the exponent of (6) is not quite of the Abel type and its evaluation in a closed form has not been accomplished. We note that $r=1$ and $n(1)=1$ satisfy (6). There is then no discontinuity in the index of refraction at the surface of the lens.

Eq. (6) has been computed by an approximate numerical method for two values of a, namely, 1) $a=1.025$, or $\epsilon=0.025$; and 2) $a=1.05$, or $\epsilon=0.05$. n vs r curves are plotted in Fig. 1. It is seen that the n values required for Luneberg lenses with defocused sources on the outside are lower than the corresponding values for on-surface excitation.

Abstracts of Papers from the IRE-URSI Joint Fall Meeting Held October 19-21, 1959—San Diego, Calif.

Precise Corrections for Atmospheric Refraction to Radar and Optical Observations of Position*—P. B. Taylor and N. A. Engler, *University of Dayton Res. Inst., Dayton, Ohio*—Tables have been prepared of the corrections for refraction to be applied to radar observations of position. The tables were computed on a Datatron but are presented as graphs.

The type of atmosphere considered is one with smooth exponential variation of the index of refraction with height. A full range of surface indexes of refraction and index gradients is covered for both radar and optical frequencies. The geometry is that of the curved earth. The standard atmosphere lies within the range covered.

Radar range correction and angle of elevation correction are charted as functions of observed radar range and observed angle of elevation for a set of atmospheres all belonging to a common functional type but with varied parameters. The index function is such that unit index is properly approached at high altitudes from every surface condition.

The charts place special emphasis on low angles of elevation, as many previous correction formulas become faulty or uncertain in this range.

An over-all accuracy of one part in 10^6 in range and sine of elevation angle was aimed at in the computation. Owing to necessary compression in the graphical presentation, this may not be attainable in all cases. For best precision, observations may be fed into a Datatron provided with the same program as that prepared for the present tables and corrections read out at full precision.

* The research reported in this paper has been sponsored by the Aerial Reconnaissance Lab., Wright Air Development Center, Air Res. and Dev. Command under Contract AF33(616)-5438.

Comparison of Experimental with Computed Tropospheric Refraction*—W. L. Anderson and R. J. Rainey, *Electrical Engineering Dept., University of New Mexico, Albuquerque*, and N. J. Beyers, *Missile Geophysics Div., White Sands Missile Range, N. Mex.*—Limits of applicability of ray tracing in computing tropospheric refraction at White Sands Missile Range have been further explored. 286 comparisons were made, all for a path from radar to fixed beacon of about 45 miles and an elevation angle of 18.06 mr. A horizontally stratified atmosphere was assumed. Refractive index profiles were prepared from a variety of weather data, and classified "A," "B," "C," or "R," in descending order of reliability prior to ray-tracing calculations. Computed bending correlated favorably with that observed.

Angle observations were made with an FPS-16 *C*-band radar having a quoted instrumental precision of ± 0.10 mr rms. Angle reading varied from 18.36 to 20.54 mr, with mean of 19.02 mr and standard deviation 0.42 mr.

The rms deviation of computed from experimental angles ranges from 0.28 to 0.42 mr for different classes of weather data. Excepting one of the classifications, there is direct correlation between quality of weather data and predictability of bending. Statistically, it is found that predictability decreases as the observed angle deviates more and more from the mean. Finally, it is concluded that within the limits of this experiment, ray-tracing methods can provide significant correction to elevation angle errors, and that, in general, predictability of bending is improved by improving the meteorological data.

* This work was performed under Contract No. DA-29-040-ORD-1238.

The Limit of Spatial Resolution of Refractometer Cavities—W. J. Hartman, *National Bureau of Standards, Boulder, Colo.*—Filter factors that determine an upper limit for the wave numbers for which refractometer measurements can be used to calculate the spectrum of refractivity are derived in this paper, based on the assumption that refractometers measure a weighted average of the refractive index in a volume of air surrounding the center of the refractometer cavity. Two models are used assuming the weighting function has spherical symmetry around the center, and one model is used assuming the function has cylindrical symmetry. All models result in a simple mathematical form which should be easy to use in further theoretical developments.

Further Analysis of Radar Terrain Return*—L. M. Spetner and I. Katz, *Applied Physics Lab., The Johns Hopkins University, Silver Springs, Md.*—The land and sea surface models used in our previous treatment of radar return† have been extended. The independent-scatterer model for land surfaces is discussed in more detail. An attempt is made to obtain a theoretical formulation which will explain in a unified fashion the grazing-angle, wavelength, and polarization dependence of land and sea clutter.

* This work was supported by the Bureau of Ordnance, Dept. of the Navy, under Contract NOrd 7386.

† Radar Return Symp., University of New Mexico, Albuquerque, May 11, 12; 1959.

Statistical Description of Terrain—R. E. Wilkerson and P. L. Rice, *National Bureau of Standards, Boulder, Colo.*—For some radio propagation studies, it is convenient to have a statistical description of average rough earth terrain profile characteristics. As a particular example, we may want to know what percentage of radio horizon elevation angles exceed one degree in typical terrain. This paper proposes a statistical description of terrain which makes such estimates possible.

Terrain heights along a radial originating at an antenna location are assumed normally distributed above and below their average value, and a certain amount of correlation of these heights is assumed for short distances along a terrain profile. A straight radio ray is drawn from the antenna, making an arbitrary angle with the horizontal. It is desired to find the probability that terrain along a radial lies entirely below this ray.

In deriving formulas presented here, an average flat earth and straight rays will be assumed. The results, however, may be generalized for any shape of earth or any type of ray.

Some Magnetoionic Phenomena of the Arctic E Region—J. W. Wright, *National Bureau of Standards, Boulder, Colo.*—Some unique *E* region phenomena observed on vertical soundings at Thule, Greenland, are interpreted as the result of magnetoionic coupling. The phenomena appear to offer opportunities for the observation of the reentrant portion (valley) above the *E* layer, and for the measurement of electron densities and collision frequencies therein.

On the Semi-Diurnal Lunar Variations of Ionospheric Layers—N. N. Rao and H. M. Swarm, *Dept. of Electrical Engineering, University of Washington, Seattle, Wash.*—A brief up-to-date review of the ionospheric "dynamo theory" of magnetic variations is presented. Evidence has been collected in support of the location of the dynamo region at 100–110 km height. From the revised dynamo theory of Baker and Martyn, and the ionospheric current systems deduced by Chapman and Bartels, vertical ionization drift velocities due to the semi-diurnal lunar tide are calculated for different ionospheric heights. It is found that there is a large height gradient of vertical drift velocity at *E*-region heights, contrary to earlier assumptions. The effect of this vertical drift on both the daytime and the nocturnal ionization of the *E* and F_2 layers is investigated. The theoretical results are compared with the available data of the harmonic coefficients of the semi-diurnal lunar oscillations of the ionospheric layers.

High-Resolution Pulse Measurements of Oblique Radio Reflections from Meteor Trails at 41 MC—R. J. Carpenter and G. R. Ochs, *National Bureau of Standards, Boulder Colo.*—Studies of multiple path radio signals received by reflection from ionized meteor trails have been made over a 1295-km path from Long Branch, Ill., to Boulder, Colo. Pulses of 3 μsec with a peak power of about 800 kw are employed. Most single meteor signals show no detectable multipath. Maximum time distortions observed cause spreading of the received pulse over a 10-μsec range with several components visible. Simultaneous occurrence of several meteor signals can result in multiple paths differing in time by as much as 500 μsec, although shorter delays are more probable.

Analysis of Meteor Echoes at 412 MC Received Over an 830-Mile Path.*—M.

* Work supported by the U. S. Air Force.

Loewenthal, P. A. Duffy, J. C. James, and H. G. Root, *Lincoln Laboratory, M.I.T., Bedford, Mass.*—More than a year of data has been obtained using instrumentation previously described at these meetings. A 48-kw signal is transmitted from the M.I.T. field station at Round Hill, Mass., and received at Elberton, Ga., as a result of scatter from meteor trails. Multiple feeds in the fixed 60-foot parabolic dishes permit the signal to be transmitted alternately from either side of the great-circle path and received on either side. An eight-digit coded representation of each meteor echo scaled from the paper tape output of the 100-cps bandwidth receiving systems is put on IBM punched cards. Preserved in this process for each meteor is some information regarding its amplitude, duration and time separation from the last occurring meteor on the same channel as well as an indication of the side of the path on which the echo was received and the time and date of occurrence. Time is measured within 15-minute intervals corresponding to the transmitter beam switching rate.

The IBM 709 Computer is used to analyze for each day the statistics of the echoes—numbers vs time, amplitude, duration, joint amplitude-duration and spacing—and places this information on a second set of punched cards which are then used to plot the data. The combined or average statistics, with appropriate weighting for periods of no transmission, for any number of days are obtained using these daily output cards and a second computer program. The results are compared with current theories on these statistics.

The Effects of Normal Cosmic Radiation on the *D*-Region of the Ionosphere—W. F. Moler, *U. S. Navy Electronics Lab., San Diego, Calif.*—During the last decade, several investigators have suggested that certain anomalous VLF radio measurements can be explained by the existence of a two-layered D region. It is shown that, for large solar zenith angles and at middle and high latitudes, normal cosmic radiation produces a second D layer below the layer produced by L_α ionization of NO. It is further shown that an appreciable electron density is maintained at night below 100 km by cosmic radiation. A series of electron density profiles shows the combined effect of cosmic ray and photoionization processes as a function of solar zenith angle and geomagnetic latitude.

Ionospheric Absorption Investigations at Hawaii and Johnston Island*—A. Fredriksen and R. B. Dyce, *Stanford Res. Inst., Menlo Park, Calif.*—In the examination of riometer records taken at Hawaii and Johnston Island, uncorrelated absorption was frequently observed on 27.5 mc in the time interval from 2000 to 0300. Qualitatively, the hourly absorption never exceeds 3.5 dbm and the variations in absorption are of the order of an hour.

The possible dependence of the absorption on the planetary magnetic index, which is supposedly a measure of the solar corpuscular streams impinging on the earth, was investigated by a scatter plot of three-hour average absorption vs the planetary magnetic index, K_P. There seems to be no correlation.

A plot of average hourly absorption vs the hour shows a maximum in absorption for both Hawaii and Johnston Island at 2300; that for Johnston Island was twice as great as that for Hawaii. This may indicate a latitude dependence for the absorption: Johnston Island is 9° south of Hawaii in geomagnetic latitude.

The possible existence of a correlation between absorption recorded at Hawaii and Johnston Island (which are 900 miles apart) was investigated by plotting a scatter diagram of hourly absorption on Hawaii vs the same hour absorption at Johnston Island. No correlation was observed, indicating that the mechanism causing the variations in absorption has a structure less than 900 miles in extent.

The Current-Jet Hypothesis for the Generation of Whistlers—W. C. Hoffman, *Hughes Res. Lab., Culver City, Calif.*—It is postulated that some types of whistler signals, for instance "long trains," are generated by the interaction of a sferic and a pinched accelerated discharge emitted upward from the top of the thundercloud at about the time of a just-preceding main ground-to-cloud stroke. Slow tails which endure for times of the order of several hundred milliseconds, or multiple discharges occurring over a like period, can accelerate the electrons in such a current jet to velocities of the order of 0.1 that of light. Thus the velocities are often of the right order for Gallet-Helliwell travelling-wave amplification to occur. A further acceleration takes place in the upper atmosphere due to the "magnetic mirror" effect, so that such accelerated current jets would also contribute to the inner Van Allen radiation belt. The apparent duct nature of whistler propagation thus corresponds to the pinching of the upward discharge, and the traveling-wave interaction explains such phenomena as long trains and such whistler anomalies as an initial increase of field strength with order of the echo followed by a rapid drop-off.

Such accelerated upward discharges of penetrating electrons have been postulated in other connections by C. R. T. Wilson, Appleton and Chapman, Watson-Watt, W. L. Taylor and others, and have been observed by several investigators* and visually by the author. The association between whistlers and multiple discharges has been noted by Norinder. G. C. Rumi's radar observations at 27.85 mc of columns of ionization moving upward in the stratosphere at speeds of up to 200 km perhaps bear most directly on the present analysis. The evidence of the current-jet hypothesis is reviewed and a crucial experiment is outlined.

A Four-Year Summary of Whistler Activity at Washington, D. C.—Harold E. Dinger, *NRL, Washington, D. C.*—Whistler and dawn chorus activity as recorded at Washington, D. C. during the period of July 1, 1955 to June 30, 1959 has been tabulated and summarized. Of the 1461 days considered in this analysis, 94 per cent had activity of some form. The equivalent of approximately 500 1800-foot reels of magnetic recording tape (1,800,000 feet of track) were analyzed. The last two years of the period covered was as part of the IGY/IGC Ionospheric Physics Program.

A Technique for Finding the Direction of Arrival of Whistlers—J. M. Watts, *National Bureau of Standards, Boulder, Colo.* and J. H. Crary, *Stanford University, Stanford, Calif.*—The results of preliminary experiments using rotating goniometers have shown that some whistlers arrive from an apparently small angular source, thereby allowing the null technique to be used in determining the direction of arrival. The use of the sound spectrograph in detecting and measuring the null pattern is shown on sample records. The possible explanations for the absence of nulls for some whistlers are discussed, together with the types of error to be expected.

The E-ϕ Azimuthal Detection System for Transient Signals—G. Hefley, R. F. Linfield and T. L. Davis, *National Bureau of Standards, Boulder, Colo.*—A new system for direction-finding on transient signals such as sferics in the VLF portion of the spectrum has been developed and tested at the National Bureau of Standards, Boulder Laboratories. The scheme has been designated E-ϕ (Ephi) because the bearing of the transient signal is determined from the relative phase (ϕ) of the vertical electrical field (E) received at spaced antennas. The basic scheme minimizes siting and polarization errors.

The system is particularly suited to sferic studies. Individual sferics whose field strength is as low as 1 to 10 mv/m can be resolved. Direction of arrival of all signals can be indicated. Those from specified azimuths can also be selected for recording and further analysis.

A minimum of three antennas must be used to resolve directional ambiguity. The antennas are closely spaced, preferably in the range of $\frac{1}{8}$ to $\frac{1}{10}$ wavelength. The relative time of arrival or phase of a signal at the antennas depends on the geometric configuration of the antennas and the direction of the signal source. In general, the optimum configuration for three antennas is an equilateral triangle. In this case, the sides of the triangle define the baselines of three hyperbolic grids with mutual azimuthal spacing of 120°.

By the appropriate use of phase detectors, delay lines, coincidence circuits and gates, the signals received in preset sectors generate a directional code. This code is ideally suited for subsequent logical circuitry designed to select specific data. Selection techniques involving the intrinsic characteristics of the signal can be conveniently incorporated in this scheme. Within practical instrumentation limits any number of sectors of variable widths can be operated simultaneously and each can be conveniently rotated about the azimuth circle.

An experimental, tri-antenna system was constructed and tested to demonstrate the feasibility of the basic principle. Sector widths of 6° were achieved with two-mile baselines. With four-mile baselines and some refinement in instrumentation, it is expected that 1° sectors can be obtained. Installation

* This work was supported by USAF Cambridge Res. Center of the Air Res. and Dev. Command under Contract AF 19 (604)-3462.

* Chalmers, "Atmospheric Electricity," Pergamon Press, New York, N. Y., sec. 300; 1957.

of such a system is now in progress near Boulder.

Quasi-Static Electric Field Studies of Thunderstorms—H. L. Jones, F. J. Boudreaux, and W. D. Woodruff, *Oklahoma State University, Stillwater, Okla.*—During the severe storm season of 1959, studies were made of the quasi-static electric fields of thunderstorms as these structures passed in the vicinity of the Atmospherics Laboratory. Recordings were made of both the rapid and the slow variations of the electric field and these variations were correlated with the wave-forms and the 10-kc and 150-kc directional pulses.

These studies were made in order to obtain a better understanding of the rapid field variations peculiar to cloud-to-cloud, cloud-to-ground, and intracloud discharges. It is believed that the techniques developed this year will lead to additional information on the tornado oscillator that is peculiar to thunderstorm structures during the tornado and pretornado stages of development. Unfortunately, there were no tornado oscillators in the vicinity of the Atmospherics Laboratory during the severe storm season of 1959.

Sferic Measurements at Three Arctic Stations—September, 1958 through March, 1959*—A. L. Whitson, *Radio and Weather Sciences Lab., Stanford Res. Inst., Menlo Park, Calif.* — From September, 1958 through March, 1959, SRI operated a three-station sferic net at Fairbanks, Alaska; Thule, Greenland; and St. Johns, Newfoundland. Three forms of data were collected: 1) broadband, 3- to 30-kc sferic waveforms and instantaneous direction of arrival were recorded on 35-mm film; 2) omnidirectional sferic rates exceeding fixed field strengths in quarter GMT days were recorded on mechanical counters; and 3) rms noise level in a 100-cycle bandwidth from a 12- to 30-kc slow-scanning receiver was recorded on a strip chart. These data have been processed to obtain monthly and diurnal variations of sferic rates, distributions of amplitude, and direction of arrival and rms atmospheric noise level from 12 to 30 kc.

Typical examples of the above data representing sferic activity in the entire northern hemisphere will be presented. Correlation of data collected at the three stations will be discussed to show the variations in received sferic activity as a function of measurement location.

* This work was sponsored by the USAF Cambridge Res. Center on Contract AF 19(604)-2409.

A Frequency Domain Theory of Parametric Amplification—B. J. Leon, *Hughes Res. Labs., Culver City, Calif.*—A linear parametric amplifier consists of one or more periodically time-variant reactances imbedded in a linear, passive , time-invariant network. In this report, a general analysis for lumped parameter parametric amplifiers is presented. For these circuits, the frequency domain equations, which define the voltages and currents as functions of complex frequency, are linear difference equations with rational coefficients. By taking a function theoretical approach to these equations, we see that the voltages and currents are well defined and can be computed exactly in the entire complex plane. Thus, these networks can be analyzed without the *a priori* assumption that the voltages and currents are nonzero at only two or three frequencies.

The case of one sinusoidally varying capacitance in an arbitrary time-invariant network is discussed in detail. From the properties of the exact solutions to the difference equation we are able to prove the following.

1) A sufficient condition for gain is the presence of a resonant circuit at the idler frequency. A circuit with a passive admittance zero at the idler frequency will have a negative over-all input resistance at signal frequency, regardless of the passive circuit admittance at the signal frequency.

2) For high frequencies, the response goes as $e^{-\mu\omega}$, where μ depends only on the percent variation in the variable parameter.

Further Theory of Group Codes—D. Slepian, *Bell Telephone Labs., Inc., Murray Hill, N. J.*—This paper presents a variety of results concerning group codes. An equivalence relation for codes is discussed. A natural dual for a code and a natural sum and product for two codes is defined. An arithmetic of equivalence classes is then developed. Irreducible codes are defined and it is proved that up to equivalence any code can be written in a unique way as a sum of irreducible codes. It is shown that the search for best codes can be limited to irreducible codes. Enumeration formulas for the various types of codes are given. Assorted theorems concerning error probabilities are presented.

A General Method of Constructing Lossless Error-Correction Codes for a Nonprime Base—R. T. Chien, *IBM Res. Lab., Yorktown Heights, N. Y.*—This paper describes a general method of constructing lossless error-correcting codes when the base is some power of a prime number (p^n). Such codes have been considered by Golay* and Cocke.† Cocke's method is limited in practical value due to the fact that all the arithmetic operations have to be performed in the Galois Fields of p^n. Realization of circuits for such operations are inevitably more complicated. Golay has tried to use modulo p arithmetic. However, his results are obtained with trial and error for a number of special cases only.

This paper presents a complete solution that is simple and practical. Modulo p arithmetic is used so that realization of encoding and decoding networks is straightforward. All codes are generated from a master iteration matrix in a simple manner, and the general master iteration matrix is written in closed form for all cases. A rigorous proof is also given utilizing the theory of finite fields.

* M. J. E. Golay, "Notes on the penny-weighing problem, lossless symbol coding with nonprimes, etc.," IRE TRANS. ON INFORMATION THEORY, vol. IT-4, pp. 103–109; September, 1958.

† J. Cocke, "Lossless symbol coding with nonprimes," IRE TRANS. ON INFORMATION THEORY, vol. IT-5, pp. 33–34; March, 1959.

A Generalization of the Sampling Theorem*—D. A. Linden† and N. M. Abramson, *Stanford Electronics Lab., Stanford, Calif.*—The sampling theorem for bandlimited functions allows one to reconstruct exactly a function containing no frequencies higher than W cycles per second, given the values of the function at equispaced sampling points $\frac{1}{2}W$ seconds apart. This theorem is generalized to allow reconstruction, given the values of the function and its first R derivatives at equispaced sampling points, $(R+1)/2W$ seconds apart. For large R, the R-derivative expansion approaches a Taylor's series weighted by a Gaussian density about each sample point.

* The work described in this paper was supported by the ONR, under Contract Nonr 225(44), NR 375 865, and by the National Science Foundation, under NSF Fellowship No. 28215.

† National Science Foundation Fellow.

The Complex Zeros of Bandlimited Gaussian Noise—B. F. Logan, *Bell Telephone Labs., Murray Hill, N. J.*—A real sample function $n(t)$ of filtered Gaussian noise, bandlimited to $(-W, W)$, with probability 1 admits of an analytic continuation $n(\tau)$, $\tau=t+i\xi$, which is regular for all finite τ; *i.e.*, $n(\tau)$ is, with probability 1, an entire function. It is the complex zeros of $n(\tau)$ which account for the ripples of $n(t)$ observed between zero crossings. In this paper, complex variable methods are used to determine the probability of zero of $n(\tau)$ occurring in the elements of area $dtd\xi$. The expected rate $\nu(\xi)$ of zeros of $n(\tau)$ occurring in the strip $|\operatorname{Im}(\tau)| > \xi$ is obtained by determining the statistical average of a contour integral. The limit of $\nu(\xi)$ as $\xi \to 0$ gives the expected rate of zero crossings of $n(t)$ and is in agreement with Rice's well-known result obtained by real variable methods. As $\xi \to \infty$, $\nu(\xi) \to 2W$, which is in accord with the theory of entire functions of exponential type $2\pi W$. The rate $\nu(\xi)$ and density $\tau'(\xi)$ are calculated for Gaussian noise having a rectangular-shaped spectrum. Of primary interest is the density function, which has the appearance of a pulse with an effective duration inversely proportional to the bandwidth of the spectrum and a rise time inversely proportional to the center frequency of the spectrum.

Intercomparison of Microwave Bolometer Mounts—G. F. Engen, *National Bureau of Standards, Boulder, Colo.*—Given a bolometer mount whose parameters have been determined in some manner such that it may be regarded as a standard of power measurement, the problem of transferring this calibration to other bolometer mounts is closely related in practical importance to that of obtaining the original calibration. A prime consideration in this transfer of calibration procedure is the necessity of properly accounting for the functional dependence of the resultant calibration upon the impedance (or reflection coefficient) of the bolometer mount being calibrated.

Recent developments in reflectometer

techniques* form the basis for a transfer standard which, when properly adjusted and calibrated, permits a direct determination of the incident and reflected powers for any termination, thus effecting a simplification in the calibration procedure.

* G. F. Engen and R. W. Beatty, "Microwave reflectometer techniques," IRE TRANS. ON MICROWAVE THEORY AND TECHNIQUES, vol. MTT-7, pp. 351–355; July, 1959.

As a special report to Commission I, the results of several international intercomparisons of bolometer mounts will be briefly reviewed.

Mismatch Errors in Cascade-Connected Variable Attenuators—G. E. Shafer and A. Y. Rumfelt, *National Bureau of Standards, Boulder, Colo.*—The treatment of mismatch errors is extended to cover variable attenuators cascade-connected in a system which is not free from reflections. The method of analysis is applicable to any number of cascaded attenuators, but only the analysis of two and three variable attenuators in cascade is presented. Graphs are given to aid in estimating the limits of mismatch error.

In an example, which is considered representative of rigid rectangular waveguide systems, the limits of error are: for two attenuators in cascade, 0.19 db in a 3-db measurement, and 0.17 db in a 40-db measurement; and for three attenuators in cascade, 0.25 db in a 40-db measurement, and 0.23 db in a 75-db measurement.

Atmospheric Turbulence as a Factor in Microwave Standard Frequency Broadcast Systems—M. C. Thompson, Jr., H. B. Janes, and A. W. Kirkpatrick, *National Bureau of Standards, Boulder, Colo.*—Under certain circumstances, there may be numerous advantages of using VHF, UHF, or microwave systems for providing standard frequencies transmission services. Whereas with the HF distribution systems the limitation of accuracy of the signals as received is set by the behavior of the ionosphere, in the higher frequency systems the corresponding limit is imposed by atmsospheric turbulence. Variations in radio refractive index resulting from this turbulence produce variations in transit time over any given path and corresponding phase/frequency modulation on the signal as received. Several series of measurements have been conducted to evaluate the nature of these effects. Data have been obtained from paths in Colorado and the island of Maui, Hawaii, also using different path lengths, antenna sizes, frequencies and polarizations. The results are presented in terms of the power density spectra of the frequency modulation observed.

The effects of weather conditions where observed are illustrated and discussed as well as some general practical considerations influencing choice of operating frequencies for such systems.

An *X*-Band Intensity Recording Receiver with Extremely Narrow Bandwidth—R. W. Hubbard and J. V. Cateora, *National Bureau of Standards, Boulder, Colo.*—This paper describes a specialized field intensity recording receiver for operation of the *X*-band portion of the radio spectrum. It has been designed and developed at the Central Radio Propagation Laboratory, National Bureau of Standards, Boulder, Colo., to augment the program of basic research into radio propagation through the lower atmosphere.

A design criterion of extremely narrow bandwidth was established and fulfilled in the development of this receiver to provide a maximum of signal-to-noise ratio. Crystal filters and a double heterodyne technique are employed to provide an over-all bandwidth of 5×10^{-7} per cent, or 50 cps at the 6-db points. This requires extreme stability of the first local oscillator klystron frequency which is achieved in a unique manner and described in the paper.

Another unique feature of the receiver is the means by which the recorded spectrum has been divided within the receiver, providing essentially a constant signal-to-noise ratio over the long-term variations in received signal. This technique lends itself nicely to expanded scale recordings of the fast fluctuations.

The design has utilized gain-stable techniques throughout, and automatic monitoring circuits and plug-in modular construction. These features, together with an automatic self-calibrating feature, render the receiver nearly ideal for remote unattended operation.

A Radio-Frequency Voltage Standard for Receiver Calibration in the Frequency Range of From 2 to 1000 mc*—G. U. Sorger, A. L. Hedrich, and B. O. Weinschel, *Weinschel Engineering, Kensington, Md.*—An accurate and convenient method of producing very small voltages is that employed in the common dc potentiometer where a voltage in the order of one volt is produced to a high accuracy, and then smaller voltages produced by relying on a precise voltage divider.

A scheme quite analogous to this is described wherein a thermistor through-mount and a precise power bridge serve to establish a voltage level of either 1.0 or 0.1 volt across a coaxial line. Precise *L*-pad voltage dividers having division ratios of 10:1, 100:1, 1000:1 and 10,000:1 are used to reduce the input voltage, in decade steps, down to 10 μv.

The thermistor through-mount establishes the 1.0 or 0.1 volt level to an accuracy of +2 per cent.

The four *L*-pad voltage dividers each have input impedances of 50 ohms and show an input VSWR not greater than 1.02 up to 1000 mc when terminated in 50 ohms, while the output impedance is very small, thus essentially producing a constant voltage source. They are calibrated for voltage division to the following accuracies:

10:1 pad—0.6 per cent
100:1 pad—1.2 per cent
1000:1 pad—1.8 per cent
10,000:1 pad—2.3 per cent.

* This work was done under Contract DA 36-039 SC64431 with the Signal Corps Engineering Labs.

Combining all systems errors, the maximum probable error occurs at 10 μv and 1000 mc and is about 3 per cent. Since the output plane of the voltage divider is only 9 mm away from the output resistor (about 0.03 wavelength at 1000 mc), the output voltage change with RF frequency for different load impedances is negligible.

An Improved Microwave VSWR Measurement System for Coaxial Systems Using Type *N* Connectors—R. W. Beatty and W. J. Anson, *National Bureau of Standards, Boulder, Colo.*—The accuracy of microwave VSWR measurements in coaxial systems using type *N* connectors is limited by a number of factors such as the residual VSWR of the measuring system and variance in mechanical dimensions and construction of the connectors.

An improvement in accuracy may be obtained by standardizing the coaxial line and connector of the measuring system and the location of a terminal surface in the coaxial line at which the VSWR is to be determined. Further improvement in accuracy is obtained by minimizing discontinuities between this coaxial line and the type *N* connector, and by employing a modified reflectometer technique with an appropriate impedance standard.

Radar Investigation of Field-Aligned Ionization Irregularities Located Within the Ionosphere at the Magnetic Equator—R. D. Egan, *Radio Propagation Lab., Stanford University, Stanford, Calif.*—As a part of the International Geophysical Year program in ionospheric physics, a three-frequency, swept-azimuth backscatter sounder was installed at Huancayo, Peru, in cooperation with the Institute Geofísico de Huancayo. During the routine operation of the sounder, a new type of echo was observed* during the local daytime hours on over 90 per cent of the days. The basic Booker† theory for scattering from nonisotropic, field-aligned irregularities, with suitable modifications for the equatorial geometry, has been used to show that these observed echoes are, in fact, produced by the presence of field-aligned ionization irregularities within the *E*- and *F*-regions of the ionosphere.

By means of the pulse observations, it has been possible to determine the size and extent of the scattering region. The *E*-region echoes are observed to begin at heights near 100 km and normally extend to about 150 km, but at times they extend up into the *F*-region at 200 km or more. The *F*-region echoes have not been observed as frequently, but appear to originate at heights near 300 to 350 km around local noon.

Observations of the strength of the echo have made it possible to estimate the magnitude of the mean square fractional deviation of the electron density $\overline{(\Delta N/N)^2}$ as between 10^{-3} and 10^{-5}. This oblique incidence echo is apparently closely related to the equatorial electrojet and is probably an

* A. M. Peterson, R. D. Egan, and D. S. Pratt, "The IGY three-frequency backscatter sounder," PROC. IRE, vol. 47, pp. 300–314; February, 1959.

† H. G. Booker, "A theory of scattering by nonisotropic irregularities with application to radar reflections from the aurora," *J. Atmos. Terr. Phys.*, vol. 8, p. 204; 1956.

oblique incidence manifestation of the "Huancayo *Es*," as is seen on the vertical incidence ionosphere sounder.

Auroral-Like Radar Echoes Observed from 17° Latitude*—R. B. Dyce, L. T. Dolphin, R. L. Leadabrand and R. A. Long, *Stanford Res. Inst., Menlo Park, Calif.*—Anomalous echoes are regularly observed by a ship-borne radar located at Antigua, in the British West Indies. These echoes, observed at 32 and 140 mc, have many of the characteristics of echoes from aurora observed in the arctic, although visible aurora should not be observable at Antigua more frequently than once in seven years. Similar observations at Stanford University indicate a correlation with one kind of sporadic-*E* ionization.

* This work is supported by the USAF Cambridge Res. Center under Contract AF 19(604)-5209.

Peculiarities of the Ionosphere in the Far East—a Report on IGY Observations of Sporadic *E*- and *F*-Region Scatter—E. K. Smith, Jr. and J. W. Finney, *National Bureau of Standards, Boulder, Colo.*—This paper considers the results for the period October 1, 1957-October 1, 1958 from the IGY "VHF Oblique-Incidence Sporadic-*E* Measurements" program which operated circuits at 50 mc in the Far East and the Caribbean. Sporadic *E* is found to be three to five times more frequent in the Far East than in the Caribbean for reflection coefficients of −20 to −80 db relative to inverse distance. Negligible dependence of magnetic activity is observed in either area; however, diurnal and seasonal variations are more regular in the Far East. It is suggested that this longitudinal difference may be due to the influence of the East-Asiatic Monsoon, perhaps through the mechanism proposed by Martyn.*

A peculiar evening signal enhancement, referred to as the "evening signal anomaly," appeared quite regularly in the Far East, and pulse delay measurements indicate the probable source of the reflection to be *F*-region. The corresponding effect in the Caribbean is about 100 times less frequent if it exists at all. The "*F* (layer tilt) reflection mechanism proposed by workers at Stanford† does not appear too promising in this case, due to the pulse broadening of the order of 1 msec which is normally encountered in the evening signal anomaly. A mechanism, which would explain the structure of the observed signal, involves reflection from field-aligned ionization similar to the mechanism invoked to explain the "low-latitude auroral echoes" observed at Stanford.[1]

* D. F. Martyn, *Nature*, vol. 183, p. 1382; May 16, 1959.
† Villard, Stein, and Yeh, *J. Geophys. Res.*, vol. 62, pp. 399–412; September, 1957.
[1] Peterson, Villard, Leadabrand, and Gallagher, *J. Geophys. Res.*, vol. 60, p. 497; 1955.

Night-Time Equatorial Propagation at 50 mc—First Results from an IGY Amateur Observing Program*—M. P. Southworth, *Radio Propagation Lab., Stanford University, Stanford, Calif.*—During IGY, the American Radio Relay League collected logs of VHF ionospheric propagation from radio amateurs, evaluated these reports, and transcribed them onto punched cards. Analysis relating to 50-mc equatorial work, begun this summer at Stanford, has revealed three apparent, and apparently related, modes of nocturnal low-latitude propagation. These are: 1) long-range transequatorial, as first noticed by amateurs in 1957; 2) medium-range, between stations working mode 1) and those near the magnetic equator itself; and 3) short-range, over typical sporadic-*E* distances and perhaps the same as the anomaly reported by Bateman, *et al.*,† in the Far East. Wherever they appear, these modes are extremely consistent during certain months, and evening propagation of frequencies up to 1.5 times the daylight MUF is not uncommon. The IGY discovery by amateurs that such phenomena are not confined to the Americas has also disclosed a variation in seasonal behavior at different meridians. Pronounced negative correlation with magnetic activity is a worldwide feature, however, which helps imply a direct relation to equatorial spread *F*. Quantitative professional data at the frequencies of interest are rather rare, but comparisons with Dueño's 40-mc backscatter soundings made at the University of Puerto Rico have been helpful.

* This work was sponsored at the USAF Cambridge Res. Center.

† Bateman, Finney, Smith, Tveten, and Watts, "IGY observations of *F*-layer scatter in the Far East," *J. Geophys. Res.* vol. 64, pp. 403–405; April, 1959.

The Equatorial Ionosphere and the Electrojet*—S. Matsushita, *High Observatory of the University of Colorado, Boulder, Colo.*—The electrojet in the magnetic equatorial region was first studied using the IGY geomagnetic data obtained at Huancayo, Koror, and Jarvis Island. Day-to-day changes and a seasonal variation of the electrojet were estimated. Also, an explanation of double electrojet layers was provided. Then effects of the electrojet, of changes of the lunar phase, and of geomagnetic disturbances on *q*-type E_s, *F*2, and *F*-scattering at Huancayo were investigated. One finding of this study was that the electron profiles of the *F*-layer reached a higher density in the early mornings of disturbed days than they did at the same time on quiet days.

* The research reported in this paper has been sponsored by the Geophysics Res. Directorate of the USAF Cambridge Res. Center, Air Res. and Dev. Command, under Contract AF 19(604)-2053.

Peculiarities and Seasonal Variations of TE Backscatter Echoes Observed at Mayaguez, Puerto Rico—B. Dueño, *Dept. of Electrical Engineering, University of Puerto Rico, Mayaguez, P. R.*—A backscatter experiment on 21.6 mc and 40.68 mc has now been in progress for approximately two years at the University of Puerto Rico at Mayaguez. Examination of the data has revealed several interesting anomalies which seem to bear relation to the peculiar morphology of the equatorial ionosphere.

Among these anomalies, the most striking one is the occurrence of long-range transequatorial echoes. These have been previously reported by Villard, Stein, and Yeh (1957). The Villard, Stein, and Yeh experiment was performed in the Virgin Islands during August and September, 1956.

In the present experiment, the period of observation covers a much longer span of time. As a result of this extended observation time, it has been found that these long-range transequatorial echoes exhibit a well-defined seasonal variation when examined at the 40.68-mc frequency. At the lower frequency of 21.6 mc, the long-range echoes occur practically every day through the year without any evident seasonal variation in their intensity. On the other hand, during the summer months their average range tends to decrease by approximately 1000 km.

A strong tendency for the transequatorial echo at 40.68 mc to be followed after or during subsidence by a southerly echo at half-range has been observed. The corresponding effect on the 21.6-mc scans seems to be a southerly gap in the normal F_2 echoes during the times of transequatorial long-range echoes. Normally, the gap fills in during or after the time the long-range echo disappears. These observations do seem to confirm the theory for the formation of long-range transequatorial echoes put forth in the paper by Villard, Stein, and Yeh (1957).

Atmospherics and the Propagation of Radio Waves of Frequencies Less than 1 kc—E. T. Pierce, *AVCO Res. and Advanced Dev. Div., Wilmington, Mass.*—The simplified mode theory of propagation in a waveguide, formed by the earth and a concentric ionosphere of constant height, is applied to the experimental observations of Chapman and Macario, for the frequency range between 100 cps and 1000 cps. The experimental data discussed were obtained from observations of atmospherics originating at different distances. It is demonstrated that the discrepancies between the simple theory and the night-time experimental results may be removed by a modification that postulates an effective increase in the ionospheric height at the frequency decreases. The modification that is introduced is consistent with existing information on ionospheric parameters such as electron density and electron collisional frequency. It is also shown that the modified theory is not necessarily incompatible with the experimental results for day.

Effect of Earth Curvature and Ionospheric Anisotropy on the VLF Modes (For Both Vertical and Horizontal Dipole Excitation)—J. R. Wait and K. Spies, *National Bureau of Standards, Boulder, Colo.*—After giving a brief review of prior work, some recent theoretical developments are described. An attempt has been made to remove many of the earlier restrictions. Some of the factors considered are: 1) influence of ground conductivity; 2) effect of earth curvature; 3) stratification at the lower edge of the ionosphere; and 4) influence of the earth's magnetic field. Particular attention is paid to the behavior of the reflection coefficients for highly oblique incidence, since these are the ones which are important for calculating the dominant modes. It is indicated that for a sharply-bounded ionosphere, the earth's magnetic field does modify the attenuation and phase characteristics of the dominant modes. Furthermore, there is a coupling be-

tween the TE- and the TM-mode types because of the anisotropy of the reflecting layer. It is seen that the full solution including earth curvature effects may be adequately treated by perturbation methods starting with a simple flat-earth model with isotropic boundaries.

In addition to the usual assumption of a vertical dipole source, the treatment for a horizontal electric dipole is also considered, since the horizontal component of the radiating currents in lightning discharges and certain VLF antennas can be large. It is shown that there are both TE- and TM-type modes excited by a horizontal dipole, even when the ionospheric reflection is effectively isotropic.

VLF Phase Characteristics Deduced from Atmospheric Waveforms—A. G. Jean, W. L. Taylor, and J. R. Wait, *National Bureau of Standards, Boulder, Colo.*—The waveforms of the electric field of atmospherics recorded at four widely-separated stations are analyzed to yield the phase characteristics of radio waves at very low frequencies. It is indicated that the relative phase velocity for propagation to great distances is about three per cent greater than c (velocity of light in a vacuum) at 4 kc. Above this frequency, it gradually decreases, being about one per cent greater than c at 8 kc. The form of the dispersion curve is very close to that predicted by the mode theory.

Comparison of Sferics Propagated along the Fairbanks-Thule Great Circle*—J. H. Priedigkeit, *Radio and Weather Sciences Lab., Stanford Res. Inst., Menlo Park, Calif.*—More than 50 sferics have been identified as having originated on the great circle passing through the SRI Sferics Measuring Stations located at Fairbanks, Alaska, and Thule, Greenland. These sferics have been simultaneously recorded at both sferic stations with equipment that has a bandwidth of 3 to 30 kc. Spectrum analysis of these waveforms makes it possible to speculate on the relative attenuation of the various frequency components for a specific arctic propagation path. Comparison between sferic waveforms whose sources are in Europe or in the South Pacific make it possible to investigate reciprocal path propagation.

* This work was sponsored by the USAF Cambridge Res. Center on Contract AF 19(604)-2409.

Waveforms Consisting of Unusually Long Trains of Oscillations—C. J. Chilton, *National Bureau of Standards, Boulder, Colo.*—Waveforms consisting of unusually long trains of oscillations have been transcribed from magnetic tape recordings made by the Automatic Whistler Recorders of the IGY Whistlers-West Program. These waveforms are characterized by a VLF head having a spectral peak in the 5–15-kc region and a duration of 1 to 2 msec. Following the head, unusually long trains of oscillations are frequently seen attaining durations of 40 msec or more and consisting of 100 or more individual cycles. This long train is characterized by build-up and decay times of a few milliseconds and a decrease in frequency content with increasing time approaching a frequency of approximately 2 kc. The character of these atmospherics is reminiscent of unusually long tweeks or unusually short whistlers; however, difficulties arise in attempting to characterize them. They are rare, which suggests the possibility of being associated with a unique discharge and/or propagation mechanism.

Mid-Field Forward Scattering—C. I. Beard and V. Twersky, *Sylvania Electronic Defense Lab., Mountain View, Calif.*—Experimental and theoretical results are given for forward scattering by spheres with radii large compared to wavelength, and with index of refraction n near unity. Both the intensity and phase of the scattered field (relative to that incident) are measured and computed (for several spheres and several sets of horns) as functions of the separations of transmitter and receiver from the scatterer. The scattering function of primary interest is that which reduces to the usual scattering amplitude in the limit of transmitter and receiver essentially at infinity—say, the function F such that $F \to f$, where f is defined for plane wave excitation through the scattered far-field form $(f/R)e^{ikR-i}$ t $k=2\Pi/\lambda$. Except for the near vicinity of the scatterer, it is shown that $F \to f$ linearly as the "quadratic phase error"

$$Q = A\frac{ka^2}{2}\left(\frac{1}{T}+\frac{1}{R}\right)+\frac{kb^2}{4T}+\frac{kc^2}{4R}$$

vanishes; here T and R are the distances of transmitter and receiver from the scatterer, and a, b, and c are the radii of the scatterer, transmitter, and receiver horns respectively; A depends only on $(n-1)ka$. In the "mid-field region" (where the sphericity of the wave fronts as indicated by Q is significant), we find that the magnitude of the corrections introduced in F is of the order of Im f, and Im f itself is an order of magnitude smaller than Re f: consequently, although the finite geometry has only a second-order effect on the intensity F^2, it has a first-order effect on the forward scattered phase arc tan [(Im F/Re F)]. Note, however, that the usual forward scattering theorem states that Im f is directly proportional to the total scattering cross section; thus the sphericiy has a first-order effect on the intensity integrated over all angles. Hence it is significant that Im F (as well as the associated phase) may be twice Im f even in regions where the usual "far-field criterion" (which ignores a) is satisfied.

An experimental extrapolation procedure has been developed to obtain f by measuring F for several values of T and R in the usual laboratory geometry.

An Accurate Boundary Condition to Replace Dielectric Media*—J. Kane and S. Karp, *Institute of Math. Sciences, Div. of Electromagnetic Res., New York University, N. Y.*—Most problems involving dielectrics cannot be solved exactly, *e.g.*, diffraction by a dielectric wedge. It is the purpose of this report to describe a technique by which a dielectric medium can be accurately replaced by an approximate boundary condition at its surface. It is proved that (for a dielectric half space) such a replacement leads to a small maximum percentage error over the *entire* far field of an arbitrarily placed line source. For example, we can tabulate the *maximum* percentage error for transverse electric excitation as

index of refraction	percentage	1.2	1.4	1.6	1.8	2.0
maximum percentage error in far field		4.5	1.1	0.4	0.2	0.1

The percentage error becomes very large for $n \sim 1$, because for $n=1$ there is no reflection at the interface; however, the absolute error remains small and bounded.

Applications of this approximation to unsolvable problems are discussed: in particular, propagation of radiation in a duct bored through layered media.

* The research in this report was sponsored in part by the AF Cambridge Res. Ctr., Air Res. and Dev. Command, under Contract No. AF19(604)-5238, and in part by the American Petroleum Institute.

Recent Studies of "Surface Waves" on Curved Boundaries—J. R. Wait, *National Bureau of Standards, Boulder, Colo.*—It is well known that a flat reactive surface will support a wave which propagates along the interface with virtually no radiation. At the risk of oversimplification, this wave will be called a surface wave, if for TM waves the surface is purely inductive and if for TE waves the surface is purely capacitive. The effect of curing the boundary is now considered in some detail. The models chosen are circular and elliptic cylinders and spheres whose surfaces are reactive. It is shown that for large radii of curvature, the field existing near the structure is a quasi-surface wave and bears a close resemblance to that on a flat surface since the energy still "clings" to the surface. For smaller radii of curvature, radiation from the structure may be large if the surface reactance is less than a certain value. In this case, it becomes hardly appropriate to describe the field as any kind of surface wave since there is copious leakage of energy from the structure.

In the case of small radii of curvature where the surface reactance is greater than a certain value, very strong resonance effects may occur. In the case of a corrugated sphere, it is possible to resonate the sphere in a single mode with electric dipole excitation if the surface reactance is chosen in a certain way. Such resonances have been studied recently by Cullen for corrugated cylinders (Toronto URSI Symposium, June, 1959).

A Solution to the Equiangular Spiral Antenna Problem*—B. R. Cheo, V. H. Rumsey, and W. J. Welch, *Electronics Res. Lab., Dept. of Electrical Engineering, University of California, Berkeley, Calif.*—In order to simplify the boundary value problem and yet retain the essential features of the frequency independent modes, we consider an antenna consisting of an infinite number of coplanar equiangular spiral wires. By considering solutions of Maxwell's equations for which the electric field phasor equals a constant times the magnetic field phasor, we can express the solution in terms of a single scalar wave function. Since this antenna has an infinite number of input terminals, an infinite set of solutions is obtained corresponding to the various possible input excitations. The Fourier-Bessel transform of the

* This research was sponsored by the U. S. Army Signal Corps under Contract DA-36-039-SC-78256.

wave function is a fairly simple function. From it, the pattern and other far-field parameters can be calculated easily and exactly. The pattern goes to zero in the plane of the antenna, which is characteristic of any frequency independent mode, and shows that the current distribution must die out more rapidly than the radiation field.

A New Wavequide for Millimeter Waves—G. Goubau and J. R. Christian, *U. S. Army Signal Res. and Dev. Lab., Fort Monmouth, N. J.*—A well-known problem in theoretical optics is to find a light source whose diffraction image has the same intensity distribution as the source. In the microwave range, where coherent sources are available, a similar but more stringent problem can be formulated, namely, find a source and the appropriate optical system which yields an image which coincides with the source not only intensity-wise, but also phase-wise.

A study of this problem led to a new method for guiding millimeter waves. It is based on the fact that wavebeams of special cross-sectional field distributions can be maintained over large distances by resetting the phase distribution in the beam at periodic intervals. An experimental model of such a transmission system has been built and investigated. It consists of periodically-spaced lens-like phase correcting means, and launching devices on both ends to develop and receive a beam with the required cross-sectional field distribution. The experimental results obtained bear out the theory. Assuming reasonable dimensions, the theoretical loss of this "beam waveguide" compares to that of a TE-mode circular waveguide.

Scattering of Electromagnetic Energy by an Acoustic Wave—E. D. Denman, R. W. Fetter, J. C. Gravitt, and B. L. Jones, *Midwest Res. Inst., Kansas City, Mo.*—Scattering of electromagnetic energy by an acoustic wave is enhanced, if a proper choice of the wavelength ratio is made. The predictions of Tonning,* Norwood,† and Eyges[1] are proven. In addition, the theoretical work of Brillouin[2] and Slater[3] on crystal studies have been applied to the electromagnetic-acoustic scattering problem.

Using the Mathieu equation[2] as the starting point of the theoretical studies, the various scattering "modes" are investigated. These modes occur at the wavelength ratio

$$\frac{\lambda e}{\lambda a} = \frac{2}{a} \cos \phi$$

where a is of integral values and the angle dependency arises from the use of separate antennas. With a single antenna, X-band energy is scattered by acoustic energy of approximately 20 kc for the first mode.

Calculation of voltage reflection coefficients ρ for the various wavelengths indicates that maximum scattering occurs for $a=1$; this value gives a ratio of $P_r/P_t=10^{-9}$ for a 160-db sound wave.

In addition to the verification of scattering from the acoustic wave in accordance with the theoretical predictions, the effective bandwidth of the scattering agrees quite closely with that predicted by Tonning. This bandwidth is

$$\frac{2\Delta f_a}{f_a} = \frac{0.442\lambda a}{\sin(\theta/2)L}$$

where θ defines the scattering angle. Since $L=n\lambda a$ where L is the length of the wavetrain, the scattering "mode" becomes quite narrow as n, the number of waves in the wavetrain, is increased.

Frequency Spectra of Transient EM Pulses in a Conducting Medium—W. L. Anderson and R. K. Moore, *Electrical Engineering Dept., University of New Mexico, Albuquerque, N. M.*—The energy density spectra of transient electromagnetic fields generated by a pulsed dipole source in an infinite conducting medium have been investigated for various distances from the source. At large distances, the frequency corresponding to the peak of the spectrum varies inversely as the square of the distance. This peak roughly defines a frequency ω_p, around which most of the pulse energy is centered. Thus, as the pulse is observed at various distances from the source, it appears that the attenuation factor corresponding to ω_p,

$$\exp\left\{-r\sqrt{\frac{\sigma\mu\omega_p}{2}}\right\},$$

is independent of distance, due to the constancy of the product $r\sqrt{\omega}$. From this point of view, the transient fields do not decrease exponentially as r, but as inverse powers of r.

This should not be construed as meaning that the transient possesses an advantage over CW. The exponential attenuation factor applies to the monochromatic components of the pulse just as to a continuous wave, and at large distances the energy put into the high-frequency components is wasted.

The phenomenon is illustrated by calculations that have been carried out for the case of pulses in sea water.

Scatter Propagation at 915 mc over a 395-Mile Path—W. K. Klemperer, *Cornell Aeronautical Lab., Inc., Buffalo, N. Y.*—The purpose of this note is to present the results of a detailed examination of the period of stationarity and the probability amplitude distribution for various record lengths of the signal received on a typical UHF scatter link. The period of stationarity can be estimated from data on the variability of the sample medians and from the after-effect function. The probability amplitude distributions for the shorter records are occasionally Rayleigh, but the significance of fitting such a theoretical curve to the data is then limited by the smaller number of independent samples the records contain. The limits imposed by finite sampling are defined and the results applied to the observed distributions and various parameters thereof, such as the medians and fading ranges. A few contaminating effects (such as the presence of aircraft in the antenna beams) leading to peaks on the records are also discussed. The conclusion drawn is that the statistics of the scattering process are not stationary for periods long enough to rule out one description (turbulence) as opposed to another (layers).

Atmospherically-Perturbed Modes and X-Band Propagation over Optical Paths—T. J. Carroll, *Bendix Radio, Baltimore, Md.*—After the region of strong attenuation with distance in the vicinity of the horizon is passed, microwaves propagated into the twilight region somewhat beyond the horizon, in the absence of atmospheric ducts, become weak and randomly fading, but only slowly attenuated with distance. Mode theory interprets these fields at all distances as waves guided around the earth bulge by partial reflections in a tapered layer of air dielectric assumed to be terminated in free space at some convenient height below the ionosphere. So long as a rigidly static atmosphere and coherence of the modes is assumed, the modes add up constructively to the classical lobe result within the horizon, and increasingly destructively to the classical diffraction theory beyond. The twilight region sets in when inevitable phase and amplitude perturbations of the modes resulting from propagation over long paths through the time-variable index of the lower atmosphere become great enough to prevent further mutual cancellation of the air guided modes.

Recent X-band observations within the optical range by the University of Texas and the British Navy have indicated frequent failure of the measured direct wave field to be equal to the free-space value, sometimes by more than 10 db. The detailed way in which the individual modes add up coherently to give the simple direct and reflected wave resultant of the lowest few lobes has been previously calculated for 10-cm waves.* Relatively small but plausible phase perturbations of these modal fields by the real atmosphere after propagation over path lengths of 10^6 or more wavelengths are a simple way of understanding the failure of X-band measured fields over long optical paths to equal the free-space value. These observations may be an experimental indication of the onset of phase incoherence among modes within the horizon, even before the twilight zone is reached.

On the Interpretation of Beam Sweep Profiles—D. E. Johansen, *Hermes Electronics Co., Cambridge, Mass.**—Experimental data recently published by A. T. Waterman, Jr.,† provide "instantaneous" profiles of troposcatter signal strength as a function of orientation of a narrow beam receiving antenna. The resulting patterns are

* A. Tonning, "Scattering of Electromagnetic Waves by an Acoustic Disturbance in the Atmosphere," Norwegian Defense Research Establishment, Rept. No. 18; January, 1957.

† V. Norwood, "Further Discussion of the Feasibility of Tracking Sound Waves by Electromagnetic Waves," Evans Signal Lab., Signal Corps, Rept. M1172.

[1] L. J. Eyges, "Proposal for Improving Tropospheric Propagation," Lincoln Lab., M.I.T., Lexington, Mass., Rept. No. 151.

[2] L. Brillouin, "Wave Propagation in Periodic Structures," Dover Publications, Inc., New York, N. Y.

[3] J. C. Slater, "Interaction of waves in crystals," *Rev. Mod. Phys.*, vol. 30, pp. 197–222; January, 1958.

* T. J. Carroll and R. M. Ring, "Twilight Region Propagation of Short Radio Waves by Modes Contained in the Normal Air," M.I.T. Lincoln Lab., Lexington, Mass., Tech. Rept. 190, chs. 7 and 8; 1958.

* Now with Applied Res. Lab., Sylvania Electronic Systems, Waltham, Mass.

† A. T. Waterman, Jr., "The Mechanism of Transhorizon Propagation: Layers vs Turbulence," presented at URSI Meeting, Washington, D. C., May, 1959.

characterized by frequent strong and discrete lobes having a half-power beamwidth about equal to the beamwidth of the experimental receiving antenna system. Such patterns have qualitatively been interpreted as evidence for a discrete ray (specular layer reflection) theory of troposcatter propagation.

It is the purpose of this paper to show theoretically that a continuum of scatterers will also yield the qualitative features shown by the experimental patterns. A Monte Carlo approach is used. The mathematical model represents a reception from an extended source, equivalent to the limiting case of a continuous distribution of scatterers along a line. The signal emanating from each element on the line is assumed to have a randomly varying amplitude and phase. An antenna receiving pattern is then assumed and statistics of the sweep profiles are derived. Using these statistics and a table of random deviates, a sequence of samples of the sweep profile are computed, and taken as statistically analogous to the experimental patterns. A large number of computed sweep samples show a marked qualitative similarity to the experimental data.

Measured Distribution of the Duration of Fades in Tropospheric Scatter Transmissions—K. F. Wright, J. E. Cole, and J. G. Gibson, *Collins Radio Co., Tucson, Ariz.*—Although the amplitude distribution characteristics of a tropospheric scatter signal are well known, very little information exists regarding the number and duration of fades below a specified level. Knowledge of this distribution is important in estimating the data transmission performance of a tropospheric scatter system.

This paper presents the results of experimental measurements of noise distribution at the output of a tropospheric scatter receiver operating at 1000 mc over circuits 100 to 150 miles in length. The results of these tests are presented as a family of curves showing the number of times per hour the noise exceeded a fixed value as a function of median signal level. The accumulated time the noise exceeded the specified value as a function of median level is also presented. The information is provided for both diversity and nondiversity reception. The results are compared to analytical studies previously made.

The special test equipment required to perform these tests is described briefly.

On the Spectral Density of Multiple-Scattered Electromagnetic Waves in Dielectric Noise—D. S. Bugnolo, *Dept. of Electrical Engineering, Columbia University, New York, N. Y.*—It is well known that the expectation of Poynting's vector for a multiple-scattered field can be obtained as a solution of the transport equation of diffusion.*

Since changes in the spectral density as well as the intensity are often of interest, this paper will be concerned with the introduction of a transport equation suitable for this more general case.

The spectral density in an element of positional wave number space is defined by:

$$S(\boldsymbol{r}, \boldsymbol{k}) = \frac{1}{2\pi}\int_{-\infty}^{\infty} G\boldsymbol{E}(\boldsymbol{r}, t)\cdot\boldsymbol{E}(\boldsymbol{r}, t)\epsilon^{-j\omega\tau}d\tau.$$

The time-variable notions introduced in a previous paper† will be used to construct a suitable transport equation under the assumption of stationarity in the wide sense for both the signal and the dielectric noise.

A solution will be presented for both a monochromatic and band-limited source. Bounds on the information capacity will be discussed. The results will be applied to the special case of a tropospheric multiple scattering at very high frequencies and to multiple scattering in the ionosphere during spread F conditions.

* Morse and Feshback, "Methods of Theoretical Physics," chs. 2 and 12.

† D. S. Bugnolo, "Correlation function and power spectra of radio links affected by random dielectric noise," IRE Trans. on Antennas and Propagation, vol. AP-7, pp. 137–141; April, 1959.

An Investigation of the Perturbations of the Carrier Frequency on an Over-the-Horizon Tropospheric Link*—S. J. Goodman, L. B. Lambert, and J. M. Kennedy, *Electronics Res. Labs., Columbia University, New York, N. Y.*, and J. F. Roche and L. P. Rainville, *Lincoln Laboratory, M.I.T., Bedford, Mass.*—An experiment was performed over a 161-mile path between Alpine, N. J., and Round Hill, Mass. to determine the frequency perturbations produced by the propagation mechanism on a highly stable signal in an over-the-horizon tropospheric circuit. A signal at 388.0 mc was transmitted from Alpine using a 10-kw transmitter and a 12° beamwidth antenna. These transmissions were received at Round Hill with a 5° beamwidth antenna and heterodyned to 416.7 mc using a highly stable local oscillator and retransmitted to Alpine. Using coherent reception techniques, the retransmitted signal was received at Alpine and heterodyned with the signal originally transmitted. The difference frequency was fed to a bank of narrow bandwidth crystal filters. An analysis of the data obtained from these filters indicated the frequency perturbations of the signal encountered on the two-way path, when CW transmission was employed.

* This work reported in this paper was performed jointly by the Electronics Research Labs. of Columbia University and Lincoln Laboratory, M.I.T., with the joint support of the U. S. Army, Navy, and Air Force.

Whistlers East During the IGY-Whistlers—M. G. Morgan and W. C. Johnson, *Thayer School of Engineering, Dartmouth College, Dartmouth, N. H.*—Data gathered during the course of the IGY indicate that at Whistlers-East stations: 1) naturally occurring noise levels are higher in the Northern Hemisphere than in the Southern; 2) whistlers are observed over a fairly widespread area; 3) stations in the Northern hemisphere receive mainly long whistlers, while those in the Southern receive mostly short whistlers, independent of local season; 4) at most antarctic stations, many short whistlers are followed by a burst of hiss after a time interval of one second; 5) most all antarctic whistlers (short) show a pronounced fine structure indicating four to ten coherent paths, while most Northern whistlers (long) do not exhibit this fine structure; 6) on many occasions echo trains are observed simultaneously at both Port Lockroy and Ellsworth, and can be observed at Dartmouth as well; 7) whistler activity seems to diminish north of N55° geomagnetic and south of N50° geomagnetic; 8) nose whistlers having nose frequencies less than 7 kc are fairly common, occurring usually during period of high ionosferics activity; 9) high whistler activity seems to occur in cycles of 10- or 11-day period; and 10) whistler activity peaks at all stations in June and July, both in Northern and Southern hemispheres.

Deduction of the Electron Density Distribution in the Outer Ionosphere from Nose Whistler Observations*—L. Owren, *Geophysical Inst., College, Alaska.*—The dispersion of a whistler propagating in the outer ionosphere is determined by the well-known relation between the time of flight $T(\omega)$ and the group velocity $U(\omega, p, x, y)$

$$T(\omega) = \int_{\text{path}} \frac{ds}{U}.$$

$T(\omega)$ is an observed quantity and therefore a known function. When the path of propagation and the gyromagnetic and collisional frequencies along the path, $x(s)$ and $y(s)$, can be prescribed, the integral becomes an integral equation for the unknown electron density distribution over the path $N(s) \propto p(s)^2$. An inversion of this integral equation would permit us to determine the latter. If we assume that whistlers propagate in a strictly longitudinal mode tied to a line of force of the earth's dipole field, and further that the local plasma frequency $p(s)$ everywhere exceeds the geometric mean of the wave frequency ω and the modulus of $z=x+iy$, the integral is well approximated by

$$f(\omega) = i\int_a^b (\omega - z)^{-3/2}g(z)dz$$

where $f(\omega)$ is a known function and the kernel as well as $g(z)$ are analytic functions on the path of integration. Formally, the equation is a Fredholm integral equation of the first kind. When we neglect collisions, the same equation in terms of the gyromagnetic frequency x as independent variable results. Now $g(x)$ and the kernel both have singularities at the midpoint of the path. In order that the equation have mathematical meaning, the effect of the collisions at the midpoint must be simulated by a suitable redefinition of $g(x)$. The singularity of the kernel implies that only a principal value solution may be obtained. The convolution form of the integral equation is used to invert it by 1) the method of generalized functions, and 2) a finite Fourier transform. The first method gives a principal value solution in terms of an integral over known functions and the second a Fourier series. These solutions determine the functional form of the electron density distribution and make it possible to infer the field line of propagation from the observed nose frequency of the whistler. The solutions, their physical implications, and the advantages of the method

* This work was supported by the Electronics Res. Directorate, USAF Cambridge Res. Center, under Contract No. AF 19(604)-6574.

over the usual numerical integrations with assumed electron density functions are discussed.

Ray Tracing for Whistler-Mode Signals at Low Frequencies—E. R. Schmerling, *Pennsylvania State University, University Park, Pa.*, R. Goerss and S. Miluschewa, *RCA, Astro-Electronics Products, Hightstown, N. J.*, and P. Hertzler and I. Pikus, *RCA, Camden, N. J.*—A number of whistler-mode ray-paths have been traced in an IBM 650 computer using Haselgrov's equations. A frequency of 5 kc was taken at a geomagnetic latitude of 50° for various initial propagation angles. A centered dipole was used for the earth's field, and a simple ionospheric electronic-density model based on Seddon's (1957) composite curve. The purpose of the work was to examine the path spreading as a function of initial angle, not to obtain the exact conjugate points, so that the simple model was considered adequate. This problem has a special bearing on second-hop signals and satellite-originated signals, since signals originating on the ground are not expected to have a large spread of angle at heights of the order 100 km. A decided shift of the downcoming rays towards the equator, and a large spread of the order 1000 km for the angular spectrum, were found.

Observations on NSS Propagated by Double-Hop Whistler Mode—H. O. Peterson and R. Ewing, *RCA Labs, Riverhead, L. I., N. Y.*, D. Riggs and R. Lending, *RCA, Camden, N. J.*, and E. R. Schmerling, *Pennsylvania State University, University Park, Pa.*—Signals from NSS ANNAPOLIS have been regularly received on low-noise narrow-band receivers at Riverhead, N. Y. and Camden, N. J. These have been identified as propagated by the double-hop whistler mode from time-delay measurements. The signals are heard regularly between the hours of 10:00 P.M. and 4:00 A.M. During ionospherically disturbed conditions the signals have been heard at other times, and, in particular, during the day. Statistical data and correlations with ionospheric disturbances are presented and discussed. Measurements of signal amplitude, together with the observations of Helliwell on the simple bounce, enable the ionospheric attenuation to be estimated.

Simple day and night absorption calculations using plausible models of electron-density-height profiles and Nicolet's (1958) model of collision frequency indicate the reason for the difference between day and night reception.

Linear Array Design—J. Blass, *W. L. Maxson Corp., New York, N. Y.*—This paper presents diverse considerations in the design of linear arrays. In particular, the effect of mutual coupling in two-dimensional scanning arrays is discussed. The beam shift due to this coupling is analyzed. A simplified statistical analysis of the effect of tolerances in array construction on beam pointing and sidelobes is presented. The design features of an antiphased, linear array of radiating waveguides, illustrating the use of a differential phase shifter and multimode matching element is also presented.

A New Technique for Electronic "Scanning"—H. E. Shanks, *Microwave Lab., Hughes Aircraft Co., Culver City, Calif.*—The concept of time-modulated antennas has recently been demonstrated as a means of overcoming many of the limitations currently restricting advances in the antenna art. Of special importance is the mathematical possibility of generating a pattern complex capable of providing simultaneous scan operation. This characteristic is realized by periodic time modulation of the aperture distribution. This paper discusses the theory of simultaneous "scanning" using time modulation techniques and shows that the required j pattern complex is generated by a progressive-pulse aperture excitation. The fundamental equations and relationships concerning the form of pulse excitation and "scanning" coverage are derived. In addition, practical methods of physically generating the proper pulse-excited aperture are described and the necessary detection requirements are delineated.

Utilization of Space Frequency Filters in Antenna Design—J. B. Smyth and S. Weisbrod, *Smyth Res. Associates, San Diego, Calif.*—Recently* a theory has been advanced which appears to satisfactorily account for the various characteristics of tropospheric radio fields. A natural consequence of this theory is the "glinting-in"† of the radio signal from directions more-or-less centered around the great-circle path.

In a homogeneous atmosphere, the system sensitivity may be increased by decreasing the bandwidth or increasing the aperture of the antenna. In other words, for a given signal power and the quantity of information one may trade time for space. Unfortunately, in a real atmosphere, this interchange of time and space is limited by the phenomenon referred to above, since very high-gain antennas are particularly vulnerable because of the narrow beamwidths.

In this paper, the interchange of space and time is reviewed. A concept of space frequency and space noise is introduced and some of the basic ideas of the time-frequency domain are extended to the space-frequency domain. Methods are also suggested by which the difficulties of trading space for time may be materially reduced.

Phase-Modulated Antenna—C. J. Drane, Jr., *Electromagnetic Rad. Lab., Electronics Res. Directorate, AF Cambridge Res. Center, Bedford, Mass.*—The resolution of a passive antenna system can be improved by phase-modulation, cross-correlation, and synchronous detection of the signals received by a compound antenna. In this paper, it is shown that signals received at various portions of the antenna structure are selectively phase-modulated, then cross-correlated (time-averaged), yielding a signal which can be considered to be composed of several terms each having a particular spatial dependence. By use of synchronous detection, the term of desired spatial characteristics is selected. Control over the shape of the antenna radiation pattern, in addition to an increase in the resolving power by at least a factor of two over conventional discrete antenna arrays, can be obtained by these techniques using fewer elements in the array. In particular, analysis is carried out for the realization of a pattern of the form $(\sin x/x)$.

Consideration is also given to the equivalence between the conventional mathematical representation of the signal received by a linear, discrete additive array and its representation by a polynomial generated in powers of the pattern of a much smaller array. This is illustrated by considering two examples—one, an array having a uniformly illuminated aperture, and the other an array having a binomial distribution.

Correlation Techniques Applied to Antenna Pattern Control*—H. E. Band and J. E. Walsh, *Pickard and Burns, Inc., Needham, Mass.*—We have investigated the application of correlation techniques to the controlling of multielement antenna patterns and the enhancement of the signal-to-noise ratio of signals derived from such systems. The primary objective is the production of single-lobed patterns of high resolution using a minimum number of antenna elements. One of the simplest configurations involves two linear arrays of fixed lengths and phase center spacing. The element spacing of the two arrays differs, but exceeds one wavelength. This, of course, results in a loss of gain over that of a closely spaced, nonambiguous array, but allows reduction of the number of elements.

Correlation of the added output of one array with that of the other will reduce all major lobes but one, provided only one signal of a given frequency is incident on the antenna system. The correlator also reduces incident noise, especially if an additional fixed time delay is introduced between the additive array signals prior to correlation.

We have also attempted to produce given patterns by judicious multiplication of signals from individual antenna elements, including that from a continuous aperture antenna, combined with prescribed (nonuniform) spacing of the array elements. Various amplitude distributions over the antenna elements may be used in connection with the multiplicative techniques.

For the purposes of drift-free multiplication, amplitude modulation is imposed on the RF signal, preferably at the transmitter. The multiplier is followed by an audio filter tuned to the modulation frequency, from which the desired product signal is obtained.

The experimental set-up for testing these ideas is described, and the results reported.

* This work was performed under USAF Cambridge Res. Center Contract AF 19(604)4535.

Switched Interferometers—R. N. Bracewell, *Radio Propagation Lab., Stanford University, Stanford, Calif.*—"Radio interferometers"* are a class of antennas consisting of two or more well-separated parts. An early example is afforded by the air-warning height-finding radars installed before World War II; the second part in this case is the image of the part supported on a tower. Exploitation of two-element interferometers incorporating transmission line links set in vigorously at the end of the war in connection with radio astronomy.

* J. B. Smyth, "Radio phase distortion—a mechanism for transhorizon radio propagation," *1959 URSI Washington Meeting*, p. 49.

† A. T. Waterman, Jr., "The mechanism of transhorizon propagation: layers vs turbulence," *1959 URSI Washington Meeting*, p. 37.

* R. N. Bracewell, "Radio interferometry of discrete sources," PROC. IRE, vol. 46, pp. 97–105, January, 1958.

Insertion of a controlled phase shift in the transmission line had led to numerous special developments: switched interferometers (Ryle), beam-scanning interferometers (Little and Payne-Scott), Mills crosses, and tees. The behavior of switched interferometers and the related devices is greatly clarified by use of *spectral sensitivity island diagrams*. This important diagram is carefully explained and illustrated by numerous examples.

Tropospheric Path Loss in the Arctic over High-Altitude Paths—A. E. Teachman, *Page Communications Engineers, Inc., Washington, D. C.* and J. P. McMillan, *Western Electric Co., Inc., New York, N. Y.*—During the summer of 1958, tropospheric path-loss measurements were made on a series of five paths extending from Baffin Island to Iceland via the Greenland Ice Cap to determine the feasibility of using tropospheric-scatter communications in that area. Approximately 400 hours of signal level data were obtained for each path. Cumulative distributions of the path loss are shown. A graphic comparison of these data is made with overland path loss data obtained by M.I.T. Lincoln Laboratory and also with overwater data obtained jointly by the Naval Research Laboratory and M.I.T. The results indicate increased loss for tropospheric transmission between points on a high-altitude plateau. Fading rate test results indicate that the intervening terrain has a bearing on the fading rate and the magnitude of enhancements. Strong enhancements were observed on top of the Ice Cap. The short-term correlation of received signal level with surface refraction index and dew point was generally poor. Diurnal effect was not established.

Simultaneous Angular Diversity-Frequency Sweep Measurements at 2290 MC Over a 188-Mile path Between Round Hill and Crawfords Hill, N. J.*—J. H. Chisholm, L. P. Rainville, J. F. Roche, and H. G. Root, *Lincoln Laboratory, M.I.T., Bedford, Mass.*—Simultaneous angular diversity and frequency sweep measurements were performed over a tropospheric scatter path. These experiments were designed to extend the results presented in previous papers†,[1] based upon separate frequency sweep and angular diversity measurements.

Transmissions at 2290 mc from Round Hill, Mass., were received over a 188-mile path at Crawfords Hill, N. J., simultaneously on two 1° beamwidth antennas separated from 8° to 1.2°. The transmitter was swept over an 8-mc band at a rate of 100 cps and the received signals on each of the two beams were recorded simultaneously.

The correlation as a function of frequency spacing was determined for separation of 0.25 mc to 8 mc. Correlations were also determined for various separations of frequency and the angular spacing of two receiving beams. Comparison of correlations for frequency and angular separations are made with those predicted using some theoretical scattering models.

The possible diversity improvement to a system using both frequency diversity and angular diversity was evaluated by programming a digital computer using measured values of signals with several frequency and angular separations.

Successful VHF Communications for 2540 Miles at 144 MC and 222 MC.—J. T. Chambers, *Hughes Aircraft Co., Communications Div., Culver City, Calif.*—In 1956, a nightly test program was initiated, the goal of which was VHF Communications from the Island of Oahu and the California coast on a frequency of 144 mc. These tests were not without foundation, as the built-in Pacific inversion is well known, and in several instances VHF signals had been reported well beyond line-of-sight. Two-way communication was established July 8, 1957, and again August 18, 1957. Extensive plans were made for the inversion season of 1958; however, a large antenna was destroyed by the weather, ending the 1958 tests. For 1959, it was decided to move up to 222 mc. Success was almost immediate.

Signals were of great strength (approximately 30 db s/n). The contact was repeated 8 days later and on August 1, the test frequency was moved to 432 mc. As of the date of writing, no results have been achieved. Furthermore, the visual indications associated with the earlier successful transmission have not reappeared.

Experimental Investigations of the Tropospheric Scatter Mechanism—R. Hopkins, *U. S. Navy Electronics Lab., San Diego, Calif.*—Simultaneous measurements of atmospheric turbulence spectra and X-band scattered power received as a function of scatter angle dependence were determined by synchronized beam swinging tests for both horizontal and vertical directions. Index-of-refraction fluctuations were sampled at 2000-foot intervals from near the surface of the sea to 12,000-feet elevation. Continuous profiles of refractive index were recorded over the same range of heights. Some of the measured scatter angle dependencies have been found to be in good agreement with those predicted from the index-of-refraction power spectra both for horizontal and vertical beam swinging. The effect of elevated inversions on the scatter angle dependence is shown for both directions of antenna beam swinging. The effect of elevated inversions on the scatter angle dependence is shown for both directions of antenna beam swinging.

Scaled-Beam Multiple Frequency Measurements for Transhorizon Microwave Scattered Fields—N. R. Ortwein, *U. S. Navy Electronics Lab., San Diego, Calif.*—Simultaneous scaled-beam measurements at X, S, and L bands were obtained on a 190-mile overwater path using broad-beam antennas. The observed wavelength dependence is compared with that predicted using airborne microwave refractometer measurements of the dielectric spectrum obtained at the same time. Although the scattering angle dependence observed on a shorter 92-mile path in the same meteorological area was observed to obey the predicted dependence, the wavelength measurements indicate anomalous behavior.

Distance dependence, aperture-medium coupling loss, and fading rate measurements are also reported.

Physical Equivalents of Mathematical Approximations in Propagation Problems—M. Katzin, *Electromagnetic Res. Corp., Washington, D. C.*—In attempting to solve complicated propagation problems, one is confronted with the necessity either of approximating the actual problem by one which can be solved exactly, or of introducing approximations in the mathematical solution of the given problem. It is demonstrated that in the latter procedure, the mathematical approximations often are equivalent to a change in the physical problem, such as a change in the refractive index distribution, the shape of the boundaries, or both. As an example, it is shown that, in the rigorous theory of propagation in a homogeneous atmosphere over a spherical earth, the evaluation of the normal modes in terms of the Airy function actually gives the exact height-gain function for a slightly inhomogeneous atmosphere. Other cases are also discussed.

Some Preliminary Ionosphere Rocket Measurements at Fort Churchill, Canada—W. W. Berning, *Ballistic Res. Lab., Aberdeen Proving Ground, Md.*—As a part of their contribution to the IGY, the Ballistic Research Laboratories installed and operated the radio Doppler (DOVAP) rocket tracking instrumentation at Fort Churchill, Canada. The trajectories of more than 50 research rockets were obtained from DOVAP tracking with peak altitudes ranging to greater than 400 km.

Using a technique developed at Ballistic Research Laboratories more than 10 years ago, the DOVAP tracking data furnish a measure of ionosphere electron densities if the true trajectory is known. The latter is closely approximated by a precise vacuum trajectory computed from DOVAP initial conditions chosen above the sensible drag region, but below the appreciable ionosphere.

The ionospheric data from five flights are presented. In addition to electron density profiles from DOVAP data, profiles computed from P'-f soundings (using J. E. Jackson's method) and total electron content obtained from Faraday measurements are presented where available. The five flights chosen either illustrate some interesting features of the arctic ionosphere or furnish comparison data for other direct ionospheric measurements.

Measurements of Ionospheric Stratification by High-Altitude Rockets—J. C. Ulwick, *Geophysical Res. Directorate, USAF Cambridge Res. Center, Bedford, Mass.*—Electron density distributions are obtained from the delay data of pulsed signals as a function of rocket position. The analysis is carried out on the IBM 704 computer for curved-ray paths in the horizontally stratified ionosphere. The delay data are recorded at several ground stations for transmissions to and from the rocket for rocket ascent and descent.

The results of three recent rocket flights, two in New Mexico and the third at Churchill, Canada, are considered. The data from the New Mexico flights are for both upward

* The work reported in this paper was performed with the joint support of the U. S. Army, Navy, and Air Force.

† J. H. Chisholm, L. P. Rainville, J. F. Roche, and H. G. Root, "Measurement of the Bandwidth of Radio Waves Propagated by the Troposphere Beyond the Horizon," presented at URSI Meeting, Washington, D. C.; April, 1958.

[1] J. H. Chisholm, L. P. Rainville, J. F. Roche, and H. G. Root, "Angular reception at 2290 mcps over a 188-mile path," *Record of Natl. Symp. on Extended Range and Space Communications*, sponsored by the IRE together with the George Washington University; October 6–7, 1958.

and downward transmissions, whereas previous results depended only on one or the other. The electron density distributions obtained confirm previously reported results of the E region where stratification of the ionosphere at preferred levels approximately 5 km apart were noted. The results, with good agreement between upward and downward transmissions over different ray paths, could be interpreted as the variation of the mean electron density as a function of height. The Churchill results, with three ground stations recording the data to over 200 km, indicate that similar stratifications are present at this latitude and to higher altitudes.

Electron Temperature Measurements in the Ionosphere—N. W. Spencer and L. H. Brace, *Space Physics Lab., University of Michigan, Ann Arbor, Mich.*—Measurements of electron temperature and local ion density in the 110-km to 175-km region of the ionosphere have been made through application of the Langmuir probe technique. The temperatures obtained are higher than predicted neutral particle temperatures in the region, but roughly comparable to neutral particle temperatures measured by totally different means at a different time.

The technique employed in measuring the electron temperatures involves the ejection from a rocket into the ionosphere of an ordered electrode geometry designed to satisfy the requirements of a Langmuir probe as indicated by appropriate theoretical studies. Electron temperatures and ion densities are deduced from volt-ampere curves telemetered from the probe instrumentation. The computation of ion densities employing the measured electron temperatures results in data which are comparable to preliminary electron densities obtained from a DOVAP system used on the same rocket.

The General Equation for Magneto-Ionic Effects Observed with Artificial Earth Satellites' Radio Emission—P. R. Arendt, *Inst. for Exploratory Research, U. S. Army Signal Res. and Dev. Lab., Ft. Monmouth, N. J.*—Based on the Appleton-Hartree formula for the propagation of the two modes of magneto-ionic splitting, a general formula is derived for the fading period to be observed from a satellite's CW radio emission. This period is a function of the continuously changing position of the satellite, that is, a function of the effective magnetic field and the electric charge distribution along the ray's path. Without any assumption regarding the geometry of the ray's path, the distribution of the charges, and the direction of the magnetic field, a general formula is derived which consists of two main terms and two correction terms. One of the main terms is proportional to the charge density at the satellite and also proportional to the velocity component of the satellite's movement which is directed towards the observer at the ground. This velocity component is the velocity observed in Doppler frequency measurements. For many practical cases, the velocity term is of the same order of magnitude as the other main term which is proportional to the integrated charge density. However, the velocity term is applicable only for satellite movements within an ionosphere. The paper discusses possible simplifications of the general formula which finally lead to the equation first used by T. V. Evans (1956) in moon reflections. The applicability of such simplifications is discussed.

On the Analysis of Polarization Rotation Recordings of Satellite Radio Signals—R. S. Lawrence and C. G. Little, *National Bureau of Standards, Boulder, Colo.*—At frequencies as low as 20 mc, the rotation of the plane of polarization of satellite signals cannot be assumed to be proportional to $\int NB \cos \theta dl$ along the line of sight. A method of analysis is presented which eliminates this assumption and permits accurate estimates of total electron content below the satellite height to be obtained from 20-mc observations. Some of the results obtained using the method to determine the subsatellite electron content, through a satellite pass, are presented. These analyses permit the study of ionospheric tilts, and have revealed the presence of large-scale irregularities in the ionospheric electron content. The deviation in subsatellite content of these irregularities is of the order 2 per cent of the running mean value; the lateral extent of the irregularities is of the order of a few hundred kilometers. The effects of such irregularities upon ionospheric refraction and satellite Doppler curves are briefly discussed.

Integrated Electron Densities from Satellite Radio Doppler Frequency Observations—W. J. Ross, *Ionosphere Res. Lab., The Pennsylvania State University, University Park, Pa.*—For a satellite moving horizontally near the observer's zenith, and whose radio waves propagate with small refraction through a horizontally stratified ionosphere, it can be shown that the ionosphere reduces the Doppler frequency by an amount proportional to the average electron density up to the height of the satellite.

In practice corrections must be applied for the effects of: 1) passage off-zenith; 2) larger refraction; 3) the probable electron distribution; and 4) vertical satellite motion, as well as for the possible nonuniformity of the ionosphere.

Refractive Doppler frequencies, measured during a typical passage of Satellite 1958 Delta 2 near noon, are analyzed by this method and the above corrections listed to yield the columnar electron density to a height of 800 km. Concurrent reduced ionograms are included for comparison and the results are discussed.

The Scintillation of Radio Signals from Satellites—K. C. Yeh, *Dept. of Electrical Engineering* and G. W. Swenson, *Depts. of Electrical Engineering and Astronomy, University of Illinois, Urbana, Ill.*—Signals from Satellites $1957\alpha_2$ and $1958\delta_2$, recorded during a 20-month period, are analyzed to determine the diurnal and seasonal variations of the incidence of scintillation. Marked diurnal effects are noted, scintillation being much more frequent at night. Night-time scintillation correlates with the occurrence of ionospheric "spread-F" and apparently originates in inhomogeneities at heights of about 220 km and, in most cases, at latitudes greater than 40° north. Daytime scintillation appears to originate in smaller, inhomogeneous regions below 220 km and more widely distributed in latitude.

Detection Techniques for Interplanetary Radar Observations*—P. E. Green, Jr., *Lincoln Lab., M.I.T., Lexington, Mass.*—This is a review paper intended to summarize the specific techniques necessary to most efficiently probe planetary bodies and interplanetary material by radar. After setting forth the radar equations for distributed targets (both of the type that do and do not fill the antenna beam), the discussion concentrates on specific waveform coding techniques appropriate to this problem. It is pointed out that "pulse coding" into long sequences of individual pulses in principle allows one to discriminate in range to within the individual pulse width while discriminating in Doppler frequency to within the reciprocal of the over-all sequence length. Practical limitations on this procedure are discussed and a particular scheme of pulse coding and received data processing we have used in radar probing of Venus is presented.

* The work reported in this paper was supported jointly by the U. S. Army, Navy, and Air Force.

Threshold Probability—R. H. Dishington, *Ramo-Wooldridge Corp., Los Angeles, Calif.*—Sometimes, in systems involving noise as well as signals, threshold probability will be the criterion for evaluating the whole system. This detection probability is determined by four basic factors, false alarm probability, signal-to-noise ratio, noise-to-noise ratio, and the probability distribution of the output. The latter is difficult to determine, and is often assumed to be Gaussian as a result of filtering and the Central Limit Theorem. A companion paper shows that the latter assumption is not necessarily true. This paper shows that, in most practical cases, the output is "equivalent" to Gaussian *even where there is no filtering and the Central Limit Theorem does not apply.*

A Criterion for the Filtering Required to Produce Gaussian Noise—K. Moe, *Ramo-Wooldridge Corp., Los Angeles, Calif.*—The probability distributions encountered in electronic circuits often approach the normal distribution as a consequence of filtering. This situation has frequently been described in connection with radar receivers. In the past several years, filtering problems have arisen in correlators and countermeasures receivers as well. The approach of this paper is to regard bandwidth reduction as equivalent to integration over n independent samples, where n is the ratio of input to output bandwidth. An estimate is given for the error introduced by this simplifying assumption. The output probability density is then given by the Edgeworth Series in terms of n and the input probability density. The first term in the Edgeworth Series is the Gaussian distribution. The criterion for the approach to the normal distribution is that the ratio of the largest value of the second nonzero term to the largest value of the first term be a small number, f. The relationship between f and n for symmetric and skewed distributions is presented in analytical and graphical form. The first few moments of the input distribution are the only information needed to use the graphs. The method is intended to be of practical value to engineers who make measurements on circuits which include filters.

Optimum Signals for Finite Memory Matched Filters*—W. H. Kim and R. J. Schwarz, *Dept. of Electrical Engineering, Columbia University, New York, N. Y.*—In the problem of detecting a signal imbedded in additive noise, a matched filter gives maximum signal-to-noise ratio at a specified instant provided the noise is white or the filter has infinite memory. If the signal is subject to control by the designer, however, a matched filter may be optimum for any piecewise continuous noise correlation function and for finite filter memory. The optimum signal, hence the optimum filter impulse response, is given by the solution of a linear integral equation of the second kind with a symmetric kernel. Approximation methods for solving this integral equation are discussed which lead directly to the filter realization. The performance of such filters is compared with that given by an exact solution.

* The research for this report was partially supported by the ON Research under contract Nonr 266(60) and by National Science Foundation Grant NSF G-3676.

On a Characterization of Processes for Which Optimal Mean Square Filters are of Specified Form—A. V. Balakrishnan, *Dept. of Mathematics, University of California, Los Angeles, Calif.*—This paper presents the first results in an unconventional approach to the problem of not-necessarily-linear mean square optimization. Instead of obtaining a representation for the optimal nonlinear operator for a process, we seek to characterize the class of processes for which the optimal operator is of specified form. If the processes are given, so that the multivariate characteristic functions are known, then our results can be used to tell whether it is possible for the optimal operator to have a specified form. The bulk of the paper pertains to the signal extraction problem where the signal and noise are independent and additive, and it is desired to estimate some function of the signal. Here, with a slight shift in viewpoint, we phrase the characterization problem in the following way: given say, a noise process, determine the class of signal processes for which the optimal extraction filter is of specified form. The case where the noise process is Gaussian comes in for special attention.

Contributors

P. R. Arendt was born in Dresden, Germany, on July 1, 1900. In 1924 he received the Ph.D. degree in physics from the University of Berlin, Germany (M. Plank and F. Haber).

P. R. Arendt

In 1924 he joined Siemens and Halske A. G., Berlin, where, until 1929, he participated in the research and development of multiple carrier, picture telegraphy over loaded cables, and acoustical standards. From 1929 to 1935 he worked for the International Telephone and Telegraph Company in London, Paris, and Berlin, as chief engineer of Standard Elektrizitaets Gesellshaft. There he performed engineering and research in all fields of communication, including magnetic sound recording, wired-wireless and common-frequency broadcasting. From 1935 to 1957, as technical director of Allgemeine Electrizitaets Gesellschaft, Berlin and Frankfurt, he supervised the research, and development, and patent policy of the concern and other associated companies, including Telefunken and Osram. He was consultant to the president of the Board of Directors, and, during the war, produced an infrared proximity fuze for the V-2. Since 1957 he has been chairman of the Radiation Effects Committee at the Institute for Exploratory Research, U. S. Army Signal Research and Development Laboratory, Fort Monmouth, N. J., where he has done special research on satellite radio propagation.

Dr. Arendt is a member of the American Nuclear Society and Deutsche Physikalische Gesellschaft.

J. William Carr (S'49–A'50–M'53) was born on December 27, 1920, in Killdeer, N. D. He received the B.S. degree in electrical engineering in 1949 from the University of California, Berkeley, and the M.S. degree in electrical engineering in 1951 from Ohio State University, Columbus.

J. W. Carr

He served for six years in the U. S. Navy as a radio operator and electronics technician. From 1949 to 1951, he was employed at Wright-Patterson Air Force Base, Dayton, Ohio and from 1951 to 1958, was employed at Gilfillan Bros., Inc., Los Angeles, Calif., where he was engaged in the design and development of RF components and systems. In 1958, he joined the staff of the Lockheed Missiles and Space Division, Electromagnetics Department, where he is primarily engaged in antenna research and development.

❖

Edward S. Cassedy, Jr. (A'52–M'57) was born in Washington, D. C., on August 19, 1927. He received the B.S. degree in electrical engineering from Union College, Schenectady, N. Y., in 1949. In 1950 he received the S.M. degree from Harvard University, Cambridge, Mass., and in 1959 the Eng.D. degree from Johns Hopkins University, Baltimore, Md.

In 1950 he worked for the Potomac Electric Power Co., Washington, D. C., and in 1951 he joined the U. S. Naval Ordnance Laboratory, White Oak, Md., working there on telemetering problems, UHF circuit and antenna design. In 1954 he joined the Radiation Laboratory of Johns Hopkins University, where he has been engaged in research on electromagnetic scattering and microwave problems.

E. S. Cassedy, Jr.

Dr. Cassedy is a member of Sigma Xi and the American Association for the Advancement of Science.

❖

David H. Denton, Jr. (S'57–M'59) was born on December 25, 1929, in Wichita Falls, Tex. He served in the Army from 1953 to 1955, and later attended Texas Christian University, Fort Worth. He received the B.A. degree in mathematics in 1957 and the B.S.E.E. degree in 1958 from Texas Technological College, Lubbock.

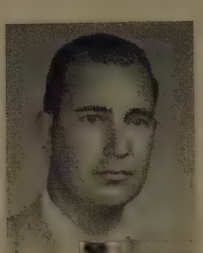

D. H. Denton, Jr.

In 1958, he joined the Antenna Research and Development Section at the Sandia Laboratory, Albuquerque, N. M., where he has been engaged in work on missile antennas, dielectric lenses, and wave propagation in dissipative media. He is concurrently carrying out graduate studies at the University of New Mexico, Albuquerque.

Mr. Denton is a member of Eta Kappa Nu and Tau Beta Pi.

J. FAINBERG

Joseph Fainberg was born in Passaic, N. J., on October 18, 1930. He received the B.A. degree from the College of the University of Chicago, Chicago, Ill., in 1950. In 1951 he received the B.S. degree in mathematics and in 1953 the M.S. degree in physics, both from the University of Chicago.

From 1951 to 1957, he worked as a research assistant in cosmic rays and meson physics at the University of Chicago. In 1957 he joined the Radiation Laboratory of Johns Hopkins University, Baltimore, Md., where he is presently employed, and where he has worked on electromagnetic scattering and diffraction problems.

Mr. Fainberg is a member of Phi Beta Kappa, Sigma Xi, and the American Association for the Advancement of Science.

❖

W. J. FAY

William J. Fay (S'46–M'57) was born in New York, N. Y., on November 8, 1919. He received the B.S. degree in electrical engineering from Stanford University, Stanford, Calif., in 1956.

From 1940 to 1942 he worked with the Bethlehem Steel Company, New York, N. Y. From 1942 to 1946 and again from 1951 to 1953, he was with the U. S. Navy, where he gained experience in fire control, ship gyroscopes, electronic and mechanical computers, hydraulic drives, servo systems, and radar and communication systems. He worked on the installation and maintenance of telephone exchange systems with the Bell Telephone System from 1947 to 1950, and from 1956 to 1957 he worked with the U. S. Navy Electronics Laboratory in San Diego, Calif. Since 1957, he has been with Smyth Research Associates, San Diego, Calif., where he has done research work in ionospheric propagation, meteor trail propagation and ionospheric physics, and has developed experimental equipment and techniques for meteor trail studies.

❖

Robert C. Hansen (S'47–A'49–M'55–SM'56) was born on August 8, 1926, in St. Louis, Mo. He attended the Missouri School of Mines and Metallurgy, Rolla, from which he received the B.S. degree in electrical engineering in 1949. He received the M.S. and Ph.D. degrees in 1950 and 1955, respectively, from the University of Illinois, Urbana.

While at the University of Illinois he worked at the Antenna Laboratory, on ferrite loops and streamlined airborne antennas. From 1955 to 1959 he was at the Microwave Laboratory of Hughes Aircraft Co., Culver City, Calif., where, as senior staff engineer, he worked on surface-wave antennas, slot arrays, and related fields. At present he is senior staff engineer at the Telecommunications Laboratory of Space Technology Laboratories, Inglewood, Calif.

R. C. HANSEN

Dr. Hansen is a member of the American Physical Society, Commission VI of URSI, Tau Beta Pi, Sigma Xi, Eta Kappa Nu, and Phi Kappa Phi.

❖

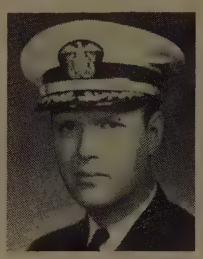

C. W. HARRISON, JR.

Charles W. Harrison, Jr. (SM'57) was born on September 15, 1913, in Virginia. He attended the U. S. Coast Guard Academy, New London, Conn., and received the B.S.E.E. and E.E. degrees in 1939 and 1940, respectively, from the University of Virginia, Charlottesville. He received the M.S. degree in communication engineering in 1942 from Harvard University, Cambridge, Mass., and under the sponsorship of the ONR, received the M.E. and Ph.D. degrees in applied physics from Harvard in 1952 and 1954, respectively.

He completed the Navy course in radar engineering at the Massachusetts Institute of Technology, Cambridge, in 1942, and subsequently was engaged in lecturing to officers of the Armed Forces assigned to the radar schools at Harvard and Princeton University, Princeton, N. J., for several years. He has had four tours of duty in the Electronics Design and Development Division, Bureau of Ships; two at the U. S. Naval Research Laboratory; one at the Signal Corps Engineering Laboratories (Evans Signal Laboratory); one at the Philadelphia Naval Ship Yard; one as Electronics Officer, Staff of Commander Operational Development Force; and one on the Staff of the Chief, Armed Forces Special Weapons Project. He left active service as a Commander in the regular Navy in 1957 to join the Scientific Staff of the Sandia Laboratory, Albuquerque, N. M.

Dr. Harrison is a member of the Research Society of America, the American Scientific Affiliation, URSI, and Sigma Xi. He is a registered professional engineer in Virginia, the District of Columbia, and Massachusetts.

❖

Gedaliah Held (A'54) was born in Warsaw, Poland, on January 4, 1926. He attended the Hebrew University in Jerusalem and received the M.S. degree in physics in 1950. Shortly thereafter, he came to the United States as a graduate student at the University of California, Berkeley, where he received the Ph.D. degree in electrical engineering in 1954.

From 1952 to 1954, he was a member of the technical staff of the University of California Antenna Laboratory and an instructor in the department of electrical engineering. He then joined the staff of the University of Washington in Seattle, where he is presently an associate professor in electrical engineering, specializing in microwave radiation and propagation.

G. HELD

Dr. Held is a member of Sigma Xi.

❖

J. L. HERITAGE

James L. Heritage (A'49–M'55) was born in Baltimore, Md., on July 11, 1920. He received the B.S. degree in electrical engineering from the University of Alabama, University, Ala., in 1942.

From 1942 to 1943 he worked with the General Electric Co., Schenectady, N. Y., and from 1943 to 1946 with the U. S. Navy. He was with the U. S. Navy Electronics Laboratory, San Diego, Calif., from 1947 to 1955 as an electronic scientist, where he did development work in communications, diversity systems and high power transmitters, and was in charge of a group engaged in research studies concerned with ionospheric and VLF propagation problems. He is now with Smyth Research Associates, San Diego, Calif., where he is a senior engineer, engaged in system studies, research in ionospheric physics and meteor trail studies, and antenna development.

❖

A. ISHIMARU

Akira Ishimaru was born on March 16, 1928, in Fukuoka, Japan. He received the B.S. degree in electrical engineering in 1951 from Tokyo University, and the Ph.D. degree in electrical engineering in 1958 from the University of Washington, Seattle.

Having been a research engineer at the Electrotechnical Laboratory in Japan, and an instructor at the University of Washington, he was then employed by the Bell Telephone Laboratories where he worked on antenna problems. Now assistant professor of electrical engineering at the University of Washington, he has done research in microwave antennas, and antenna synthesis problems.

Dr. Ishimaru is a member of Sigma Xi.

Ronold W. P. King, for a photograph and biography please see page 115 of the January, 1959 issue of these TRANSACTIONS.

❖

Roger Manasse (M'56) was born in New York, N. Y., on April 9, 1930. He received the B.S. degree in physics in 1950, and the Ph.D. degree in physics in 1955, both from the Massachusetts Institute of Technology, Cambridge.

R. MANASSE

During the period 1950–1952, he was on the staff of the M.I.T Instrumentation Laboratory, where he was engaged in research and development of components for inertial guidance systems. From 1954 to 1959 he was a staff member of the M.I.T. Lincoln Laboratory, Lexington, Mass., where he was mainly concerned with the application of statistical methods to the analysis and design of radar systems. In September, 1959, he joined the MITRE Corporation, Bedford, Mass., where he is a subdepartment head in the Radar Systems and Techniques Department.

Dr. Manasse is a member of Sigma Xi.

❖

John J. Myers (S'43–A'45–M'47–SM'50) was born in Columbus, Ohio, on August 3, 1920. He received the B.E.E. degree from Ohio State University, Columbus Ohio, in 1943 and the M.S. and Ph.D. degrees in electrical engineering from the University of Illinois, Urbana, Ill., in 1947 and 1959, respectively.

J. J. MYERS

In 1943 he went on active duty with the U. S. Navy and was assigned to the Fire Control Section of the Radio Division of the Naval Research Laboratory, Washington, D. C., as a development engineer for monopulse radar. In 1946, upon return to inactive duty, he joined the Radio Direction Finding Laboratory of the University of Illinois as a Research Associate and remaining there during the period 1946–1949, during which time he completed the required course work and examinations, except the thesis, for the doctorate.

During the academic year 1949–1950 he conducted a radio propagation survey in the Hawaiian Islands for the Hawaiian Telephone Company, Honolulu, returning to the University of Illinois Radio Direction Finding Laboratory for the 1950–1951 academic year. In 1951 he joined the Automatic Electric Co., Chicago, Ill., as Division Manager for microwave communication systems. In 1954 he was sent to Milan, Italy, to organize and head the Electronics Department of the Automatic Electric affiliated organization, Autelco Mediterranea. After his return to the U. S. in 1956, he was a member of the administration staff of the Automatic Electric Laboratories (now General Telephone Laboratories), Northlake, Ill., until he joined Stewart-Warner Electronics, Chicago, Ill., in 1956. In 1957 he returned to the University of Illinois as a Research Associate in the Coordinated Science Laboratory (formerly the Control Systems Laboratory). He was then appointed Research Assistant Professor and was engaged in radar countercountermeasures, high-resolution radar, and antenna studies.

He is presently affiliated with the Hoffman Science Center, Santa Barbara, Calif., as head of the Industrial Electronics Group. In this position he is responsible for new product studies in industrial and transportation electronics.

Dr. Myers is a member of Sigma Xi and of Eta Kappa Nu.

❖

Louis E. Raburn (S'41–A'44–M'46–SM'50) was born in Manhattan, Kans. on June 4, 1919. He received the B.S. degree in communications engineering from Kansas State College, Manhattan, Kans. in 1941, and from 1942 to 1943 did graduate work at Harvard University, Cambridge, Mass., specializing in antenna and field theory.

L. E. RABURN

In 1941 and 1942 he was a carrier engineer with the American Telephone and Telegraph Company. From 1942 to 1945 he was a research associate in the Harvard Radio Research Laboratory developing electronic countermeasures modulators and receivers. He was antenna group supervisor at Electronics Research, Inc., Evansville, Ind., from 1946 to 1953. Here he supervised the development of aircraft radio antennas, radar antennas, and commercial antennas for FM broadcasting and mobile UHF reception. From 1954 to 1957 he was the staff consultant on antennas at the Crosley Division of AVCO, where he participated in the theoretical analysis of large-aperture antenna cross polarization. From 1957 to 1959, he was coordinator of antennas and special systems for General Electric's Missile and Ordnance Systems Department, and there supervised the development of several antennas, and ancillary components. He came to Philco Corp., Philadelphia, Pa. in 1959, where he is now manager of the Antenna and Microwave Components Section in the Government and Industrial Division.

Mr. Raburn is listed in "Who's Who for Engineers of the Midwest."

❖

Dipak L. Sengupta, for a photograph and biography, please see page 306 of the July, 1959 issue of these TRANSACTIONS.

S. R. Seshadri, for a photograph and biography, please see page 443 of the October, 1950 issue of these TRANSACTIONS.

❖

Raymond Tang (S'53–M'55) was born on December 18, 1933 in Shanghai, China. He received the B.S.E.E. degree from the Polytechnic Institute of Brooklyn, N. Y., in 1955, and the M.S.E.E. degree from the University of Southern California, Los Angeles, Calif., in 1958.

R. TANG

From 1955 to 1959, Mr. Tang worked at the Antenna Department of the Microwave Laboratory of the Hughes Aircraft Co. at Culver City, Calif. He transferred to the Microwave Department of the Radar Laboratory of the Hughes Aircraft Co. at Fullerton, Calif., in 1959. He has been engaged in work on microwave antenna design and development since 1955.

Mr. Tang is a member of Eta Kappa Nu.

❖

Thomas T. Taylor (A'43–M'50) was born in Montpelier, Ind. on April 18, 1921. He received the B.S. degree in physics from Purdue University, Lafayette, Ind., in 1942 and the M.S. and Ph.D. degrees in physics from the California Institute of Technology, Pasadena, in 1953 and 1958, respectively.

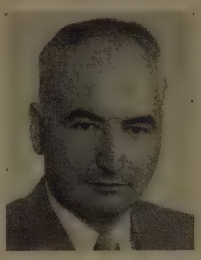

T. T. TAYLOR

From 1942 to 1946, Dr. Taylor was employed as an engineer by the General Electric Company and was connected with several radar and microwave projects; from 1946 to 1954 he was with the Hughes Aircraft Company as a research physicist specializing in antenna theory. Although primarily engaged in graduate studies from 1954 to 1958, he also served as a part-time consultant for the Consolidated Electrodynamics Corporation of Pasadena, Calif.

Dr. Taylor was a part-time instructor in the engineering extension, University of California, Los Angeles, during the years 1947–1950 and 1957–1958. Since 1958, he has been with the Division of Physical Sciences, University of California, Riverside, as an assistant professor of physics.

Dr. Taylor is a member of the American Physical Society, the American Association for the Advancement of Science, Sigma Pi Sigma, and Sigma Xi.

❖

Steven Weisbrod (S'49–A'50–M'55), was born in Warsaw, Poland, on July 30, 1925. He came to the United States in 1939, and

received the B.S. degree in physics in 1949 from the California Institute of Technology, Pasadena, and the M.S. degree in engineering in 1959, from the University of California at Los Angeles. During World War II he served with the American expeditionary forces in Europe. From 1949 to 1955, he was employed as a physicist at the Navy Electronics Laboratory, San Diego. Calif., where he specialized in problems of ionospheric radio propagation, backscatter and diversity systems. In 1953, for work on the High Frequency backscatter system, he received the Navy Superior Accomplishment Award. In 1955, together with colleagues, he helped form Smyth Research Associates in San Diego. He is now senior physicist there, and in this capacity is continuing basic research in the field of ionospheric physics, electromagnetic wave propagation and meteor and field aligned scatter.

S. Weisbrod

Mr. Weisbrod is a member of the American Mathematical Society.

William J. Welch was born in West Chester, Pa., on January 17, 1934. He attended Oberlin College, Oberlin, Ohio, and received the B.S. degree in physics from Stanford University, Stanford, Calif., in 1955. From 1956 to the present, he has been at the University of California, Berkeley. During 1956 and 1957, he was a Research Assistant in the Antenna Laboratory, and in 1958, he received the M.S. degree in engineering science. Since 1958, he has been a Teaching Associate in the Electrical Engineering Department and is currently completing the requirements for the Ph.D. degree in engineering science. His major interest is in the scattering and diffraction of electromagnetic waves.

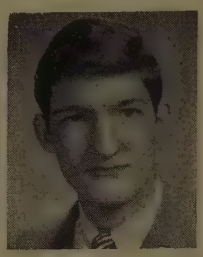

W. J. Welch

❖

Tai Tsun Wu was born in Shanghai, China, on December 1, 1933. He received the B.S. degree from the University of Minnesota, Minneapolis, in 1953, and the M.S. and Ph.D. degrees from Harvard University, Cambridge, Mass., in 1954 and 1956, respectively.

T. T. Wu

He was a Junior Fellow of the Harvard Society of Fellows from 1956 to 1959. He has carried on research during the summers at Brookhaven National Laboratories, Upton, N. Y., at Stanford University, Stanford, Calif., and with Bell Telephone Laboratories, New York, N. Y. and also spent a year at the Institute for Advanced Study in Princeton, N. J.

At present, he holds the position of assistant professor of applied physics at Harvard University.

Dr. Wu is a member of Tau Beta Pi, Eta Kappa Nu, Sigma Xi, the American Mathematical Society, and the American Physical Society.

ANNOUNCEMENT

IRE-URSI Joint Spring Meeting

Sheraton Park Hotel, Washington, D. C.

May 2—5, 1960

Index to

IRE TRANSACTIONS

ON

ANTENNAS AND PROPAGATION

Volume AP-7, 1959

IRE Transactions on Antennas and Propagation

Index to Volume AP-7, 1959

Contents

Volume AP-7, Special Supplement, December, 1959

Index to Authors

Index to Subjects

PROCEEDINGS OF THE URSI INTERNATIONAL SYMPOSIUM ON ELECTROMAGNETIC THEORY, Toronto, Canada, JUNE 15-20, 1959

PGAP members and subscribers are urged to order their copies now, accompanied by remittance made payable to The Institute of Radio Engineers, 1 East 79th Street, New York 21, N.Y., at the following rates:

	Price per Copy
PGAP Members	$ 8.00
Other IRE Members	$11.00
Libraries	$12.00
Nonmembers	$16.00

AVAILABLE BACK ISSUES OF IRE TRANSACTIONS ON ANTENNAS AND PROPAGATION

PUBLICATION	PRICES		
	Group Members	IRE Members	Non-* Members
Vol. AP-2, No. 2, April, 1954	$2.00	$3.00	$6.00
Vol. AP-4, No. 4, Oct., 1956	$2.10	$3.15	$6.30
Vol. AP-5, No. 1, Jan., 1957	$3.20	$4.80	$9.60
Vol. AP-5, No. 2, April, 1957	$1.75	$2.60	$5.25
Vol. AP-5, No. 3, July, 1957	$2.00	$3.00	$6.00
Vol. AP-5, No. 4, Oct., 1957	$1.70	$2.55	$5.10
Vol. AP-6, No. 1, Jan., 1958	$3.85	$5.80	$11.55
Vol. AP-6, No. 2, April, 1958	$1.15	$1.75	$3.45
Vol. AP-6, No. 3, July, 1958	$2.40	$3.60	$7.20
Vol. AP-6, No. 4, Oct., 1958	$1.50	$2.25	$4.50
Vol. AP-7, No. 1, Jan., 1959	$2.50	$3.75	$7.50
Vol. AP-7, No. 2, April, 1959	$1.75	$2.60	$5.25
Vol. AP-7, No. 3, July, 1959	$1.75	$2.60	$5.25
Vol. AP-7, No. 4, Oct., 1959	$2.55	$3.85	$7.65
Vol. AP-7, SS†, Dec., 1959	$8.00	$12.00	$16.00

* All libraries and subscription agencies may purchase at the IRE Member rate.

† Special supplement.

EXPANSION

to keep pace with

the growing challenge of

ELECTRONICS

at GRUMMAN AIRCRAFT

Grumman Aircraft Engineering Corporation's long and continuing responsibilities for the design of Avionics Systems for ASW, AEW, Reconnaissance, and all-weather attack aircraft has necessitated vast facilities expansion. A new five million dollar Avionics Center will provide 62,000 square feet of floor space devoted exclusively to activities involving test, evaluation and integration of Avionics Systems.

Concurrent expansion of our staff of electronics engineers and scientists has created positions for men anxious to participate in varied and intellectually stimulating programs utilizing the most modern of facilities.

★ **Communications Engineer.** EE or Physicist with knowledge of communication theory including advantages of various modes of modulation and effects of propagation within and out of the atmosphere. To keep advised of the state of the art of communications systems for data, voice and video links for air-to-ground, air-to-air, space-to-ground transmissions and reception; to recommend radio frequencies and modulation techniques for various missile and space craft communication applications; to conduct preliminary design of communication systems in order to estimate weight and power requirements; to propose and conduct research on advanced communication systems.

★ **Radio Interference Control Engineers.** Engineers to analyze the source of conducted and radiated interference caused by the interaction of complex electronic equipments and systems, and develop methods and techniques to suppress the interference in the advanced design state of aircraft and missiles.

★ **Radome or Antenna Design Engineer.** BSEE or Physics degree with a minimum of 3 years' experience in radome design. Background in classical Electromagnetic theory and advanced math essential. Work consists of analysis and synthesis of radomes or antennas on current and advanced designs including the use of the IBM computer facilities to develop design techniques.

★ **Communications Equipment Engineer.** BSEE with a minimum of 5 years' experience with thorough knowledge of single sideband theory and its application. Should possess a complete understanding of AM, FM, PM and single sideband modulation processes and their application as well as techniques. Must have experience in analyzing and testing communications receivers and transmitters, and should be thoroughly familiar with HF and UHF antennas and associated propagation problems. A background in digital equipment, encoders, decoders and magnetic storage devices is an important consideration.

★ **Radar Systems Engineer.** BSEE with a minimum of 5 years' experience in design development and analysis of advanced radar systems. Capable of integrating the Radar into complex airborne Avionics Systems including the following specific skills; Analysis of System, Compatibility with Weapons System, Preparation of Specifications, Vendor Liaison and Direction, Test and Evaluation, Flight Development.

You are invited to investigate these opportunities by sending your resume to Mr. A. Wilder, Engineering Personnel Director, Dept. GR-71, who will arrange an interview at your convenience. (U.S. Citizenship required).

GRUMMAN AIRCRAFT ENGINEERING CORPORATION

Bethpage • Long Island • New York

For Information

Concerning Advertising

Rates Contact

Mr. Delmar C. Ports

Jansky and Bailey, Inc.

1339 Wisconsin Ave.,

N.W.

Washington 7, D.C.

Telephone:

Federal 3-4800

INSTITUTIONAL LISTINGS

The IRE Professional Group on Antennas and Propagation is grateful for the assistance given by the firms listed below, and invites application for Institutional Listing from other firms interested in the field of Antennas and Propagation.

ANDREW CORPORATION, 363 E. 75th St., Chicago 19, Ill.
Antennas, Antenna Systems, Transmission Lines, Development and Production.

ANTLAB, INC., 6330 Proprietors Rd., Worthington, Ohio
Antenna Pattern Range Systems—Recorders & Mounts.

BLAINE ELECTRONETICS, INC., 14757 Keswick St., Van Nuys, Calif.
Antennas, Paraboloids, Scale Models, Antenna Radiation Pattern Measurement Towers.

DEVELOPMENTAL ENGINEERING CORP., 1001 Conn. Ave. N.W., Washington, D. C. and Leesburg, V
Research, Development, Installation of Antennas and Antenna Equipment for Super Power Stations.

THE GABRIEL LABORATORIES, Div. of the Gabriel Co., 135 Crescent Road, Needham Heights 94, Mas
Research and Development of Antenna Equipment for Government and Industry.

HUGHES AIRCRAFT COMPANY, Culver City, Calif.
Research, Development, Mfr.: Radar, Missiles, Antennas, Radomes, Tubes, Solid State Physics, Computers.

I-T-E CIRCUIT BREAKER CO., Special Products Div., 601 E. Erie Ave., Philadelphia 34, Pa.
Design, Development and Manufacture of Antennas, and Related Equipment.

JANSKY & BAILEY, INC., 1339 Wisconsin Ave. N.W., Washington 7, D. C.
Radio & Electronic Engineering; Antenna Research & Propagation Measurements; Systems Design & Evaluatio

MARK PRODUCTS CO., 6412 W. Lincoln Ave., Morton Grove, Ill.
Multi Element Grid Parabolas, Antennas for Two-Way Communications, R & D.

THE W. L. MAXSON CORP., 475 Tenth Ave., New York 18, N.Y.
Research, Development, & Manufacture of Airborne, Missile & Ordnance Systems & Equipment.

TRANSCO PRODUCTS, INC., 12210 Nebraska Ave., Los Angeles 25, Calif.
Res., Design, Dev., & Mfr. of Antenna Systems & Components for Missile, Aircraft & Ground Installations

WEINSCHEL ENGINEERING COMPANY, INC., Kensington, Md.
Antenna Pattern Receivers; Bolometer Amplifiers; Modulated Microwave Sources;
Insertion Loss Measuring Systems

WHEELER LABORATORIES, INC., Great Neck, N. Y.; Antenna Lab., Smithtown, N. Y.
Consulting Services, Research and Development, Microwave Antennas and Waveguide Components.

WIND TURBINE COMPANY, West Chester, Pa.
Complete Antenna Systems and Towers

The charge for an Institutional Listing is $25.00 per issue or $75.00 for four consecutive issues. Application may be made to the Technical Secretary, The Institute of Radio Engineers, 1 East 79th Street, New York 21, N. Y.